SANDIA REPORT

SAND2017-11289
Unlimited Release
Printed October 2017

RANS Based Methodology for Predicting the Influence of Leading Edge Erosion on Airfoil Performance

Christopher M Langel, Raymond Chow, C.P van Dam

David C. Maniaci, Sandia Technical Manager

Prepared by
Sandia National Laboratories
Albuquerque, New Mexico 87185 and Livermore, California 94550

Sandia National Laboratories is a multimission laboratory managed and operated by National Technology and Engineering Solutions of Sandia, LLC, a wholly owned subsidiary of Honeywell International, Inc., for the U.S. Department of Energy's National Nuclear Security Administration under contract DE-NA0003525.

Sandia National Laboratories

Issued by Sandia National Laboratories, operated for the United States Department of Energy by Sandia Corporation.

Available to DOE and DOE contractors from
U.S. Department of Energy
Office of Scientific and Technical Information
P.O. Box 62
Oak Ridge, TN 37831

Telephone: (865) 576-8401
Facsimile: (865) 576-5728
E-Mail: reports@adonis.osti.gov
Online ordering: http://www.osti.gov/bridge

Available to the public from
U.S. Department of Commerce
National Technical Information Service
5285 Port Royal Rd
Springfield, VA 22161

Telephone: (800) 553-6847
Facsimile: (703) 605-6900
E-Mail: orders@ntis.fedworld.gov
Online ordering: http://www.ntis.gov/help/ordermethods.asp?loc=7-4-0#online

SAND2017-11289
Unlimited Release
Printed October 2017

RANS Based Methodology for Predicting the Influence of Leading Edge Erosion on Airfoil Performance *

Christopher M. Langel, Raymond Chow, and C.P. van Dam
Department of Mechanical and Aerospace Engineering
University of California, Davis
Davis, CA 95616

Sandia Contract No. 1228734

Technical Manager:

David C. Maniaci
Wind Energy Technologies Department
Sandia National Laboratories
P.O. Box 5800
Albuquerque, NM 87185-1124

Abstract

The impact of surface roughness on flows over aerodynamically designed surfaces is of interested in a number of different fields. It has long been known the surface roughness will likely accelerate the laminar-turbulent transition process by creating additional disturbances in the boundary layer. However, there are very few tools available to predict the effects surface roughness will have on boundary layer flow. There are numerous implications of the premature appearance of a turbulent boundary layer. Increases in local skin friction, boundary layer thickness, and turbulent mixing can impact global flow properties compounding the effects of surface roughness. With this motivation, an investigation into the effects of surface roughness on boundary layer transition has been conducted. The effort involved both an extensive experimental campaign, and the development of a high fidelity roughness model implemented in a RANS solver. Vast amounts of experimental data was generated at the Texas A&M Oran W. Nicks Low Speed Wind Tunnel for the calibration and validation of the roughness model described in this work, as well as future efforts. The present work focuses on the development of the computational model including a description of the calibration process.

The primary methodology presented introduces a scalar field variable and associated transport equation that interacts with a correlation based transition model. The additional equation allows for non-local effects of

*The work described in this report was performed for Sandia National Laboratories under Contract No. 1228734

surface roughness to be accounted for downstream of rough wall sections while maintaining a "local" formulation. The scalar field is determined through a boundary condition function that has been calibrated to flat plate cases with sand grain roughness. The model was initially tested on a NACA 0012 airfoil with roughness strips applied to the leading edge. Further calibration of the roughness model was performed using results from the companion experimental study on a NACA 63_3-418 airfoil. The refined model demonstrates favorable agreement predicting changes to the transition location, as well as drag, for a number of different leading edge roughness configurations on the NACA 63_3-418 airfoil. Additional tests were conducted on a thicker S814 airfoil, with similar roughness configurations to the NACA 63_3-418. Simulations run with the roughness model compare favorably with the results obtained in the experimental study for both airfoils.

Acknowledgment

Numerous parties have contributed to the completion this report. The authors gratefully acknowledge the support of the US Department of Energy's Wind Energy Technologies Office (WETO) and Sandia National Laboratories. Additionally the work was supported by the National Science Foundation GK-12 RESOURCE program under grant No. DGE-0948021.

Significant contributions were provided by Professor Edward White, Dr. Robert Ehrmann, and Dr. Benjamin Wilcox of Texas A&M University. In addition to conducting the large wind tunnel campaigns described in the report, they supplied a large source of knowledge, and shared valuable insights that helped push this work forward.

Contents

Appendix

List of Figures

List of Tables

Nomenclature

Re_k — Roughness Reynolds number ($Re_k = U_k k_s/\nu$)

$Re_{k,cr}$ — Critical roughness Reynolds number

U_k — Flow velocity at roughness height

k — Roughness height

k_s — Equivalent sand grain roughness height

k^+ — Dimensionless equivalent sand grain roughness height ($k^+ = \mu_t k_s/\nu$)

R_a — Centerline average roughness height

R_q — RMS roughness height

R_z — Average peak to valley roughness height

A_r — Roughness amplification quantity

$\P_{\theta t}$ — Production term for $\tilde{R}e_{\theta t}$ transport equation

$F_{\theta t}$ — Boundary layer indicator function

F_{A_r} — Roughness amplification function in modified $\tilde{R}e_{\theta t}$ production term

λ_θ — Thwaites pressure gradient parameter

θ — Boundary layer momentum thickness

δ^* — Boundary layer displacement thickness

H — Boundary layer shape factor (δ^*/θ)

Re_θ — Momentum thickness Reynolds number ($Re_\theta = \theta U_e/\nu$)

$\tilde{R}e_{\theta t}$ — Local transition onset momentum thickness Reynolds number (computed from transport equation)

$Re_{\theta t}$ — Transition onset momentum thickness Reynolds number (computed from correlation function)

Re_v — Vorticity/strain-rate Reynolds number

γ — Intermittency variable in Langtry-Menter transition model

Tu — Freestream turbulence intensity

c — Chord length

DNS — Direct numerical simulation

LES — Large eddy simulation

DES — Detached eddy simulation

RANS – Reynolds averaged Navier-Stokes

SST — Shear stress transport turbulence model

LCTM – Local correlation transition model

FSTI — Freestream turbulence intensity

LSWT – Low Speed Wind Tunnel

Chapter 1

Introduction

Surface roughness has been the topic of countless studies over the past century. While it is not difficult to make broad generic statements regarding the impact roughness may have on the flow over a contaminated surface, a more acute description of what these effects might be has proven exceptionally challenging. A closer look at the problem reveals the true depth of the topic, and all the inherent challenges of fully quantifying the effects of surface roughness. To begin, there is the problem of describing the roughness itself; that is the height, width, shape, uniformity, and so forth. The measurement of simply the roughness topology carries challenges, not to mention the measurement of the flowfield surrounding it. To this day experimentalists struggle to accurately measure flow parameters without introducing invasive instruments, and without losing meaningful information due to the spatial and temporal resolution required to capture the measurements (including parts of this study). All of these complications arise even before the problem of modeling or generating an analytical description of the effects. It would be unreasonable to expect a single study to fully envelop all the associated elements of surface roughness and its impacts. Therefore it is important to break down the affiliated components, and select a reasonable scope.

There are two questions that must immediately be asked when looking at the problem of surface roughness effects. One must first define what roughness means, as at some microscopic level, nothing is truly *smooth*. Secondly, there is the question of exactly what effects are being measured or modeled. Does every individual perturbation need to be accounted for or simply some change to a global performance coeffecient? These questions will be addressed both here and in relevant sections to provide as much clarity to the reader as possible. In the context of the current work, surface roughness refers to some type of contamination on a object or surface that has been designed aerodynamically. This includes, but is not limited to, lifting surfaces of an aircraft, wind turbine blades, and gas turbine vanes. The present work also does not seek to model the exact flow behavior around the roughness, such as vortex structures or small stagnation regions behind individual roughness elements. Rather, it attempts to reproduce some aggregate behavior in the form of locally increased turbulence intensity and changes to the laminar-turbulent transition region. Accounting for only these changes can still yield much more accurate performance predictions such as lift and drag coefficients.

Furthering the explicit definition of roughness, there are some bounds to be established on the relative size of the "bumps" that will be represented by the model presented. Below some admissible height, viscous dampening effectively cancels out any perturbation introduced by the roughness. If a surface only contains imperfections below this level, it is usually referred to as a being "hydraulically smooth". On the other hand, perturbations above certain height will cause such major changes in flow behavior the geometry is essentially redefined. The present work focuses primarily on the region in between, where the roughness is large enough to introduce some change, but not at the size where it becomes much larger than the original turbulent length scale. This limited range is still of great interest as even subtle disturbances can have a compounding effect on the flow properties of a system.

The role of surface roughness in many flow applications is of great practical importance as a well known effect is the acceleration of the laminar-turbulent transition process. The implications of the premature appearance of turbulent flow are vast due to the changes in skin friction, heat transfer, and gas mixing properties. There is an interest in understanding the effects of surface roughness across many engineering disciplines, including the effects seen in gas turbines to better approximate maintenance cycles [2], applications to icing effects seen on aircraft wings [3], combustion analysis [4], and more.

The wind industry in particular has seen a recent rise in interest regarding the effects of surface roughness for several reasons [5]. For one, accurate prediction of wind turbine power output is fundamental to integration of wind power systems into existing infrastructure. Surface roughness can have a substantial impact on the aerodynamic properties of the blades by influencing boundary layer development over contaminated sections [6]. Furthermore, the changes in the flow over rough portions extends to the performance of the full turbine, potentially reducing power output and annual energy capture significantly. Many airfoils intended specifically for use on utility scale wind turbine were designed to be lift insensitive to surface roughness due to the expected environmental conditions [7, 8]. Field observations are showing this is frequently not the case, so there is a renewed interest in examining roughness sensitivity for airfoil design [9]. This poses numerous challenges due to the limited number of roughness configurations that have been thoroughly analyzed, and the non-trivial extension of roughness effects. As physically testing each profile is not practical, numerical design and optimization methods are used to generate airfoils with desired properties. However, there are limited computational techniques available to analyze the effects that surface roughness will have on the aerodynamic performance.

Much of the focus is directed at modeling the impact of roughness on the laminar-turbulent transition process. Surface roughness does in general and logically, accelerate the transition process through the introduction of disturbances into the laminar boundary layer. There are instances where carefully placed roughness elements are used to delay the onset of transition by attempting to dampen the natural viscous wave instability, however, any realistic configuration would not follow such a precise layout. Despite an abundance of work on the topic, details of the exact physical mechanism involved in roughness induced transition remain unknown or not fully understood. If the scope is limited to singular roughness elements or carefully spaced arrays, more theoretical approaches can be used. Unfortunately, the interaction of randomly sized and spaced roughness elements introduces a level of complexity no current methodology can physically reproduce. Transition prediction has only recently become reasonably compatible with modern general purpose CFD codes, so the lack of available tools to predict roughness effects on transition is not surprising.

To overcome the challenge involved in precisely representing each and every perturbation introduced by roughness, a more empirical, data driven approach is taken. Through the use of a scalar transport equation, a region where the surface roughness impacts the flow is defined. The formulation is such that it can capture upstream and time history effects with only a boundary condition at rough walls. This scalar variable is then calibrated to modify an existing correlation based transition model. Additionally, by defining this region, the possibility of further modifying the production of turbulent kinetic energy can be explored. This process is documented in detail with the hopes future researchers will be able to use a similar approach to developing models for problems that contain intractably complicated physical phenomena.

The creation of this model has been part of a collaborative effort between UC Davis, Texas A&M University, and Sandia National Laboratories. Two different airfoils with a large number of leading edge roughness configurations were tested at the Texas A&M University Oran W. Nicks Low Speed Wind Tunnel. The airfoils were chosen with the constraints that the geometries should be publicly available, the pressure distributions should be sufficiently different from one another, and each should be representative of a span-

wise portion of what is typically used on a wind turbine blade. The roughness was produced using vinyl decal material such that the individual roughness elements were produced with no substrate. The height of the roughness was chosen using flow simulations to determine a range that would represent a number of different types of transition behavior. Finally, the roughness patterns were generated by randomly distributing points on the leading edge of an airfoil surface to try and imitate what would be found in realistic applications.

The organization of the report is as follows:

- Chapter 2 contains a review of the literature on transition and roughness effects, with a selected account of experimental studies as well as modeling attempts at both.
- Chapter 3 describes the experimental campaign associated with the present work, including a complete description of the wind tunnel set up and procedures used for computing the results shown.
- Chapter 4 contains a description of the governing equations and the numerical methodology used in the computational simulations as well as a details of the grid topology and generation methods.
- Chapter 5 is a detailed description of the underlying transition model used, including a number of practical use tips and representative results.
- Chapter 6 documents the development of the roughness model including why the formulation was selected and a detailed account of the calibration process
- Chapter 7 provides an extensive number of results of the roughness model applied to various geometries and roughness types.
- Appendix A outlines a low order method for predicting roughness effects on transition, as well as some preliminary results.

  The remaining appendices provide additional data that is referenced throughout the report.

Chapter 2

Literature Review

Transition Overview

The laminar-turbulent transition region has been the subject of scientific investigation nearly as long as the process has been known to exist. In nearly every example of a solid bounded flow, the result is a growth of a laminar boundary layer profile followed by breakdown into a fully turbulent state. As the difference between a laminar and turbulent flow are substantial from both a physical and practical engineering standpoint, it has long been the objective of researchers to better understand the transition process. It is often viewed as a stability problem, where the laminar boundary layer is considered the ground state, and transition to turbulence analogous to a system going unstable. The transition of laminar flows to turbulence was initially and famously studied by Reynolds in 1883. Using dye to track the state of flow through a pipe, he constructed the relationship between the fluid velocity (U), dynamic viscosity (μ), density (ρ), and characteristic length scale (L), well known today as the Reynolds number.

$$Re = \frac{\rho U L}{\mu} \tag{2.1}$$

The analytical understanding of the transition process has evolved over time, and as more mathematical tools become available, fewer simplifications need be applied to the governing equations. The primary equations in fluid dynamics are the Navier-Stokes (NS), along with the mass and energy conservation equations. The complexity of the system of equations renders a full analytical solution essentially impossible. For the study of boundary layers, the simplification of incompressibility and locally parallel flow is usually made. Applying the principles of linear stability analysis to the simplified NS equations yields the Orr-Sommerfeld (OS) equation. At the present, solutions are obtained numerically for various initial disturbances, as even with the simplifications introduced the OS equation does not have a general analytical solution. However, when the stability of laminar boundary layers was initially studied, modern computational techniques were unavailable so the assumption of inviscid flow was made to further simplify the OS equation. Lord Rayleigh studied the inviscid OS equation extensively around the turn of the 20th century, and determined that a laminar boundary layer should remain stable unless there is an inflection in the velocity profile [10]. Although this is indeed a criterion to trigger transition onset, which is now referred to as a Rayleigh instability, the condition proved to be insufficient. It was observed experimentally that even very simple flows would transition to turbulence without ever experiencing an inflection.

Following the initial work, Prandtl indicated that the reason inviscid analysis failed to predict other transitional mechanisms was the effect of viscosity. The destabilizing effect of viscosity, and the existence of wave like perturbations causing transition was debated until the famous experiment of Schubauer and Skramstad [11]. Moving forward the scientific community began a rigorous study of the non-linear stability

of the OS equation and a large number of experiments on the transition process. Under stable, conditions small disturbances within the boundary layer are dissipated away and the flow remains laminar. However, as the laminar boundary layer grows, the flow becomes susceptible to destabilizing disturbance frequencies that can cause the perturbations to grow in magnitude. The initial viscously amplified growth of disturbances became known as Tollmien-Schlichting (TS) waves [11].

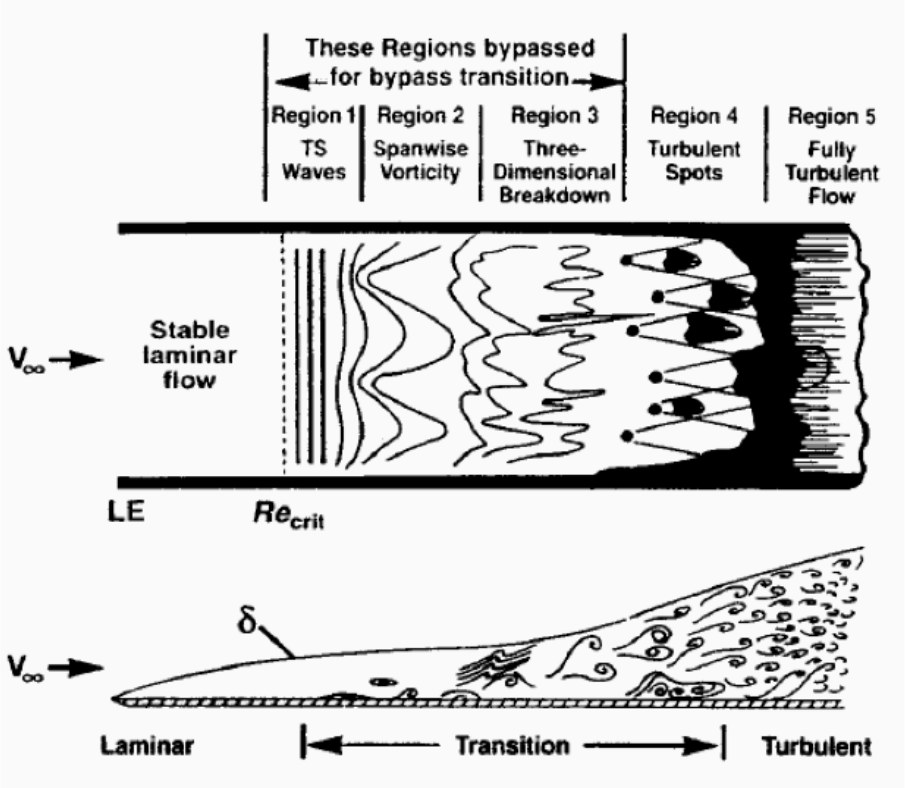

Figure 2.1. Stages of natural transition and sketch of developing boundary layer, adapted from Schlichting [12]

The appearance of Tollmien-Schlichting waves marks the first step in the "natural transition" process. Once the disturbance has grown to a point where the mean flow profile is altered, the boundary layer becomes susceptible to another band of disturbance frequencies which accelerates the process by which fluctuations are amplified. These secondary instabilities are three dimensional in nature and can take multiple forms. They are referred to as K-type, H-type, and C-type instabilities and named after Klebanoff [13], Herbert [14], and Craik [15] respectively for their initial contributions. After secondary disturbances are introduced, there is a rapid appearance of isolated turbulent spots, followed by a complete breakdown into a turbulent boundary layer. The natural transition process occurs over smooth surfaces if the freestream turbulence intensity is relatively low ($<1\%$). In highly turbulent environments, or in the presence of external forcing factors such as surface roughness, one or more of the initial steps can be bypassed and secondary instabilities may appear without the amplification of Tollmien-Schlichting waves ever occurring.

Early transition studies essentially divided transition behaviour into two categories, natural transition dominated by Tollmien-Schlichting wave growth, and "bypass" transition caused by large amplitude external disturbances. As more detailed experimental measurements and direct numerical simulation (DNS) results

have been analysed, a broader understanding of the process has been developed. The linearized NS equations are typically treated as an eigenvalue problem, where the unstable modes are analysed and the physical realization of that mode represents a path to transition. Tollmien-Schlichting wave growth falls into the normal mode category along with transition driven by crossflow instability and surface curvature. The tendency of a flow to produce streamwise vortex structures over concave surfaces is known as a Görtler instability. A similarity across these primary instability modes is the introduction of additional vorticity into the boundary layer. Also, the initial conditions for the primary growth modes are known from the geometry of the surface or body.

Much of the analysis described concerns the evolution of a disturbance once it has physically created a perturbation in the boundary layer. There is also a great interest in understanding how external forcing functions can enter the boundary layer and generate the initial instability. Morkovin introduced the term "receptivity" to describe how the boundary layer transforms some external disturbance into a flow perturbation [16]. This step is critical to understanding the transition process as it represents the initial conditions for the stability problem. The receptivity phase can also impact the path to transition the flow will follow, as shown in Figure 2.2. Lower amplitude disturbances are typically associated with "natural" external excitations such as freestream turbulence, where as large magnitude disturbances typically come from artificial sources, such as surface roughness.

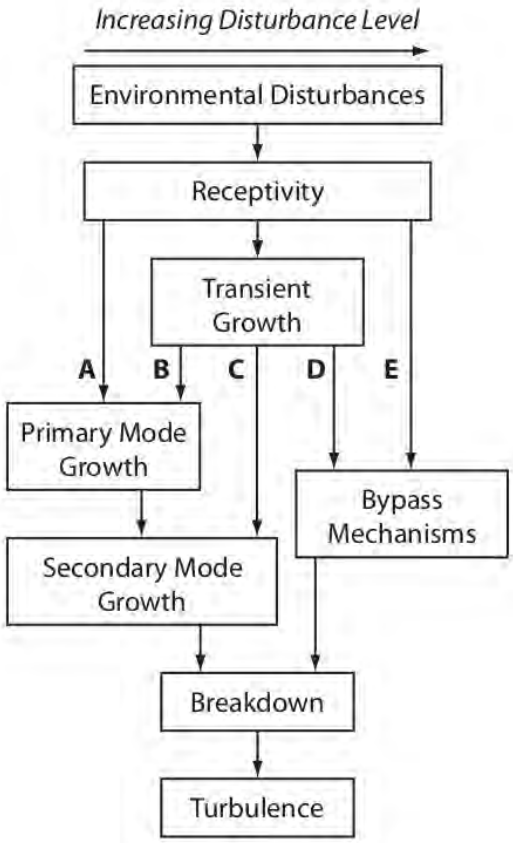

Figure 2.2. Paths to Transition - adapted from Morkovin et al. [17]

Primary growth mechanisms make up only a portion of all possible paths to transition. As mentioned, initially it was tempting to group all forms of transition that did not follow one of the primary modes into the bypass category. As the OS equation has been studied more rigorously, additional modes have been uncovered and new mathematical frameworks established. These intermediate mechanisms are attributed to what is known as "transient growth". Transient growth arises due to the interaction of non-normal modes of the OS equation that would traditionally decay. The current perspective on the OS eigenvalue problem is that the modes can be divided into a "discrete" and "continuous" set. This is due to the fact that the OS operator is not self-adjoint. In a finite dimensional space, this means a linear operator defined by a matrix is equal to its own conjugate transpose. More importantly, an operator that is not self-adjoint has non-orthogonal eigenfunctions. A consequence of the non-orthogonality is the interactions between the eigenmodes may be both amplifying and destructive. That is, stable modes may actually contribute to some disturbance growth before ultimately decaying. If only the discrete modes are considered, the primary transition mechanisms are uncovered, but many other paths to transition are left unknown.

The area of transient growth has the potential to explain the mechanism that is responsible for roughness induced transition. Physically, roughness generates a spatially stationary disturbance that can alter the receptivity of the boundary layer in addition to the actual disturbance it introduces. From a theoretical standpoint, this means the effect of roughness becomes extremely hard to model as it both introduces a physical perturbation and makes the boundary layer more susceptible to other external disturbances.

Transition Prediction Models

The following section describes various methods for transition prediction and published models based on these strategies. The models are loosely divided in transition prediction based on linear stability, and prediction based on empirical correlations. A constant theme is the idea of compatibility with parallel 3-D RANS simulations. One of the primary requirements is that a model must not rely on non-local operations, e.g. integrations and line searches. Additionally many transition prediction methods are inherently restricted to 2-D, preventing a more general adoption. Due to the importance of both these restrictions, a final section is devoted to models that meet the requirements for implementation in fully parallel 3-D RANS codes.

Transition Prediction Based on Linear Stability

Applying a generalized traveling wave perturbation to the linearized Navier-Stokes, with the further assumption of locally parallel flow, results in the well known Orr-Sommerfeld (OS) equation. The disturbance can be expressed as a stream function:

$$\Psi(x,y,t) = \Phi(y)e^{[i(\alpha x-\omega t)]} \tag{2.2}$$

α is the wavenumber, ω the phase speed. Using this representation, the OS equation can be written:

$$\left(\frac{\partial^2}{\partial y^2}-\alpha^2\right)^2\Phi = i\alpha Re\left[(U-\omega)\left(\frac{\partial^2}{\partial y^2}-\alpha^2\right)-\frac{\partial^2 U}{\partial y^2}\right]\Phi \tag{2.3}$$

When approaching the problem of temporal stability, α is real and ω complex, therefore if $Im(\omega) > 0$ the flow is unstable. Likewise for spatial stability where ω is real, and α complex, $Im(\alpha)$ must be less than

zero. Looking at the OS equation for a particular disturbance frequency results in an eigenvalue problem [18]. While possible, obtaining solutions is difficult and traditionally numerical methods are used.

The most widely used transition model based on linear stability analysis, and engineering applications in general, is the e^N method of van Ingen [19] and Smith & Gamberoni [20]. The position of neutral stability (x_{crit}) is determined, and the disturbance growth rates are integrated spatially starting at x_{crit} in the flow direction. This can be expressed:

$$A/A_0 = \int_{x_{crit}}^{x_{tr}} (-\alpha_i)\, dx \tag{2.4}$$

here α_i represents the spatial disturbance growth rate at a particular location. If the growth rate is determined by the Orr-Sommerfeld equation directly, it is referred to as the "full" e^N method. Solving the OS equation numerically is computationally expensive, so for a majority of applications some simplifying assump-tion must be made. An "envelope" version of the e^N uses the maximal amplification ratio for each particular frequency as interpolation points for an approximate curve. Drela and Giles developed a linear envelope version of the e^N that computes disturbance growth rates given the kinematic shape factor (H_k) and momentum thickness Reynolds number ($Re_\theta = \rho U_e \theta/\mu$) [21]. Using the self-similar Falkner-Skan velocity profiles, and the spatial version of the OS equation, they derived the following:

$$\tilde{n} = \frac{d\tilde{n}}{dRe_\theta}[Re_\theta - Re_{\theta,crit}] \tag{2.5}$$

where $\tilde{n}$ is the amplification ratio, and $Re_{\theta,crit}$ is computed with the momentum thickness at the location of neutral stability. Both $d\tilde{n}/dRe_\theta$ and $Re_{\theta,crit}$ are given in terms of the kinematic shape factor ($H_k = \delta_k^*/\theta_k$), computed with the incompressible displacement (δ_k^*) and momentum thickness (θ_k). The approximate relationships are given by:

$$\log_{10} Re_{\theta,crit} = \left(\frac{1.415}{H_k - 1} - 0.489\right) \tanh\left(\frac{20}{H_k - 1} - 12.9\right) + \frac{3.295}{H_k - 1} + 0.44 \tag{2.6}$$

$$\frac{d\tilde{n}}{dRe_\theta} = 0.01\sqrt{[2.4H_k - 3.7 + 2.5\tanh(1.5H_k - 4.65)]^2 + 0.25} \tag{2.7}$$

The integrated growth rate is then determined by:

$$\tilde{n} = \int_{Re_{\theta,crit}}^{Re_\theta} \left(\frac{d\tilde{n}}{dRe_\theta}\right) dRe_{\theta,crit} \tag{2.8}$$

Transition is predicted to occur when $\tilde{n}$ reaches N_{crit}. The value of N_{crit} is empirically driven and strongly dependent on freestream turbulence levels, meaning it should vary depending on application. The value of N_{crit} is commonly assumed to average around 9, and then is adjusted from there for higher or lower than usual freestream disturbances. This envelope method described in Equations 2.5 - 2.8 was designed for use in the vortex panel code XFOIL [21].

XFOIL has seen wide use in the aerospace community and is still regarded as a valuable tool for aerodynamic performance analysis of single-element airfoils. Nonetheless, panel methods in general are restricted

in the geometries that can be accurately represented, so a more general approach has been sought after. Reynolds-averaged Navier-Stokes (RANS) solvers are more flexible in terms of configurations that can be simulated, so it naturally follows to try and implement an e^N type method in a RANS code. Motivated to insure tight coupling between the underlying flow solver and the disturbance growth rate calculation, Brodeur and van Dam implemented the envelope method of Drela and Giles directly in the 2-D RANS code INS2D [22]. Favorable results were produced with the method applied to several airfoil configurations, however, the code was written in 2-D and carried limitations with regards to the accuracy of the envelope method.

An alternative to an envelope type e^N simplification, is to use a database look up determine local disturbance growth rates. An advantage to using this type of approach is that more physical parameters may be tabulated and incorporated in the calculation. Notably excluded from the simplified envelope method described above is the effect of compressibility and specific disturbance frequency (the envelope method effectively attempts to cluster frequencies into a single curve). To include these parameters in an transition prediction scheme, Mayda [23] generated a database of disturbance growth rates based on Mach number at the boundary layer edge, kinematic shape factor (H_k), displacement thickness Reynolds number (Re_{δ^*}), and disturbance frequency. He then implemented an interpolation strategy for this database in the RANS code ARC2D [23]. Database methods have generally proven to be more faithful to a "full" e^N calculation in terms of disturbance growth rate calculation, with a relatively small computational overhead over an envelope type method. One downside is that implementation is a bit more challenging.

Although very successful as applied to 2-D configurations, one of the biggest obstacles moving forward for an e^N type method is the extension to 3-D. Much of the boundary layer analysis is inherently restricted to two dimensions, and while one may be able to reduce certain flows to 2-D, it is extremely challenging to create a generalized formulation. Another restrictive property is the reliance on integral boundary layer quantities, which restricts use in a parallel computational architecture.

Correlation Based Transition Models

The idea behind correlation based models is that certain local properties can be used to approximate the relative stability of the boundary layer at a particular position. Most correlation based transition models are based on the momentum thickness Reynolds number, Re_θ, defined:

$$Re_\theta = \frac{\rho U \theta}{\mu} \tag{2.9}$$

where the characteristic length is the momentum thickness of the boundary layer, θ. It is important to keep in mind computation of θ is very much a non-local operation, restricting direct implementation in general purpose CFD codes. Nonetheless, a number of different strategies have been developed to eliminate the non-local dependence. A transition prediction model would then define a threshold "transition onset" momentum thickness Reynolds number, $Re_{\theta t}$, that marks the value at which the laminar boundary layer will begin transition. Figure 2.3 provides a rough sketch of a developing boundary layer and the behavior of the momentum thickness Reynolds number.

The threshold value must be defined as a function of other flow quantities as there is no universal constant to describe this behavior. Most correlations rely on a combination of a global parameter, such as freestream turbulence intensity (Tu), and a more localized quantity. One of the simplest correlation based models was that of Mayle [4], who established a direct relationship between freestream turbulence intensity and $Re_{\theta t}$:

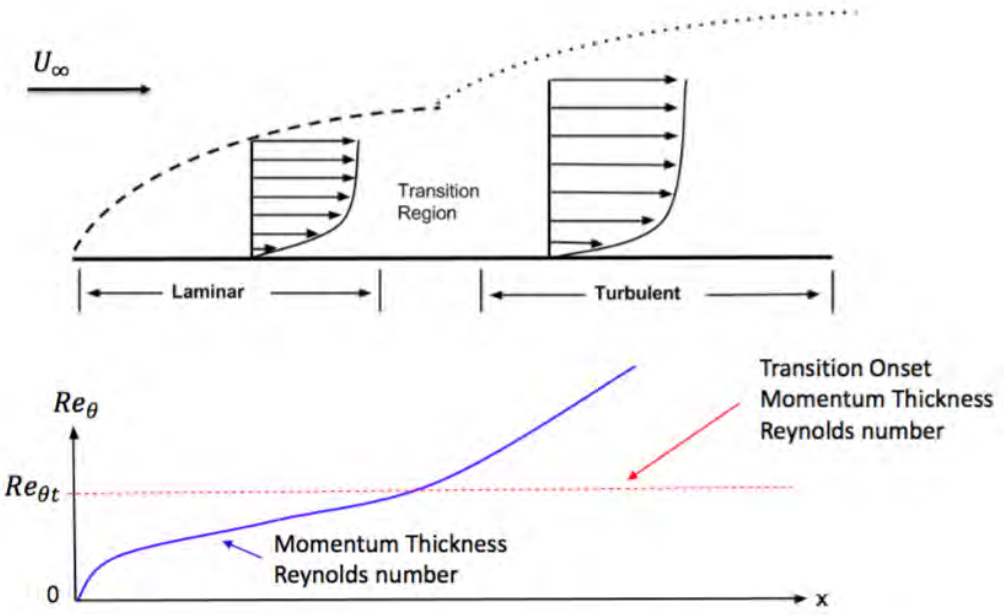

Figure 2.3. Sketch of developing boundary layer to demonstrate the approximate behavior of momentum thickness Reynolds number.

$$Re_{\theta t}^{\text{Mayle}} = 400.0Tu^{5/8} \tag{2.10}$$

A more popular and complete model is that of Abu-Ghannam and Shaw [24]. They extended the relationship between freestream turbulence intensity and $Re_{\theta t}$ to include a local pressure gradient parameter (λ_θ):

$$Re_{\theta t}^{\text{Abu-Shaw}} = 163.0 + \exp\left\{F(\lambda_\theta) - Tu\frac{F(\lambda_\theta)}{6.91}\right\} \tag{2.11}$$

$$F(\lambda_\theta) = \begin{cases} 6.91 + 12.75\lambda_\theta + 63.64\lambda_\theta^2, & \lambda_\theta \leq 0 \\ 6.91 + 2.48\lambda_\theta - 12.27\lambda_\theta^2, & \lambda_\theta > 0 \end{cases} \tag{2.12}$$

$$\lambda_\theta = \frac{dU}{ds}\frac{\theta^2}{\nu} \tag{2.13}$$

Figure 2.4 is provided to graphically demonstrate what this relationship looks like. It is important to note the asymptotic behavior of the $Re_{\theta t}$ variable as this will cause large sensitivities to changes in the freestream turbulence intensity parameter, Tu. The parameter is typically a user defined input in flow simulations and small changes can produce radically different results. This is especially true at lower Tu values, which happen to represent the conditions in many aerodynamic wind tunnels and external flows on commercial aircraft at cruise altitude.

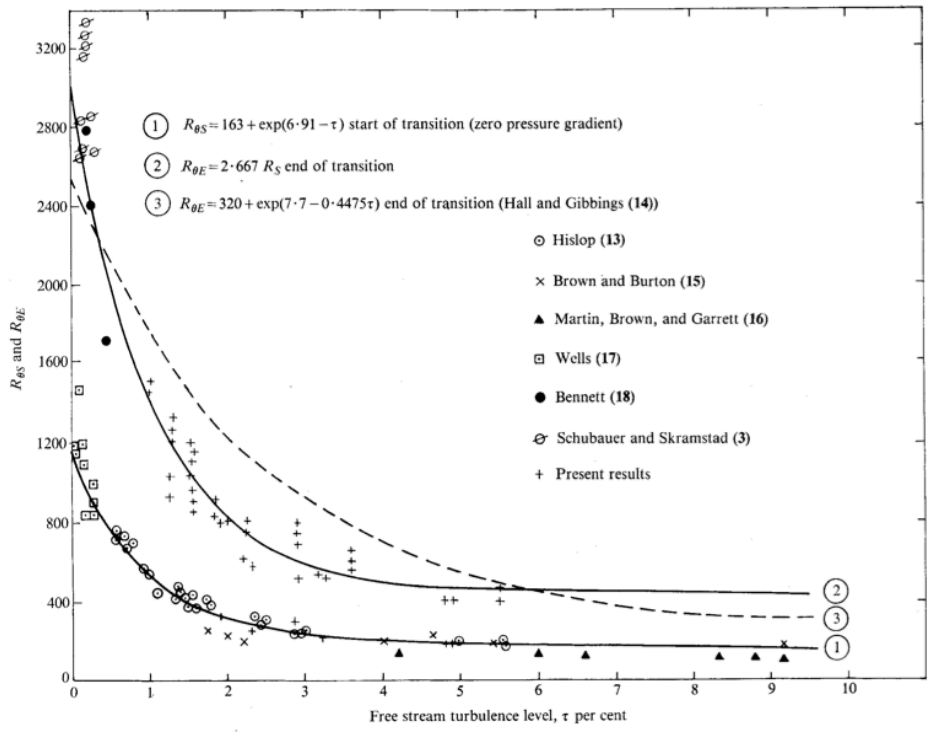

Figure 2.4. Plot of $Re_{\theta t}$ correlations against freestream turbulence intensity, adapted from Abu-Ghannam and Shaw [24]

Recognizing that physically the transition from laminar to turbulent flow does not occur instantaneously, many researchers have sought to model the build up of turbulence intensity that occurs after transition begins. $Re_{\theta t}$ correlations provide an indication of where the onset of transition will occur, however, additional information is needed to describe how the process will evolve. Most models that attempt to predict the length of the transition region rely on an intermittency variable (γ) that acts as a scaling of the turbulent eddy viscosity (μ_t). Dhawan and Narasimha introduced an intermittency model based on transition experiments on a flat plate [25]:

$$\gamma = \begin{cases} 0, & x < x_t \\ 1.0 - \exp\left[-\frac{(x-x_t)^2 n\sigma}{U}\right], & x \geq x_t \end{cases} \tag{2.14}$$

where x_t represents the transition location, n is the turbulent spot formation rate, σ is the spot propagation parameter, and U the freestream velocity. The model requires some tuning of the constants n and σ and can be difficult to implement due to the fact the distance to the transition location is required. Steelant and Dick designed what can be considered a close predecessor to many modern transition models [26], with a transport equation that defines an intermittency distribution. The source term of the transport equation is designed to produce the γ correlation of Dhawan and Narasimha.

There have been numerous attempts to produce a transition model that includes both a correlation for the onset as well as the extent of transition. Warren and Hassan developed one of the first combined models take

was successfully coupled with the $k-\zeta$ and Spalart-Allmaras turbulence models [27]. Suzen and Huang developed a similar model that was applied to SST and $k-\omega$ turbulence models [28]. Both of these models unfortunately rely on non-local operations and are therefore considered incompatible with general purpose CFD codes.

Parallel RANS Compatible CFD Models

The desire to maintain compatibility in parallel codes is driven by the computational cost of solving the RANS equations on large computational grids. In many applications, a single CPU is insufficient for generating a solution in a reasonable time frame. To take advantage of parallel CPU architecture, the domain must be divided such that there is minimal communication between processors outside of passing information between directly adjacent grid cells. Quantities such as the boundary layer edge, and furthermore the directly computed momentum and displacement thickness, are challenging to compute in a parallel environment as the direction and bounds of the integration are not easily provided by the grid topology. Additional line searches or other auxiliary computations must be performed, potentially across multiple CPUs, and then information relayed throughout the domain. This not only directly consumes CPU time from the calculations, but more seriously can cause a bottleneck for the global iteration. The following models described all meet the requirements of a fully local formulation and compatible with 3-D geometries. All are available in the open literature and have been validated to a certain degree.

Laminar Kinetic Energy Model

Walters and Leylek have proposed a model based on the $k-\omega$ turbulence model that includes an additional transport equation for "laminar kinetic energy", k_L [29]. It is based on the principle first introduced by Mayle and Schulz [30] that a laminar boundary layer experience fluctuations inherently different than what are typically considered "turbulent". With this consideration, an additional transport equation is used to account for the development of these alternative fluctuations that are not properly described by the usual k equation. The production of k_L can be modeled locally and generally corresponds to low frequency velocity fluctuations. The growth of this type of energy has been shown to be independent of the spectrum of the external forcing disturbance. This is a highly desirable property and is promising for use in transition prediction methodologies. The model has been validated on a few simple geometries, but likely needs further testing and development before wide spread use.

N-factor Transport Equation Model

In an attempt to fully localize a linear stability based approach Coder and Maughmer [31] introduced an *N*-factor transport equation:

$$\frac{\partial(\rho\tilde{n})}{\partial t}+\frac{\partial(\rho U_j\tilde{n})}{\partial x_j}=\rho\Omega F_{\text{crit}}F_{\text{growth}}\frac{d\tilde{n}}{dRe_{\delta 2}}+\frac{\partial}{\partial x_j}\left[\frac{1}{\sigma_{\tilde{n}}}(\mu+\mu_t)\frac{\partial\tilde{n}}{\partial x_j}\right] \tag{2.15}$$

the source term of equation represents the growth of Tollmien-Schlichting waves in the streamwise direction. It can essentially be viewed as a different form of an integrated growth rate used in the method of Drela and Giles [21]. The equation is coupled with the one equation Spalart-Allmaras model through an expression

that compares the local $\tilde{n}$ to a critical N factor (N_{crit}) that turns on production of the turbulence variable. The N_{crit} quantity is computed using an equation based on the relationship with freestream turbulence levels from Mack [32]. The model has been validated on a variety of 2-D flat plate and airfoil test cases, along with a full 3-D wing. The results are promising and upon further validation, it should become more common among RANS transition models.

Langtry-Menter $\gamma - \tilde{Re}_{\theta t}$ model

The most widely used 3-D RANS compatible transition model to date is the $\gamma - \tilde{Re}_{\theta t}$ model of Langtry and Menter [33]. The model solves two transport equations that correspond to the transition onset criterion, $\tilde{Re}_{\theta t}$, and an intermittency variable (γ) that switches on turbulent kinetic energy production in the SST $k-\omega$ turbulence model. A key component of the model is the ability to compute an accurate estimation of the momentum thickness Reynolds number locally using an approximate relationship to the vorticity Reynolds number, Re_v:

$$Re_v = \frac{\rho y^2}{\mu}\left|\frac{\partial u}{\partial y}\right| = \frac{\rho y^2}{\mu} S \tag{2.16}$$

$$Re_\theta \approx \frac{\max(Re_v)}{2.193} \tag{2.17}$$

where the $\max(Re_v)$ corresponds to the maximum value Re_v obtains in a plane normal to a viscous wall. A unique property is that this quantity will naturally obtain its maximum value near the middle of the boundary layer. This behavior is used to construct a switching function for the production of the intermittency variable γ. The variable is controlled using a transport equation:

$$\frac{\partial(\rho\gamma)}{\partial t} + \frac{\partial(\rho U_j \gamma)}{\partial x_j} = P_\gamma - E_\gamma + \frac{\partial}{\partial x_j}\left[\left(\mu + \frac{\mu_t}{\sigma_f}\right)\frac{\partial \gamma}{\partial x_j}\right] \tag{2.18}$$

The production term P_γ contains the comparison to the local Re_v value. The onset value $Re_{\theta t}$ is computed as a function of λ_θ and Tu, much like the correlation of Abu-Ghannam and Shaw. Unfortunately the λ_θ parameter is somewhat ill defined within the boundary layer. To overcome this, an additional scalar variable $\tilde{Re}_{\theta t}$ and corresponding transport equation are used:

$$\frac{\partial(\rho\tilde{Re}_{\theta t})}{\partial t} + \frac{\partial(\rho U_j \tilde{Re}_{\theta t})}{\partial x_j} = P_{\theta t} + \frac{\partial}{\partial x_j}\left[\sigma_{\theta t}(\mu + \mu_t)\frac{\partial \tilde{Re}_{\theta t}}{\partial x_j}\right] \tag{2.19}$$

The purpose of the equation is to "pull" the value of the $Re_{\theta t}$ into the boundary layer. The production term acts to set the transported variable equal to the empirical correlation outside the boundary layer. As the model is a core component of the roughness model presented in this work, a more detailed explanation and full equation set is presented in Chapter 5.

$SA-\gamma-\tilde{R}e_{\theta t}$ Model

The Langtry-Menter $\gamma-\tilde{R}e_{\theta t}$ model was specifically designed for use with the SST $k-\omega$, however, the concept of switching on production of turbulent kinetic energy can easily be extended to other turbulence models. Medida used the same γ and $Re_{\theta t}$ variables and re-calibrated the transport equations for use with the one equation Spalart-Allmaras (SA) turbulence model [34]. This has an advantage in that one fewer equation needs to be resolved, lowering the computational cost. The so called $SA-\gamma-\tilde{R}e_{\theta t}$ model was tested on a wide range of test cases, and the results were similar to the original SST variant. The $SA-\gamma-\tilde{R}e_{\theta t}$ is not really a new class of transition model, but it does extend the $\gamma-\tilde{R}e_{\theta t}$ family.

One Equation γ Model

In both $\gamma-\tilde{R}e_{\theta t}$ models described, the primary purpose of the $\tilde{R}e_{\theta t}$ variable is to set the quantity within the boundary layer. A number of research groups have attempted to eliminate the need for the additional transport equation and formulate a local expression for $\tilde{R}e_{\theta t}$ valid throughout the flow domain. Coder and Maughmer introduced an expression similar to a shape parameter to include the local pressure gradient term inside the boundary layer [35]. More recently Menter et al. introduced an expression similar to the original λ_θ that depends on the gradient of the wall normal velocity component and an additional empirical correlation. The model was extensively calibrated on the same test cases as the two equation $\gamma-\tilde{R}e_{\theta t}$ model [36]. Once more, fundamentally the one equation γ model is closely related to other $\gamma-\tilde{R}e_{\theta t}$ type methods but does have the advantage that only one transition model equation needs to be solved. Additionally, the new formulation is Galilean invariant which corrects one of the deficiencies of the original two equation model. Logically, one can see the combination of a one equation γ model and the SA turbulence model as a new turbulent-transition model, but this has yet to be attempted to the best of the author's knowledge.

Summary of Transition Models

Throughout this section, a number of physics and correlation based models have been presented. An argument can be made for either approach and until more is understood regarding the transition process, there will likely be no universal agreement on which methodology is best. A physics based approach, by definition, must rely on a detailed physical understanding of the problem. The attempt is then to model the physical process itself while empirical methods seek to model the effect. The distinction is important as adding arbitrary functions to model new modes of transition is perfectly valid if one is only trying to model the effect. On the other hand, additions to physics based methods must accurately represent some new physical mechanism. In the case of transition, there are several modes that are not entirely understood so a true phenomenological based method will inherently lack the ability to predict these unknown mechanisms. Additionally, modifying physical quantities related to the primary flow variables can have unintended consequences due to the sensitivity of the governing equations. A true physically based model is clearly desirable from a fundamental accuracy perspective, however, in practice correlation based models are often the best option.

Roughness Effects

Surface roughness can significantly alter the flow field over a contaminated surface, introducing velocity perturbations, increasing the momentum deficit in the boundary layer, and altering transition characteristics. [37]. A frequently studied effect of surface roughness is the premature transition of a laminar boundary layer to a turbulent profile [38]. Additionally, even more effects are seen as a fully developed turbulent boundary layer has a tendency to thicken over rough sections. This is due to the increase in turbulent fluctuations and subsequent turbulent kinetic energy production over rough surfaces. The early onset of transition and modifications to the fully turbulent boundary layer on an airfoil can increase drag, alter stall characteristics, change the lift-curve slope, and even force the flow to become unsteady.

The characterization of surface roughness has received considerable attention throughout studies of roughness effects. The relationship between the height of the roughness element and the flow disturbance induced is dependent on a number of other parameters. Roughness elements lower than the height of the viscous sublayer generally have little effect on the transition process as the disturbances are dissipated away due to the high levels of viscous damping [39]. Additionally as the boundary layer does not have a constant thickness, the effects can not be generalized along the boundary layer of a rough surface. Accord-ingly, roughness heights are usually nondimensionalized with respect to the displacement thickness (k/δ^*) or described using a roughness Reynolds number, Re_k. The roughness Reynolds number is defined:

$$Re_k = \frac{\rho U_k k}{\mu} \tag{2.20}$$

where U_k is the velocity in an undisturbed boundary layer at height k. Frequently, experimental studies have attempted to identify a critical roughness Reynolds number, $Re_{k,crit}$. This represents the critical value Re_k has to reach to immediately trigger the transition process at the location of the roughness.

Types of roughness have been broadly characterized into three different subsets, beginning with 2-D isolated roughness (such as a trip strip or other protuberance that consistently covers the entire span). A second category describes three dimensional isolated roughness, such as a single hemisphere, cylinder, or other three dimensional shape. Finally, there is distributed roughness, which encompasses any sort of clustered group of roughness elements and is an inherently three dimensional occurrence. The first two have been studied extensively and relatively consistent results have been seen in various experiments. However, studies on distributed roughness have been plagued by inconsistencies and difficulties generalizing the observed effects [37, 40]. The extremely non-linear nature, and interactions between individual structures create complex flow features that can vary substantially across experiments, and are not practically represented analytically.

Isolated 2-D Roughness

Characterized by a consistent spanwise protuberance, two-dimensional roughness is known to create pockets of separated flow both down and upstream of the rough e lement. The downstream separation can extend vastly beyond the location of the trip strip or other isolated 2-D feature. The flow separation causes an inflection i n t he v elocity p rofile an d pr oduces an in viscid Ra yleigh in stability. De spite in troducing a relatively large disturbance, 2-D isolated roughness does not immediately introduce turbulent spots into the boundary layer but rather accelerates the amplification o f n aturally o ccurring Tollmien-Schlichting waves

[41]. The increase in amplification depends strongly on the height of the roughness relative to the boundary layer thickness (k/δ^*) and can immediately trigger the onset of transition or may only slightly change in the transition location compared to a "clean" configuration. 2-D trip strips are considered a controlled way to promote the onset of the natural transition process as the resulting amplification of instability waves can be described by linear stability analysis.

In conjunction with physically altering the boundary layer profile, the roughness element can have additional secondary effects on the boundary layer development. The separated region promotes the receptivity to external disturbances such as freestream turbulence and sound pulses by increasing the momentum deficit downstream of the roughness. Therefore, despite being an ideal way to amplify the natural transition process in a closed controlled environment (such as a low turbulence wind tunnel), a 2-D isolated feature can increase the likelihood of a bypass transition in an external environment [42].

Isolated 3-D Roughness

The effects of a three dimensional rough feature on the boundary layer flow are considerable different than those of a 2-D disturbance. A separation pocket does frequently appear behind the isolated element; however the downstream extent is considerably less than a 2-D disturbance. Additionally, distinctive flow features appear at the location of the isolated feature. Qualitatively, it has been observed that isolated rough elements of various symmetrical shapes introduce similar vortical structures, however differences in $Re_{k,crit}$ have been observed [43]. A number of early investigations on isolated roughness elements were conducted by Tani et al. [44], Gregory and Walker [45], and Mochizuki [46] in the 1940's and 50's. Gregory and Walker utilized a cylindrical shaped rough element, while Mochizuki [46] utilized a single sphere of varying diameters and smoke visualization to explore the flow characteristics. The results from the two studies show similar flow features, and some details from Mochizuki are presented as a canonical representation of flow features around an isolated rough element. Figure 2.5 shows the effect of varying freestream velocity on the flow behind the rough element.

The distinctive flow feature of an isolated element is a primary vortex filament that wraps around the sphere creating two symmetric trailing vortices on either side. These symmetric vortices behind the element induce a downwash in the wake [47]. The induced flow structure has been the name "horseshoe vortex" due to its shape. Smoke streaks at various heights providing details of the overall structure are shown in Figure 2.6.

It can be observed in Figure 2.5 at low freestream velocities ($U = 0.9m/s$) a single smoke trail appears behind the rough element. As the velocity is increased ($U = 1.1 - 1.3m/s$), the trailing vortices begin to periodically deform introducing "hairpin" vortex structures, with the symmetric feature seen in between the two primary trailing vortices in Figure 2.5 ($U = 1.3m/s$). The existence of hairpin vortices was observed in Mochizuki's experiment [46], however it was not explored in great detail until Acarlar and Smith [43]. The rotation of the hairpin vortices is opposite that of the primary horseshoe structure.

At low Re_k values ($Re_k < 300$), the system of vortices are steady and do not affect the stability of the flow around them. The vortex structures remain isolated until they are pushed up out of the shear layer and dissipated away. As the the value of Re_k increases ($300 - 400$), the horseshoe vortex system becomes unstable and the protuberance begins to shed hairpin vortices periodically. The shedding frequency of the vortices is higher than the critical disturbance band for the amplification of Tollmien-Schlichting waves, therefore the transition process is only slightly accelerated in this range of Re_k. A further increase in Re_k to

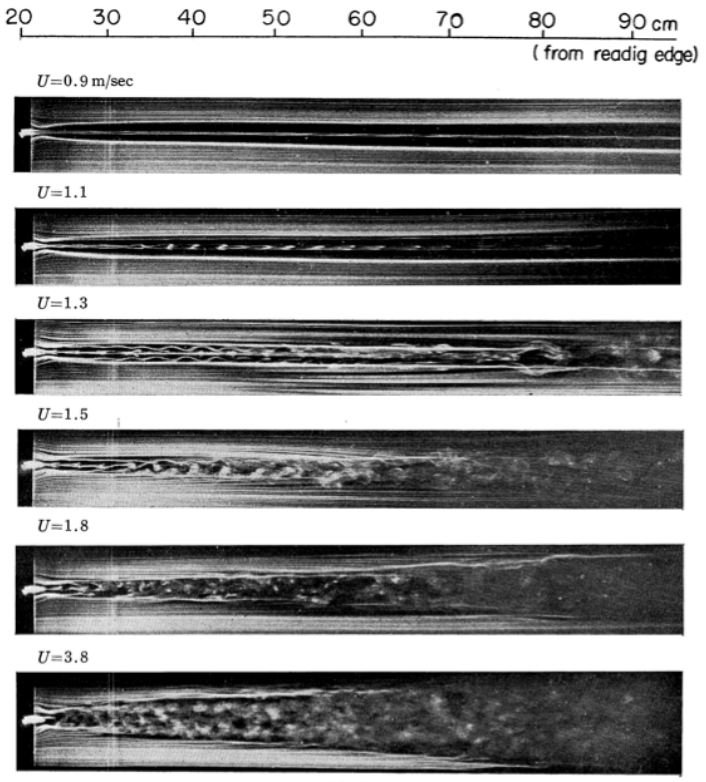

Figure 2.5. Varying freestream velocities and the flow feature generated behind the roughness element, adapted from Mochizuki [46]

the critical range (on the order of 400 to 600 depending on the shape of the roughness element) results in the sudden appearance of a turbulent wedge behind the rough element ($U = 3.8m/s$ in Figure 2.5). The wedge rapidly extends and soon causes a transitional boundary layer bypassing the traditional 2-D amplification process.

Furthermore, a study by Morkovin and Norman showed that if the roughness element extended outside the boundary layer additional vortex structures are generated up-stream of the roughness [48]. Similarly, at relatively low Re_k values, the vortices remain stable and do not promote the transition process. Shedding begins after an increase in Re_k and can result in the collapse and reappearance of the system of vortices as a whole, referred to as "burping". An increase past a critical level will even trigger the transition process upstream of the roughness due to the induced vortex.

Distributed Roughness

Single isolated roughness elements have been studied experimentally, and DNS experiments have been performed at low Reynolds numbers with good agreement and consistency [49]. Despite the susceptibility of the shedding properties to freestream conditions and external disturbances, the effects of isolated rough structures are considerably better understood than the influence of distributed surface roughness. Even after almost a century of study on distributed roughness, there is still much unknown about the effects in various

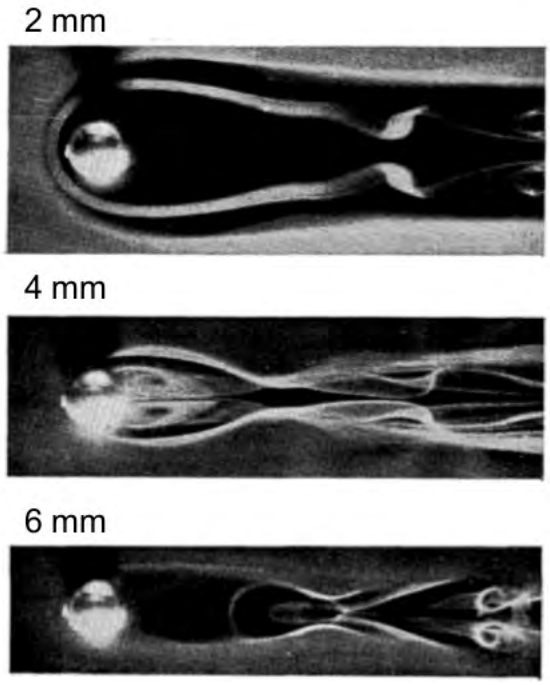

Figure 2.6. Details of the horseshoe vortex system using smoke streaks at various heights, the hairpin structure can also be seen, adapted from Mochizuki [46]

flow applications. The well behaved and relatively understood vortex structures seen in the presence of isolated 3-D roughness vanish under the influence of multiple clustered roughness elements.

The study of distributed roughness began with the work of Nikuradse [50] in 1933 and continued shortly thereafter with the extension of roughness correlations by Schlichtling [12]. The primary focus of the early experiments was not to study the influence of roughness on transition, or to provide a detailed analysis of the surrounding flow field, but to study the practical friction factor increases in pipe flows. After a quiet period the influence of distributed roughness on external flows sparked the interest of the scientific community around World War II. Aircraft design played a dominant role and the study of scaling and similarity became necessary to determine the effects of roughness at higher flight speeds [45, 39]. Dryden [38], Braslow and Knox [51] all contributed significantly to the early era of roughness investigations. Much of their early work attempted to identify the critical height necessary to trip the flow under given conditions, and despite changes in the shape of the individual roughness elements, $Re_{k,crit}$ remained constant at a value of approximately 600.

One of the first studies that attempted to detail the effects of distributed roughness on the transition process was Feindt in 1956 [52]. By using various roughness heights across the length of a flat plate, he determined the effect of changing the roughness Reynolds number on the transition onset location. From here, he was able to correlate the Reynolds number based on the equivalent sand roughness height, Re_{k_s}, to the Reynolds number based on the transition onset location, Re_{x_t}, for various pressure gradients. Additionally, the study documented that for flow over a surface with an $Re_k < 120$ the roughness does not influence the location of transition. Walls contaminated with roughness below this minimum are regarded as "hydraulically smooth". This value has since been proven to not be universal and is used as a rough estimate rather

than a hard limit. Morkovin has more recently suggested a threshold of $Re_k < 25$ for a surface to remain hydraulically smooth.

A study by Levanthal provided more insight in determining the effects of distributed roughness with Re_k values of 10 and 150 [53]. At the lower $Re_k = 10$ value, the boundary layer profiles observed were Blasius in shape and the mean profile remained unaffected. At the higher $Re_k = 150$ value, the mean profile was observed to be Blasius in shape for the initial laminar portion of the boundary layer with the exception that it was shifted upwards. Additionally, the amplification rate of the initial disturbances was found to be three times larger than the equivalent smooth Tollmien-Schlichting waves. The frequencies that were amplified under the influence of distributed roughness were all below that of the natural Tollmien-Schlichting frequencies, indicating that the mechanism that influenced transition was markedly different than an isolated roughness element at $Re_k = 300$. A study by Kendall further confirmed the existence of an outwardly displaced Blasius profile in the intermediate range of Re_k [40]. Additionally, Kendall reported an inflection in the velocity profile, that he attributed to the vertical transfer of streamwise momentum caused by the shape of the roughness elements. An inflection in the profile is a significant observation as it is known to be a powerful amplifier of Tollmien-Schlichting waves from inviscid stability analysis.

Following the investigation by Kendall, an experiment conducted by Corke, Bar-Sever, and Morkovin utilized randomized grit type roughness with the hope of finding amplified Tollmien-Schlichting waves [37]. The investigators were also careful taking measurements near the top of the roughness to try and observe an inflection similar to what was seen by Kendall. Once again, no disturbances in the natural Tollmien-Schlichting band were found, and despite the increased focus, no inflection in the mean profile was observed. It was further speculated the reason for the inflection in Kendall's experiment was the uniform shape and distribution of the roughness elements that promoted the vertical transfer of streamwise momentum. In the study of Corke et al., the receptivity of the roughness influenced boundary layer to external disturbances was also examined. It was postulated that the low inertia fluid below the top of the roughness increased the susceptibility of the fluid to freestream disturbances. The discrepancies in the results from the two experiments exemplify the nature of many distributed roughness studies as inconsistencies are frequently seen, and limitations in measurement techniques often inhibit further explanations.

Moving on to more complex geometries, much of the work aims once more to quantify the effect of roughness on practical performance quantities, such as lift and drag. For airfoil applications the effects of icing has motivated a large amount of work, and especially in the earlier years of roughness study, many experiments did not detail the effects of the roughness on the transition process. A case study that did provide a detailed account of a boundary layer development along the surface of an airfoil with large scale leading edge erosion was performed by Kerho in 1996 [3, 54]. The experiment provided a number of insights regarding the nature of roughness induced transitional boundary layers and the influence of Reynolds number on roughness effects. The study confirmed the importance of streamwise location as a primary factors influencing the effects of various distributed roughness patterns on boundary layer development. The results from this study are used as benchmark calibration runs in the current work as very detailed boundary layer profiles and turbulence variables were recorded.

Although a large portion of the work on the influence of surface roughness was through experimentation, analytical attempts have slowly progressed through the years. A few noteworthy early analytical studies attempting to describe the influence of surface roughness were conducted by Singh and Lumley [55] as well as Lessen and Gangwani [56]. Both studies took a spectral route and amplified specific Fourier components to represent the influence of roughness. In both studies, an inflection was observed above rough sections. This result provides insight into the nature of these spectral amplification methods and the inherent limitations. The only experimental study that found an inflection in the mean profile was that of Kendal [40], and the

uniform spherical roughness pattern used was supposed as the cause of the inflection. As this phenomena was only observed when using very specific homogenous roughness distributions, it is not hard to see that applying a similar spectral approach to realistic non-uniform roughness may not adequately represent the configuration. The analytical approaches inherently produce uniform redistributions and transport of momentum, producing solutions that do alter the mean profile, but can lack the ability to represent unsteady effects and modifications to turbulent properties.

Roughness Models

Many early roughness models were nothing more than a single value defining the critical roughness Reynolds number, $Re_{k,crit}$, that would trip the flow. It has long been understood that roughness introduces highly complicated flow behavior, so initially researchers did not even attempt to go beyond these simple critical value type correlations. The advancement of both RANS type simulations and an analytical understanding of the transition process has opened up new avenues for the development of roughness models. Progress in the understanding of transient growth as a path to transition has prompted the development of models that view roughness as an alteration of the spectrum of the OS equation. Outside of discretely modeling each roughness element and running a highly resolved DNS simulation, there is really no way to directly model the effects of roughness. There is value in understanding the exact physical mechanism associated with the disturbances roughness introduces into the flow, however, from a modeling perspective, accounting for every individual perturbation is not practical now or in the foreseeable future. RANS methods represent the current state of the art for flow simulations at the present, so it follows to try and generate RANS compatible roughness models.

Modifications to the governing equations in RANS simulations can come at a number of different levels. Roughness is often viewed as a source of pressure drag and can be modeled with a sink term in the momentum equation [57]. Less direct modifications come in the form of changes to boundary conditions for turbulence or transition models. A number of specific attempts to model roughness are outlined in the following sections. A portion is dedicated to what is known as continuous spectrum analysis, which although not directly related to roughness model developed in this work, contains more specific insights into the transient growth mechanism associated with roughness induced transition. Following the presentation of the more analytic approach, methods that focus on roughness effects on the turbulent boundary layer are presented. Finally, methods that seek to model the effect of roughness on laminar-turbulent transition are discussed.

Analytic Methods For Roughness Modeling

One of the most successful analytical attempts to analyze how roughness impacts transition behavior has been through what is known as continuous spectrum analysis. In general the method attempts so determine the signature a particular roughness pattern will have on the spectrum of the OS equation. This signature can be represented as a function that modulates various wavenumbers in Fourier space. Taking a closer look at the OS equation with the general perturbation extended to 3-D:

$$\mathbf{u}'(x,y,z,t) = \hat{\mathbf{u}}(y)e^{[i(\alpha x+\beta z-\omega t)]} \tag{2.21}$$

where the hat represents the variable transformed into Fourier space, and the prime represents the fluctuating

component. A standard condition is that $\hat{\mathbf{u}} \to 0$ as $y \to \infty$. This however, yields only the discrete eigenvalues of the system. If the condition is relaxed and $\hat{\mathbf{u}}$ is only required to be bounded, (i.e. $|\hat{\mathbf{u}}| < \infty,\ y \to \infty$), the continuous spectrum can be obtained [58]. A state space representation of the linearized system (Eq. 2.22) can be used in Fourier space as partial derivatives are replaced with multiplication by wavenumber. The system can be written:

$$\frac{\partial \hat{\phi}}{\partial y} = \mathscr{L}_{OS}\hat{\phi} \tag{2.22}$$

with the state vector, $\hat{\phi} = [\hat{u}, \partial\hat{u}/\partial y, \hat{v}, \hat{p}, \hat{w}, \partial\hat{w}/\partial y]^T$. The details of the $\mathscr{L}_{OS}$ operator are expressed:

$$\mathscr{L}_{OS} = \begin{bmatrix} 0 & 1 & 0 & 0 & 0 & 0 \\ i(\alpha U-\omega)Re+\beta^2+\alpha^2 & 0 & ReDU & i\alpha Re & 0 & 0 \\ -i\alpha & 0 & 0 & 0 & -i\beta & 0 \\ 0 & -\frac{i\alpha}{Re} & \frac{-\beta^2-\alpha^2}{Re} - i(\alpha U-\omega) & 0 & 0 & -\frac{i\beta}{Re} \\ 0 & 0 & 0 & 0 & 0 & 1 \\ 0 & 0 & 0 & i\beta Re & i(\alpha U-\omega)Re+\beta^2+\alpha^2 & 0 \end{bmatrix} \tag{2.23}$$

It is the spacial stability of the equation that is considered when looking at a roughness induced disturbance as one occurs at a fixed location. Furthermore taking the x-direction as the streamwise, the particular wavenumber of interest is α. Therefore, Eq. 2.22 becomes an eigenvalue problem solved for complex values of α, with both β and ω real. In the freestream, where the velocity gradient, $\partial U/\partial y$, goes to zero, the $\mathscr{L}_{OS}$ operator becomes a matrix of constant coefficients. Solutions take the usual form $\hat{\phi} \propto e^{\lambda y}$, with λ a corresponding eigenvalue of the $\mathscr{L}_{OS}$ matrix.

In the discrete case where solutions approach 0 as $y \to \infty$, solutions must be a combination of the eigenvectors associated with the negative eigenvalues. Once more, if the condition is relaxed and the solutions are merely required to be bounded, the continuous spectrum can be represented. In this case, $\Re(\lambda) = 0$, giving rise to the representation, $\lambda_j = i\kappa$, and $\hat{\phi} \propto e^{i\kappa y}$ [58]. As κ is varied along the real line, α traces out paths in the complex plane. This occurs as α must take particular values to insure that eigenvalues remain purely imaginary. These paths represent what is considered the continuous spectrum of the OS equation.

An arbitrary disturbance can be represented by decomposing it into the modes of the continuous spectrum amplified. This is accomplished by creating a function of coefficients (C_α) that alter the excited modes (given by wavenumber α). Unfortunately the nature of this procedure requires a reconstruction of the coefficient function based on experimental or extremely high fidelity computational results. When complete flow information is available, it is possible to analytically divide a disturbance into its respective continuous spectrum modes. This technique, referred to as multimode decomposition, was developed by Tumin using the orthogonality property of the adjoint equation [7]. A distinct feature of the $\mathscr{L}_{OS}$ operator is that it is not self-adjoint. In this regard, the adjoint basis will form a set distinct from the solution to the direct problem. Therefore the solutions can be a combination of both the eigenvalues and elements of the adjoint basis. The mathematical intricacies of the adjoint problem are discussed in [59]. The formulation for the adjoint solution involve multiplying Eq. 2.22 by a vector function $\hat{\psi}$, and integrating over y:

$$\int_0^\infty \hat{\psi}^T \left(\frac{\partial \hat{\phi}}{\partial y} - \mathscr{L}_{OS}\hat{\phi} \right) dy = 0 \tag{2.24}$$

Integrating by parts will exchange the derivatives:

$$\int_0^\infty \hat{\phi}^T \left(\frac{\partial \hat{\psi}}{\partial y} - \mathscr{L}_{OS}^T\hat{\psi} \right) dy = 0 \tag{2.25}$$

producing the adjoint equation:

$$-\frac{\partial \hat{\psi}}{\partial y} = \mathscr{L}_{OS}^{T} \hat{\psi} \tag{2.26}$$

There are a number of mathematical details omitted, which can be found in reference [60]. Using the orthogonality of the adjoint equation, one can define the equation for the modal amplitude coefficients of the disturbance:

$$C_\alpha = \frac{i}{Q_\alpha} \int_0^\infty \frac{\partial \mathscr{L}_{OS}}{\partial \alpha} \hat{\phi}(x_0) \hat{\psi}_\alpha dy \tag{2.27}$$

with $\hat{\phi}(x_0)$ fully describing the disturbance data at the location x_0. The spanwise wavenumber (β) and Reynolds number are fixed parameters in the expression, and Q_α is a normalization constant, therefore the amplitude coefficients are simply functions of α.

After the coefficient functions have been determined with Eq. 2.27, the evolution of the perturbation can be described using the equation:

$$\phi(x,y,\beta,\omega) = \sum_{A,B} \int_{\tilde{n}} C_\alpha \hat{\phi}_\alpha(y) e^{i\alpha t} d\alpha \tag{2.28}$$

Two branches of the continuous spectrum are considered corresponding to the vorticity modes (A,B). The integral over α sums over each respective branch (Γ). It is important to remember that although Eq. 2.28 provides a means of describing the evolution of an input disturbance, it requires the C_α function, which can only be determined by an a posterori analysis. Therefore, the goal of future investigations would be to parameterize input disturbances in terms of their amplitude coefficient functions (C_α).

The method has been shown to accurately describe the disturbance energy evolution associated with a row of constantly spaced cylindrical roughness elements. Despite the success and rigorous theoretical background, there are restrictions to this type of analysis. One of the limiting factors is that the spanwise wavenumber (β) is directly related to the spacing of the roughness elements in the spanwise direction. This can cause serious issues in the case of random distributed roughness as there may not be a dominant wavenumber. Additionally, there must be either detailed experimental results or DNS type simulations of the roughness distribution that is to be modeled. In many ways even the most successful and rigorous analytic approaches are not equipped to handle realistic roughness distributions, where randomness can invalidate the equations used.

Turbulent Boundary Layer Modifications in RANS Simulations

The length scale of a physical disturbance introduced by surface roughness is frequently on the sub-grid level in RANS based methods. This implies that accounting for these changes must be done by modifying the turbulence quantities. Additionally, the effects of roughness on a fully turbulent boundary layer and the effects on the transition process require separate treatment. There have been a number of studies that document how surface roughness will alter a wall bounded fully turbulent flow [50]. Several studies have documented that roughness introduces a shift in the log layer of a turbulent boundary layer. In the presence of roughness, the "law of the wall" equation for turbulent boundary layers is modified by a function of the roughness parameters (k_s).

$$u^+ = \frac{1}{\kappa}\ln(y^+) + B \quad \rightarrow \quad u^+_{rough} = \frac{1}{\kappa}\ln(y^+) + B - f(k_s) \tag{2.29}$$

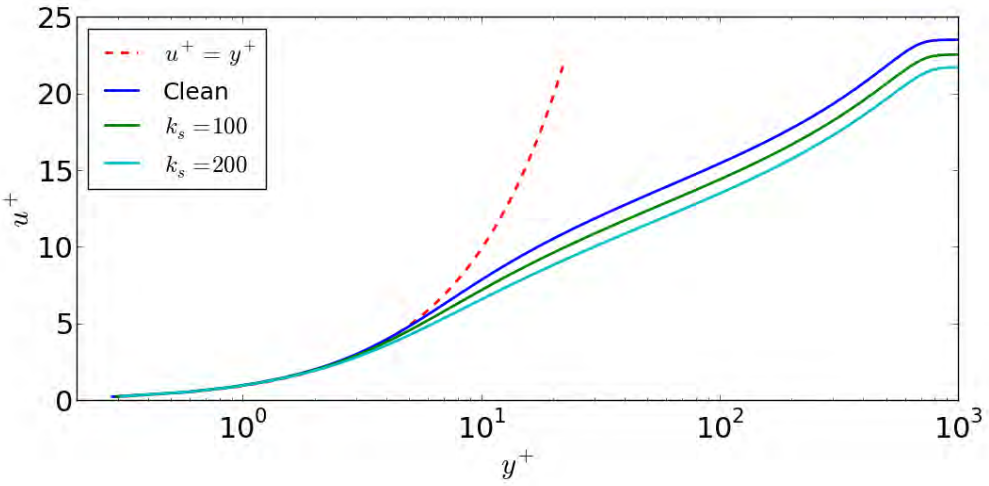

Figure 2.7. Demonstration of shift in law of the wall for two different equivalent sand grain roughness heights.

In eddy-viscosity based turbulent simulations, this shift can be approximated by changing the boundary condition of the turbulence model over a rough wall. Procedures have been documented for modifying both the Spalart-Allmaras [61] and the SST $k-\omega$ [62, 63] models to account for the effects of a rough wall on a fully turbulent boundary layer. The current work utilizes a change to SST $k-\omega$ turbulence model. Starting with the original boundary condition:

$$\omega_{smooth} = 10\frac{6\nu}{\beta(\Delta y)^2} \quad \text{with} \quad \beta = 0.09 \quad \text{at} \quad y = 0 \tag{2.30}$$

Here Δy represents the normal distance from the wall to the nearest grid point.

One of the first modifications to was proposed by Wilcox [64] as:

$$\omega_{rough} = \frac{\mu_\tau^2 S_r}{\nu} \quad \text{with} \quad \mu_\tau = \sqrt{\frac{\tau_w}{\rho_w}} \quad \text{at} \quad y = 0 \tag{2.31}$$

where S_r is dependent on the non-dimensional k^+ value.

$$S_r = \begin{cases} \left(\frac{50}{k^+}\right)^2, & k^+ \leq 25 \\ \frac{100}{k^+}, & k^+ > 25 \end{cases} \tag{2.32}$$

This will produce a shift in the logarithmic region of the turbulent boundary layer as visualized in Figure 2.7.

Other similar modifications to the rough wall boundary condition for turbulence quantities have been proposed by Hellsten and Laine [62] as well as Knopp et al. [65]. Aupoix provides a summary of some of these attempts as well as suggestions to correct some of the observed deficiencies [66, 67].

Modifications to Transition Criteria

While the modifications to the turbulence model boundary conditions can adjust the mean profiles once the boundary layer has fully transitioned, the acceleration of the transition process requires additional considerations. As there are many different methods implemented attempting to predict the onset of transition, the manner by which each are changed to accommodate surface roughness also differs greatly. Modifications to the linear stability based e^N method can be made by adjusting the N factor; however, the correlation is far from universal and the method itself suffers from incompatibilities with implementation in parallel codes [68]. It is troublesome to modify other disturbance growth rate prediction methods to account for roughness for similar reasons, and roughness induced perturbations differ substantially from the Tollmien-Schlichting wave growth that is modeled through traditional linear stability analysis.

As local correlation transition models (LCTM) have shown promise in implementation in general purpose CFD codes, it follows to try and modify the transition correlation to account for the presence of surface roughness. Recently several attempts at modeling the influence of surface roughness have sought to incorporate roughness correlations into LCTM's. Notably Stripf et al. [69] and Elsner and Warzecha [70] propose a direct modification of the transition onset criteria based on roughness height and displacement thickness (δ^*).

$$Re_{\theta t,rough} = \begin{cases} Re_{\theta t}, & k/\delta^* \leq 0.01 \\ \left(\frac{1}{Re_{\theta t}} + 0.0061 f_\Lambda \left(\frac{k}{\delta^*} - 0.01\right)^{f_{Tu}}\right)^{-1}, & k/\delta^* > 0.01 \end{cases} \tag{2.33}$$

two auxiliary functions f_{Tu} and f_Λ are included to account for local turbulence intensity and the roughness density, shape, etc.

Unfortunately the introduction of the displacement thickness into the calculation introduces a necessary integral computation non-localizing the method. Additionally, a more subtle drawback is that trying to generate an exact value, $Re_{\theta t,rough}$, where a roughness surface will transition somewhat negates flow history effects. Also, if the transition location is downstream of the edge of the roughness, where the parameter k/δ^* is no longer defined, it is unclear how to modify the original onset criteria. Despite the unfavorable characteristics, the results provide more insight how roughness will alter the transition correlations used in LCTMs.

A somewhat similar approach to modeling roughness taken by Dassler, Koluvic, and Fiala was to introduce a field quantity governed by an additional transport equation that defines a region of roughness influence. The scalar field is then used to modify the transition onset criteria [71, 72]. This approach is taken in the current work due to the generalizable nature of local correlation modeling, and its inherent ability to predict a range of transition mechanisms in RANS simulations. The physical details of the evolution of the initial roughness induced instabilities are not included in the methodology. However, the aggregate effects on transition are represented well. The formulation of the roughness amplification variable becomes an issue of modifying the transition onset correlation, a much simpler problem than representing the increased disturbance growth rates, or resolving detailed flow structures. With proper calibration, subcritical rough-

ness behavior can be represented and the incubation period determined using tunable model parameters. By not directly modifying the primary flow equations, the chances for error in the final flow solution become much lower as the impact of the roughness model is bound by a fully turbulent solution. As the method does not require redefining the computational mesh, it can be applied to existing grids. Finally, many of the cited influential parameters (streamwise location, pressure gradient, etc.) can be included through coupling with a local correlation transition model. For these reasons, this type of methodology was selected as the basis of the roughness model developed throughout the present work. Chapter 6 provides an extensive description of the model itself and the development process.

Chapter 3

Experimental Setup and Results

The present work has been part of a larger collaborative project between Texas A&M University, Sandia National Laboratories, and UC Davis. Much of the data collected and analyzed throughout this dissertation was taken at the Oran W. Nicks Low Speed Wind Tunnel at Texas A&M by Prof. Ed White, Dr. Robert Ehrmann and Dr. Benjamin Wilcox. An overview of the experimental work is provide here, including a description of the wind tunnel operating conditions, the model configurations tested, and roughness pattern generation.

Wind Tunnel

Multiple tunnel experiments were conducted at the Texas A&M Oran W. Nicks Low Speed Wind Tunnel (LSWT) on two different airfoil geometries. Much of the tunnel description has been derived from Ehrmann [73] and included here so that the reader can easily reference information about the experimental set up for the results described throughout.

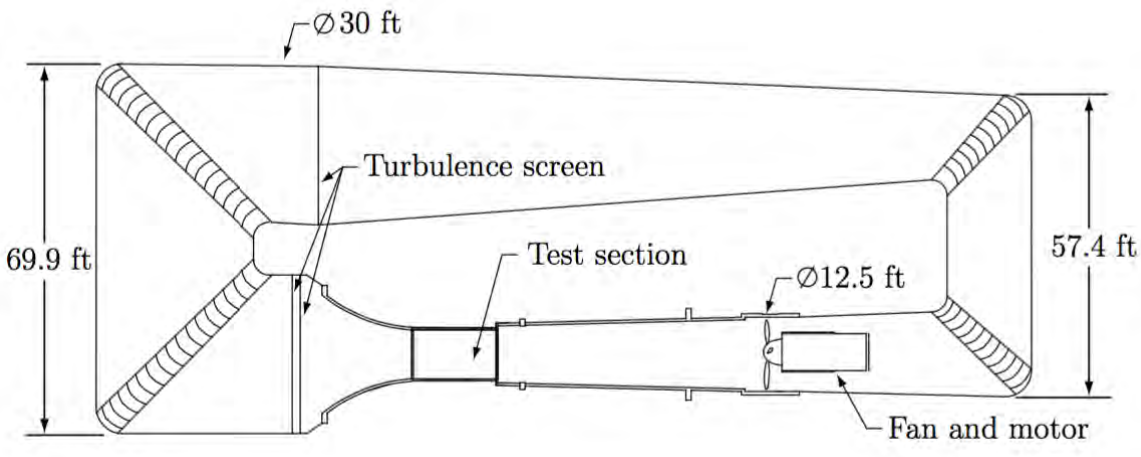

Figure 3.1. Overview of the Oran W. Nicks Low Speed Wind Tunnel.

The LSWT is a closed return tunnel with a 7ft $\times$ 10ft test section. The test section contains 1ft chamfers to reduce the sectional area and increase the maximum velocity and therefore chord Reynolds number obtainable in the tunnel. The floor and ceiling diverge one inch over the length of the test section to account for

boundary layer growth on the walls. The pressure difference between static-pressure and test section inlet is used for velocity feedback. While testing, the dynamic pressure is compared to a calibration curve related to the dynamic pressure in an empty test section. A six component floor balance allows for multiple different mounting configurations and measurements. Figure 3.1 provides a top view schematic of the LSWT.

Dynamic pressure can be adjusted by varying both the motor RPM and the fan blade pitch angle. Typically the motor speed is held constant and the blades are pitched to obtained the desired tunnel speed. Hidore performed an extensive characterization of the tunnel's freestream conditions in 2012 [74]. The freestream turbulence intensity is a function of both dynamic pressure and fan motor speed. The importance of properly characterizing tunnel turbulence intensity is discussed in detail in the section on local correlation based turbulence intensity. The tunnel typically operates at a turbulence intensity of roughly 0.25%. This is relatively "noisy" compared some other aerodynamic tunnels, which is not an inherent issue, but something to keep in mind when attempting to recreate the transition behavior computationally.

Airfoil Model Descriptions

The broader goal of characterizing the impact of leading edge erosion was considered when selecting the airfoils for use in the study. A large consideration was that the geometry be available in the public domain as to allow for future validation studies. Additionally, a desire was that the airfoils have similar aerodynamic properties as those typically used for various portions of a megawatt scale wind turbine blade. The initial geometry selected was the NACA 63_3-418, an 18% thick airfoil typical of what is used on the outboard section of wind turbine blades. The model was constructed in four sections visible in Figure 3.2.

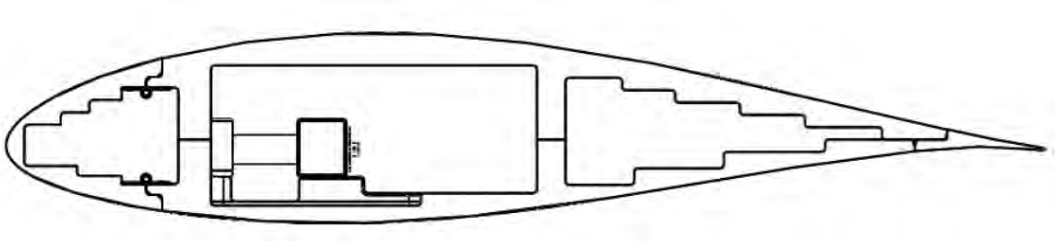

Figure 3.2. Cross sectional view of NACA 63_3-418 airfoil model.

The model contained a removable leading edge that could be replaced with one containing simulated heavy erosion. Two large sections make up most of the upper and lower surfaces, and the model was manufactured such that all bolts and connectors are accessed through the lower surface. This was done to insure smoothness on the suction side of the airfoil. The two primary components were milled from solid aluminum blocks. Additionally the trailing edge was manufactured separately, but the final machining of the airfoil surface was done with all components in place to maintain a high level of surface uniformity.

After the completion of the tunnel entries with the NACA 63_3-418, the focus was shifted towards a thicker airfoil. Testing a thicker airfoil provided a more complete understanding of how roughness impacts the power output of a wind turbine blade. Due to structural requirements, thicker airfoils are used on more inboard sections of the blades. These sections are more prone to stalling, and despite more power output coming from outboard sections, can cause compounding issues due to 3D flow effects. Also, differences

in the pressure distribution of thicker airfoils can lead to differences in surface contamination around the leading edge. Testing two different airfoils with the same roughness configurations allows for much more robust model development and provides more information regarding how roughness may impact turbine performance as a whole.

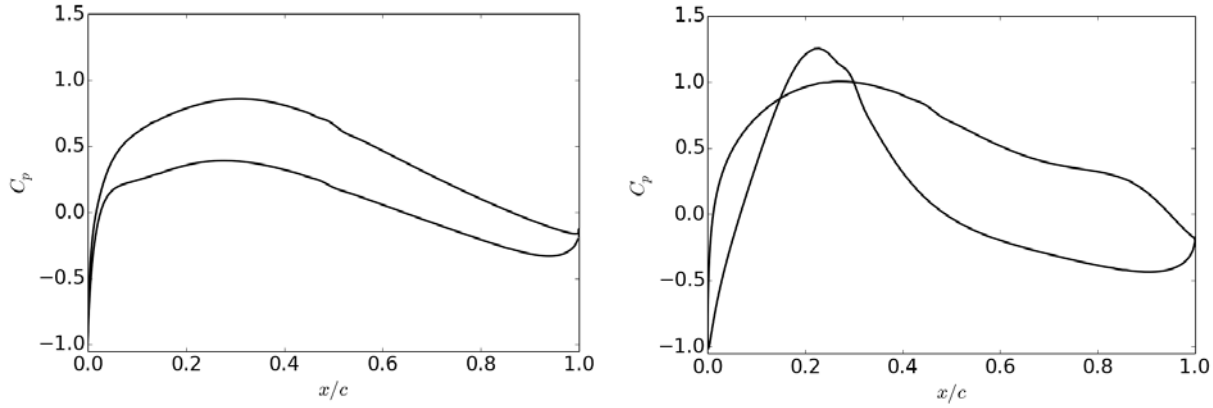

Figure 3.3. Pressure distributions of both NACA 63_3-418 (left) and S814 (right), $\alpha = 0^o$ and $Re_c = 2.4 \times 10^6$ for both.

The candidates for "thicker" airfoils to be tested were the 30% thick DU97-W-300, the 25% thick DU91-W2-250, and the 24% thick NREL S814. The roughness collection efficiency, pressure distribution, and past experimental data were examined for each of the airfoils to determine the most useful geometry to test. Ultimately, the decision was made to test the NREL S814, due to the availability of transition data from previous test results, and the substantial difference in pressure distributions from the NACA 63_3-418 as shown in Figure 3.3. The pressure surface in particular on the S814 is of interest due to the long run of a nearly constant highly favorable pressure gradient. This yielded useful data for calibration of pressure gradient effects in the CFD roughness model.

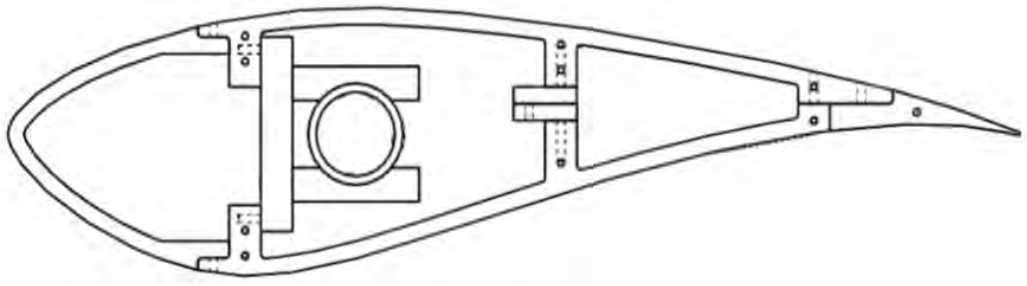

Figure 3.4. Cross sectional view of S814 airfoil model.

The model for the S814 airfoil was manufactured in a similar fashion to the NACA 63_3-418. The model is again split into four components and milled from solid aluminum blocks. A notable difference was that the internal portion of the model was milled such that the wall thickness was nearly constant; this difference

is visible in Figures 3.2 and 3.4. The reason to machine the internal portion of the model was to minimize the temperature variation from changes in heat conduction caused by uneven thickness. Preventing these temperature variations is important as the transition location measurements are performed using infrared thermography.

Roughness Patterns

In effectively any realistic application, roughness is not deposited in some uniform and orderly manner. This made the decision easy to select a randomized roughness distribution to test. A level of randomness was also desired to offset any effect that may be unwittingly produced by interactions between uniformly distributed roughness elements. Flow phenomena such as velocity profile inflections and TS wave dampening have been attributed to certain uniform roughness patterns. Another requirement was that the roughness pattern must be made so that it could be applied in a repeatable manor. To obtain both a randomized and repeatable roughness distribution, the roughness patterns were cut from vinyl decals. This had the added benefit of generating a roughness distribution without any sort of substrate, and provided the ability to isolate the effects of a change in roughness height. Variation in roughness height came from simply a variation in thickness of the vinyl.

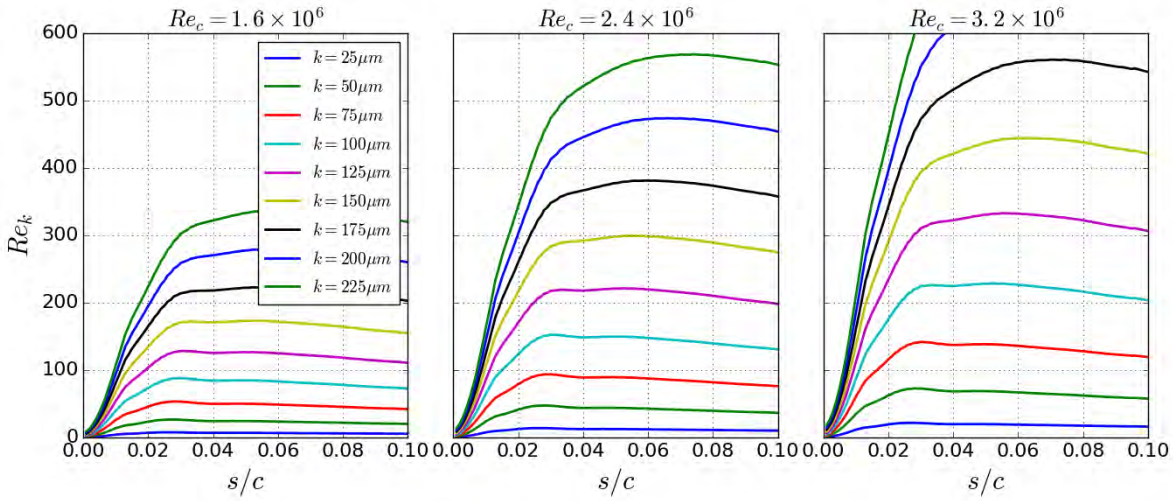

Figure 3.5. Projected Re_k values along upper surface of NACA 63_3-418, s/c measured from leading edge center, angle of attack fixed at 0 degrees. Boundary layer profiles taken from OVERFLOW RANS simulations.

The heights used for the roughness patterns were determined by looking at velocity profiles generated by RANS simulations. This allowed for a more accurate calculation of the U_k parameter in the roughness Reynolds numbers Re_k:

$$Re_k = \frac{\rho U_k k}{\mu} \tag{3.1}$$

A large goal of the project was to capture subcritical roughness behavior so a range of Re_k values below the critical threshold was desired. For the experiments, it was assumed the approximate subcritical range was between 100 - 400. RANS flow simulations were conducted across a range of Reynolds numbers from 1.6 - 3.2 million and the boundary layer velocity profiles extracted. Following this computation, a number of possible roughness heights were analyzed by looking at the Re_k values generated by that height in the region where the roughness was to be applied. Figures 3.5 and 3.6 show variations in Re_k values along the chord near the leading edge for a variety of different heights and Reynolds numbers at a fixed angle of attack.

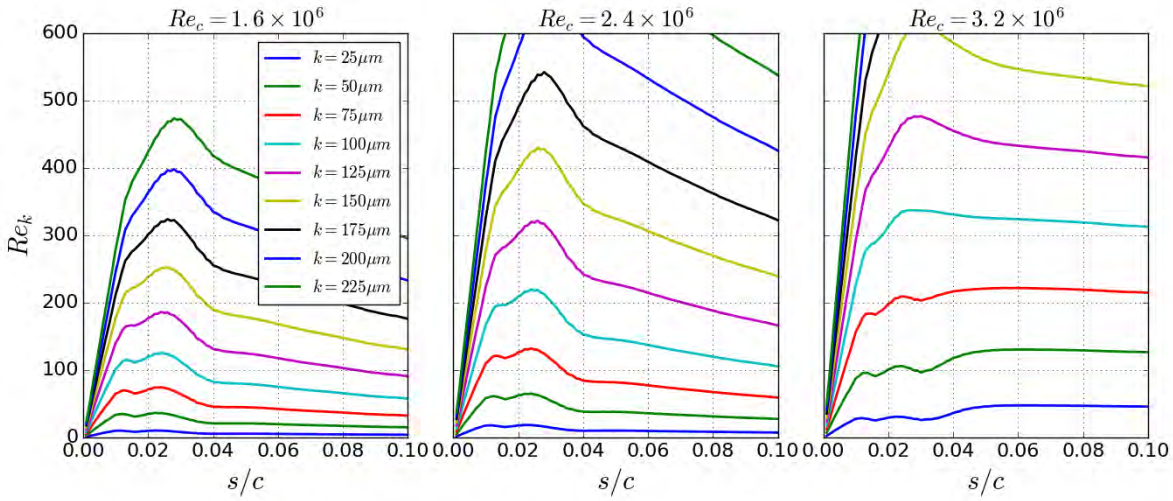

Figure 3.6. Projected Re_k values along upper surface of NACA 63_3-418, s/c measured from leading edge center, angle of attack fixed at 6 degrees. Boundary layer profiles taken from OVERFLOW RANS simulations.

Even for a fixed height there is substantial variation in the projected Re_k values due to variation in velocity profiles caused by changes in Reynolds number. This is desirable to obtain a diverse range of transition behaviors. The heights were selected by looking across all flow conditions to be tested, and trying to maximize the cases that would yield Re_k values in the subcritical range. The dimensional heights that both optimized the number of configurations in this Re_k range and were physically available as vinyl sheets were 100μm, 140μm, and 200μm.

The process of carefully selecting the roughness heights to be tested is an example of how the close collaboration between the teams conducting the experiments, and constructing the model helped produce experimental results that contained a large amount of useful data points for model calibration. As seen in the results, relatively small variations roughness height can have a large impact on flow behavior, so insuring as many cases possible fell into the subcritical Re_k range was a crucial component.

In addition to a change in height, the experiment sought to explore how differences in distribution density changes the impact of roughness patterns. The percentage cited for the roughness densities is defined as the percentage of area covered by roughness elements in the bounding box used to generate the vinyl patterns. Initially, only two different roughness densities were tested (3% and 15%), however, upon seeing the impact of roughness density, more densities were included to systematically investigate the impact. More information about the specifics of the roughness patterns and which tunnel entries tested each can be found

in Table 3.1.

Roughness Distribution for NACA 63_3-418

The roughness pattern used for the initial experiment on the NACA 63_3-418 was generated by randomly placing circles in an 152 mm $\times$ 152 mm area. The area of the circles was normally distributed at 1.2 ± 0.15 mm. If the circles intersected, an ellipse was circumscribed such that the area was minimized. This produced randomness in both the placement of the roughness elements and their size and shape. The pattern was repeated in the spanwise direction such that the entire leading edge of the model was covered. The placement of the roughness along the chord was determined using the NASA ice accretion code LEWICE [75] to determine the region that had maximum probability for insect accretion. The results from the LEWICE simulation indicated this region was from 2% chord on the upper surface to 10% chord on the lower. An additional pattern was generated that extended to 6% chord on the upper surface for completeness in the investigation.

To achieve variation in roughness density, the highest density patterns were generated first, then individual elements were removed at random until the desired density was reached. Figure 3.7 shows the patterns for the 3% and 15% distribution densities.

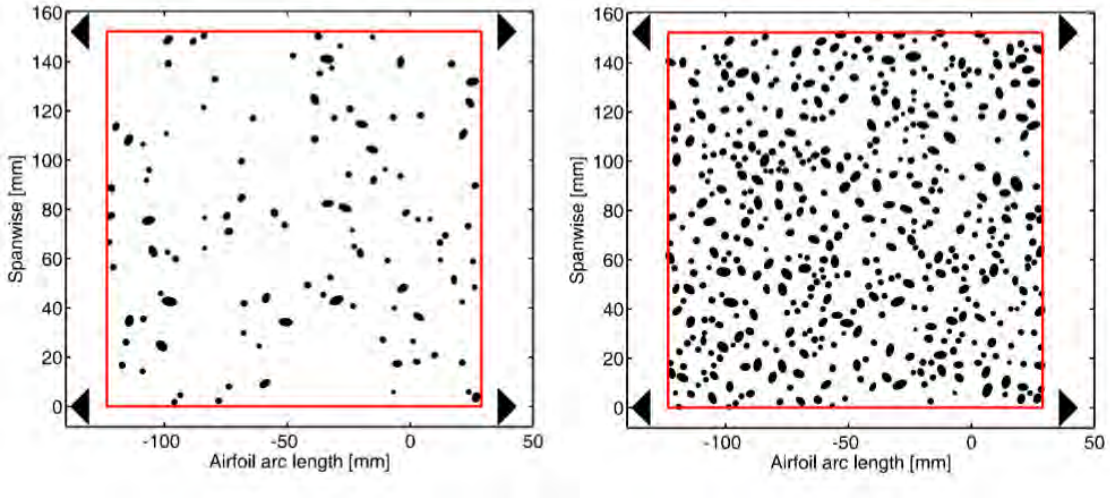

Figure 3.7. 3% and 15% density roughness distributions used for tunnel entries 1-4 on the NACA 63_3-418, negative arc lengths correspond to placement on the lower airfoil surface.

Roughness Distribution for S814

The roughness pattern generated for the S814 differed slightly from the one used for the initial set of wind tunnel entries. There was no longer a variation in the shape of the roughness elements. During the process of creating the pattern, if two circles would intersect, that point was not used and another randomized point was generated. One of the reasons for this change was to ease the manufacturing process of the

roughness decals. Additionally, there was interest in determining the effect a subtle change in roughness shape would produce. This was accomplished by using the new pattern with uniform element shapes on the NACA 63_3-418 during phase 2 of the experimental campaign.

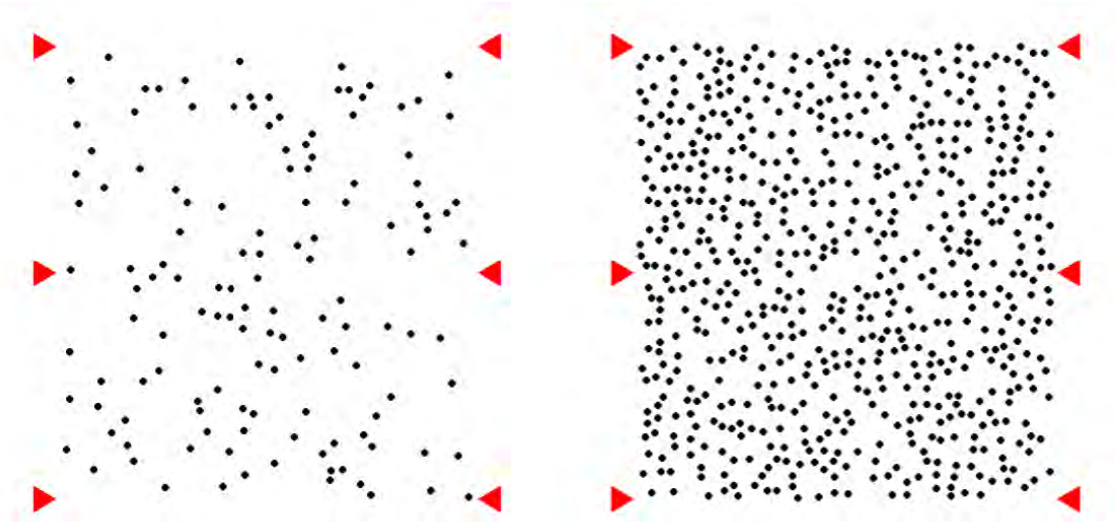

Figure 3.8. 3% and 15% density roughness distributions used for tunnel entries with the S814 and entry 5 with the NACA 63_3-418.

The pattern was applied in a similar manner, repeating in the spanwise direction until the entirety of the model was covered. Due to the changes in pressure distribution of the S814 the chordwise placement of the roughness pattern differed on the S814. The new bounds of the roughness distribution were from 14% chord on the lower surface to 2.5% chord on the upper surface as determined from the LEWICE simulations. Slightly different vinyl material was used, so the exact heights of the roughness elements differ from what was used in the initial entries. The new heights were 95μm, 125μm, and 225μm.

Wind Tunnel Entries and Configurations Tested

The experiments were conducted over the course of three years and 8 different tunnel entries. To provide more clarity, each of the entries is outlined here along with what airfoils and roughness distributions were tested. The first phase of the experimental study used only the NACA 63_3-418 while the second used both airfoils. One important consideration is that the roughness pattern used for the NACA 63_3-418 during the second phase used the roughness pattern without variation in the element shapes. This will be made explicitly clear when applicable.

Other configurations were tested, including a heavily eroded leading edge and forward facing steps and can be found in [73]. The roughness patterns indicated in Table 3.1 are simply the ones most applicable to development of the roughness model. Figure 3.9 depicts the S814 physical model in the tunnel with the roughness pattern along the leading edge.

Table 3.1. Outline of experimental wind tunnel entries.

Entry	Airfoil	Configurations Tested
1	NACA 63_3-418	Clean, Trip Strip
2	NACA 63_3-418	Clean, 100μm - 3%, 140μm - 3%, 200μm - 3%
3	NACA 63_3-418	Clean, 100μm - [3%, 9%, 15%] 140μm - [3%, 6%, 9%, 12%, 15%]
4	NACA 63_3-418	Clean, 100μm - 3%, 140μm - 3%
5	NACA 63_3-418*	Clean, 95μm - 3%, 125μm - 3%, 225μm - 3%
6	*S*814*	Clean, 95μm - 3%, 125μm - 3%, 225μm - 3%
7	*S*814*	Clean, 95μm - [3%, 9%, 15%], 125μm - 3% 225μm - 3%

* indicates use of secondary roughness pattern

Figure 3.9. S814 airfoil model positioned in test section of tunnel and image of 15% distribution density roughness pattern applied to the leading edge, wake rake also visible in images.

Measurement Techniques

The procedures for calculating the reported experimental values are described in this section. Lift and pitching moments were calculated by integrating 32 static surface pressure measurements. Drag was computed using a wake rake to compute the velocity deficit behind the model. The wake rake consisted of 25 Pitot and three static probes and was positioned $0.9c$ behind the model. More details and technical specific of the measurement devices can be found in Ehrmann [73]. Transition was computed using both infrared (IR) thermography and a variety of hotfilm measurements. It was found the easiest method for determining the transition location was through IR thermography, so the included results used this technique.

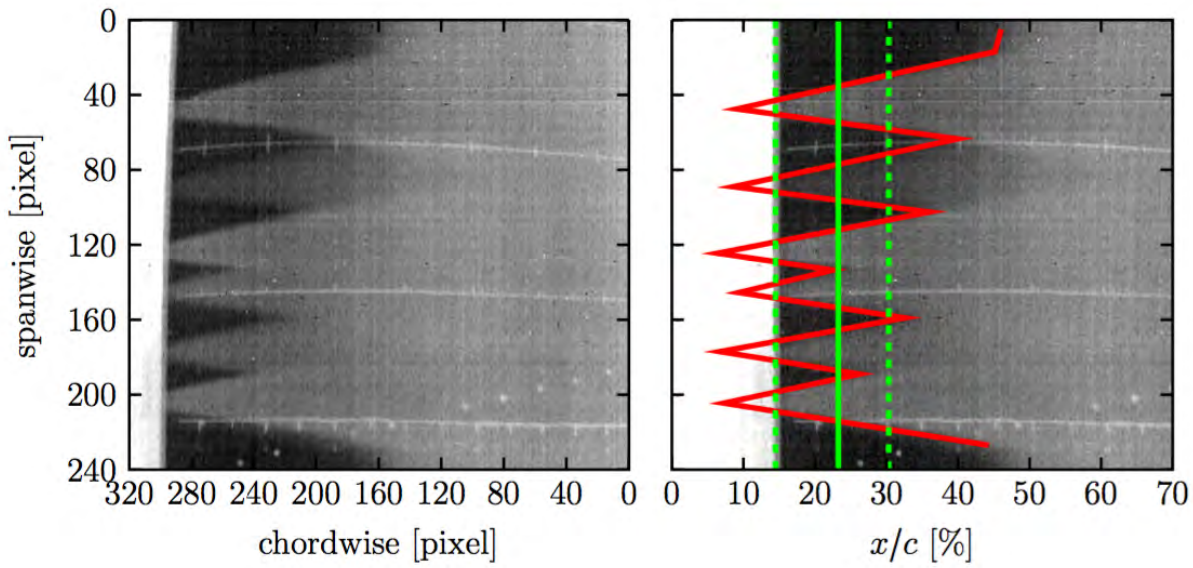

Figure 3.10. Raw (left) and processed (right) IR image demonstrating how the transition location was determined. The solid green line represents the position where 50% of the span is turbulent, while from left to right the dotted lines represent the 25% and 75% value.

The bypass transition observed at moderate to high angles of attack was inherently 3-D. This is seen in Figure 3.10 where turbulent wedges are seen across the span. As the roughness model is calibrated in 2-D, and there is a desire to obtain a scalar value for the transition location, a procedure was established to define where on the chord the flow would be considered turbulent. The metric used was the percent of the span that was turbulent at given chordwise location. The scalar valued transition location given was when this value hit 50%. Additionally, the positions where 25% and 75% of the span was fully turbulent were recorded. This is indicated by the solid, and dotted green lines, respectively, in Figure 3.10. When the transition location is indicated on the figures in the results, the bounding uncertainty bars represent these 25% and 75% locations.

Uncertainty bars are also included on drag results if these values were recorded. The uncertainty was calculated using a method described in [73] that is outlined here. For each pressure port measurement in the wake rake, it was assumed both the position of this measurement, and its recorded value were normally distributed. The location of the pressure ports were assumed to have a standard deviation of 0.1 in. The uncertainty of pressure measurement was assumed the manufacture's recorded tolerance. Drag was calculated

many times by integrating the normally distributed values until convergence. A distribution of 2500 points was shown to produce drag values that converged for all Reynolds numbers. In general, uncertainty for drag is higher at lower Reynolds numbers and at both very high and low angles of attack.

Representative Results - NACA 63_3-418

Several results are shown here that summarize some of the findings from the experimental tests. In this section, and in the proceeding portions of the dissertation, there is a set color scheme when presenting the results from the wind tunnel entries. For each roughness height there is set color hue, and changes in the distribution density are represented by adjusting the shade of that color. For example, this can be observed in Figure 3.12 where darker shades of green are used to indicate high distribution densities.

The effect of changing roughness height while fixing distribution density on drag is shown in Figure 3.11. The increase in drag comes primarily from changes to the laminar-turbulent transition behavior. As the roughness height increases, the transition location is shifted further towards the leading edge producing a longer run of a turbulent boundary layer along the chord. Of interest is that at higher Reynolds numbers, the drag polars converge for the 140μm and 200μm heights for positive C_l values. This implies that the critical Re_k value is reached for both heights, therefore further increases in roughness height don't effect transition location anymore, but may result in changes to airfoil performance if exceedingly large. The uncertainty in the drag is shown to be small for the polars shown, providing a high level of confidence for validation. There is a trend towards increasing uncertainty at higher angles of attack, but the relative error is on the order of less than 5% in the areas the roughness model is calibrated to.

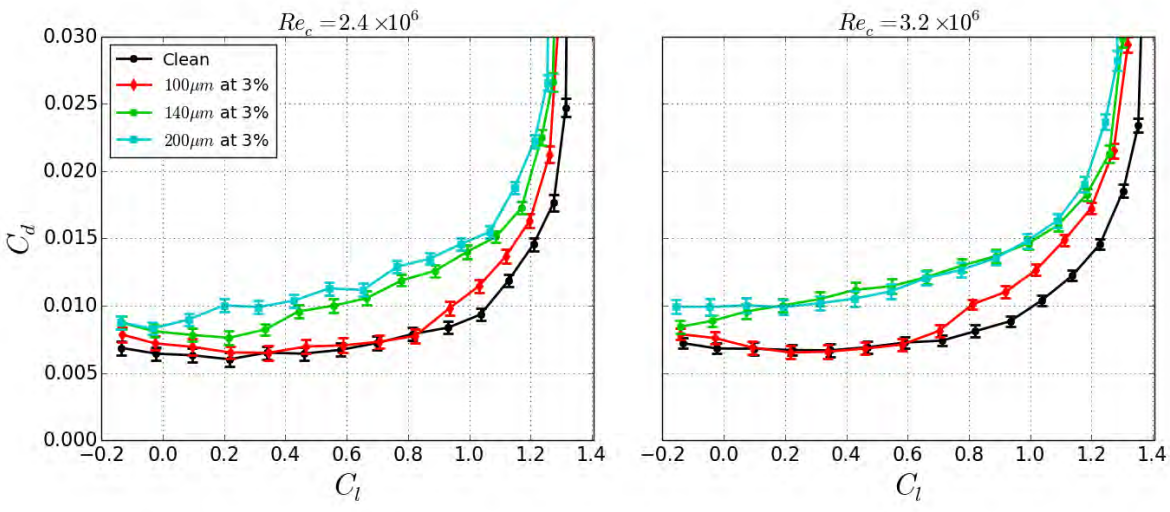

Figure 3.11. Effect of roughness height on lift and drag, NACA 63_3-418, 100μm, 140μm, 200μm heights, all at 3% distribution density and from tunnel entry 3.

The effect of changing roughness density is shown in Figures 3.12 and 3.13. There are some clear trends, but it is difficult to precisely identify the impact of changing the distribution density. In general,

increasing the distribution density increases the drag. Similar behavior to the changes in height is observed at $Re_c = 3.2 \times 10^6$, where the drag curves converge. Once more, this implies that a critical value has been reached and further changes to the distribution density do not have as profound an impact on the airfoil performance.

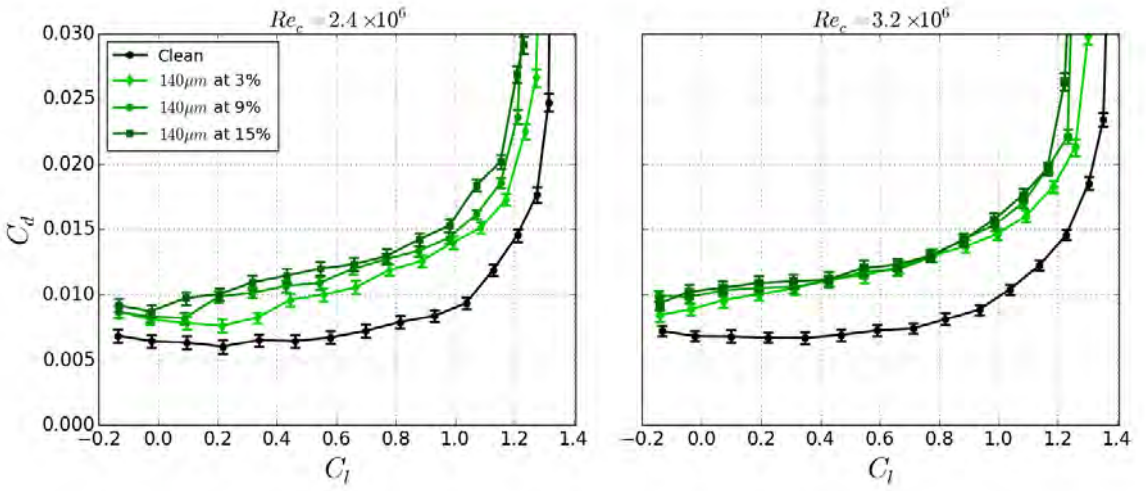

Figure 3.12. Effect of roughness distribution density on lift and drag, NACA 63_3-418, 3%, 9%, and 15% distribution densities, all at 140μm height and from tunnel entry 3.

Figure 3.13 demonstrates how the transition behavior changes as a function of chord Reynolds number for all the different density configurations. To obtain these results, the angle of attack was fixed and the chord Reynolds number varied by changing freestream tunnel velocity. The lines represent the 50% spanwise turbulent criteria established in Section 3. The bands corresponding to the 25% and 75% turbulent regions are shown for the 12% and 6% density distributions. This is really to demonstrate that there is a bimodal clustering of the distribution densities. The mean transition lines are somewhat intertwined at similar distribution densities, making the effect of changing density harder to quantify exactly.

In many ways, changes in distribution density must be thought of stochastically. Changes in distribution density represent some increased probability that one of the elements will introduce enough of a disturbance to trigger the onset of transition. As the individual elements themselves are responsible for the introduction of destabilizing disturbances, increasing the number in a finite area will add more opportunity for disturbance growth. There are competing factors which may also decrease the chances of the roughness pattern instigating transition. These include increased sheltering caused by neighboring elements, and interactions between vortex structures behind the roughness that may offset disturbances introduced. The increase in drag is slightly more consistent than the transition behavior, as a portion of the drag comes from the skin friction component. Naturally, having more protuberances along the surface will result in an increase in skin friction.

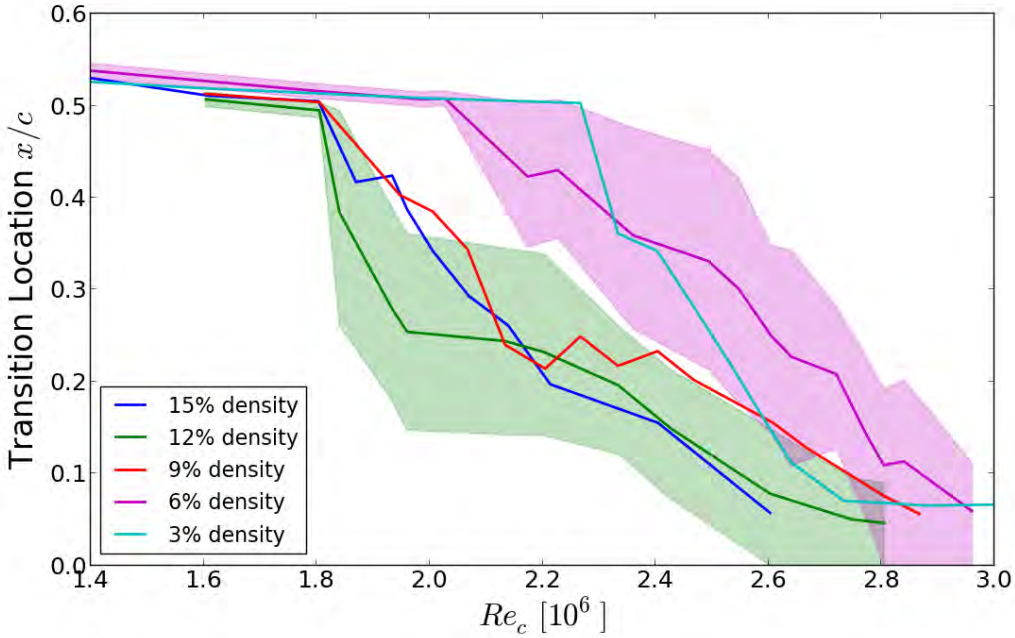

Figure 3.13. The effect of roughness distribution density on transition location, NACA 63_3-418 airfoil, 140μm roughness height from tunnel entry 2, angle of attack fixed at 0 degrees, Re_c varied by increasing freestream velocity, 25% and 75% transition bands shown on the 12% and 6% density cases.

Representative Results - S814

Similar trends are observed for the S814 as those seen with the NACA 63_3-418. Uncertainty measurement were not made for the S814 airfoil, although it should be noted they would likely be some degree greater as the thicker airfoil produces a larger wake and a wider span of measurements are taken. Nonetheless, there is still a high degree of confidence as these results were obtained in the same tunnel with similar procedures to the NACA 63_3-418. Changes in roughness height have a more profound impact on the S814 airfoil at negative angles of attach (low C_l values). This can be attributed to the highly adverse pressure gradient after the C_p minimum value on the lower, or pressure, surface (as seen in Figure 3.3). The design of the airfoil relies on the highly favorable pressure gradient near the leading edge to keep the flow laminar until the C_p minimum. If the flow is tripped near the leading edge due to roughness, the result is a premature stalling on the lower surface, which can be seen in the spike in the drag coefficient in Figure 3.14. This produces results that are particularly useful for roughness model calibration.

Changes to the distribution density are shown to have a minimal impact on the flow behavior. This may partially be attributed to the fact only the lowest roughness height was tested with a variation in density. As the lower heights tend to have less of an effect on the flow in general, differences produced by a change in the distribution density are more difficult to discern.

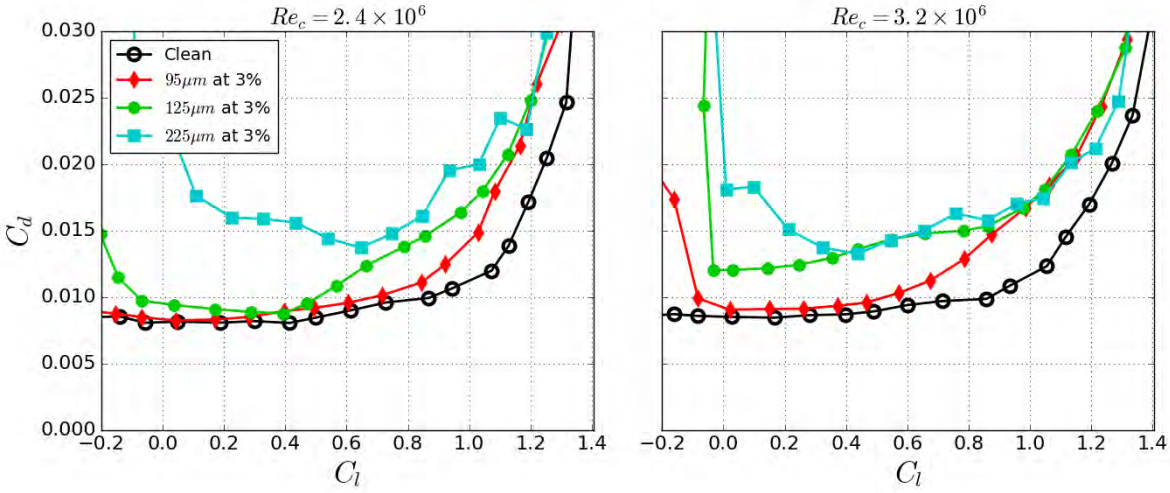

Figure 3.14. Effect of roughness height on lift and drag, S814 airfoil, 95μm, 125μm, 225μm heights, all at 3% distribution density and from tunnel entry 7.

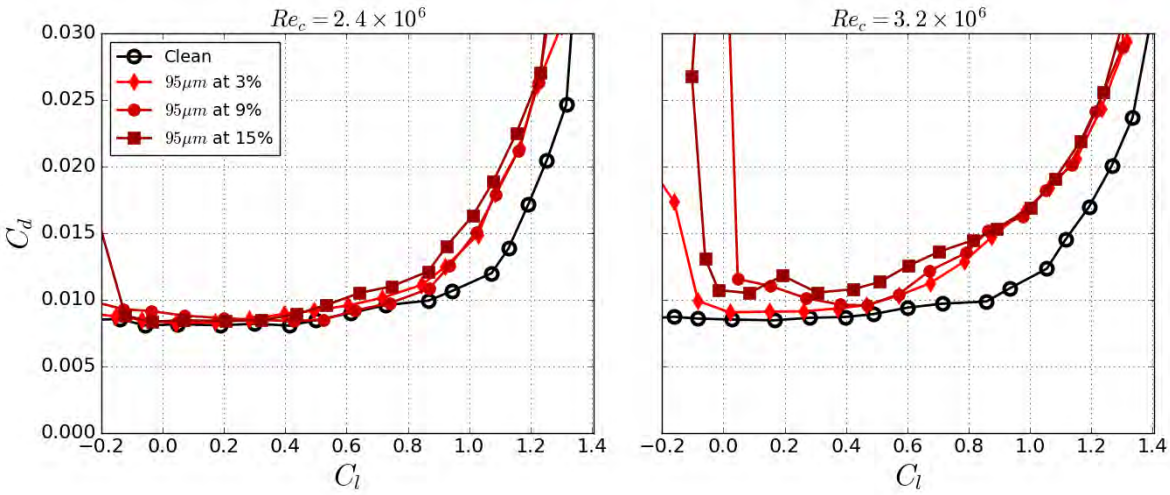

Figure 3.15. Effect of roughness distribution density on lift and drag, S814 airfoil, 3%, 9%, and 15% distribution densities, all at 95μm height and from tunnel entry 7.

The results shown in this section represent a small portion of the data generated in the experimental study. They have been selected as they provide a good indication of the overall behavior observed for changes in roughness height and distribution density. In general, as the roughness height was increased the transition location was shifted forward, closer to the stagnation point. The same trend was true with an increase in distribution density, given a fixed roughness height. Although these observations are intuitive, the carefully recorded measurements and wide parameter space covered in the experimental campaign provide new insights on the details of roughness induced transition. A full description of the NACA 63_3-418 experimental setup and results is presented in [73]. Additionally the information regarding the experimental study conducted on the S814 airfoil is presented in [76].

Chapter 4

Methodology

Navier Stokes

The development of the governing equations has a rich historical background littered with the names of some of the most influential mathematicians and scientists of all time. The Navier-Stokes equations were originally derived by Navier in 1822 however he made a few incorrect assumptions about the nature of the viscous forces [77]. The equations were re-derived by Cauchy and Poisson in 1828 and 1829 respectively [78]. The full equation set was also independently derived by Saint-Venant in 1843 and Stokes in 1845 with a more accurate consideration of the effect of viscosity [79]. Only the most fundamental information is given here, however there are countless references that detail the development and subsequent work on the equations that span a number of different fields. The Navier-Stokes (NS) and mass conservation equations can be expressed quite elegantly in vector notation,

$$\rho(\mathbf{u_t} + \mathbf{u}\cdot\nabla\mathbf{u}) = \nabla\cdot\boldsymbol{\sigma} + \mathbf{f} \tag{4.1}$$

$$\rho_t + \nabla\cdot(\rho\mathbf{u}) = \mathbf{0} \tag{4.2}$$

Here the velocity field is given by $\mathbf{u}(\mathbf{x},\, t) = u_j(x_1, x_2, x_3, t),\ (j = 1,2,3)$, where $u_{1,2,3}$ represent the measure of velocity in each direction of a three dimensional orthogonal basis. The subscript t implies a partial derivative with respect to time. The right side of the equation represents the resultant body force, $\mathbf{f}$, on the domain and the internal force tensor $\boldsymbol{\sigma}$. The ∇ operator is defined by $\nabla = \sum_{j=1}^{N} \frac{\partial}{\partial x_j}$.

There are a number of ways to arrive at the NS equations, the most common is by examining the fluid as a continuum and applying the laws of classical mechanics. However the equations can also be derived by taking spatial averages of the Boltzmann equation or from the kinetic theory of gasses. Equation 4.1 represents the laws of conservation of momentum applied to an element of fluid, and is referred to as the momentum equation. Equation 4.2 is referred to as the continuity or mass conservation equation and follows from fundamental mass conservation principles.

A third equation must be included in the set to account for thermodynamic and energy laws and is referred to as the energy equation.

$$s_t = -\mathbf{u}\cdot\nabla\mathrm{s} + \frac{\mathrm{Q}}{\mathrm{T}} \tag{4.3}$$

where s is the entropy per unit mass, Q is the heat transferred, and T is temperature. Although the full NS equation set must be considered to fully represent various flows, the momentum equation is frequently

singled out and studied more extensively.

The internal forces, $\boldsymbol{\sigma}$, can be regarded as the combination of the normal, or pressure forces, and the shearing or viscous stresses. One can consider the pressure terms as the diagonals of $\boldsymbol{\sigma}$ and all other components as the viscous stress tensor (τ), such that:

$$\tau = \boldsymbol{\sigma} - p\mathbb{I} \tag{4.4}$$

where $p(\mathbf{x},\mathrm{t})$ represents the dynamic pressure distribution. In the case of an inviscid fluid, all but the pressure terms vanish, therefore $\boldsymbol{\sigma} = p\mathbb{I}$, and Eq. 4.1 simplifies to the Euler momentum equation:

$$\rho(\mathbf{u_t} + \mathbf{u}\cdot\nabla\mathbf{u}) + \nabla\mathrm{p} = \mathbf{f} \tag{4.5}$$

The Euler equation has provided deep insight into the nature of high Reynolds number flows where the off-body flow behavior is dominated by the inertial terms and can be approximated by an inviscid assumption. Potential flow theory originated from the incompressible inviscid continuity equation and has remained a powerful analytical tool. However, for fluid-solid interfaces where boundary layers develop, the viscous stresses influence the problem substantially.

An approximation relating the strain on an element of fluid to its deformation ($\frac{1}{2}(\nabla\mathbf{u} + \nabla\mathbf{u}^{\mathbf{T}})$) must be made to close the equation for the elements of the viscous stress tensor. If a linear approximation is taken where the fluid is assumed to deform proportional to the rate of strain, it is referred to as a Newtonian fluid. The internal tensor can be expressed as:

$$\boldsymbol{\sigma} = -p + \mu(\nabla\mathbf{u} + \nabla\mathbf{u}^{\mathbf{T}}) + \left(\zeta - \frac{2\mu}{3}\right)(\nabla\cdot\mathbf{u})\mathbb{I}$$

here ζ and μ are the first and second viscosities of the fluid. Inserting into Eq. 4.1 provides a more detailed description:

$$\rho(\mathbf{u_t} + \mathbf{u}\cdot\nabla\mathbf{u}) + \nabla\mathrm{p} - \nabla\cdot\left[\mu(\nabla\mathbf{u} + \nabla\mathbf{u}^{\mathbf{T}}) + \left(\zeta - \frac{2\mu}{3}\right)(\nabla\cdot\mathbf{u})\mathbb{I}\right] + \mathbf{f}$$

The equation further simplifies assuming μ to be constant and incompressibility to:

$$\rho(\mathbf{u_t} + \mathbf{u}\cdot\nabla\mathbf{u}) + \nabla\mathrm{p} - \mu\Delta\mathbf{u} = \mathbf{f} \tag{4.6}$$

where Δ is the Laplacian given by $\Delta = \sum_{j=1}^{N} \frac{\partial^2}{\partial x_j^2}$. Assuming ρ to be constant and given the definition of Reynolds number ($Re = \rho UL/\mu$) the equation can be recast in dimensionless form as:

$$\mathbf{u_t} + \mathbf{u}\cdot\nabla\mathbf{u} + \nabla\mathrm{p} - \frac{1}{Re}\Delta\mathbf{u} = \mathbf{f} \tag{4.7}$$

In this form it is easy to see that as $Re \to \infty$, Eq. 4.7 $\to$ Eq. 4.5. However, the rate of convergence is troublesome as the $\Delta\mathbf{u}$ term does not follow the same rate of rapid decrease. Therefore, even when resolving high Reynolds number flows, the viscous term can not be excluded.

Despite almost two centuries of work since the equations were first supposed, there is no general analytical solutions to the full conservation equation set. In very specific cases where the equations can be significantly reduced, analytical solutions have been obtained [80]. However, even the existence of a solution to the full conservation equation set remains an open problem. Despite the difficultly in obtaining a closed form solution, the equations still provide an enormous insight into flow phenomena and various avenues have been developed to utilize various simplifications of the equations. Numerical simulations have helped obtain approximate solutions for a given flow configuration, and as both processing power increases and more efficient algorithms are developed, numerical methods have become more accurate.

DNS and Large Eddy Simulations

DNS

The full conservation equation set contains all forces and governing dynamics associated with a fully turbulent flow, the temporal behavior, large discrepancies in eddy scales, energy cascade, self dissipative nature and more. Direct numerical simulation (DNS) refers to the method by which the equations are directly solved numerically, even for the very small length and time scales of turbulence. The equations may be discretized directly or solved using a spectral method. The theoretical process itself is not troublesome, however a necessary condition for the accuracy of DNS is that all time and spacial scales associated with a turbulent flow must be resolved [81]. To accomplish this, the computational mesh required becomes unpractically large. As a general guideline DNS is considered to require $O(Re^3)$ mesh points for proper resolution. A few representative configurations are listed.

Automobile – $Re \approx 6 \cdot 10^5 \to \approx 10^{15}$ mesh points required for DNS simulation.

Wind Turbine – $Re \approx 4 \cdot 10^6 \to \approx 10^{19}$ mesh points required for DNS simulation.

Large Aircraft – $Re \approx 2 \cdot 10^7 \to \approx 10^{21}$ mesh points required for DNS simulation.

Clearly the processing power required to handle that magnitude of points is entirely out of reach for most organizations. Even with the most powerful supercomputers today DNS can only be applied to flows around simple geometries at relatively low Reynolds numbers. Furthermore, even if there existed a machine capable of managing a problem of the size DNS requires, complications would arise defining precise boundary conditions at each boundary node. As the full range of scales are represented, small discrepancies in the initial and boundary conditions may yield dramatically different solutions. Despite the limitations DNS, serves as a powerful validation tool and can provide detailed flow information that experimental techniques can not measure. Even with advances in processing capabilities and more efficient numerical algorithms, the use of direct numerical simulations for everyday engineering applications is still in the distant future.

Large Eddy Simulation

The most challenging motions to capture in DNS simulations are the smallest both spatially and temporally down to nearly the molecular level. Capturing these microscopic scales is the exact reason the mesh requirements are so impractical. An inclination is to define a length scale in which fluid motions below have very little influence on the macroscopic flow. This is the central idea behind Large Eddy Simulations (LES); modify the primary equations to not directly depend on the smallest scales and the mesh resolution required drops substantially. This is accomplished by defining a decomposition of the turbulent flow variables as:

$$\mathbf{u}(\mathbf{x},\mathrm{t}) = \tilde{\mathbf{u}}(\mathbf{x},\mathrm{t}) + \mathbf{u}''(\mathbf{x},\mathrm{t}) \tag{4.8}$$

where $\tilde{\mathbf{u}}$ is the spatially averaged portion of the variable and $\mathbf{u}''$ (a double prime is used to distinguish between a spatially and time averaged quantity) is the turbulent fluctuation defined based on the deviations from the averaged value. It is possible to directly average the flow variables over a cell volume, however the grid requirements to accomplish this are inhibitive, i.e. very uniform and structured. A more utilized option to accomplish the spatial average is to apply a filter kernel via convolution on the decomposed flow variables. Given a filter $g(\mathbf{x})$ and a length scale $\delta > 0$ as the minimum eddy size the filter takes the form:

$$g_\delta(\mathbf{x}) = \frac{1}{\delta^{\mathrm{d}}}\left(\frac{\mathbf{x}}{\delta}\right) \tag{4.9}$$

With the filter defined, $\tilde{\mathbf{u}}(\mathbf{x},\mathrm{t})$ becomes:

$$\tilde{\mathbf{u}}(\mathbf{x},\mathrm{t}) := (\mathrm{g}_\delta * \mathbf{u})(\mathbf{x},\mathrm{t}) = \int_\Omega \mathrm{g}_\delta(\mathbf{x}-\mathbf{s})\mathbf{u}(\mathbf{s},\mathrm{t})\,d\mathbf{s} \tag{4.10}$$

After applying the filter, LES sets out to model the influence of the removed energy scales. The modeling of the removed scales is known as closure or turbulence modeling and is discussed in more depth in the section on the Reynolds-averaged equations. A few of the more commonly used sub grid models are the Smagorinsky and Gaussian-Laplacian. As a consequence of the definition as $\delta \to 0$ so does $\mathbf{u}''$ and furthermore $\tilde{\mathbf{u}}(\mathbf{x},\mathrm{t}) \to \mathbf{u}(\mathbf{x},\mathrm{t})$. This is even more substantial if one realizes that it implies LES $\to$ DNS.

For those interested in the mathematical details of LES, Berselli et al. provide an excellent account of the primary LES tools available [82].

Despite the simplifications introduced, the grid required to properly resolve an LES problem is still enormously large. Additionally, assumptions have to be made regarding the nature of wall bounded flows, as the spatial filter encounters trouble approaching a solid boundary. As the distance to the wall goes to zero, what does one do with the δ limit? Other issues arise as certain required filter operations do not commute at wall boundaries. LES will likely serve as a stepping stone to full DNS simulations, however the process still has a few theoretical shortcomings and requires vastly more computing power than is practical for everyday use.

Reynolds-Averaged Navier Stokes (RANS) Equations

A very distinguishing characteristic of turbulence is its *unsteady* nature, eddies of all sizes are created and dissipated continuously, the mean flow might have a well defined direction but within the stream lie boundless fluctuations. An approach to eliminate the temporal behavior is to look at the flow as a combination of both a time averaged flow and a fluctuating component, similar to the LES decomposition. Given a finite time interval, there is a well defined average velocity at a particular location in the flow field, from there the instantaneous deviations from the mean can be defined as the turbulent fluctuations. Frequently the following notation is used:

$$\mathbf{u}(\mathbf{x},\mathrm{t}) = \overline{\mathbf{u}}(\mathbf{x}) + \mathbf{u}'(\mathbf{x},\mathrm{t}) \tag{4.11}$$

Here, the mean flow is represented with an overbar and defined as $\bar{u} = \frac{1}{T}\int_0^T u(t)\,dt$. The prime indicates the fluctuating component. An important consideration is that the RANS mean velocity does not carry a time dependence, unlike the LES counterpart. From a historical context, the turbulent decomposition actually began with the definition in a time averaged sense and was later progressed to the spatial variant.

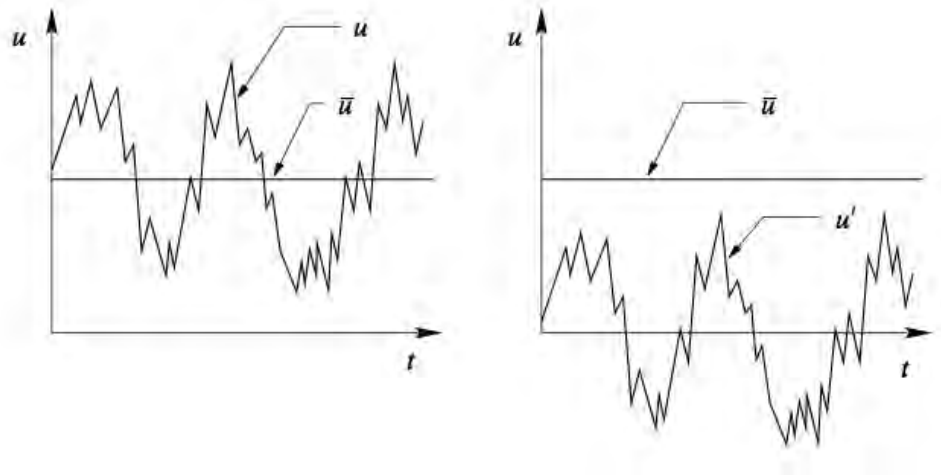

Figure 4.1. Plot of Reynolds decomposition indicating mean flow and fluctuating component

Osborn Reynolds is credited as the first to exploit the fact that without a time dependence the governing flow equations are simplified greatly. In addition two properties of the decomposition are the following.

$$\overline{\bar{u}} = \frac{1}{T}\int_0^T \bar{u}\,dt = \bar{u} \qquad \& \qquad \overline{u'} = \frac{1}{T}\int_0^T u'(t)\,dt = 0 \tag{4.12}$$

The first follows as the time average of a time averaged quantity remains the same, additionally the time average of the fluctuating component goes to zero by definition.

The Reynolds-averaged Navier Stokes equations are obtained by inserting the Reynolds decomposed

flow variables into Eqs. 4.1 and 4.2 and time averaging the entire equations. The full derivation is omitted, however the final result as applied to the momentum equation can be written generally as:

$$\nabla \cdot \overline{\mathbf{u}}^2 + \nabla \cdot \overline{\mathbf{u}'^2} = \nu \Delta \overline{\mathbf{u}} - \nabla \overline{\mathbf{p}} \tag{4.13}$$

Reynolds-stress Term

There is an inherent problem that arises during the averaging process, that is the time average of the product of two fluctuating components does not go to zero.

$$\overline{u_i' u_j'} \neq 0 \qquad (i, j = 1, 2, 3) \tag{4.14}$$

Therefore, the term $\nabla \cdot \overline{\mathbf{u}'^2}$ needs additional consideration. The quantity is referred to as the Reynolds-stress term. Traditionally, the RANS equations and complimentary turbulence models are expressed in tensor or Einstein summation notation. The subscript indices correspond to the directions in a generalized orthogonal basis and are used to differentiate scalars, vectors, and tensors. The relationship between vector and tensor notation can be observed in the following:

$$\nabla \cdot \overline{\mathbf{u}'^2} = \nabla \cdot \begin{bmatrix} \overline{u_1' u_1'} & \overline{u_1' u_2'} & \overline{u_1' u_3'} \\ \overline{u_2' u_1'} & \overline{u_2' u_2'} & \overline{u_2' u_3'} \\ \overline{u_3' u_1'} & \overline{u_3' u_2'} & \overline{u_3' u_3'} \end{bmatrix} = \nabla \cdot \overline{u_i' u_j'} = \frac{\partial}{\partial x_j} \overline{u_i' u_j'} \tag{4.15}$$

In tensor notation Eq. 4.13 can be written:

$$\frac{\partial}{\partial x_j} \overline{u}_i \overline{u}_j = -\frac{\partial \overline{p}}{\partial x_i} + \nu \frac{\partial^2 \overline{u_i}}{\partial x_j \partial x_j} - \frac{\partial}{\partial x_j} \overline{u_i' u_j'} \tag{4.16}$$

All terms are dependent on mean quantities with the exception of the Reynolds-stresses term. This poses a problem when trying to resolve the RANS equations as more unknowns are created than equations available.

Turbulence Modeling

The practice of creating a model to account for the Reynolds stress term is known as closure, or turbulence modeling. Turbulence modeling has been the subject of extensive scientific investigation over the past half century. To conduct a thorough review of all the research conducted, even if only the most significant contributions are discussed would require considerably more space than available here. Therefore, only the most fundamental details are provided. The reader is directed to Wilcox for a more complete examination of turbulence modeling [64]. It should also be stressed that most turbulence models are based on extensive numerical investigations and are not derived from first principles. Regardless, turbulence modeling has made significant progress and RANS simulations have proven to accurately represent a wide variety of flows.

The primary approximation used in the process of modeling the Reynolds stresses was originally proposed by Boussinesq in 1877. He supposed the turbulent shearing is related to the mean rate of shear of turbulent and eddy viscosity. The approximation is frequently referred to as the Boussinesq hypothesis. Closure methods that depend on it are titled eddy-viscosity models, due to the inclusion of the additional term, ν_t. It relates the Reynolds-stress term to the mean rates of shear and is given by:

$$-\overline{u_i' u_j'} = \nu_t \left(\frac{\partial \overline{u}_i}{\partial x_j} + \frac{\partial \overline{u}_j}{\partial x_i} \right) - \frac{2}{3} \delta_{ij} \left(\nu_t \frac{\partial \overline{u}_k}{\partial x_k} + k \right) \tag{4.17}$$

With δ_{ij} is the Kronecker delta function, k is the turbulent kinetic energy given by $k = \frac{1}{2}(u_i^{'2})$ and ν_t is the turbulent eddy viscosity, which is an additional quantity that needs modeling for proper RANS closure. Much like the molecular viscosity and kinematic viscosity are related, there is the relationship $\nu_t = \mu_t/\rho$. Methods for modeling ν_t can be characterized by their order of closure. The order of the method is given by the number of additional partial differential equations used in determining the approximation of turbulent eddy viscosity.

Zero and First Order Models

Zero order closure models are based off the Boussinesq approximation that do not use any additional PDE's and compute the turbulent eddy viscosity using an algebraic expression based on local flow quantities. One of the initial zero order methods was Prandtl's mixing length model, determined using dimensional analysis. It was first supposed in the 1920's with ν_t defined as:

$$\nu_t = l_m^2 \left| \frac{\partial u}{\partial y} \right| \tag{4.18}$$

From Eq. 4.18, one can see the turbulent eddy viscosity is proportional to the magnitude of the shear stress, $|\partial u/\partial y|$, and l_m, the mixing length that depends on the flow conditions and needs to be prescribed by the user. The mixing length is both a property of the fluid and of the local flow characteristics. This raises issues as the length scales at different regions in the boundary layer are markedly different. An approach to solve the problem of changing length scales is the implementation of the Van Driest damping function [83]:

$$l_m = \kappa y [1 - e^{-y^+/A_o^+}] \tag{4.19}$$

with y^+ the non-dimensional wall distance defined $(\sqrt{\tau_w/\rho_w})(y/\nu)$ and A_o^+ a model constant.

Similar approaches incorporating a damping function have been taken in LES to resolve the issue of the filter length as a solid boundary is approached [82].

Other zero order models have been developed by Cebeci and Smith [84], Baldwin [85], and Lomax. Most modern simulations do not use algebraic correlations due to non-general nature of the parameters involved. Additionally zero order models require the direct use of an empirical correlation. Transport equations are frequently used to incorporate the local flow conditions allowing the model to function without prescribing the type of flow in a region when initializing the simulation.

Models that use one additional transport equation in determining ν_t are referred to as first order closure models. They have been developed by Baldwin and Barth [85], as well as Spalart and Allmaras [86]. The Spalart-Allmaras (SA) model represented a significant leap forward in the accuracy of turbulence modeling and, provided the flow remains attached, is still regarded as one of the more trusted approximations in RANS simulations for external flows [87, 88]. The SA model has been continually developed with iterations of the model released with rotational corrections and the use of a laminar-turbulent trip specification.

Concurrent to the development of the one equation turbulence models was the initial work attempting to incorporate the length scales associated with a turbulent flow directly into the computation of the turbulent eddy viscosity. The primary quantity of interest is the turbulent kinetic energy (k) and some form of the dissipation rate. Models that solve two additional quantities for the transport of the turbulent quantities are known as two equation models.

$k-\varepsilon$ and $k-\omega$ Two Equation Models

One of the initial two equation approaches incorporates the turbulent dissipation rate (ε) along with the turbulent kinetic energy into the formulation for ν_t. Jones and Launder are credited as developing the $k-\varepsilon$ model which models the transport of turbulent kinetic energy and dissipation rate using transport equations [89]. The full development spans many different researchers and the model has evolved over the years. Much like SA model, the $k-\varepsilon$ model has proven to behave well in attached flows however it has been cited with under predicting separation. Additionally the near wall behavior is considered dubious and the use of wall damping function to better represent the near wall dynamics has become common practice. The turbulent eddy viscosity is then defined as the ratio between the turbulent kinetic energy and the dissipation rate as:

$$\nu_t = \frac{k}{\varepsilon} \tag{4.20}$$

A similar model to the $k-\varepsilon$ was developed by Wilcox [90]. Much like other two equation models it uses the turbulent kinetic energy as one of the primary quantities of interest, however a slightly different scale is used for the dissipation parameter (ω). The $k-\omega$ turbulence model, as it is referred, is known to represent near wall flows much more accurately than the $k-\varepsilon$ and does not require the use of wall damping functions. The $k-\omega$ model also includes the influence of streamwise pressure gradient, an additional upgrade from the $k-\varepsilon$ formulation. The changes when switching over to the $k-\omega$ model are not all positive however. The freestream condition for ω must be non-zero, something that is non-physical. Additionally the choice of value is not universal and can have a strong impact on the flow solution [91]. The turbulent eddy viscosity is computed similarly with the exception of using ω rather than ε, $(\nu_t = k/\omega)$.

SST Two Equation Model

The strengths and weaknesses of the $k-\varepsilon$ and $k-\omega$ models naturally suggest the two be combined to create a model that determines the flow well both near wall and in the freestream. Mentor's shear-stress transport (SST) model takes the advantages of both and creates a blending function that switches between the two [92]. The $k-\omega$ model is incorporated near a viscous wall that is switched over to the $k-\varepsilon$ near the boundary layer edge and free shear layer. The dissipation parameter is given the name "specific dissipation

rate" and is labeled ω, therefore when referring to the SST model, ω represents a blend of the turbulence dissipation scales from either model. The SST model is the underlining turbulence model that the present work looks to build upon, therefore more details will be given. The turbulent eddy viscosity is given in a similar manner to other two equation models as:

$$\nu_t = \frac{k/\omega}{\max\left[1\ ;\ \frac{\Omega F_2}{a_1 \omega}\right]} \tag{4.21}$$

The F_2 function is determined by:

$$F_2 = \tanh\left(\left[\max\left(2\frac{\sqrt{k}}{0.09\omega y}\ ;\ \frac{500\mu}{\rho y^2 \omega}\right)\right]^2\right) \tag{4.22}$$

It should be noted there is a dependence on distance to the wall, y, which can be troubling to compute in a parallel environment.

The transport equation for turbulent kinetic energy (k) and specific turbulent dissipation rate (ω) are as follows:

$$\frac{\partial(\rho k)}{\partial t} + \frac{\partial(\rho U_j k)}{\partial x_j} = P_k - \beta^* \rho \omega k + \frac{\partial}{\partial x_j}\left[(\sigma_k \mu_t + \mu)\frac{\partial k}{\partial x_j}\right] \tag{4.23}$$

$$\frac{\partial(\rho \omega)}{\partial t} + \frac{\partial(\rho U_j \omega)}{\partial x_j} = P_\omega - \beta \rho \omega^2 + 2(1-F_1)\sigma_\omega \frac{\mu_t}{k}\frac{\partial k}{\partial x_j}\frac{\partial \omega}{\partial x_j} + \frac{\partial}{\partial x_j}\left[(\sigma_\omega \mu_t + \mu)\frac{\partial \omega}{\partial x_j}\right] \tag{4.24}$$

with the production terms (P_k, P_ω) defined:

$$P_k = \left(\mu_t\left[\left(\frac{\partial u_i}{\partial x_j} + \frac{\partial u_j}{\partial x_i}\right) - \frac{2}{3}\frac{\partial u_k}{\partial x_k}\delta_{ij}\right] - \frac{2}{3}\rho k \delta_{ij}\right)\frac{\partial u_i}{\partial x_j} \tag{4.25}$$

$$P_\omega = \frac{\zeta}{\nu_t} P_k \tag{4.26}$$

The F_1 term in Eq. 4.24 represents the primary blending function between the $k-\omega$ and the $k-\varepsilon$ models. It is designed to switch from the ω variant near the wall to the ε formulation in the far field. When the F_1 functions takes a value of one, the transport equation for ω transforms into the equation for ε. The function utilizes the smooth properties of the hyperbolic tangent function and is given by:

$$F_1 = \tanh\left(\left[\min\left\{\max\left(\frac{\sqrt{k}}{0.09\omega y}\ ;\ \frac{500\mu}{\rho y^2 \omega}\right)\ ;\ \frac{4\rho\sigma_{\omega 2} k}{CD_{k\omega} y^2}\right\}\right]^4\right) \tag{4.27}$$

$CD_{k\omega}$ is the cross diffusion term given by:

$$CD_{k\omega} = \max\left[\frac{2\rho\sigma_{\omega 2}}{\omega}\frac{\partial k}{\partial x_j}\frac{\partial \omega}{\partial x_j}\ ;\ 10^{-20}\right] \tag{4.28}$$

The model constants are given by:

$$\begin{aligned} &a_1 = 0.31, \quad \kappa = 0.41, \quad \beta^* = 0.09 \\ &\sigma_{k1} = 0.85, \quad \sigma_{\omega 1} = 0.5, \quad \beta_1 = 0.075 \\ &\sigma_{k2} = 1.0, \quad \sigma_{\omega 2} = 0.856, \quad \beta_2 = 0.0828 \\ &\zeta_1 = 0.553, \quad \zeta_2 = 0.440 \end{aligned} \tag{4.29}$$

In addition to switching the transport equation for ω the model parameters are blended using the F_1 function by:

$$\phi = F_1\phi_1 + (1 - F_1)\phi_2 \tag{4.30}$$

where ϕ represents an arbitrary model constant and subscripts refer to that parameter's value in each of the respective models. A constant that does not include an explicit subscript in the model description is blended by using Eq. 4.30.

The SST model has consistently outperformed either of its built in variants particularly near separation and predicting near wall flow behavior. A primary issue is that is does not account for the laminar-turbulent transition region nor can it predict the location of the onset of transition. A partial fix was to incorporate a manually defined location to switch on the production of turbulent kinetic energy representing the position turbulent fluctuations initiate and the physical onset of transition. The trouble with using a manual specification is that a well defined location of transition onset must be known in advance, otherwise it is at best an educated guess. This shortcoming has been addressed by the development of transition models that are coupled with the turbulence model to better approximate the state of the boundary layer and its subsequent effects on the surrounding flow field. As boundary layer transition is of great interest to the current study, the topic of transition modeling is explored in much more detail in the next chapter.

Local correlation transition modeling (LCTM) is briefly mentioned in the review of transition prediction methodologies and is worth noting the interaction it has with the SST turbulence model here. A widely used LCTM is referred to as the Langtry-Menter transition model, it couples a correlation based transition onset criteria with an intermittency (γ) transport equation. In the Langtry-Menter model, γ acts as a scaling of the production of turbulent kinetic energy, P_k.

The modified production term becomes:

$$\tilde{P}_k = \gamma P_k \tag{4.31}$$

The value of γ is pushed to zero by the model in the laminar boundary layer where there is no production of turbulent kinetic energy, and then progressively switches to one where the turbulence model is fully activated. The value of intermittency is set to one in the domain outside a laminar boundary layer, however, production of turbulent kinetic energy is inherently limited if there is a lack of shear stress in the mean flow.

Eddy Viscosity Alternatives

The modeling of Reynolds-stresses by means of the Boussinesq hypothesis is not the only method for representing the fluctuating products. Another approach is to model the transport of the Reynolds stress terms directly and methods that employ this technique are known as Reynolds-stress transport models (RSTM) [93]. Frequently referred to as second order closure models, the use of these is inhibited by the significant computational costs associated with resolving the additional unknown quantities. The cost derives from the fact that five or more additional transport equations are required to use the second order closure models [94, 93].

A common critique of the approximation using an eddy-viscosity model is the assumption of isotropic turbulence at all scales. While this is generally assumed to be true for the smallest turbulent scales, the largest eddies do not behave isotropically. It can be observed from Eq. 4.15 that $\overline{u_i' u_j'}$ is a tensor, and therefore a constant value of ν_t does not account for differences in the transport of the Reynolds-stress terms in each direction. Closure models that treat ν_t as a tensor have been proposed; however, this requires each term of the tensor to be individually modeled adding even more equations [95].

Both RSTM's and the anisotropic modeling of the eddy viscosity are "physically" more accurate approximations, and one might expect that they produce more accurate solutions. However, there are trade offs that come with the discretization error that compounds due to the additional model equations. It brings up the debate of what is more accurate, a more physically correct model that has a large modeling error, or a physically less accurate model with a much smaller modeling error. In the case of turbulence modeling, the more refined but less physically accurate models have generally won out [88].

Detached Eddy Simulation

A recently developed simulation technique is that of Detached Eddy Simulation (DES). Originally proposed in 1997 by Spalart et al., DES is hybrid method that includes both RANS and LES modeling approaches [96]. DES attempts to take advantages of the strengths of both methods by applying a RANS procedure in the near wall region and an LES off body. This helps resolve the issues of near wall behavior that LES has struggled with, including the grid resolution required and spacial filtering problems encountered at solid boundaries. Applying an LES approach in the far field is desirable to retain flow structures frequently smoothed away in RANS procedures. The non-physical smoothing of vorticity or other unsteady features has plagued RANS simulations due to fundamental consequences of time averaging. Proper vortical resolution can be obtained in RANS but requires carefully designed grids for complex geometries [97].

DES is very appealing theoretically, however in practice it has been reported the method displays unfavorable sensitivity to grid spacing, in some cases creating a solution less accurate than either a pure RANS or LES performed on the same grid [98]. Other more fundamental issues arise as the LES turbulent decomposition is not the same as in RANS, i.e. $\mathbf{u}' \neq \mathbf{u}''$ & $\tilde{\mathbf{u}} \neq \overline{\mathbf{u}}$ using the notation from above. DES is currently an active area of research and it will likely see improvements in the near future. Considering the near wall flow is modeled using a RANS approach, the present work is of great interest as it can theoretically be included in DES in the future.

In terms of accuracy from the perspective of physically represented scales:

DNS > LES > DES > RANS

LES and DNS are still considered far away from practicality in an engineering sense so RANS and DES will likely remain prominent for some time. The implications of this are that a model capable of predicting the effects of roughness on near wall behavior with a RANS turbulence approach will continue to have use even if a shift is made in the engineering community towards DES simulations.

OVERFLOW

OVERFLOW is a finite difference, unsteady RANS code developed by NASA over that past few decades. The code was initially developed as a cleaner more robust version of the flux-vector splitting code F3D, originally developed by Joe Steger. Throughout its history, the code has seen input from scientists across several NASA research centers including Ames, Johnson Space center, and Langley. Although a large number of researchers have contributed to the development of OVERFLOW a few that have made a significant impact include, Joe Steger, Pieter Buning, Dennis Jespersen, Tom Pulliam, Robert Meakin, and many more [99].

OVERFLOW-2 allows the user to select a wide variety of numerical spacial discretization and time advancement techniques of varying order of accuracy [100, 101]. Additionally a number of linear factorization and flux splitting schemes are implemented for more efficient computation. The interaction the user has with the code is through an input file where the specified discretization schemes, boundary conditions, and many other flow parameters are set. OVERFLOW-2, version 2k, contains an implementation of the Langtry-Menter transition model and is the platform upon which the current work is built. The reader is directed to [99, 100, 101] for further details pertaining to the development and features built into OVERFLOW-2.

Grid Generation

As the flow solver applied in the current study is a finite difference code, the computational grids used have a structured topology. At each grid point there are well defined neighbor points in grid orthogonal directions. This has the advantage of being computational efficient, however, the generation of the grid requires much more work than an unstructured mesh. There are two primary types of grids used for the airfoil geometries used throughout the present work, referred to as O-type and C-type grids. An example of each is presented in Figures 4.2 and 4.3. The naming convention comes from the domain connectivity and its loose resemblance to the letters when viewed from a distance.

In general O-types grids use fewer points, and therefore are considered to be less computationally expensive. There are some disadvantages to using an O-type grid as due to the grid topology, the wake resolution is not nearly as good as with a C-type grid. This is visible in Figure 4.3 where there is a much higher concentration of grid points in the wake for the C-type grid. When running simulations for the calibration of the roughness model, O-type grids were used to decrease the computational cost. The transition location is dependent on the streamwise and normal point distribution along the surface, and does not heavily depend on the wake resolution. The wake resolution is important for accurate drag prediction, so C-type grids were used for all the final aerodynamic calculations performed.

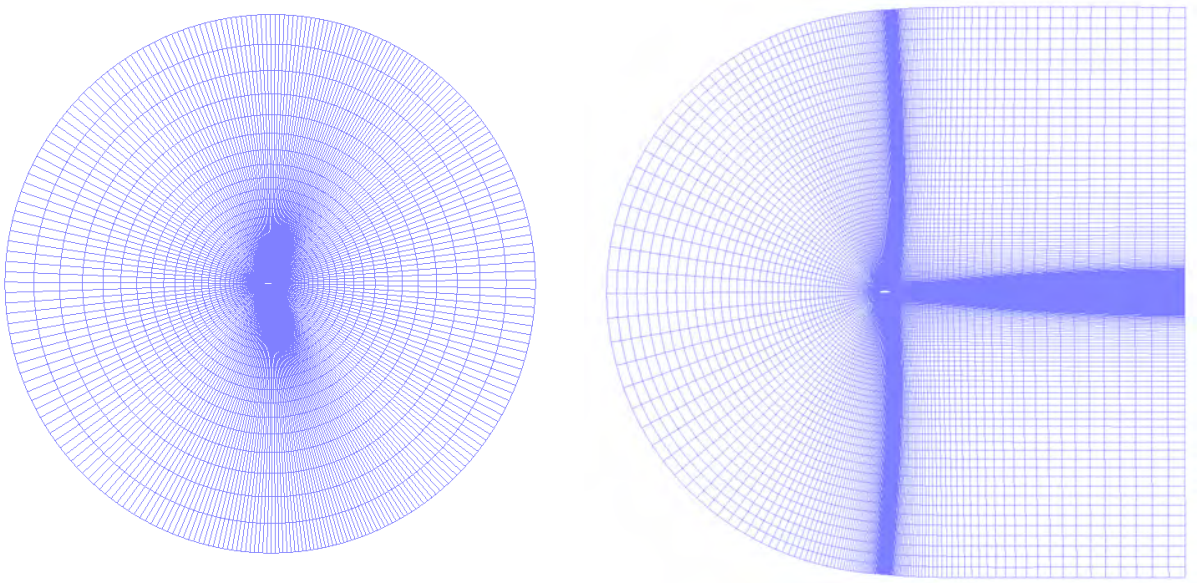

Figure 4.2. Far field view of both O-type (left) and C-type (right) grids for NACA 63_3-418 airfoil.

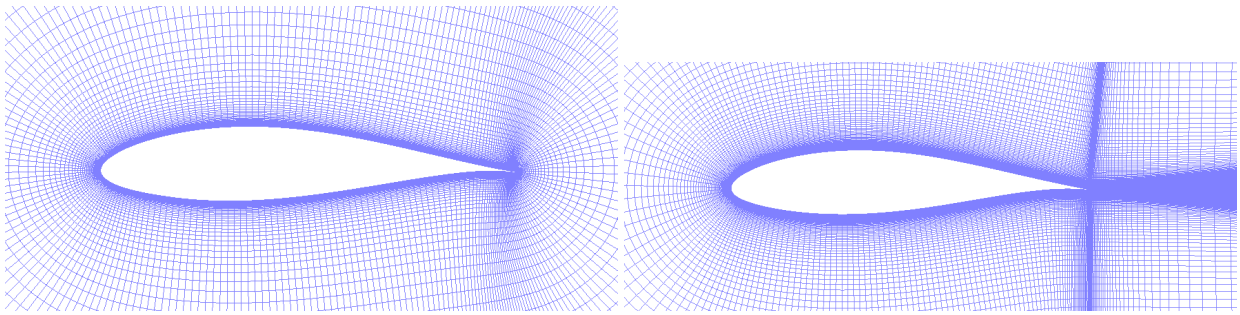

Figure 4.3. Close up of the airfoil section of both O-type (left) and C-type (right) grids for NACA 63_3-418 airfoil.

Parametric Definition of Airfoil Surface

The definition of the airfoil surfaces received considerable attention due to some observed sensitivities of the transition model used throughout the study. The problem arises as the definition of an airfoil often does not contain a sufficient number of points to generate a computational grid directly from the given points. The user must then rely on some form of interpolation scheme to fill points into the empty space. Unfortunately, this can introduce subtle "wiggles" into the surface, which result in minor pressure oscillations. Clearly this is undesirable from a physical accuracy standpoint, but the issue is amplified even more by the locally formulated transition model. This is due to the fact these subtle pressure fluctuations can alter the transition criteria enough locally to trip the model's transition prediction process. The solution devised for the smoothness problem was to parametrically define the airfoil surface as two Bezier curves. The following describes the mathematical basis of Bezier curves and how they were constructed to define the airfoil surfaces used throughout this work.

The Bernstein polynomials are typically used in the construction of a Bezier curve. Restricting the parametric variable t to the interval $[0,1]$, the polynomials take the form:

$$B_i^n(t) = \binom{n}{i}(t)^i(1-t)^{n-i}\ ,\ i = 0,1,...,n \tag{4.32}$$

where $\binom{n}{i}$ is the binomial coefficient. For example, the first few polynomials can be expressed:

$$B_0^0 = 1, \tag{4.33}$$

$$B_0^1 = 1-t,\ \ B_1^1 = t,$$

$$B_0^2 = (1-t)^2,\ \ B_1^2 = 2t(1-t),\ \ B_2^2 = t^2$$

The set of Bernstein polynomials of degree n form a basis for the space of polynomials of degree n or less, $\mathscr{P}_n$. The Bezier curve is then a combination of control points $\mathbf{b}_0, \mathbf{b}_1, ..., \mathbf{b}_n$ and the n^{th} set of basis polynomials. Restricting to $\mathbb{R}^2$ for simplicity, the general form of the parametric curve is:

$$[x(t)\ \ y(t)] = \sum_{i=0}^{n} B_i^n(t)\mathbf{b}_i^T,\ \ t \in [0,1] \tag{4.34}$$

The dimension of the curve or surface is controlled by the dimension of the control points $\mathbf{b}_i$, while the degree of the polynomial basis is determined by the number of control points used.

To provide an example of the construction of Bezier curves, consider the points $\mathbf{b}_0^T = (0,1)$, $\mathbf{b}_1^T = (1,0)$, $\mathbf{b}_2^T = (0,-1)$. The computation of the curve can be expressed in matrix form as:

$$[x(t)\ \ y(t)] = [B_0^2\ \ B_1^2\ \ B_2^2] \begin{bmatrix} \mathbf{b}_0^T \\ \mathbf{b}_1^T \\ \mathbf{b}_2^T \end{bmatrix} \tag{4.35}$$

$$[x(t)\ \ y(t)] = [B_0^2\ \ B_1^2\ \ B_2^2] \begin{bmatrix} 0 & 1 \\ 1 & 0 \\ 0 & -1 \end{bmatrix}$$

$$\begin{aligned} x(t) &= B_1^2,\ \ y(t) = B_0^2 - B_2^2 \\ x(t) &= 2t(1-t),\ \ y(t) = (1-t)^2 - t^2 \\ x(t) &= 2t - 2t^2,\ \ y(t) = 1 - 2t,\quad t \in [0,1] \end{aligned} \tag{4.36}$$

The spacing along the curve is controlled by the number of points the parameter variable t takes in the interval $[0,1]$.

One can see in Eq. 4.35 that the construction of a Bezier curve lends itself nicely to a linear algebra representation. The one drawback is that each B_i^n is a polynomial, however, this can be modified by taking advantage of the structure of the Bernstein basis functions. Consider a vector $\mathbf{t} = [t_0, t_1, ..., t_m]^T$, such that now $x(t)$ and $y(t)$ are a discrete set of points (x_j^b, y_j^b). Equation 4.35 can then be expressed:

$$\begin{bmatrix} x_0^b & y_0^b \\ x_1^b & y_1^b \\ \vdots & \vdots \\ x_m^b & y_m^b \end{bmatrix} = \begin{bmatrix} B_0^n(t_0) & B_1^n(t_0) & \dots & B_n^n(t_0) \\ B_0^n(t_1) & B_1^n(t_1) & \dots & B_n^n(t_1) \\ \vdots & \vdots & \ddots & \vdots \\ B_0^n(t_m) & B_1^n(t_m) & \dots & B_n^n(t_m) \end{bmatrix} \begin{bmatrix} \mathbf{b}_0^T \\ \mathbf{b}_1^T \\ \vdots \\ \mathbf{b}_n^T \end{bmatrix} \tag{4.37}$$

each $B_i^n(t_j)$ is now a scalar but there is still the computation of such value. Once more, it can be shown the matrix $\mathbf{B}(t)$ can be computed using only matrix multiplication operations. Letting $n = 3$ and only considering a single t:

$$\mathbf{B}(t)^T = \begin{bmatrix} B_0^3(t) \\ B_1^3(t) \\ B_2^3(t) \\ B_3^3(t) \end{bmatrix} = \begin{bmatrix} -t^3 + 3t^2 - 3t + 1 \\ 3t^3 - 6t^2 + 3t \\ -3t^3 + 3t^2 \\ t^3 \end{bmatrix} \tag{4.38}$$

$$\mathbf{B}(t)^T = \begin{bmatrix} -1 & 3 & -3 & 1 \\ 3 & -6 & 3 & 0 \\ -3 & 3 & 0 & 0 \\ 1 & 0 & 0 & 0 \end{bmatrix} \begin{bmatrix} t^3 \\ t^2 \\ t \\ 1 \end{bmatrix} = \mathbf{M}^T \mathbf{T}^T \tag{4.39}$$

It can be seen the Bernstein matrix $\mathbf{M} \in \mathbb{R}^{n \times n}$ is only dependent on the number of control points. For the case of a vector $\mathbf{t} \in \mathbb{R}^m$, the matrix $\mathbf{T} \in \mathbb{R}^{n \times m}$ also remains fixed for a given $\mathbf{t}$. Both the reliance on only matrix operations and the invariance of $\mathbf{B}(t)$ help reduce computational costs when attempting to fit Bezier curves to a profile. Returning to the original problem, one still must choose control points such that the corresponding Bezier curve interpolates a given set of points. Unfortunately, there is no solution that guarantees an optimal interpolating curve. Given enough control points, it is possible to insure the curve goes through every point, however, this in general quite impractical. The problem to consider then is how to position the control points such that the generated Bezier curve is sufficiently near each point of the given geometry.

For the present application, two separate curves were generated corresponding to the upper and lower airfoil surfaces. A C^1 constraint was placed on the connection between the two curves at the leading edge center such that the derivatives matched. The initial placement of the points was done by clustering based on the magnitude of curvature of the airfoil surface. Given that the number of control points is selected by the user as N, one seeks to minimize a norm of the distance between the set of points that define an airfoil surface and an associated Bezier curve. A formal statement of the problem can be expressed as follows. Given a set of D points, $\mathbf{d}_i$ which define the airfoil surface, determine the set of N control points, $\mathbf{b}_j$, that minimize:

$$\sum_{i=1}^{D} \min \{ \ \|\mathbf{d}_i - \mathbf{c}\| \ : \ \mathbf{c} \in C \ \} \tag{4.40}$$

where C is the Bezier curve produced by $\mathbf{b}_j$. Although C is continuous in the parametric variable t, it should really be consider a discrete set of M points. Letting $\mathbf{x}$ be the vector of control points $\mathbf{b}_j$, an objective function to minimize can be written:

$$J(\mathbf{x}) = \sum_{i=1}^{D} \min \{ \ \|\mathbf{d}_i - \mathbf{c}_m\| \ : \ m = 1, 2, ..., M \ \} \tag{4.41}$$

In this form, minimizing Eq. 4.41 is nonlinear optimization problem that needs to be solved iteratively. The objective function itself can be a computationally time consuming operation if the number of points along the Bezier curve, M, or the number of initial points, d_i, become large. The gradient of J must also be computed numerically using a finite difference or other discrete approximation. Therefore for each partial derivative, the Bezier curve must be re-computed using the perturbed vector of control points, and Equation 4.41 re-evaluated. This is indeed a very brute force method, however, the matrix form of the Bernstein basis helps minimize the computation cost to generate a new Bezier curve. Additionally for this application, one can take advantage of the distribution of points when computing the minimum distance to the curve. As the computation marches along the points in the Bezier curve, one does not need to compute the distance to previously checked points, and as soon as a local minimum is achieved, one can halt checking additional points. A code was implemented to carry out this optimization described, and the control points used for each airfoil are given in the appendix.

Figure 4.4 shows an example of the Bezier curves constructed to represent the NACA 63_3-418 airfoil. One of the primary advantages of using a parametric representation of the airfoil surfaces is that once the control points of the Bezier curves are fixed, one can add an arbitrary number of points along the surface without any change to the final geometry. Changing the distribution of points along the surface is accomplished by simply changing the distribution of the parametric variable t.

For this work, spacing and stretching ratios were computed by allocating a percentage of points on the surface to particular sections of the airfoil. The number of points along the surface was set, as well as a clustering pattern. For example, the airfoil might be generated with the constraint 30% of the points should be in the leading 15% of the chord, 25% of the points should be in the tailing 10% of the chord, and the remaining points equispaced in the middle. Using a constant spacing in the middle section of the airfoil grid was observed to produce the best behavior with the transition model, so this practice was used throughout all grids used. The spacing was determined by first allocating the total points allocated to each region. Then, the curvilinear distance was computed for the center portion of the airfoil surface. This produces a set value for the "end" of the leading edge region, and the "start" of the trailing edge region. If the stretching ratio is

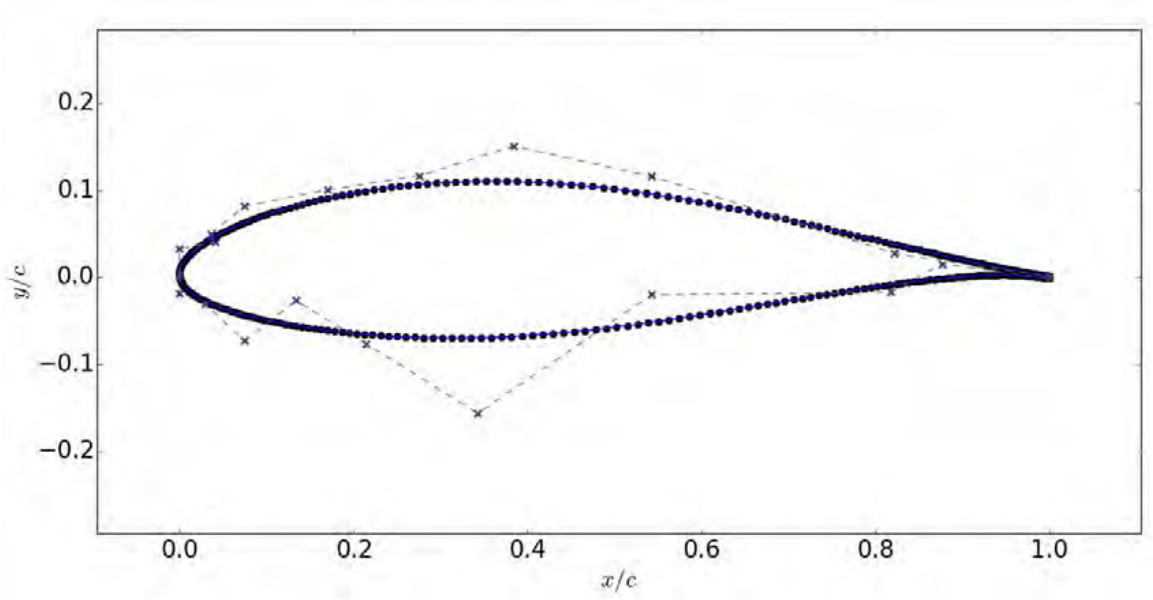

Figure 4.4. Graphical representation of Bezier curves used for NACA 63_3-418 airfoil, control points indicated by x's with the dashed line connecting them.

assumed to be constant in each region, the spacing and stretching ratio at the leading and trailing edge can be computed iteratively.

Chapter 5

Langtry-Menter $\gamma - \tilde{R}e_{\theta t}$ Transition Model

This chapter focuses on the technical details regarding local correlation transition models. Specifically the $\gamma - \tilde{R}e_{\theta t}$ model developed by Langtry and Menter, and hence colloquially known as the Langtry-Menter transition model. Many of the specifics are important when considering how to modify the transition onset criteria due to the presence of surface roughness. In addition to the mathematical description of the model, a number of sensitivities of the model are demonstrated to elucidate common errors that may occur when using the model in practice. These sensitivities range from grid spacing to turbulence model limiters and are largely user dependent parameters. It is also shown that the use of the model at high Reynolds numbers ($\approx> 5 \times 10^6$) increases the likelihood the model will produce inaccurate results due to these sensitivities.

Correlation Based Transition Prediction

The fundamental idea behind correlation based transition prediction is that estimations of boundary layer stability can be obtained by looking at local properties and comparing to an empirical correlation. Most correlation based transition models are based on the momentum thickness Reynolds number, Re_θ, defined:

$$Re_\theta = \frac{\rho U \theta}{\mu} \tag{5.1}$$

where the characteristic length scale is replaced with the momentum thickness θ. Taking the y-direction to be the wall normal, the momentum thickness is computed:

$$\theta = \int_0^\infty \frac{\rho(y)u(y)}{\rho_0 u_0}\left(1 - \frac{u(y)}{u_0}\right) dy \tag{5.2}$$

where a 0 subscript indicates the value taken as the boundary layer edge. It is clear from this formulation the computation of momentum thickness is very much a non-local operation. The next section will show how this non-local dependence is eliminated.

Once an estimation of Re_θ is obtained, the boundary layer is then determined to transition at the point where it exceeds some critical value, often termed $Re_{\theta t}$. The critical value is typically determined as a function of freestream turbulence intensity, where an increase in turbulence intensity will result in a decrease in $Re_{\theta t}$. This dependence is sketched out in Figure 5.1.

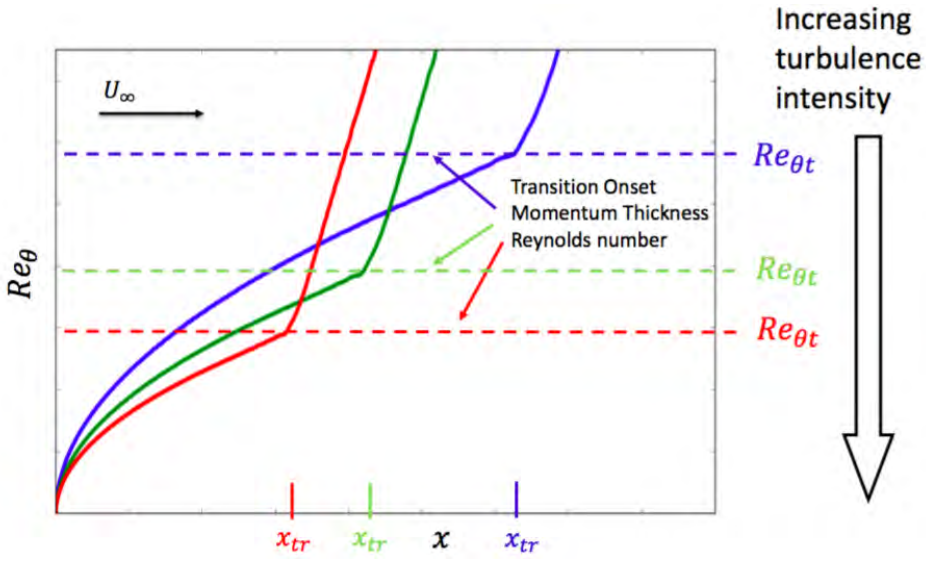

Figure 5.1. Sketch of impact of freestream turbulence intensity on the transition onset momentum thickness Reynolds number.

In addition to the freestream turbulence intensity, which is consider more of a global parameter, local effects due to pressure gradients are typically included as well.

Local Correlation Transition Modeling - $\gamma - \tilde{Re}_{\theta t}$

To localize the computation, Menter et al. introduced the relationship between Van Driest and Blumer's [102] vorticity Reynolds number (Re_v) and Re_θ. The vorticity, or strain-rate Reynolds number, is defined:

$$Re_v = \frac{\rho y^2}{\mu}\left|\frac{\partial u}{\partial y}\right| = \frac{\rho y^2}{\mu} S \tag{5.3}$$

In the transition model, Re_v is related to Re_θ by the following:

$$Re_\theta = \frac{\max(Re_v)}{2.193} \tag{5.4}$$

The $\max(Re_v)$ corresponds to the maximum value the vorticity Reynolds number obtains in the plane normal to the surface. The denominator is chosen such that for a Blasius profile, the maximum the quantity $(2.193 Re_\theta)/Re_v$ obtains in the boundary layer is unity (1). The model does not actually compute a search, rather the value of the Re_v will naturally obtain its maximum value within the boundary layer. This is a crucial feature, and removes the need to define boundary layer edges or perform any integrations. Figure 5.2 demonstrates the variation in Re_v along the wall normal direction, along with a comparison between Re_θ computed directly, and the $\max(Re_v)$ relationship for a flat plate.

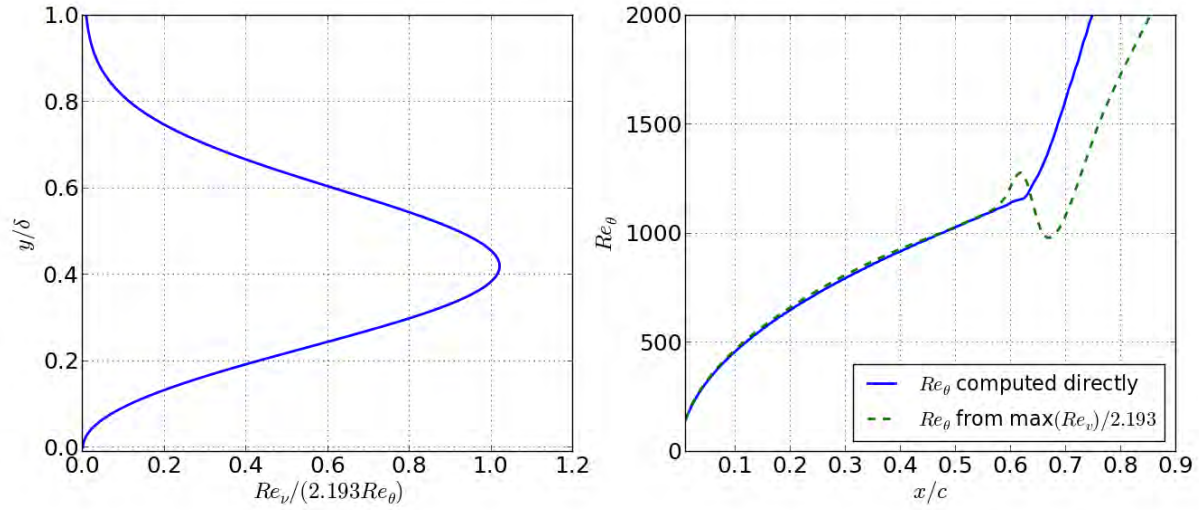

Figure 5.2. (left) Profile of vorticity Reynolds number normalized by $2.193Re_\theta$, with Re_θ computed directly, profile taken at $x/c = 0.2$. (right) Plot of momentum thickness Reynolds number along flat plate computed both directly and using relationship with Re_v, $Re_c = 5.0 \times 10^6$.

The estimation of momentum thickness based on the maximum value of Re_v in the boundary layer is in very good agreement to the computed value for a flat plate, as shown in Figure 5.2. There is a rise in the value of max(Re_v) shortly before transition, however this actually helps the transition model activate the turbulence model throughout the entire boundary layer. The accuracy of this approximation is related to the boundary layer shape factor, and for moderate gradients ($2.3 < H < 2.9$) the error is less than 10% [33]. For larger pressure gradient flows the model has an explicit pressure gradient function that helps account for the discrepancy in the estimated momentum thickness.

The behavior of Re_v allows for the creation of a triggering function (F_{onset}) based on the ratio $Re_v/2.193$. Once this quantity reaches a threshold value, defined as $Re_{\theta c}$, the model reacts by producing the intermittency (γ) variable from within the boundary layer. The production of intermittency attempts to simulate the transition process by progressively switching on the underlying SST $k-\omega$ turbulence model. The distribution of intermittency is governed by a transport equation:

$$\frac{\partial(\rho\gamma)}{\partial t} + \frac{\partial(\rho U_j\gamma)}{\partial x_j} = P_\gamma - E_\gamma + \frac{\partial}{\partial x_j}\left[\left(\mu + \frac{\mu_t}{\sigma_f}\right)\frac{\partial\gamma}{\partial x_j}\right] \tag{5.5}$$

The production term is then defined:

$$P_\gamma = F_{\text{length}} c_{a1} \rho S [\gamma F_{\text{onset}}]^{0.5} (1 - c_{e1}\gamma) \tag{5.6}$$

where S is the strain-rate magnitude, ρ is the fluid density, and c_{e1} and c_{a1} are constants. The function F_{length} controls how quickly the turbulence model is activated once the onset criteria is satisfied. The F_{onset} function is based on a sequence of functions defined:

$$F_{\text{onset1}} = \frac{Re_v}{2.193 Re_{\theta c}} \tag{5.7}$$

$$F_{\text{onset2}} = \min(\max(F_{\text{onset1}}, (F_{\text{onset1}})^4), 2.0) \tag{5.8}$$

$$F_{\text{onset3}} = \max\left(1 - \left(\frac{R_T}{2.5}\right), 0\right), \quad \text{with:} \quad R_T = \frac{\rho k}{\mu \omega} \tag{5.9}$$

$$F_{\text{onset}} = \max\left(F_{\text{onset2}} - F_{\text{onset3}}, 0\right) \tag{5.10}$$

The threshold value of $Re_{\theta c}$ is defined as a function of the local $\tilde{R}e_{\theta t}$. It is lower than the onset value, $\tilde{R}e_{\theta t}$, and is described as the position where turbulent fluctuations begin in the boundary layer.

An additional transport equation is used to distribute the empirical correlation, $Re_{\theta t}$, throughout the flow field to facilitate the comparison between the estimated Re_θ and a localized onset value. For that purpose, an additional scale variable defined as the "transition onset momentum thickness Reynolds number", $\tilde{R}e_{\theta t}$, is determined by the equation:

$$\frac{\partial(\rho \tilde{R}e_{\theta t})}{\partial t} + \frac{\partial(\rho U_j \tilde{R}e_{\theta t})}{\partial x_j} = P_{\theta t} + \frac{\partial}{\partial x_j}\left[\sigma_{\theta t}\left(\mu + \mu_t\right)\frac{\partial \tilde{R}e_{\theta t}}{\partial x_j}\right] \tag{5.11}$$

The production term, $P_{\theta t}$, contains the empirical correlation, referred to as $Re_{\theta t}$ and is defined:

$$P_{\theta t} = c_{\theta t}\frac{\rho}{t}(Re_{\theta t} - \tilde{R}e_{\theta t})(1 - F_{\theta t}) \tag{5.12}$$

$Re_{\theta t}$ is a direct computation of the correlation. It is a function of both turbulence intensity, Tu, and the Thwaites pressure gradient parameter, λ_θ, defined:

$$Re_{\theta t} = \begin{cases} \left(1173.51 - 589.428Tu + \frac{0.2196}{Tu^2}\right) F(\lambda_\theta), & Tu \leq 1.3 \\ 331.50\left(Tu - 0.5658\right)^{-0.671} F(\lambda_\theta), & Tu > 1.3 \end{cases} \tag{5.13}$$

with:

$$F(\lambda_\theta) = \begin{cases} 1 + \left(12.986\lambda_\theta + 123.66\lambda_\theta^2 + 405.689\lambda_\theta^3\right) e^{-\left(\frac{Tu}{1.5}\right)^{1.5}}, & \lambda_\theta \leq 0 \\ 1 + 0.275\left(1 - e^{-35.0\lambda_\theta}\right) e^{-\left(\frac{Tu}{0.5}\right)}, & \lambda_\theta > 0 \end{cases} \tag{5.14}$$

the pressure gradient parameter λ_θ is computed:

$$\lambda_\theta = \frac{dU}{ds}\frac{\theta^2}{\nu} \tag{5.15}$$

The appearance of the momentum thickness, θ, in the pressure gradient parameter necessitates an iterative method to solve for $Re_{\theta t}$. The quantity $(\nu = \rho/\mu)$ acts to viscously dampen the influence of momentum thickness and dU/ds is the acceleration in the streamwise direction. U is the magnitude of the velocity $(U = \sqrt{u^2+v^2+w^2})$ and the derivative dU/ds is then computed:

$$\frac{dU}{ds} = \left[(u/U)\frac{dU}{dx} + (v/U)\frac{dU}{dy} + w/U)\frac{dU}{dz}\right] \tag{5.16}$$

with dU/dx, dU/dy, dU/dz:

$$\frac{dU}{dx} = \frac{1}{2\sqrt{(u^2+v^2+w^2)}} \cdot \left[2u\frac{du}{dx} + 2v\frac{dv}{dx} + 2w\frac{dw}{dx}\right] \tag{5.17}$$

$$\frac{dU}{dy} = \frac{1}{2\sqrt{(u^2+v^2+w^2)}} \cdot \left[2u\frac{du}{dy} + 2v\frac{dv}{dy} + 2w\frac{dw}{dy}\right]$$

$$\frac{dU}{dz} = \frac{1}{2\sqrt{(u^2+v^2+w^2)}} \cdot \left[2u\frac{du}{dz} + 2v\frac{dv}{dz} + 2w\frac{dw}{dz}\right]$$

A slight weakness of the model is that the use of stream direction is not Galilean invariant. However, this only poses an issue with multiple moving walls in close vicinity.

Due to the presence of the streamwise velocity gradient, the paramter λ_θ is not well defined in the boundary layer. For this reason an indicator function $F_{\theta t}$ was constructed to shut off the production term in the boundary layer. This function is defined:

$$F_{\theta t} = \min\left\{\max\left(F_{\text{wake}} \cdot e^{-\left(\frac{d}{\delta}\right)^4},\ 1.0 - \left(\frac{\gamma - 1/c_{e2}}{1.0 - 1/c_{e2}}\right)^2\right),\ 1.0\right\} \tag{5.18}$$

$$\delta = \frac{50\Omega d}{U} \cdot \delta_{\text{BL}}, \quad \delta_{\text{BL}} = 7.5\theta_{\text{BL}}, \quad \theta_{\text{BL}} = \frac{\tilde{Re}_{\theta t}\mu}{\rho U} \tag{5.19}$$

$$F_{\text{wake}} = e^{\left(\frac{Re_\omega}{1E5}\right)^2}, \quad Re_\omega = \frac{\rho\omega d^2}{\mu} \tag{5.20}$$

This function takes a value of unity (1) within the boundary layer and therefore the production term $P_{\theta t}$ (Equation 5.12) is shut off. Outside this region $P_{\theta t}$ acts to drive the scalar quantity, $\tilde{Re}_{\theta t}$ towards the directly computed $Re_{\theta t}$. The value of $\tilde{Re}_{\theta t}$ in the boundary layer is then determined purely by the transport equation, as visualized in Figure 5.3.

The freestream value of intermittency is set to unity (1). This differs from the usual definition where an intermittency of unity (1) is reserved for a fully turbulent state. This is necessary to accurately account for freestream turbulence decay rates and to allow the SST $k-\omega$ turbulence model to function undisturbed outside the boundary layer. Additionally, even though it is not shut off directly using the intermittency

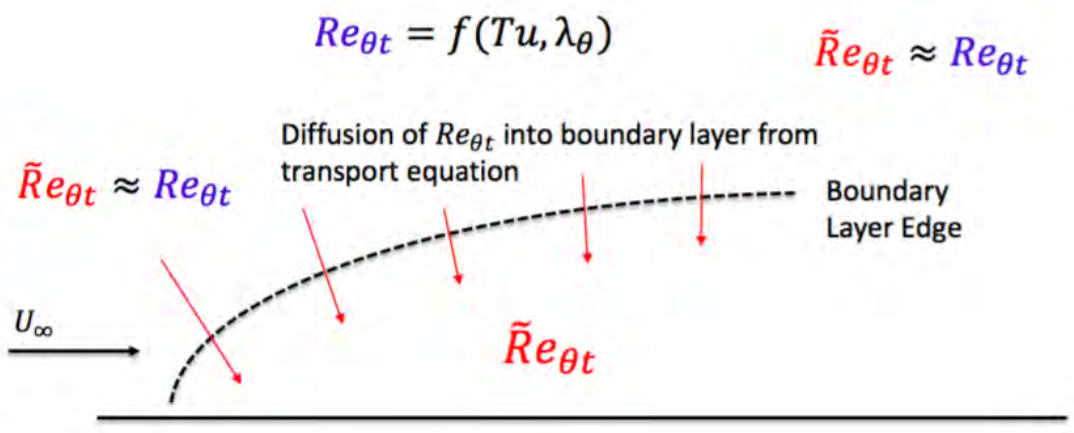

Figure 5.3. Sketch of diffusion of $Re_{\theta t}$ into the boundary layer.

variable, production of turbulent kinetic energy is limited in the freestream if there is a lack of shearing stress in the mean flow. E_γ is included in the intermittency transport equation to account for the possibility of re-laminarization under the influence of a highly favorable pressure gradient. Once the onset criteria has been met, the intermittency variable is used to progressively activate k production by scaling the production term in the SST $k-\omega$ turbulence model:

$$\frac{\partial(\rho k)}{\partial t} + \frac{\partial(\rho U_j k)}{\partial x_j} = \tilde{P}_k - \tilde{D}_k + \frac{\partial}{\partial x_j}\left[(\sigma_k \mu_t + \mu)\frac{\partial k}{\partial x_j}\right] \tag{5.21}$$

with,

$$\tilde{P}_k = \gamma_{eff} P_k; \qquad \tilde{D}_k = \min(\max(\gamma_{eff}, 0.1), 1.0) \cdot D_k \tag{5.22}$$

where γ_{eff} is defined as $\max\{\gamma_{sep}, \gamma\}$ to allow the model to rapidly induce k production if the flow separates. A more detailed description of the separation-caused trigger, γ_{sep}, and full equation set is presented by Langtry & Menter [33].

Local Correlation Model Sensitivities

A disadvantage of moving to a purely local formulation is an increased sensitivity to various user dependent simulation parameters. Although undesirable from the perspective of creating a parallel CFD code, integrated quantities can dampen subtle flow imperfections due to both the grid and choice of turbulence model. As described, the $\gamma - \tilde{R}e_{\theta t}$ model will begin to simulate the transition process when the vorticity Reynolds number (Re_v) reaches a local threshold level, $Re_{\theta c}$. Small pressure fluctuations can be sufficient to drive down $Re_{\theta c}$ in the boundary layer to the point it causes the model to begin k production at that location. This process is self amplifying and can ultimately lead to premature prediction of transition onset. This

sensitivity to pressure fluctuations, in addition to several other factors, is exaggerated as the Reynolds number of the simulation is increased. Therefore, it must be stressed when using a local correlation based model at higher Reynolds numbers, extra care must be taken to insure these sensitivities do not have a detrimental effect on the accuracy of a simulation.

Freestream Turbulence Levels

The correlation function for $Re_{\theta t}$ is strongly dependent on freestream turbulence intensity. As such, attention must be paid to insuring the flow solver has the correct freestream levels specified. Figure 5.4 demonstrates how a variation in freestreem turbulence levels can impact transition location.

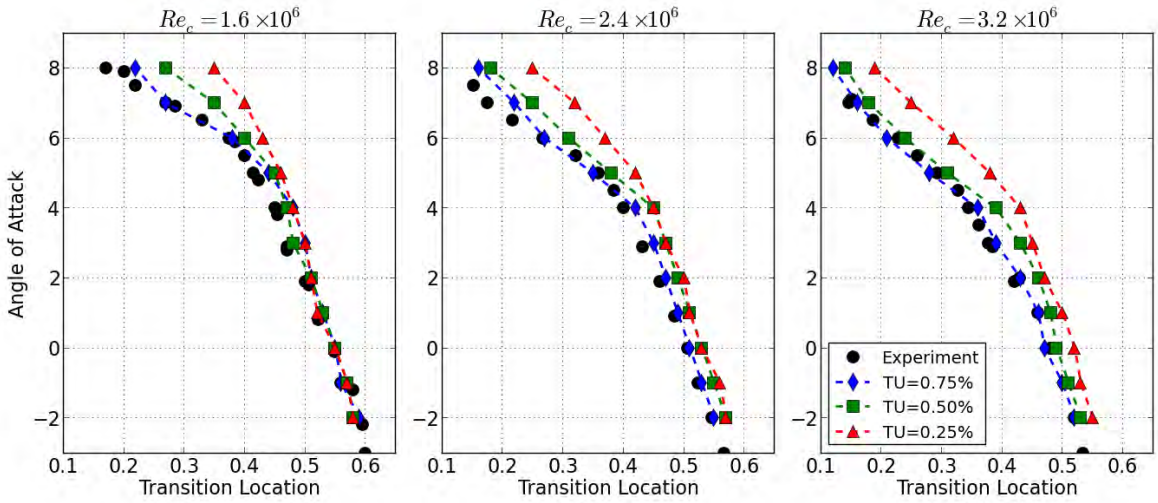

Figure 5.4. Comparison of upper surface transition location prediction with variation in input turbulence intensity (Tu) compared to experimental results of Ehrmann and White [1], NACA 63_3-418.

The specification of freestream turbulence levels can be challenging as in many RANS codes the freestream turbulence quantities are set at the boundary of the grid and decay according to the user specified dissipation rate. Frequently this is just set to some default value, and if the user is not careful can be significantly different than what was encountered when collecting the experimental data. This unfortunately also introduces a grid dependence as the distance between the grid boundary and model can change across grids, meaning the turbulence levels can vary significantly at locations the transition model is a ctive. Additionally many flow solvers set the freestream turbulence decay rate nonphysically high for numerical stability, so some manual tuning is required to arrive at the proper freestream turbulence level [103]. Turbulence levels tend to be very difficult to measure accurately, so the user must exercise judgment based on the conditions under which the experiment occurred.

Grid Quality

The quality of the computational grid, both in terms of smoothness and point distribution, can have a large effect on the accuracy of the predicted transition location. A persistent issue is representing a model with a sufficiently dense collection of points. Often the definition of an airfoil or other component does not have the resolution to create a mesh directly from the given coordinates. This forces the user to rely on some form of interpolation to fill in the undefined spaces. The choice of a high order interpolating scheme can introduce small "wiggles" along a surface which will result in pressure fluctuations. Often, these small perturbations do not have a large impact on the transition model at low to moderate Reynolds numbers. However, as the Reynolds number rises, even small pressure fluctuations can result in the triggering of turbulent kinetic energy production. This is due to the fact that at high Reynolds numbers, the local momentum thickness Reynolds number of the boundary layer, Re_θ, is much closer to the critical value for the duration of the chord. In order to overcome this sensitivity, the airfoil surfaces used throughout this work were defined parametrically using Bezier curves, as described in Chapter 4.

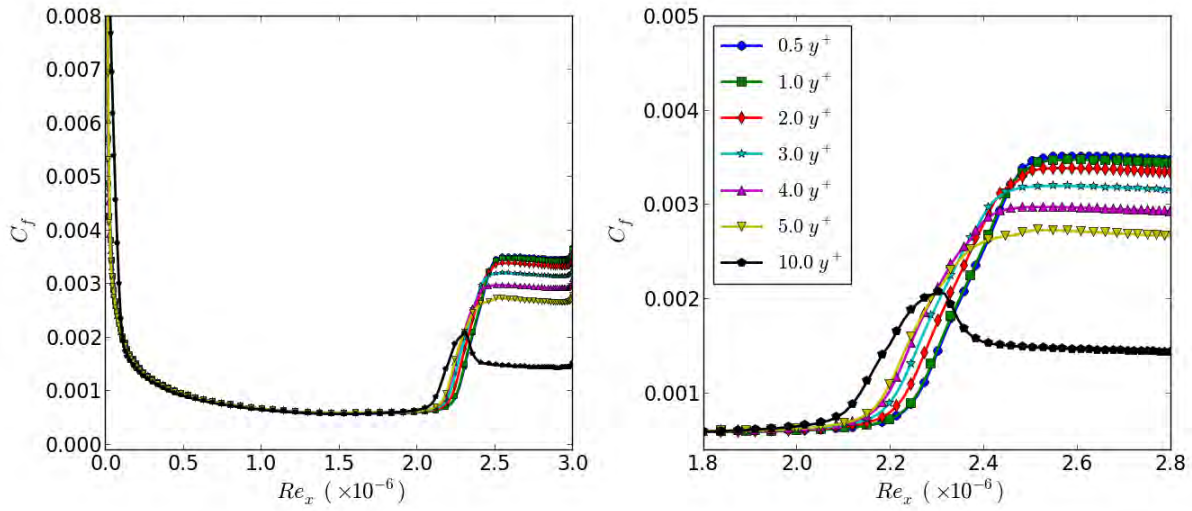

Figure 5.5. Skin friction along a flat plate, with a variation in initial wall spacing. $Tu = 0.5\%$.

The model carries a dependence on grid spacing in the normal direction. Figure 5.5 demonstrates the shift in transition location due to a change in initial wall spacing. In the normal direction, the first 5 grid cells off the wall had uniform spacing before being extended 25 chords with a stretching ration of 1.03 The conditions of the simulation were such that an initial spacing of 1.3×10^{-6} chord lengths is roughly equivalent to the turbulent length scale y^+, (i.e. 1.0 y^+). An increase in initial wall spacing will move the location of transition onset upstream. Changes in wall spacing also have an impact on turbulent skin friction, with a reduction in skin friction following the increase in initial spacing. It can be seen in Figure 5.5, for the transition model to function properly an initial wall spacing value corresponding to 1.0 y^+ or less is required, as noted by Langtry and Menter [33]. At wall spacing values of 2.0 y^+ or greater, the fully activated turbulence model begins to lose accuracy, with the projected skin friction values deviating as the wall spacing increases. At the largest value shown (corresponding to 10 y^+), the prediction of the turbulent boundary layer is very inaccurate.

Tables 5.1 and 5.2 present the predicted lift and drag coefficients along with the transition location for a variety of grid sizes. All simulations were run in 2-D using OVERFLOW. The number of points along the surface (J-pts) was varied and then the number of points in the normal direction (K-pts) was slightly adjusted so that the aspect ratio of the grid cells did not become an issue. The initial wall spacing, and therefore y^+, was held constant across all grids. An O-type grid was used for the convergence study, so the number of points along the trailing edge varried slightly. It can be seen that at roughly 400 points along the surface, the aerodynamic properties are essentially converged. This is slightly higher than what is expected if conducting a RANS simulation without the use of the transition model [36]. For all simulations conducted in the present work, at least 500 points along the surface and 250 points in the normal direction were used with a maximum initial spacing of $0.5y^+$.

Table 5.1. Coefficients of lift and drag as well as transition location for various grid sizes, NACA 63_3-418 airfoil, $\alpha = 0^o$, $Re_c = 2.4 \times 10^6$, clean surface, initial spacing of $0.2y^+$ used for all grids.

J-pts	K-pts	C_l	C_d	Transition Location (x/c)
210	150	0.3664	0.006595	0.4895
313	200	0.3672	0.006377	0.5016
416	250	0.3677	0.006196	0.5076
520	250	0.3677	0.006213	0.5040
624	250	0.3679	0.006222	0.5016

Table 5.2. Coefficients of lift and drag as well as transition location for various grid sizes, S814 airfoil, $\alpha = 0^o$, $Re_c = 2.4 \times 10^6$, clean surface, initial spacing of $0.2y^+$ used for all grids.

J-pts	K-pts	C_l	C_d	Transition Location (x/c)
227	150	0.4434	0.009722	0.3613
340	200	0.4583	0.008790	0.4629
448	250	0.4652	0.008245	0.4643
553	250	0.4645	0.008265	0.4652
666	250	0.4647	0.008271	0.4629

Turbulence Model Settings

An important consideration is how changes to the underlying turbulence model can impact the functions within the transition model. The SST $k-\omega$ model is known to generate slightly too much turbulent kinetic energy near stagnation points. When running a RANS simulation in a fully turbulent configuration, this anomaly does not have a noticeable impact on the global solution. However, due to the formulation of the

transition model, the slight overproduction can lead to more significant effects. As mentioned, the value of $\tilde{Re}_{\theta t}$ in the boundary layer is determined purely by a transport equation. Ideally, the value of the correlation variable, $Re_{\theta t}$, at the stagnation point would be the freestream value based on far-field turbulence levels. Additionally, the value of the transported variable in the boundary layer would be determined primarily by diffusion down from just outside the boundary layer. Unfortunately, even very small amounts of turbulent kinetic energy can drive the computed correlation variable down significantly at the stagnation point, as the model treats this as an increase in freestream turbulence. This relatively low value of $Re_{\theta t}$ is then convected into the boundary layer and essentially acts as a sink for the $\tilde{Re}_{\theta t}$ variable. Reduced values of $\tilde{Re}_{\theta t}$ will lead to an early prediction of transition onset.

There have been a number of corrections added to the SST $k-\omega$ model to account for some of the known deficiencies. The Kato-Launder production limiter was specifically designed to address the overproduction of k near a stagnation point and in regions of re-circulation [104]. The application of the limiter is one way to address the problem of low values of $Re_{\theta t}$ convecting into the boundary layer. The change is relatively simple to implement and involves a modification to the production term of the k equation. Rather than using the strain-rate magnitude (S) squared, the vorticity magnitude (Ω) is substituted for one of the strain-rates.

$$P_k = \mu_t SS \quad \rightarrow \quad P_{k,\text{mod}} = \mu_t S\Omega \tag{5.23}$$

in 2-D:

$$S = \sqrt{\frac{1}{2}\left(\frac{\partial u_i}{\partial x_j} + \frac{\partial u_j}{\partial x_i}\right)} \quad \text{and} \quad \Omega = \sqrt{\frac{1}{2}\left(\frac{\partial u_i}{\partial x_j} - \frac{\partial u_j}{\partial x_i}\right)} \tag{5.24}$$

In pure shear-flows, where $\partial u_j/\partial x_i$ goes to zero, the modified production term is identical to the original. In stagnation regions and areas outside the boundary layer and wake, the production term essentially goes away. This is not entirely accurate either. However, for the purpose of more accurate transition prediction, the positive effects largely outweigh the associated drawbacks.

The impact of the effect of low values of $Re_{\theta t}$ convecting into the boundary layer is somewhat difficult to observe. To get a qualitative picture, Figure 5.6 shows contour plots of the $\tilde{Re}_{\theta t}$ variable with and without the Kato-Launder limiter active. A C-type grid was used with 500 points along the airfoil surface, and 350 points in the normal direction. The initial wall spacing was set at $0.3y^+$ for the cases shown, and a snapshot of the grid can be seen in Figure 5.10.

At a scale where most of the flow field around the airfoil is visible, the differences between the two images is not entirely clear. To see the true magnitude of the change, one must look very closely at the boundary layer near the leading edge. Figure 5.7 shows the leading edge of the airfoil with the scalar field expanded 20 times in the direction normal to the airfoil surface. Here the difference becomes more clear with noticeably lower levels of $\tilde{Re}_{\theta t}$ in the boundary layer in the simulation ran without the Kato-Launder limiter activated.

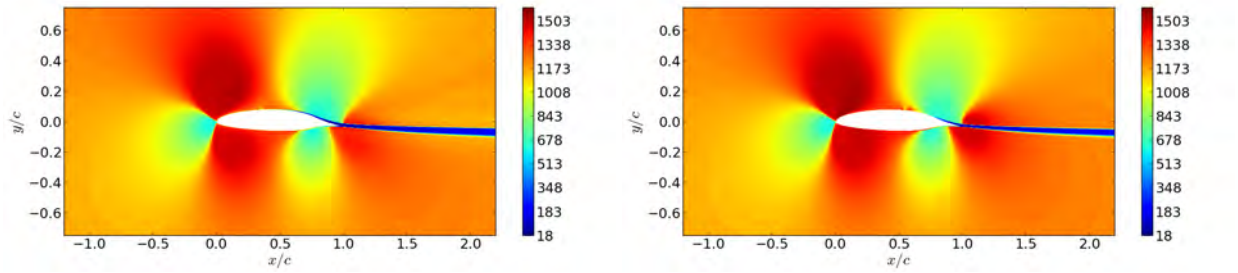

Figure 5.6. Contour plots of $\tilde{Re}_{\theta t}$ variable both without (left) and with (right) the Kato-Launder limiter activated. NLF(1)-0414F airfoil, $Re_c = 6.1 \times 10^6$, $\alpha = 0^o$, $Tu = 0.05\%$.

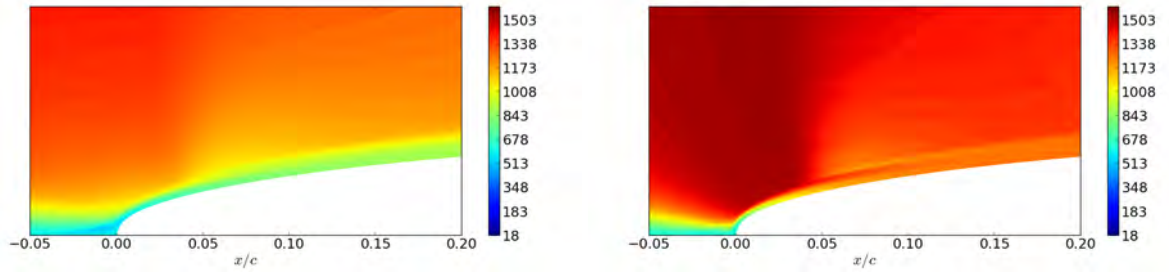

Figure 5.7. Enlargement near the leading edge of the $\tilde{Re}_{\theta t}$ variable both without (left) and with (right) the Kato-Launder limiter. NLF(1)-0414F airfoil, $Re_c = 6.1 \times 10^6$, $\alpha = 0^o$, $Tu = 0.05\%$. The images have been enlarged 20 $\times$ in the wall normal direction to show the boundary layer details, the airfoil profile is to scale.

The reduced values of $\tilde{Re}_{\theta t}$ in boundary layer is of particular significance due to the transition onset triggering function. The onset function in the transition model is based on the vorticity Reynolds number, Re_v, and this quantity obtains its maximum value in the boundary layer. Therefore, the value of $\tilde{Re}_{\theta t}$ that is most influential, is the value at the position in the boundary layer where Re_v is reaches its maximum value.

To provide a more quantitative depiction, Figures 5.8 and 5.9 plot some variables of interest for both a flat plate and an example airfoil. The three quantities shown are the computed momentum thickness Reynolds number, Re_θ, the value of $\tilde{Re}_{\theta t}$ just outside the boundary layer, and $\tilde{Re}_{\theta t}$ in the boundary layer at the position of the maximum value of Re_v. If the model behaves as designed, there should not be a large discrepancy in the value of $\tilde{Re}_{\theta t}$ at the two positions. The transport equations should act to drive the value of $\tilde{Re}_{\theta t}$ in the boundary layer to the computed correlation, $Re_{\theta t}$. This value is only directly computed outside the boundary layer where the pressure gradient function is well defined.

The onset of transition can be observed in Figures 5.8 and 5.9 where the momentum thickness Reynolds number, Re_θ, begins to rise rapidly. There is some fluctuation in the $\tilde{Re}_{\theta t}$ at transition, but this is to be expected as the turbulence model is activating and $\tilde{Re}_{\theta t}$ is strongly dependent on k.

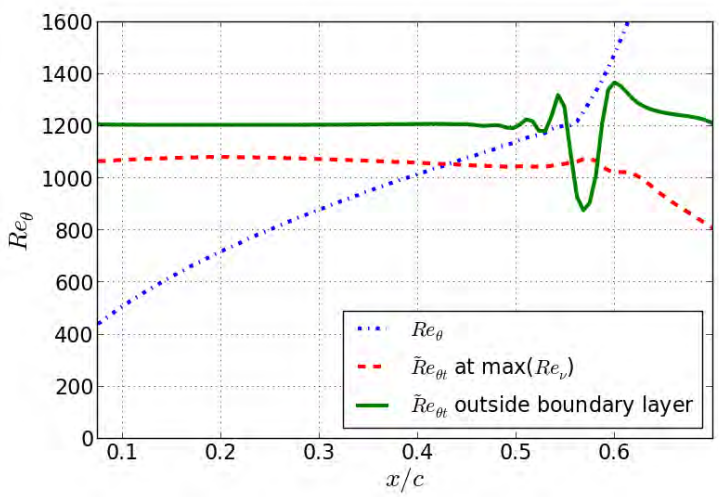

Figure 5.8. Re_θ along with the critical value, $Re_{\theta c}$ both just outside the boundary layer and at the position where Re_v obtains its maximal value in the boundary layer, the solution is identical whether or not the Kato-Launder modification is applied. Flat-plate geometry, $Re_c = 6.1 \times 10^6$, $\alpha = 0^o$, $Tu = 0.05\%$.

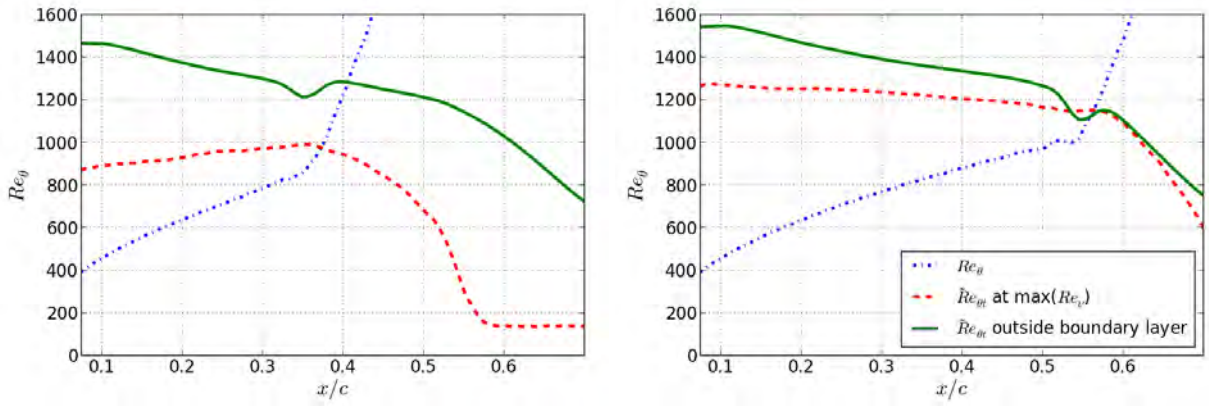

Figure 5.9. Re_θ along with the critical value, $Re_{\theta c}$ both just outside the boundary layer and at the position where Re_v obtains its maximal value in the boundary layer without (left) and with (right) the Kato-Launder modification applied. NLF(1)-0414F airfoil, $Re_c = 6.1 \times 10^6$, $\alpha = 0^o$, $Tu = 0.05\%$.

Both the flat plate and the airfoil geometry shown were run with identical settings in the flow solver. The results with and without the limiter are identical for the flat plate so only a single plot is shown in Fig. 5.8. However, once a stagnation point is introduced there is a large drop in magnitude of the value of $\tilde{Re}_{\theta t}$ in the boundary layer if the Kato-Launder modification is not used. The growth of the boundary layer is similar in both the flat plate and airfoil cases. With the Kato-Launder limiter active, the prediction transition location is similar between both geometries. When the airfoil simulation is run without the modification, however, the predicted onset of transition is moved forward due to lower levels of $\tilde{Re}_{\theta t}$ in the boundary layer.

OVERFLOW Simulations with Transition Model

A variety of test cases showing predictions from the Langtry-Menter transition model are provided. The cases were run in 2-D with the flow solver OVERFLOW-2. All simulations were non-time accurate and were run until convergence of lift and drag was reached. The surfaces of the airfoils were defined parametrically using Bezier curves, the details of which can be found in Appendix A. The grids were generated with minimal stretching in the streamwise direction, as this was observed to produce better results with the transition model.

NLF(1)-0414F

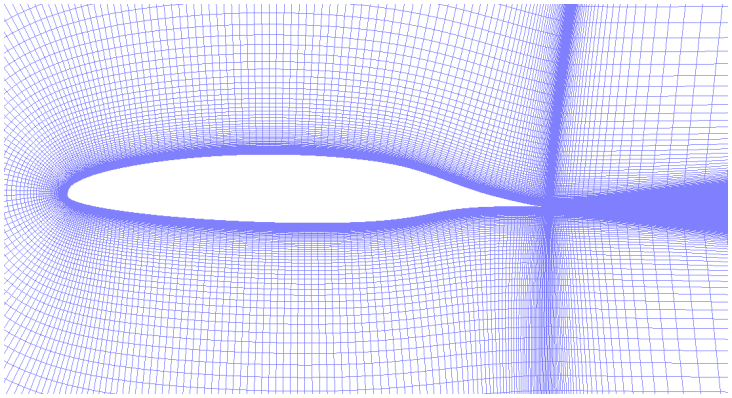

Figure 5.10. Grid used for NLF(1)-0414F simulations, grid has 500 points along the airfoil surface with 350 points in the normal direction, every other grid line shown for clarity.

The NLF (natural laminar flow) family of airfoils were designed to maintain extended regions of laminar flow, even at high Reynolds numbers. This makes them an ideal choice for testing out the capabilities of transition prediction schemes. The particular airfoil of choice was the NLF(1)-0414F as experimental data at high Reynold numbers is available [105]. A C-type grid was used to insure maximal wake resolution and accurate drag prediction. The spacing in the normal direction was selected such that for each Reynolds number, the initial spacing corresponded to 0.5 y^+ or lower. Figure 5.10 provides a snapshot of the grid used. The experimental results only provide lift and drag measurements so the transition location must be inferred from the drag. Although it is not possible to precisely identify the location of transition onset, very clear trends can be observed.

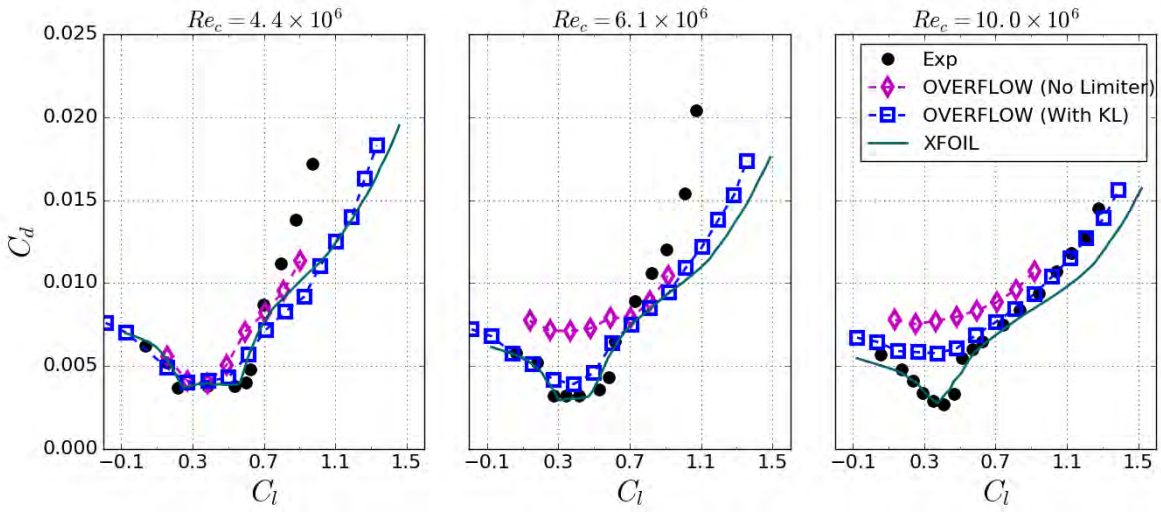

Figure 5.11. Comparison of lift and drag at three different Reynolds numbers for both an e^N type and local correlation method on the NLF(1)-0414F airfoil. Freestream turbulence level set to 0.05% for $\gamma - \tilde{Re}_{\theta t}$ model, $N_{crit} = 9$ used for XFOIL.

Figure 5.11 shows the drag polars for NLF-0414F as predicted by OVERFLOW-2 and XFOIL. At the lowest Reynolds number shown ($Re_c = 4.4 \times 10^6$), there is not a significant difference between the three methods shown. As the Reynolds number is increased, there is a divergence in predicted drag. In the cases using the $\gamma - \tilde{Re}_{\theta t}$ where the Kato-Launder modification is not used, drag is overestimated dramatically. The minimum drag is 83% above the experimental data at $Re_c = 6.1 \times 10^6$, and overpredicted by 187% at $Re_c = 10.0 \times 10^6$. At $Re_c = 6.1 \times 10^6$, both XFOIL and the $\gamma - \tilde{Re}_{\theta t}$ model with the Kato-Launder model activated produce similar predictions. Even with the limiter, the minimum value of drag is still overestimated at $Re_c = 10.0 \times 10^6$, however, it is still an improvement over cases without the limiter activated.

Figure 5.11 and 5.12 also provide an excellent example of the increased sensitivity of the $\gamma - \tilde{Re}_{\theta t}$ model as the Reynolds number is increased. As demonstrated, there is a large difference in the value of $\tilde{Re}_{\theta t}$ in the boundary layer when the Kato-Launder limiter is used and without it. Despite this, the predictions of drag at $Re_c = 4.4 \times 10^6$ are similar both with and without the limiter. This implies that changes to the $\tilde{Re}_{\theta t}$ variable do not have as large of an impact on the solution in this Reynolds number range. As the Reynolds number is increased, the difference in both drag and the transition location predicted with and without the limiter begin to deviate substantially. This can be deceptive for a user; if the $\gamma - \tilde{Re}_{\theta t}$ model is first applied to a simulation where the Reynolds number is in a more moderate range (roughly < 5 million), then the predicted drag will not be too different regardless of whether or not a limiter is used. Lower Reynolds number simulations can also mask subtle grid issues, such as insufficiently small initial wall spacing and minor oscillations along the surface. If one simply increases the Reynolds number without careful consideration of the sensitivities described, the results can be inaccurate.

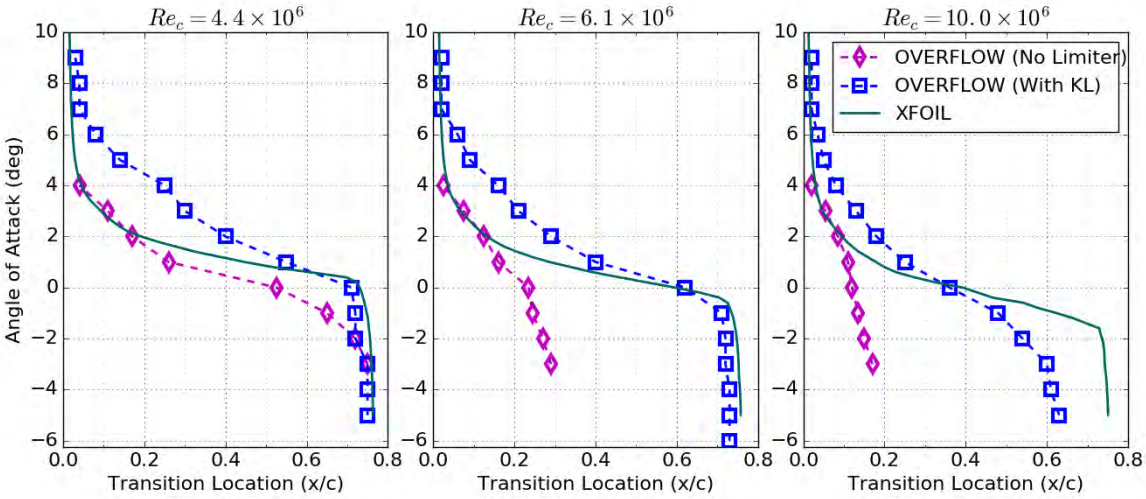

Figure 5.12. Comparison of upper surface transition location at three different Reynolds numbers for both an e^N type and local correlation method on the NLF(1)-0414F airfoil. Freestream turbulence level set to 0.05% for $\gamma - \tilde{Re}_{\theta t}$ model, $N_{crit} = 9$ used for XFOIL.

NACA 63_3-418

The transition model was also run on the NACA 63_3-418 and compared to the clean results from the Texas A&M experiments. Figure 5.13 provides a snapshot of the computational grid used.

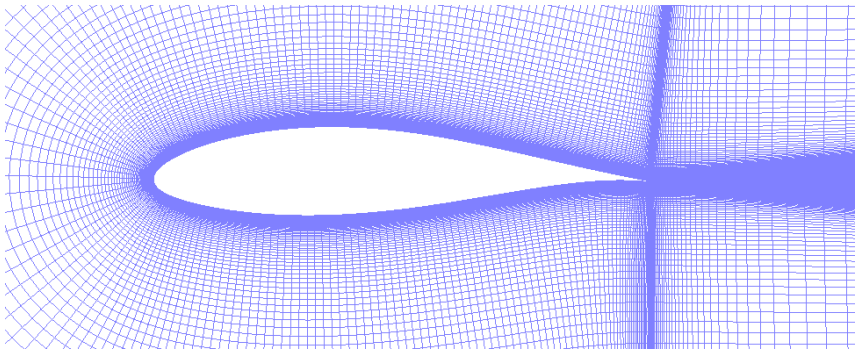

Figure 5.13. Grid used for NACA 63_3-418 simulations, grid has 500 points along the airfoil surface with 350 points in the normal direction, every other grid line shown for clarity.

The initial wall normal spacing was such that it corresponded to 0.4 y^+ for the highest Reynolds number tested (3.2 million). The same grid was used for each Reynolds number, therefore all cases will have an initial normal spacing of less than 0.4 y^+.

Figure 5.14 shows the predicted lift and drag for the NACA 63_3-418 airfoil. Due to the impact on the

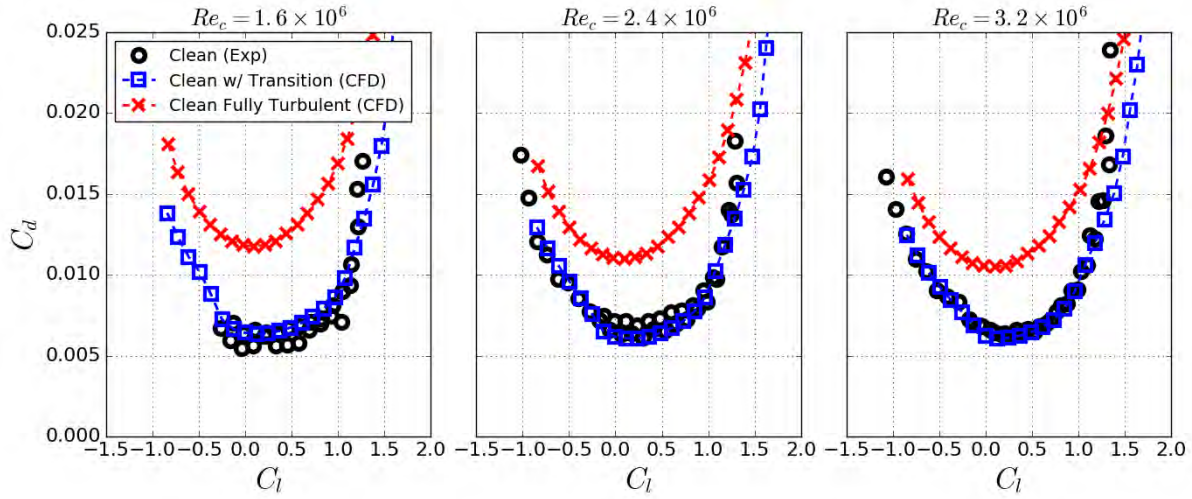

Figure 5.14. Drag polar for NACA 63_3-418, experimental results taken from multiple tunnel entries at Texas A&M, freestream turbulence set to 0.75%.

accuracy of the model, the Kato-Launder limiter is activated for the simulations shown, and any simulation that uses the transition model hereafter. The results from the transition model are in good agreement with the experimental results. The freestream turbulence was set to a value of 0.75%, which is slightly higher than the reported level for the Texas A&M LSWT [74]. The rational behind setting the parameter as such is that it should really contain all the freestream/external disturbance types, such as acoustic noise and mechanical vibrations in the tunnel. Also shown are the results from simulations run with out the transition model active. Clearly the transition model improves the predictions compared to the baseline turbulence model.

S814

Additionally, the transition model was run on the S814 airfoil and compared to the clean results. The computational grid is shown in Figure 5.15, and once more the initial wall normal spacing was such that it was less than 0.4 y^+ for all simulations conducted.

Drag polars for the S814 airfoil are shown in Figure 5.16. The predicted values in the drag bucket match up well with the experimental results, however at both high and low C_l values the predictions begin to deviate. Stall type behavior is seen for both negative and positive angles of attack and the model does not quite capture this. The ability to predict stall and massively separated flows is something RANS simulations have long struggled with. Many of the turbulence models that have been developed begin to lose validity in this flow regime. Often too much turbulent kinetic energy production is predicted and the model will force the flow to remain attached even though it physically should separate. This is also evident in the fully turbulent simulations where the slope of the drag curve at high C_l values does not indicate stalling or massively separated behavior. RANS predictions for separated flows remain an active area of research.

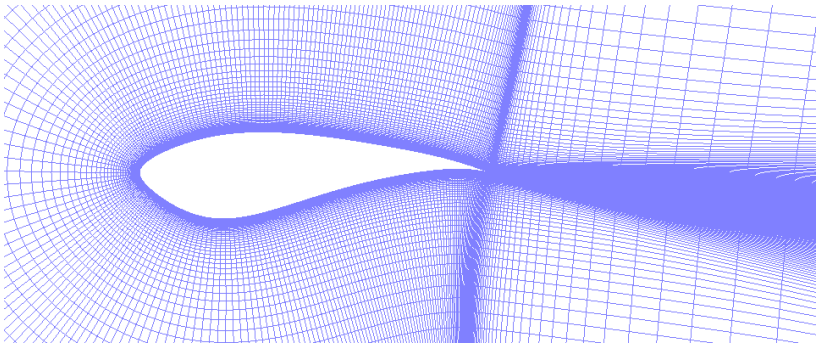

Figure 5.15. Grid used for S814 simulations, grid has 500 points along the airfoil surface with 350 points in the normal direction, every other grid line shown for clarity.

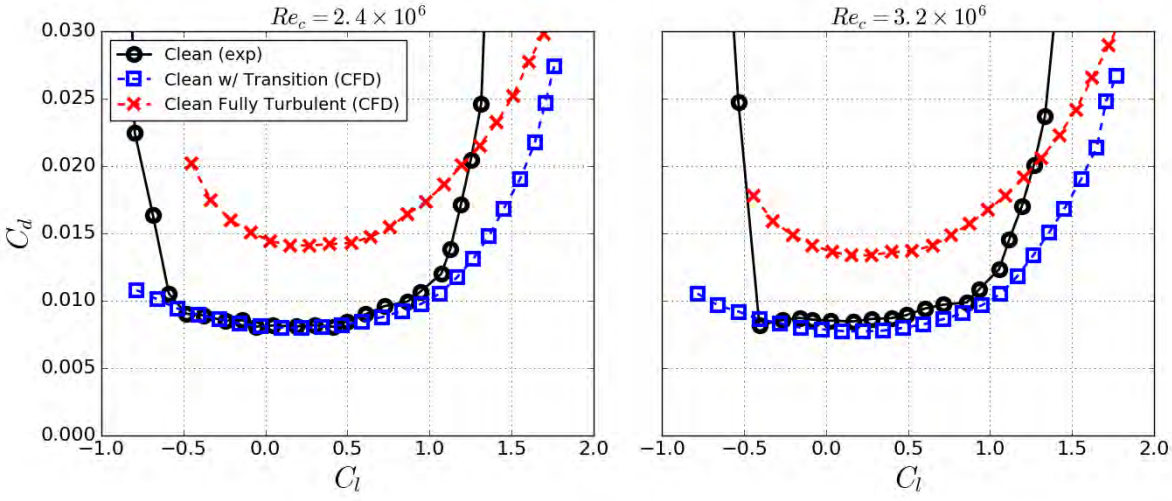

Figure 5.16. Drag polar for S814, experimental results taken from tunnel entries at Texas A&M, freestream turbulence set to 0.75%.

Chapter 6

Surface Roughness Model Development

The importance of the transition process in aerodynamic applications, and the impact of surface roughness on it, necessitates the inclusion of these effects in a roughness model. Much like the requirements for a modern CFD compatible transition model to be parallelizable and locally formulated, any model that attempts to account for roughness effects on transition should follow the same guidelines. Additionally, the process of building a transition model from the ground up would require an unreasonably large effort, so the option of modifying an existing method is very desirable. With these considerations, the appeal of extending a local correlation transition model is clear, and the present work follows this strategy. Despite the reduction in scope due to building off an existing method, the process of modeling surface roughness still carries abundant challenges. A discussion of the surface roughness model development is presented in this chapter, including why the form of the model was selected, and a detailed description of the calibration process.

Roughness Model Preliminaries

There are a few restrictions that can immediately be placed on the problem. Information about the roughness can only be passed into the model at rough wall boundaries. Therefore, all the dependencies of the rough wall function must be available at the wall. Also to accommodate the local information only constraint, it must not rely on some integration along the surface or normal to the boundary layer. Both of these constraints are addressed with the use of a scalar transport equation in the underlying transition model, so naturally it follows to use a similar strategy to account for roughness.

At a high level, the model defines an additional scalar field quantity, A_r, that is defined by a boundary condition at rough walls. A transport equation is used to set the distribution throughout the flowfield. This allows for the effects of roughness to convect downstream and modify the transition criteria in areas that are not directly in contact with rough wall boundaries. This is necessary to model the "incubation distance" described in many of the experimental studies, where often a significant distance is passed between the roughness itself and the point of transition. The transport equation for A_r is expressed:

$$\frac{\partial(\rho A_r)}{\partial t} + \frac{\partial(\rho U_j A_r)}{\partial x_j} = \frac{\partial}{\partial x_j}\left[\sigma_{ar}(\mu + \mu_t)\frac{\partial A_r}{\partial x_j}\right] \tag{6.1}$$

An additional benefit of using the transport equation is that it can pass along information from the rough wall boundary to other regions of the flowfield where additional physical parameters are well defined locally. The scalar quantity A_r is then used to modify the onset criteria of the Langtry-Menter $\gamma - \tilde{Re}_{\theta t}$ transition

model. This modification was calibrated over an extensive number of test cases and should be regarded as a primarily empirical formulation.

A notable consideration made was to directly change the boundary condition of the $\tilde{Re}_{\theta t}$ variable. As the production term is shut off in the boundary layer, the effect would be quite similar to that of the third transport equation proposed in that region. One could theoretically calibrate the boundary condition based on the roughness effects, however there were several reasons this option was not taken. The lack of adjustable parameters played a large roll, as one would only be able to change the function at the rough wall boundary. Even a change to the diffusion constant to adjust the behavior would ultimately impact the transition model globally as there would be no way to only adjust it in regions impacted by roughness. Additionally, there would be no way to adjust other parameters in both the turbulence and transition models as again there is no distinction between regions impacted by roughness and not. Despite the fact further modifications based on the scalar variable are not explored in detail in the current work; the form of the model opens the door for this type of extension.

This same methodology could be coupled with the $SA-\gamma-Re_{\theta t}$ of Medida [34] almost directly as the equation for $Re_{\theta t}$ is of the same form. The reason for selecting the original SST variant of the $\gamma-Re_{\theta t}$ was based on the fact that it has been more extensively validated, not due to any inherent limitations of the SA version. Additional local compatible transition models that could also be modified using the strategy of an additional scalar transport equation include the laminar kinetic energy transport model of Walters and Leylek [29], the one equation intermittency model from Menter et al. [36], and the N-factor transport model of Coder [31]. Although, it may be considerably more difficult to modify these models as the transition onset criteria is not defined by the same transport equation.

As mentioned in the review of literature, a number of direct modifications to the transition onset momentum thickness Reynolds number have been proposed by various authors [70, 69]. The trouble with defining the onset criteria as a direct function of the surface roughness, is that in many cases the flow will transition beyond the edge of the roughness. The change to the onset criteria should be thought of as an integrated change based on the sum of the interactions between the flow and the extent of the surface roughness. Looking at the roughness properties in a singular location does not give a full indication of how the roughness may impact the flow. In many ways the model described throughout this section can be thought of as numerically generated functions, activated over and downstream of rough walls. These functions act to combine information regarding the roughness provided by the A_r variable and locally defined physical parameters to make modifications to the transition onset criteria.

Roughness Model Outline

The idea behind adding an additional transport equation to account for roughness effects was originally proposed by Dassler, Kozulovic, and Fiala in 2010 [71]. Initially, the formulation involved a source term for the transport equation that is only active at rough wall boundaries. A slightly different version of the model was presented by the same authors in 2012 with the primary change of eliminating the source term and adding a boundary condition for the A_r variable [72]. The model as presented in 2012 was implemented in the flow solver OVERFLOW by the current author and re-calibrated to match the results of Dassler et al. [106]. The initial results were promising but the calibration was conducted on a limited number of geometries and roughness types. Given the success of these results, the general form of the model was selected to be re-formulated and calibrated to the results obtained in the companion experimental study described in Chapter 3.

The original implementation of the roughness amplification model set A_r as a function of the dimensionless roughness height parameter k^+, $A_r\|_{wall} = f(k^+)$, and modified the transition model production term using only the A_r variable:

$$P_{\theta t,mod} = P_{\theta t} - F(A_r) \tag{6.2}$$

This formulation proved successful on a number of different calibration cases, however when applying the roughness model to the results obtained at Texas A&M on a NACA 63_3-418 airfoil, the model demonstrated some unfavourable behavior. At low angles of attack the modified transition location was predicted accurately; however, when the airfoil was pitched further away from a zero degree angle (in both the positive and negative directions), the predictions began to deviate. On the suction side of the airfoil, where adverse pressure gradients develop at higher angles of attack, the model would predict transition further aft of the experimental results. The opposite was true of the pressure side. There the model kept predicting transition prematurely. The conclusion derived from this behavior was that the function that modified the transition model was only valid for cases under the influence of little or no pressure gradient.

The effects of localized pressure gradients are accounted for in the Langtry-Menter transition model, and initially it was assumed this would naturally extend to the roughness model. Upon further examination, it became clear why this assumption was not entirely valid. As the pressure gradient term, λ_θ, is ill defined in the boundary layer under the formulation of the transition model, the pressure gradient correction to $\tilde{R}e_{\theta t}$ is shut off. This is how the transition model is designed to function [107]. However, the roughness model strongly modifies the $\tilde{R}e_{\theta t}$ variable within the boundary layer. The changes to the onset criteria generated by the roughness model were large enough inside the boundary layer that the pressure gradient correction term outside could not alter the behavior. This effect is especially pronounced as the value of A_r will naturally obtain its largest magnitude at the wall. Modifying the onset criteria as only a function of A_r will therefore always produce the largest change at or near a rough wall. This initially seems like a favorable property, but when the transition criteria is modified too much at the wall, other flow effects are negated.

A number of considerations have to be made when attempting to apply a pressure gradient correction term to the roughness model. Due to the strong coupling with the Langtry-Menter transition model, it was decided to use the same Thwaites parameter λ_θ as the pressure gradient indicator. As mentioned, this parameter is not well defined at the wall so it cannot be used to directly modify the boundary condition for A_r. Relatively large values of A_r at the wall are inevitable as that is the only place the variable is introduced into the flowfield. In order to have a workable quantity away from a rough wall (which is necessary to predict subcritial roughness effects), the value at the wall must be sufficiently large. Adding to the complications, the shear stress at the wall, and therefore k^+, increases under the influence of a favorable pressure gradient and decreases in an adverse gradient.

To overcome these obstacles, a similar strategy to the Langtry-Menter pressure correction was used. Using the boundary layer indicator function $F_{\theta t}$, separate functions are constructed inside (f_1) and outside (f_2) of the boundary layer. The function of A_r and λ_θ that modifies the onset criteria now takes the form:

$$F_{Ar} = f_1(A_r) \cdot F_{\theta t} + f_2(A_r, \lambda_\theta) \cdot (1 - F_{\theta t}) \tag{6.3}$$

This function is modeled after the production term for $\tilde{R}e_{\theta t}$. In addition to shutting off the pressure gradient term inside the boundary layer, it is designed to help dampen out the influence of A_r near the wall. The feature this is trying to capture is that large values of A_r away from the wall imply a much larger disturbance

than large values near. To a certain extent this also provides an indication of the boundary layer thickness, as the $F_{\theta t}$ function will "switch on" the f_2 function closer to the wall. The diffusion of the A_r variable in the wall normal direction combined with the f_2 function, allows the model to react strongly in regions the boundary layer has a relatively small thickness.

The modification to the transition model is still through the production term for $\tilde{R}e_{\theta t}$:

$$P_{\theta t,mod} = c_{\theta t}\frac{\rho}{t}\left[(Re_{\theta t} - \tilde{R}e_{\theta t})(1 - F_{\theta t}) - F_{Ar}\right] \tag{6.4}$$

The general form of the F_{Ar} function is defined in Equation 6.3. This new formulation allows the effects of localized pressure gradients to be explicitly accounted for in the roughness model.

Input Parameter

A singular input parameter for rough walls was selected due to the difficulty of measuring roughness distributions and the large amount of parameters that would need to be included to fully describe every roughness configuration. Much like many other roughness studies, the equivalent sand grain roughness (k_s) is used as the input. The parameter is defined as the sand grain roughness size that would produce the same change in skin friction as the roughness configuration being parameterized. By this definition k_s is not a physically defined quantity, but a representation of the "effect" of a particular roughness distribution. Numerous studies have attempted to relate physically measurable parameters to an equivalent sand grain roughness height. Typically, the two primary factors involved in the mapping to a representative k_s are some height and a density parameter. Also, frequently considered is the incident angle of the roughness elements, the skewness, height to diameter ratio, and more. Some past efforts to generate k_s values are presented in Table 6.1, and the reader is directed to Bons [2] for more information on the topic of roughness parameterization.

Table 6.1. Sample of physical roughness relationships mapped to k_s, as presented in Bons [2].

Year	Reference	k_s relation	Surface type
1962	Speidel	$k_s = R_z/5$	Milled surface with groves parallel to flow (R_z grove height)
1976	Koch and Smith	$k_s \approx 6R_a$	Sandgrains
1976	Bammert and Sandstede	$k_s \approx 2.2R_a^{0.88}$	Mechanically produced surface and emery grain surface
1990	Civinskas and Bogard et al.	$0.5 < k_s/k < 5$ as $f(\Lambda_s)$	Isolated 2D and 3D roughness elements of height k
1997	Barlow and Kim	$k_s \approx 2.7k$ or $k_s \approx 16R_a$	Ordered array of pedestals of height k
1998	Kind et al.	$2.4 < k_s/k < 6.1$ as $f(\lambda)$	Sparsely distributed sandgrains of average size k
2005	Bons	$0.5 < k_s/R_z < 3.5$ as $f(\alpha_f)$	Scaled turbine blade roughness
2006	Yuan and Kind	$k_s \approx 1.8k$	Sparsely distributed sandgrains of average size k

A consensus across many groups is that this is still very much an unresolved problem, and looking at Table 6.1, it is easy to see why.

Roughness Characterization

Unfortunately, due to the inherent difficulties in measuring skin friction changes and directly capturing the k_s value in the experiments conducted throughout the study, an indirect computation was used. A look through the literature on the topic reveals a wide variety of ad hoc correlations that really only fit a small subset of roughness configurations. There is, however, a trend to the general form of such correlations. The k_s mapping typically involves a representative height parameter (R_a, R_z, R_q), and some correction for density and shape. Recognizing the importance of parameterizing the roughness distributions used, while also wanting to maintain some generality (i.e. not introducing constants calibrated to only very specific distributions), the following argument was constructed.

Assuming there is a relationship:

$$\frac{k_s}{k} = f(\Lambda_k) \tag{6.5}$$

where Λ_k is some general function related to density of the distribution, which could include the relative diameters, incident angle of the roughness elements, etc. In this expression, k is the physical height of roughness. Under this assumption, fixing the distribution density and the shape of the elements should then create a direct proportionality between k and k_s. Therefore, even though $f(\Lambda_k)$ may not be known exactly, relative changes in k_s and the resulting impact on the flow can be used to establish a functional relationship between k_s and the roughness model variable A_r. The idea is that if the roughness height doubles, and the other parameters remain the same, the k_s value should also double. The patterns used in the experimental studies accompanying the present work provide a fixed distribution density so that the changes to the flow behavior can be attributed to changes in height:

$$\Delta k_s \approx \Delta k \cdot f(\Lambda_k) \tag{6.6}$$

Additionally, the method used to produce the roughness patterns provides a well defined measure of the height parameter k, so there is a high level of confidence in this value.

Another more broad characterization of roughness elements is into k-type and d-type. If the effects of the roughness depend primarily on the height of the roughness elements, then the roughness is considered k-type. If the roughness is tightly packed and therefore another outer length scale is dominant, such as pipe diameter, the roughness distribution is classified as d-type. The assumption that the k_s parameter depends primarily on the height implies the roughness model described throughout is designed to represent k-type roughness.

Model Calibration

In general there are two functions that primarily control the behavior of the roughness model. The first is the function at rough wall boundaries that sets the A_r distribution. The second is the function that controls the modified source term of the $\tilde{Re}_{\theta t}$ equation. By nature, neither of these functions are unique so it is possible to make adjustments to either function to modify and make corrections to the model. The final calibration was performed by fixing either the boundary condition function or the source term function, and varying the other. The formal calibration of the functions is described in the following sections. This process began after the original model was implemented, so the first iteration involved fixing the functions originally described by Dassler et al. [71]. When presenting the calibration of the boundary condition function, there is also discussion on the treatment of the k_s parameter. This is of specific importance when trying to generalize the roughness model formulation.

Boundary Condition Function

The process of calibrating the rough wall function that ultimately determines the global A_r distribution is described first, including a discussion of the physical parameters used. It should be noted that the boundary condition function is the only place in the roughness model where physical information regarding the roughness can be used. Assuming the input parameter to the model will be k_s, a useful quantity available at the wall is the dimensionless height parameter k_s^+:

$$k_s^+ = \sqrt{\frac{\tau_w}{\rho}}\frac{k_s}{\nu} \tag{6.7}$$

where ν is the kinematic viscosity, ρ the fluid density and τ_w the shear stress at the wall. All of these parameters are available at the wall in most general purpose CFD codes, so formulating the boundary condition as a function of k_s^+ should not introduce incompatibilities into the model. Including the wall shear stress helps provide proper Reynolds number scaling and can help provide an indication of relative location in a developing boundary layer, such as near the leading edge or stagnation point of an airfoil. For these reasons the boundary condition function was chosen to be a function of k_s^+.

In many experimental studies, the roughness is described using the roughness Reynolds number, Re_k:

$$Re_{k_s} = \frac{\rho U_{k_s} k_s}{\mu} \tag{6.8}$$

where U_k is the velocity in an undisturbed boundary layer at height k. There is an approximate relationship between Re_k and k_s^+:

$$Re_{k_s} \approx (k_s^+)^2 \tag{6.9}$$

The assumptions that must be made to arrive at Eq. 6.9 are that of a linearly varying velocity near wall, and incompressibility. Therefore:

$$U_{k_s} \approx k_s \left(\frac{\partial u}{\partial y}\right)_{wall} = \frac{k_s \tau_w}{\mu} \tag{6.10}$$

$$Re_{k_s} \approx \frac{\rho\left(\frac{k\tau_w}{\mu}\right)k}{\mu} = \frac{\rho\tau_w k^2}{\mu^2} = \frac{\tau_w}{\rho}\frac{k_s^2}{\nu^2} = (k_s^+)^2 \tag{6.11}$$

This relationship can be used to include empirically correlated values of $Re_{k,crit}$ within a function of k_s^+.

The functional dependence is most critical in the range between a minimum height, $k_{s,min}^+$, that will alter the transition behavior, and the critical height, $k_{s,crit}^+$, that will immediately trip the boundary layer. In the regions above and below these levels, the value of A_r really need only be above or below some threshold.

$$A_r|_{wall} = \begin{cases} A_r < C_{\text{small}} & k_s^+ < k_{s,min}^+ \\ f(k_s^+) & k_{s,min}^+ \leq k_s^+ \leq k_{s,crit}^+ \\ A_r > C_{\text{large}} & k_s^+ > k_{s,crit}^+ \end{cases} \tag{6.12}$$

while strictly speaking, constant values are not exactly physically correct, the middle range of k_s^+ is sub-stantially more important to the behavior of the roughness models. Numerous different types of functions were considered, from various order polynomials to exponentials, with the final form being a sigmoid:

$$A_r|_{wall} = f(k_s^+) = \frac{C_{A_{r1}}}{1 + e^{-(C_{A_r2}\cdot k_s^+ + C_{A_r3})}} \tag{6.13}$$

This form allows the function value to remain sufficiently small in the lower range of k_s^+, while rising sufficiently fast in the critical range, and finally having a bound which prevents unfavorable numeric properties are very high values. The function is bounded by the constant in the numerator $C_{A_{r1}}$ and is chosen such that $C_{A_{r1}} >> C_{\text{large}}$ in Equation 6.12. That is, a value significantly above the threshold that would induce transition immediately.

The function at the rough wall boundary was calibrated using both zero pressure gradient flat plate data from Feindt [52] and the NACA 63_3-418 airfoil cases from the current study. The calibration was initially done separately due to the differences in the roughness types used for each geometry. As mentioned, assumptions were made regarding the nature of the k_s variable and the calibration was focused on the relative changes to the height parameter. When calibrating the function on the airfoil cases an initial value of $f(\Lambda_k) = 1$ was taken and the k_s input into the model was simply the dimensionless height (k/c). While this was never expected to hold true, it allowed for the tuning of other model parameters and the form of the wall function to be determined. Even the shape of the function could be computed with a change in the density parameter, $f(\Lambda_k)$, only resulting in a translational shift of the rough wall function.

The procedure for calibrating this function began on the zero pressure gradient flat plate cases by looking at each case individually. For each roughness height the boundary condition function was set as a linear function of k_s^+:

$$A_r|_{wall} = C_{\text{temp}} \cdot k_s^+ \tag{6.14}$$

with C_{temp} varied until the desired transition behavior was obtained for the i^{th} case, at a constant C_i. As A_r is a conserved scalar quantity, the integral of the variable effects the model more than local values. For this reason the integrated quantity along the wall is of more interest:

$$\int_{s.p.}^{r.e.} A_r \, ds \tag{6.15}$$

This represents the value of the A_r quantity along the rough surface from the stagnation point (s.p.) to the roughness edge (r.e.).

Once each case had been matched individually, the objective was to find constants in Equation 6.13 such that all of the desired integrated values were matched. Taking k_s^+ as the value at the wall, this can be expressed:

$$\sum_{i=1}^{\#\text{ cases}} \left[\int_{s.p.}^{r.e.} C_i \cdot k_s^+ \right]_i = \sum_{i=1}^{\#\text{ cases}} \left[\int_{s.p.}^{r.e.} \frac{C_{A_{r1}}}{1 + e^{-(C_{A_{r2}} \cdot k_s^+ + C_{A_{r3}})}} \right]_i \tag{6.16}$$

This system of equations is indeterminate and the constants $C_{A_{r1}}, C_{A_{r2}}$, and $C_{A_{r3}}$ must be solved for iteratively by setting up an objective function:

$$J(\mathbf{x}) = \sum_{i=1}^{\#\text{ cases}} \left\| \left[\int_{s.p.}^{r.e.} C_i \cdot k_s^+ \right]_i - \left[\int_{s.p.}^{r.e.} \frac{C_{A_{r1}}}{1 + e^{-(C_{A_{r2}} \cdot k_s^+ + C_{A_{r3}})}} \right]_i \right\| \tag{6.17}$$

and solving using some optimization technique, with $\mathbf{x} = [C_{A_{r1}}, C_{A_{r2}}, C_{A_{r3}}]^T$.

This procedure was repeated for the NACA 63_3-418 cases at the distribution density of 15%. The density parameter was unknown, but assumed to be constant and set at 1 (one) so that k_s equaled the nondimensional roughness height. The functions produced from both cases produced results that supported the hypothesis the boundary condition function could be generated by looking at simply the relative changes in the roughness height k. The optimal functions were essentially identical in what would be the critical range of k_s^+. This is seen in Figure 6.1 where the two functions plotted are very similar with the exception of a translation shift.

Even though only three different physical heights were used to calibrate the model with the NACA 63_3-418 cases, the k_s^+ value covers a more substantial range due to variation in angle of attack and Reynolds number.

The decision was made to use values for the boundary condition function that the flatplate calibration sweep produced. This function still produced accurate results on the airfoil test cases if the k_s parameter was adjusted accordingly. As mentioned, this corresponds to a change in the density parameter $f(\Lambda_k)$ if the relationship $k_s = k \cdot f(\Lambda_k)$ is assumed. More discussion of how the representative k_s parameter was selected for each roughness distribution is presented with the results of the model applied to the NACA 63_3-418 and S814 cases.

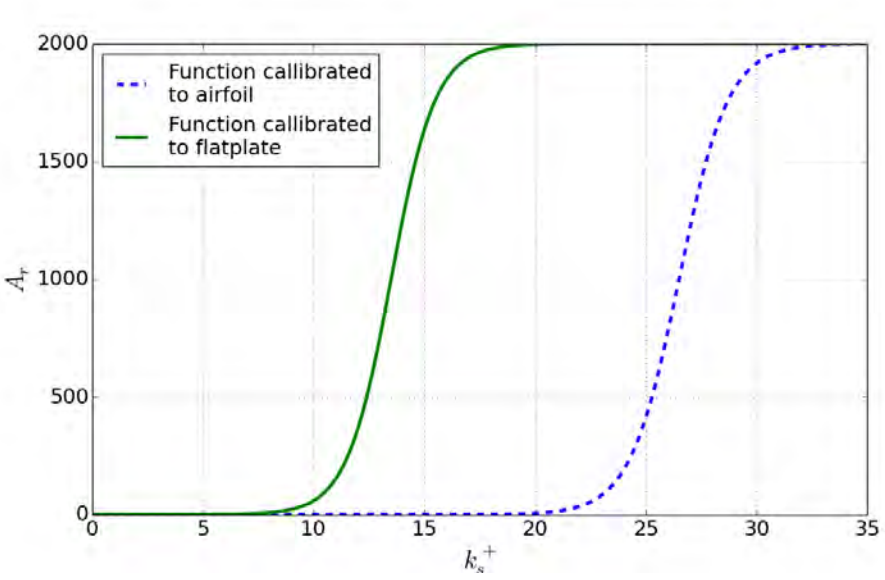

Figure 6.1. Functions calibrated to both the airfoil and flat plate geometries with two different types of roughness.

Modified Source Term Function

The calibration sweep for the source term modification was more intricate as this function is activated globally. The boundary condition function was fixed during the calibration of the source term function. It is not too difficult to match each individual case by modifying some of the constants in the model, however, these changes in the function parameters can produce discrepancies in other areas. With this in mind, the idea was to start by matching each case to the experimental data independently, and then try to construct a new function that would simultaneously match, or minimize some error, between all of them. To do this, for each case the baseline function containing the A_r modification to the $\tilde{Re}_{\theta t}$ source term, F_{Ar}, was scaled linearly until the transition location matched up with the experimental. The general form of the source term function is:

$$F_{Ar} = f_1(A_r) \cdot F_{\theta t} + f_2(A_r, \lambda_\theta) \cdot (1 - F_{\theta t}) \tag{6.18}$$

Rather than just simply taking some weighted average of the constants from each case, an optimization problem was formulated for the functions f_1 and f_2 as follows.

Let $\mathbf{x}$ be a vector of constants that parameterize the functions f_1 and f_2:

$$\mathbf{x} = [c_1, c_2, ..., c_n]^T \tag{6.19}$$

The objective function is then formulated such that the vector $\mathbf{x}$ is modified to generate an optimal solution. To construct an objective function to minimize, a measure of error must be established. At this point in the calibration run, the known global parameters are A_r, λ_θ, $F_{\theta t}$, and some scaling of the A_r function, $C_n F_{A_r}$.

Therefore at each grid point, there is a desired value for the function F_{A_r} to obtain as determined by the constant sweeps. For notation purposes, let the desired value at each point be labeled $\hat{F}_{A_r}$, and the value F_{A_r} would obtain using the most updated vector of function parameters $F_{A_r}(\mathbf{x})$.

One choice for an error metric is take the norm of the error at each grid point:

$$\left\| F_{A_r}(\mathbf{x}) - \hat{F}_{A_r} \right\| \tag{6.20}$$

and sum over the region of interest. There is also value in matching integrated quantities, due to the nature of the transport equations within the model. The region that will actually have an effect on the model behavior is everything from the stagnation point to the transition location, extending from the surface to a position above where A_r magnitudes have dropped below a threshold. This differs from the integral constructed to calibrate the boundary condition function as it is active beyond the surface roughness itself. Referring to this portion of the domain as Ω, a surface integral can be taken to compare the total modification to the $\tilde{Re}_{\theta t}$ source term in this region:

$$\left\| \int_{\Omega} F_{A_r}(\mathbf{x})\, dA - \int_{\Omega} \hat{F}_{A_r}\, dA \right\| \tag{6.21}$$

Rather than matching the integral over the entire portion of the domain, it makes more sense to partition it into smaller subspaces Ω_n such that:

$$\Omega = \bigcup_{\mathrm{n}=1}^{\mathrm{D}} \Omega_{\mathrm{n}} \tag{6.22}$$

This division is made by taking bands moving away from the surface in the normal direction as demonstrated in Figure 6.2. From here, the same integral as Equation 6.21 is used for each sub-domain. A combination of the pointwise and integrated error measures is used as the objective function to minimize. This can be expressed:

$$\min_x J(\mathbf{x}) = \sum_{i=1}^{\#\,\text{cases}} \left[d_1 \left(\sum_{n=1}^{D} \left\| \int_{\Omega_n} F_{A_r}(\mathbf{x})\, dA - \int_{\Omega_n} \hat{F}_{A_r}\, dA \right\| \right) + d_2 \left\| F_{A_r}(\mathbf{x}) - \hat{F}_{A_r} \right\| \right]_i \tag{6.23}$$

The inner summation represents the combination of all the surface integrals over the sub domains, and the constants d_1 and d_2 can be adjusted to weight one measure over the other. The discretization of the integrals is fairly straightforward as the computational grids used have a structured topology. An image of the grid along with a sketch of the domain partition is presented in Figure 6.2.

The objective function presented in Equation 6.23 was coded into an optimizer that used a Quasi-Newton algorithm to minimize the combined norms. The form of the source term function was selected as:

$$F_{A_r}(\mathbf{x}) = \begin{cases} c_1 A_r^{c_3} F_{\theta t} + c_2 A_r \left(\frac{1}{F(\lambda_\theta)} \right) (1 - F_{\theta t}), & F(\lambda_\theta) \leq 1.0 \\ c_1 A_r^{c_3} F_{\theta t} + c_2 A_r \left(\frac{1}{F(\lambda_\theta)} \right)^{c_4} (1 - F_{\theta t}), & F(\lambda_\theta) > 1.0 \end{cases} \tag{6.24}$$

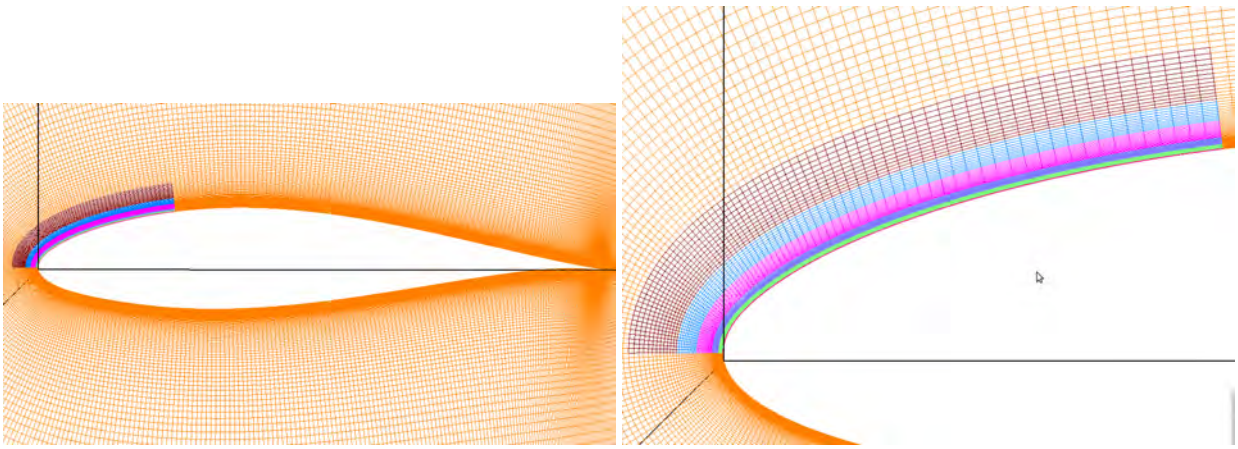

Figure 6.2. Sketch of domain partition used in integrated norm for function optimization.

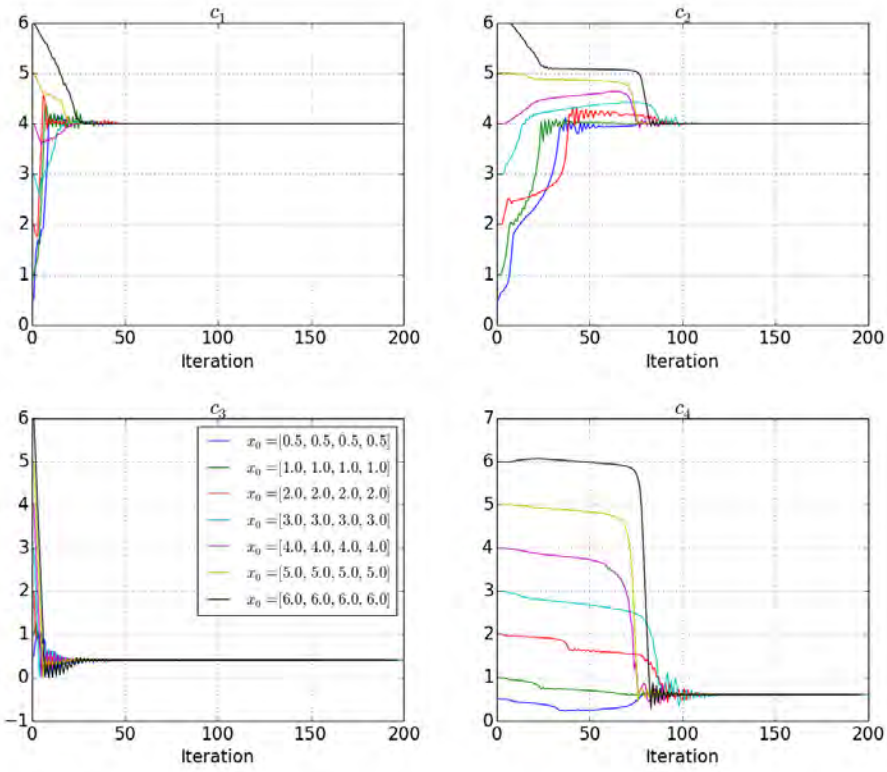

Figure 6.3. Test of optimizer convergence, plots show parameters in coefficient vector with different initial conditions.

Figure 6.3 shows the convergence of the vector $\mathbf{x} = [c_1, c_2, c_3, c_4]^T$ under a variety of initial conditions. The data shown was generated using the same function coefficients, therefore the parameters are expected to converge to the values the data was generated with. This corresponds with setting $\hat{F}_{A_r} = F_{A_r}(\mathbf{x}^*)$ in Equation 6.23 with $\mathbf{x}^* = [4.0, 4.0, 0.4, 0.6]^T$. The purpose of using cases with the same coefficients was to test convergence of the code that optimized the objective function described. As demonstrated in Figure 6.3, the optimizer robustly converges to $\mathbf{x}^*$ under a variety of initial conditions.

Once the optimizer was shown to converge as implemented, the perturbed data set was used to generate the optimal function coefficients. Numerous initial conditions were used for the optimizer, and again a clear optimal set of parameters was observed. Regardless of the starting vector used, the optimizer converged on $\mathbf{x}^* = [4.0, 4.0, 0.42, 0.60]^T$. The convergence history of the model parameters is demonstrated in Figure 6.4. These were the function coefficients used in the final form of the roughness model.

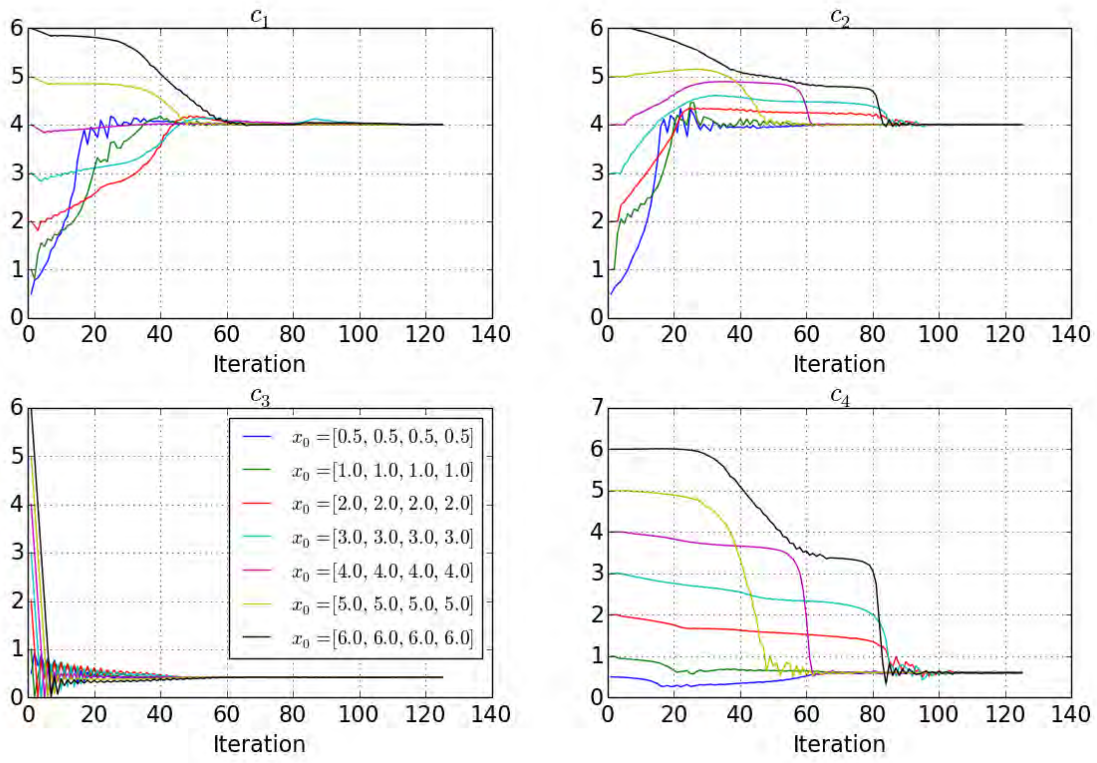

Figure 6.4. Model parameters determined by optimizer for various initial conditions.

Additionally shown is the sensitivity of the objective function, $J(\mathbf{x})$, to the model parameters. Figure 6.5 plots the function value for all iterations and initial conditions of the optimizer.

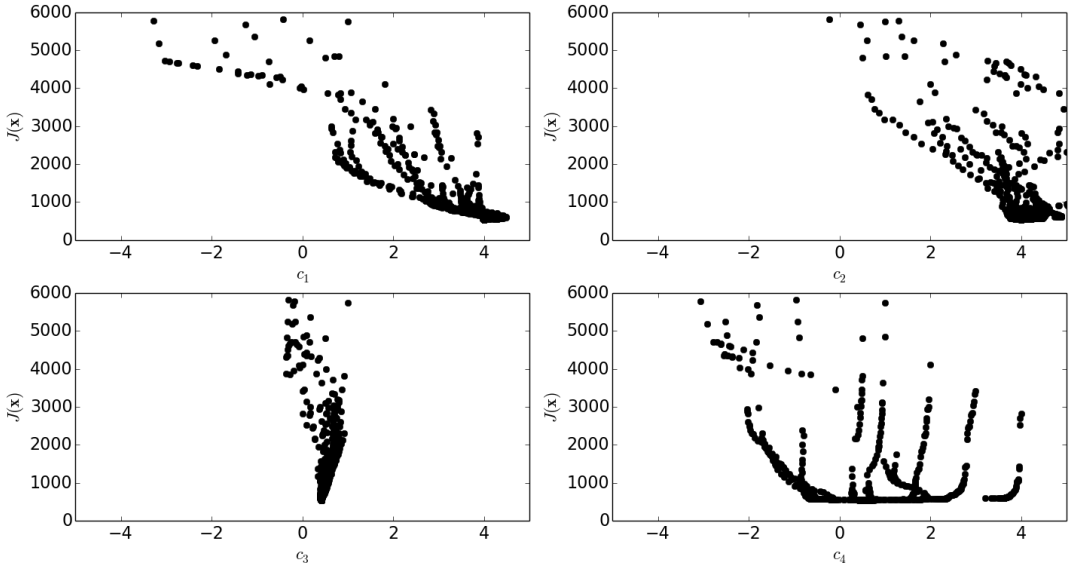

Figure 6.5. Sensitivity of objective function $J(\mathbf{x})$ to model parameters, iteration history for all initial conditions plotted.

Final Form of the Roughness Model

The following section presents all the equations used throughout the roughness model including the constants that have been calibrated to the cases described. The transport equation that governs the distribution of the roughness variable A_r is:

$$\frac{\partial(\rho A_r)}{\partial t} + \frac{\partial(\rho U_j A_r)}{\partial x_j} = \frac{\partial}{\partial x_j}\left[\sigma_{ar}(\mu + \mu_t)\frac{\partial A_r}{\partial x_j}\right] \tag{6.25}$$

the diffusion constant used for the A_r transport equation is:

$$\sigma_{ar} = 30.0 \tag{6.26}$$

The boundary condition function with the constants calibrated on the flat plate

$$\underset{\text{cases:}}{A_r|_{wall}} = f(k_s^+) = \frac{2000.0}{1 + e^{-(1.0 \cdot k_s^+ + 13.5)}} \tag{6.27}$$

The modified source term takes the form:

$$F_{A_r} = \begin{cases} 4.0A_r^{0.42}F_{\theta t} + 4.0A_r\left(\frac{1}{F(\lambda_\theta)}\right)(1 - F_{\theta t}), & F(\lambda_\theta) \leq 1.0 \\ 4.0A_r^{0.42}F_{\theta t} + 4.0A_r\left(\frac{1}{F(\lambda_\theta)}\right)^{0.6}(1 - F_{\theta t}), & F(\lambda_\theta) > 1.0 \end{cases} \tag{6.28}$$

the $F(\lambda_\theta)$ function is taken directly from the Langtry-Menter transition model as:

$$F(\lambda_\theta) = \begin{cases} 1 + \left(12.986\lambda_\theta + 123.66\lambda_\theta^2 + 405.689\lambda_\theta^3\right) e^{-\left(\frac{Tu}{1.5}\right)^{1.5}}, & \lambda_\theta \leq 0 \\ 1 + 0.275\left(1 - e^{-35.0\lambda_\theta}\right) e^{-\left(\frac{Tu}{0.5}\right)}, & \lambda_\theta > 0 \end{cases} \tag{6.29}$$

Once F_{A_r} is computed, it is used to modify the $\tilde{R}e_{\theta t}$ source term as follows:

$$P_{\theta t,mod} = c_{\theta t}\frac{\rho}{t}\left[(Re_{\theta t} - \tilde{R}e_{\theta t})(1 - F_{\theta t}) - bF_{A_r}\right] \tag{6.30}$$

$$b = 0.5\sin\left(\frac{\pi}{155}\tilde{R}e_{\theta t} - \frac{97\pi}{155}\right) + 0.5 \tag{6.31}$$

the modification to the source term acts to drive down the local transition onset criteria, $\tilde{R}e_{\theta t}$. There is an additional blending function b that serves two purposes. The $\tilde{R}e_{\theta t}$ variable is strictly positive, and the transition model has an imposed minimum non-zero value. As the $\tilde{R}e_{\theta t}$ variable approaches this minimum, the b function smooths the transition. This value is already below what would essentially cause the flow to transition immediately, so the blend does not have an impact on the behavior outside of smoothing out the numerics. Additionally, once the flow has transitioned, excessively small $\tilde{R}e_{\theta t}$ values in the boundary layer will cause a rapid non-physical increase in the shear stress at the wall [33]. The blending function effectively switches off the roughness modification to the $\tilde{R}e_{\theta t}$ source term after transition.

It should be stressed once more that this modification is based primarily on non-physical quantities with the equations constructed to match the experimental results. The goal is through calibration on a sufficiently large data set, the model will be able to remain accurate on novel geometries and cases where experimental data does not exist.

Modification of SST Boundary Condition

The inclusion of the A_r variable in the transition model allows the model to account for the early onset of transition under the influence of surface roughness. However, the effects on a fully turbulent boundary layer and the lowering of the turbulent dissapation rate along both the laminar and turbulent portion of the boundary layer need additional consideration. Modifying the near wall turbulence model behavior can adequately represent the effects of distributed surface roughness on a fully developed turbulent boundary layer by shifting the expected mean profile in the law of the wall region [108]. The transformation of the logarithmic function for the mean velocity profile can be expressed:

$$u^+ = \frac{1}{\kappa}\ln y^+ + B \quad \rightarrow \quad u^+ = \frac{1}{\kappa}\ln y^+ + B - \Delta B \tag{6.32}$$

$$\Delta B = \frac{1}{\kappa}\ln k^+ - 3.65 \tag{6.33}$$

Originally, Nikuradse assumed the values of $\kappa = 0.40$ and $B = 5.5$. However, these have been subsequently changed to $\kappa = 0.41$ and $B = 5.0$ [62].

This roughness induced change at the rough wall is accounted for using a modification of the boundary condition of the specific dissipation rate, ω.

The original boundary condition:

$$\omega_{smooth} = 10\frac{6\nu}{\beta(\Delta y)^2} \quad \text{with} \quad \beta = 0.09 \quad \text{at} \quad y = 0 \tag{6.34}$$

Here Δy represents the normal distance from the wall to the nearest grid point.

The update to account for roughness, originally proposed by Wilcox:

$$\omega_{rough} = \frac{\mu_\tau^2 S_r}{\nu} \quad \text{with} \quad \mu_\tau = \sqrt{\frac{\tau_w}{\rho_w}} \quad \text{at} \quad y = 0 \tag{6.35}$$

where S_r is dependent on the non-dimensional k^+ value.

$$S_r = \left(\frac{50}{k^+}\right)^2 \quad \text{if} \quad k^+ \leq 25 \tag{6.36}$$

$$S_r = \frac{100}{k^+} \quad \text{if} \quad k^+ > 25 \tag{6.37}$$

The modified boundary conditions allow the model to not only account for roughness induced transition, but also the effects on the fully turbulent boundary layer, including the increase in local skin friction.

Implementation in OVERFLOW

The model as described was coded into OVERFLOW-2.2k by the author. The structure of the code is such that the turbulence variables are resolved separately from the primary flow variables. All of the turbulence models are coded with a fixed discretization scheme and solver for the linear system generated. When the user selects a particular scheme in the input file, the selection is only used for the fundamental flow variables and does not extend to the turbulence or transition model.

The version of OVERFLOW used had an implementation of the Langtry-Menter transition model, and those routines where cloned and used as the basis for the roughness model implementation. As the roughness model uses an additional scalar variable, and no other existing models used as many global variables, numerous high level routines had to be modified to accommodate the addition variable. The variables in the transition model are discretized using a second order HLLC upwind scheme, and the roughness model variable follows the same procedure. The linear system is solved using a successive symmetric over-relaxation

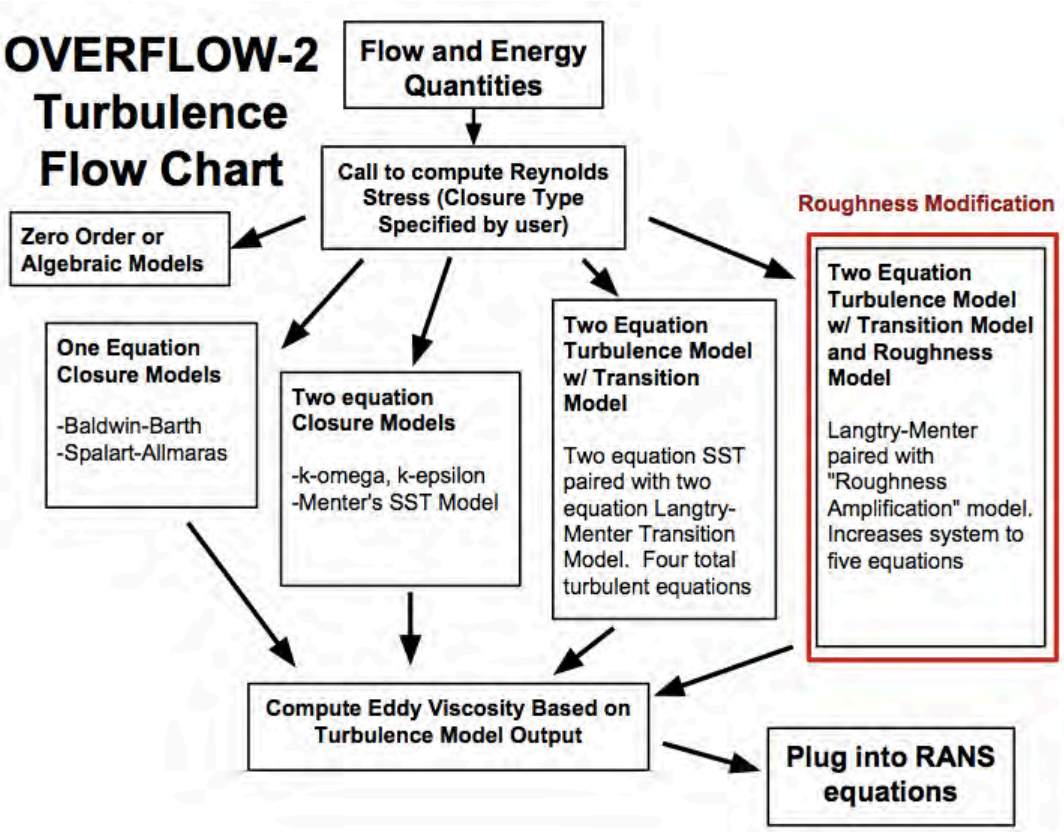

Figure 6.6. Graphical description of turbulence model implementation in OVERFLOW-2

(SSOR) algorithm where the transition roughness model variables are resolved simultaneously. Additionally, a new boundary condition was added corresponding to a rough wall, and the input parameter k_s is set using the existing framework to pass in boundary condition parameters. The code modification was validated extensively, including inputting in a 0 value for k_s and comparing the solution to the unmodified transition model.

Convergence and Grid Recommendations

Grid convergence was checked by fixing the Bezier points for each airfoil and adjusting the number of points in the parameter vector. Spacing and stretching ratios were computed by allocating a percentage of points on the surface to particular sections of the airfoil, with the procedure described in Chapter 4. Tables 6.2 and 6.3 present the predicted lift and drag coefficients along with the transition location for a variety of grid sizes. All simulations were run in 2-D using OVERFLOW. The set of grids used were the same as when checking grid independence with the transition model. Much like for simulations conducted with only the transition model, it can be seen that at roughly 400 points along the surface, the aerodynamic properties are essentially converged. Based on this observation, the roughness model does not appear to require a finer mesh than what would be needed for the transition model itself. For all simulations conducted with the

roughness model in the present work, at least 500 points along the surface and 250 points in the normal direction were used with a maximum initial spacing of $0.4y^+$.

Table 6.2. Coefficients of lift and drag as well as transition location for various grid sizes, NACA 63_3-418 airfoil, $\alpha = 0^o$, $Re_c = 2.4 \times 10^6$, slight surface roughness specified in leading edge region, initial wall spacing of $0.2y^+$ used for all grids.

J-pts	K-pts	C_l	C_d	Transition Location (x/c)
210	150	0.3550	0.008549	0.3076
313	200	0.3567	0.008197	0.3319
416	250	0.3577	0.008008	0.3258
520	250	0.3577	0.008029	0.3295
624	250	0.3577	0.008059	0.3319

Table 6.3. Coefficients of lift and drag as well as transition location for various grid sizes, S814 airfoil, $\alpha = 0^o$, $Re_c = 2.4 \times 10^6$, slight surface roughness specified in leading edge region, initial wall spacing of $0.2y^+$ used for all grids.

J-pts	K-pts	C_l	C_d	Transition Location (x/c)
227	150	0.4198	0.01136	0.206
340	200	0.4320	0.01053	0.275
448	250	0.4402	0.009945	0.275
553	250	0.4407	0.009866	0.284
666	250	0.4409	0.009858	0.283

Chapter 7

Roughness Model Results

The following chapter documents the results of the roughness model by applying it to a variety of different test cases. First presented is the model applied to a series of flat plate cases, followed by a NACA 0012 airfoil with large scale roughness on a small portion of the leading edge. Both of these geometries were tested in the previous iteration of the model, and are presented here having been re-run with the most current version of the roughness model. A large portion of the results is the comparison of the roughness model predictions to the experimental results generated at Texas A&M for the current study. For all cases, the actual input value is the non-dimensional equivalent sand grain roughness height (k_s/c) as the computational grids are generated with a unit chord length.

The numerical schemes used are held consistent throughout all cases presented in this chapter. In general, the grids used are excessively fine, and the highest order stable schemes are selected as computational resources were not limited during the development. Minimal levels of artificial dissipation were specified to promote physical accuracy. The primary flow variables are discretized using a 6th order central difference stencil, and the linear system solved with a Beam-Warming scalar pentadiagonal scheme. The turbulence variables, including the roughness model variable A_r, are discretized with a 2nd order HLLC upwind scheme. The linear system generated by the turbulence variables is then solved with a successive symmetric over-relaxation (SSOR) algorithm using the transition model and roughness model variables simultaneously. These schemes are implemented in OVERFLOW 2.2k, and were used by selection in an input file so limited discussion is provided here. An example input file is provided in Appendix D. The Kato-Launder production limiter is applied for all cases due to the favorable properties on the transition model observed. Cases were run non-time accurate until convergence of lift and drag was reached. If steady oscillations were observed, the solution was averaged over several oscillation periods.

Flat Plate Cases

The calibration of the roughness model began with the flat plate test cases of Feindt [52] used in the original validation of the model by Dassler et al. [71]. Figure 7.1 is provided to show the distribution of the A_r variable over a rough flat plate. The large magnitudes of A_r near $x/c = 0.0$ is due to the leading edge singularity of the flat plate.

The experimental results of Feindt are used in a baseline calibration study. Three different pressure gradients are simulated using the grid geometry where the inlet height and length of the plate were fixed. In addition to the baseline zero gradient test, two of the grids utilized an upslope or downslope upper wall along the chord to provide an adverse or favorable pressure gradient respectively. The profile of the upper wall for the non-zero gradients was determined with the function:

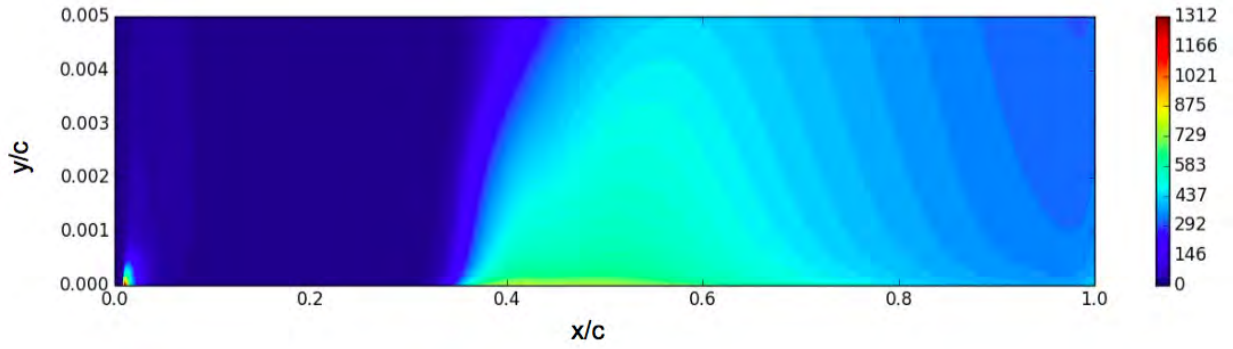

Figure 7.1. Contours of A_r over rough flat plate, $k_s/c = 200 \times 10^{-6}$, $Re_c = 1.3 \times 10^6$, zero pressure gradient, roughness applies $x/c = 0.02 - 1.0$

$$r(x) = \sqrt{\frac{r_0^2}{\sqrt{1.0 - PG}}} \quad \text{with:} \quad PG = \frac{p_1(x) - p_0}{q_0} \tag{7.1}$$

where r_0 represents the distance from the flat plate to the upper wall at the inlet, p_0 and q_0 the static and dynamic pressure at the inlet respectively, and p_1 the static pressure along the plate. The PG parameter was set to match the conditions in the Feindt experiment for the two non-zero pressure gradient tests. The initial distance from the plate to the upper wall, r_0 was set as $0.1495c$ to match the grid used in the original CFD tests of Dassler, Kozulovic, and Fiala [71]. An outline of the grid geometries can be seen in Figures 7.2 - 7.4.

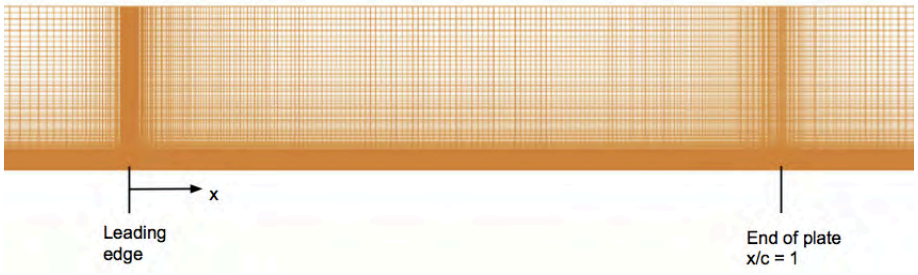

Figure 7.2. Sketch of grid used for zero pressure gradient test cases, inflow and outflow sections continue 10 and 25 chord lengths respectively in either direction (not shown).

As information regarding freestream turbulence levels were not recorded in the Feindt experiment, the turbulent intensities were set according to those used in Dassler et al. [71] and are such that the smooth wall behavior matches up with the experimental results. The tests used a Tu of 0.91% for the zero pressure gradient and adverse pressure gradient test cases. The favorable pressure gradient case required a higher Tu than the condition used in Dassler et al. to retain an accurate simulation of the smooth wall transition location. This could potentially be a product of the differences in implementation of the Langtry-Menter

Figure 7.3. Sketch of grid used for adverse pressure gradient test cases, inflow and outflow sections continue 10 and 25 chord lengths respectively in either direction (not shown).

Figure 7.4. Sketch of grid used for favorable pressure gradient test cases, inflow and outflow sections continue 10 and 25 chord lengths respectively in either direction (not shown).

model in OVERFLOW-2 and in the code used by Dassler et al. Although not an ideal method to produce proper smooth wall behavior, the purpose of the flat plate cases was to determine how the roughness model compared to the original CFD implementation. Additionally, the age of the data set introduces higher levels of uncertainty due to the more limited measurement techniques. Despite the inherent limitation of the flat plate data, the results serve as an appropriate first check for the implementation of the roughness amplification model. Additionally, due to the simple geometry the skin friction profiles can be compared to what is expected theoretically.

Figure 7.5 demonstrates the effect of varying Re_{k_s} on the local skin friction coefficient (C_f). Transition onset can be seen as the location where the local C_f spikes. Additionally, the large discrepancy in skin friction between the laminar portion (before the rapid increase) and the turbulent portion of the boundary layer emphasizes the importance of accurately locating transition onset in drag calculations. As expected, there is a clear trend as the value of Re_{k_s} increases, the location of transition onset moves upstream. There is only a slight change in transition location between the smooth and the lowest roughness configuration due to the physically observed phenomena of small roughness heights having a very small impact on the location of transition onset. Another trend is the modulation of the skin friction graphs upward in the "turbulent" portion with increasing Re_{k_s}. This effect can be attributed to the roughness modification of the boundary condition for ω as discussed above.

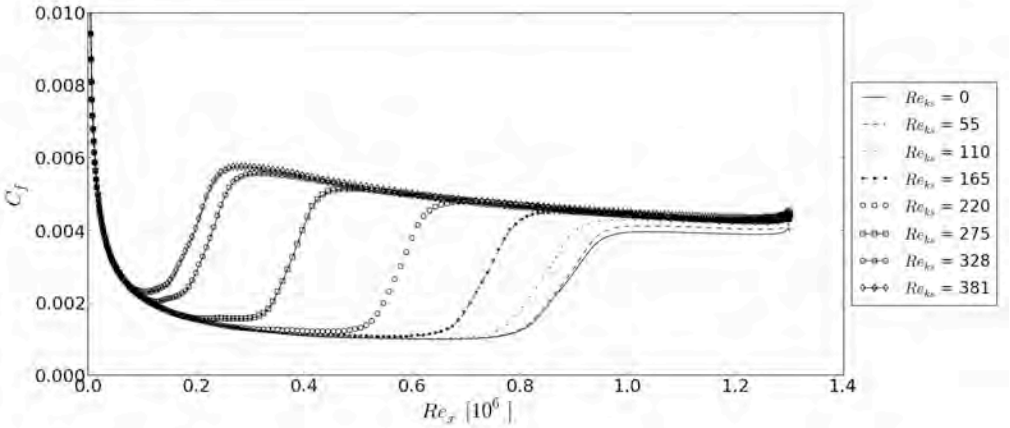

Figure 7.5. The effect on local skin friction coefficient (C_f) of varying Re_{k_s}. Zero pressure gradient flat plate, freestream turbulence intensity = 0.91%.

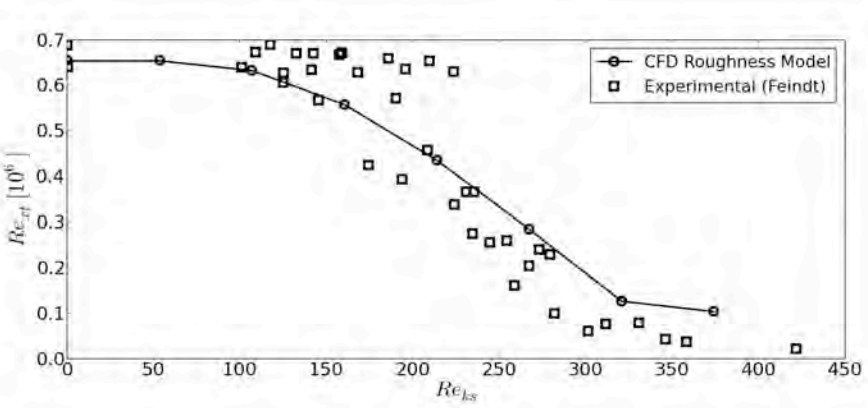

Figure 7.6. Roughness Reynolds number (Re_{k_s}) plotted against location of transition onset (Re_{xt}) for zero pressure gradient flat plate.

After defining the location of transition onset as the location just before the skin friction plot rises rapidly, the correlation between the Reynolds number of transition onset, Re_{xt}, and Re_{k_s} can be made. Despite the scatter in the experimental data, the model does a good job at predicting the overall trends up until large Re_{k_s} values. The model can be adjusted to behave better in the high Re_{k_s} range, however this has a converse effect on accurately representing the boundary layer development. This issue is discussed more thoroughly in the section regarding the calibration study on the NACA 0012 airfoil. The critical range is roughly between $Re_k = 100 - 350$ which matches up with many experimental investigations on determining an $Re_{k,crit}$ for distributed roughness.

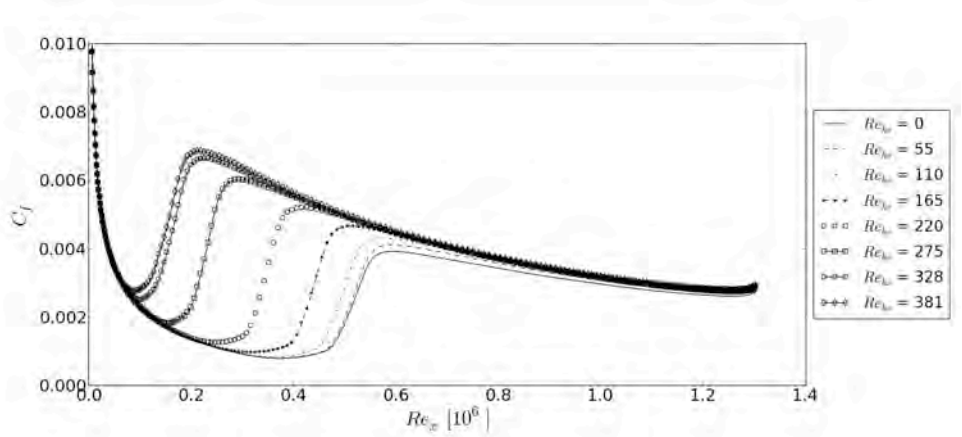

Figure 7.7. The effect on local skin friction coefficient (C_f) of varying Re_{k_s}. Flat plate, adverse pressure gradient, freestream turbulence intensity = 0.91%.

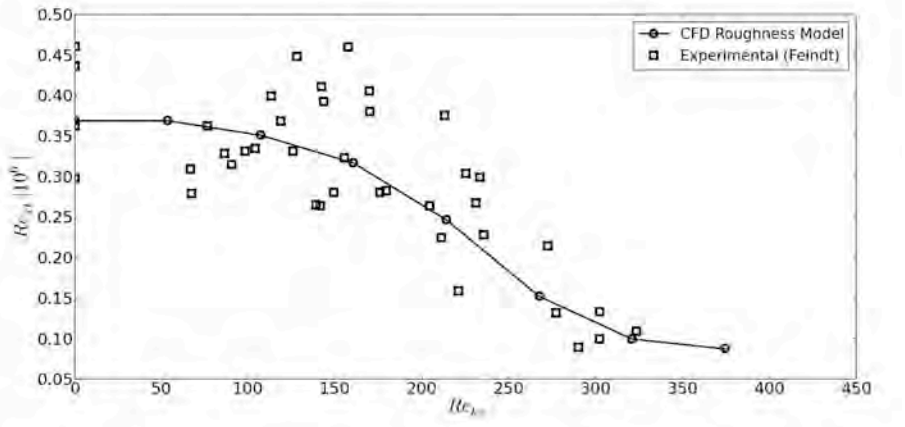

Figure 7.8. Roughness Reynolds number (Re_{k_s}) plotted against location of transition onset (Re_{xt}) for flat plate, adverse pressure gradient.

The results from the two non-zero pressure gradient configurations (Figures 7.7 - 7.10) also show agreement throughout the Re_k range, and once more despite the scatter and uncertainly in the experimental data, predict the overall trends well. Another favorable characteristic of the method is the ability to represent subcritical roughness heights that will not immediately trigger the transition process. Crude roughness correlations often assume the boundary layer transitions at the location of the roughness, which can result in large discrepancies in drag predictions.

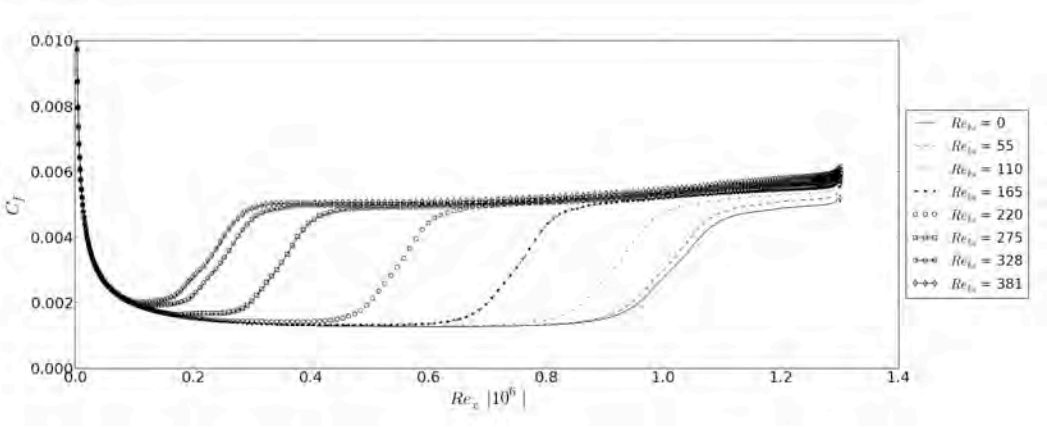

Figure 7.9. The effect on local skin friction coefficient (C_f) of varying Re_{k_s}. Flat plate, favorable pressure gradient, freestream turbulence intensity = 2.10%.

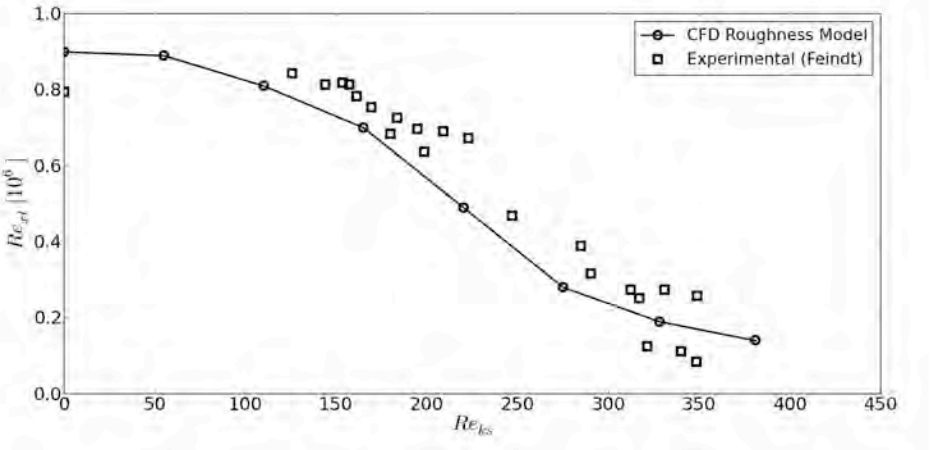

Figure 7.10. Roughness Reynolds number (Re_{k_s}) plotted against location of transition onset (Re_{xt}) for flat plate, favorable pressure gradient.

NACA 0012 Airfoil Cases

The experimental results of Kerho and Bragg were used to assess the behavior of the model applied to an airfoil with large scale leading edge erosion at varying locations and extents [54, 3]. All experimental tests were performed on a NACA 0012 airfoil of chord length 0.5334 m using a tape strip with hemispherical shapes simulating distributed roughness. The roughness strips were nominally 0.35 mm high ($k/c = 656 \times 10^{-6}$) including the tape substrate and the center to center spacing of the rough elements was 1.3 mm. The k_s input to the roughness model was simply the non-dimensional roughness height due to the similarity of the roughness pattern to an array of sandgrains. Figure 7.11 provides a picture of the simulated roughness used in the experiment.

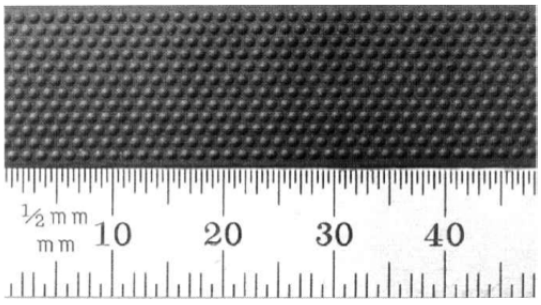

Figure 7.11. Image of simulated roughness used by Kerho and Bragg, adopted from [3].

The authors report the location of the start of the roughness measured in mm from the leading edge center and chordwise length of the rough region in inches. More information regarding the experimental configuration can be found in [3]. The same labeling convention is used in this study to provide a means of referencing particular test configurations. A summary of the test configurations can be found in Table 7.1. A noteworthy characteristic is the particularly high Re_k values across all test configurations. Due to these high Re_k values, the test cases are useful in establishing the extremum behavior of the roughness amplification model.

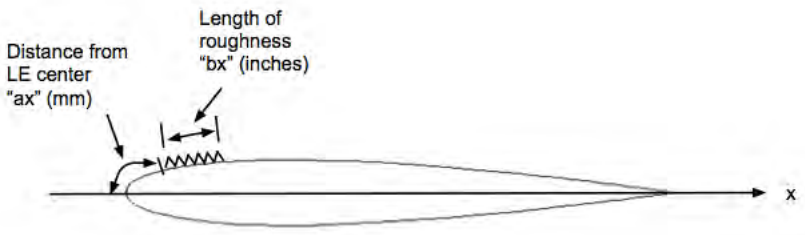

Figure 7.12. Sketch of NACA0012 airfoil to demonstrate labeling convention.

Table 7.1. Summary of roughness characteristics for $Re_c = 1.25 \times 10^6$ test cases [3]

Case bx @ ax	k/c $(\times 10^{-6})$	Re_k (start of roughness)	Re_k (end of roughness)	x/c of roughness
1/4" @ 7 mm	656	656	834	0.00490 - 0.0138
1/2" @ 4 mm	656	479	878	0.00187- 0.0191
1/2" @ 8 mm	656	701	907	0.00612 - 0.0258
1/2" @ 12 mm	656	811	920	0.0117 - 0.0327
1/2" @ 18 mm	656	899	918	0.0212 - 0.0432
1/2" @ 24 mm	656	919	899	0.0314 - 0.0539

In the computational simulations, an O-type grid was used with 415 points along the surface and 191 in the normal direction. The initial wall grid spacing was such that $y^+ \approx 0.35$. Figure 7.13 depicts the grid used for the simulations conducted. In addition to the grid used, grid independence was checked with solutions computed on grids with 829 and 277 number of points along the airfoil surface.

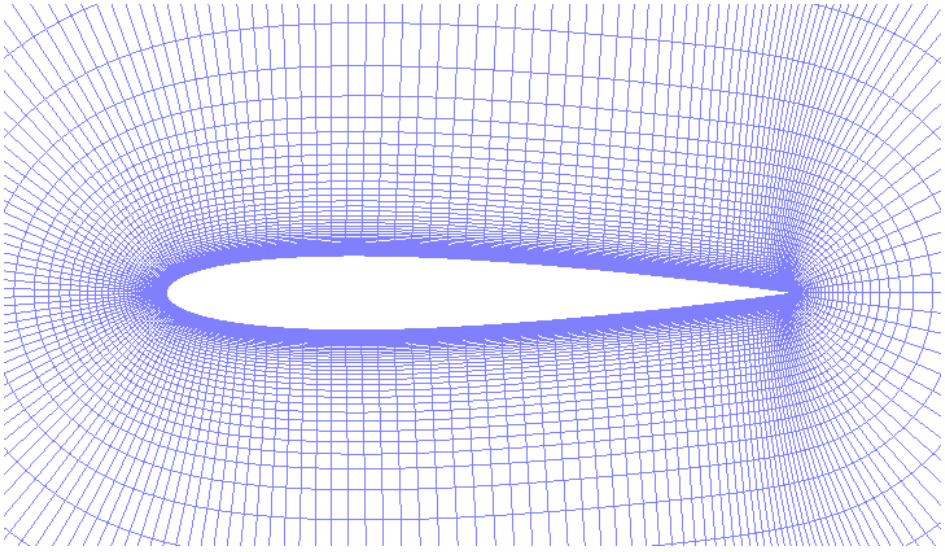

Figure 7.13. Grid used for NACA 0012 simulations, every other grid line shown for clarity.

An attribute that made the Kerho and Bragg study particularly useful was the inclusion of detailed boundary layer profiles for many of the configurations as well as turbulence intensity data. Boundary layer profiles from a few of the test cases are compared to the roughness model and baseline Langtry-Menter transition model to demonstrate the impact the roughness has on the development of the boundary layer.

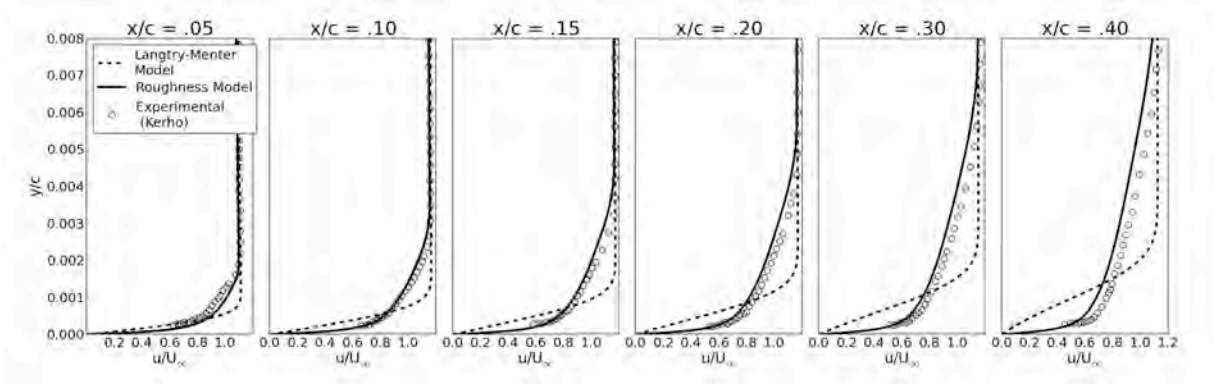

Figure 7.14. Boundary layer profiles: Kerho [54], unmodified Langtry-Menter transition model, computational roughness model. NACA 0012 airfoil, $Re_c = 1.25 \times 10^6$, $\alpha = 0^o$, $Tu = 0.1\%$, distributed roughness applied $x/c = 0.0018 - 0.0191$

The first two cases (Figures 7.14 and 7.15) demonstrate significant improvement in comparison to the baseline Langtry-Menter model, and good agreement with the experimentally measured profiles. However, with the roughness located relatively far aft (Figure 7.16), slight discrepancies occur. As seen in the first two frames of Figure 7.16 ($x/c = 0.075$ & $x/c = 0.10$), the roughness model displays a lag in transition onset prediction, and the profile produced by both the roughness and Langtry-Menter transition model follow a typical laminar profile. By $x/c = 0.15$, the roughness model has influenced the transition model enough such that the boundary layer profile begins to shift closer to the experimental.

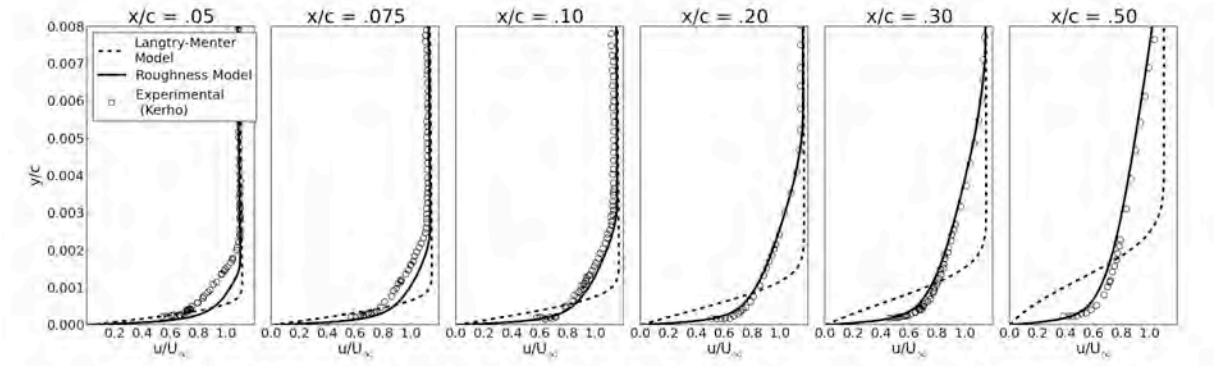

Figure 7.15. Boundary layer profiles: Kerho [54], unmodified Langtry-Menter transition model, computational roughness model. NACA 0012 airfoil, $Re_c = 1.25 \times 10^6$, $\alpha = 0^o$, $Tu = 0.1\%$, distributed roughness applied $x/c = 0.0061 - 0.0258$

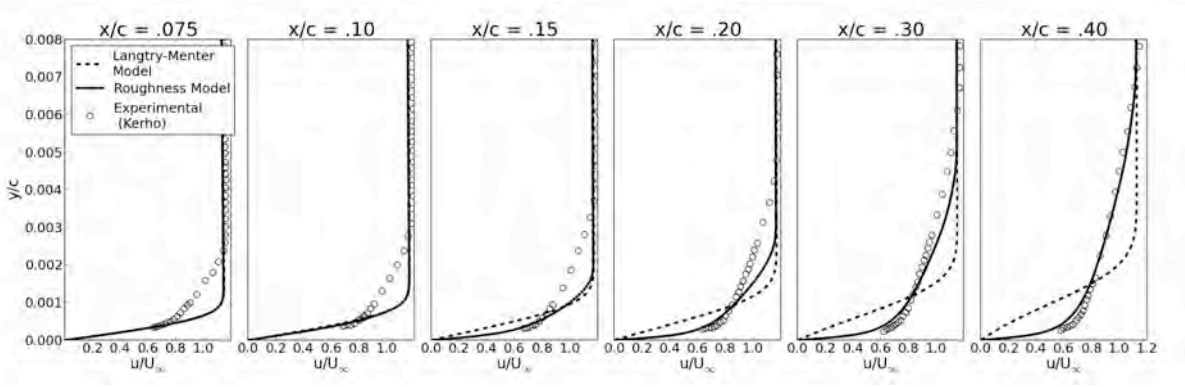

Figure 7.16. Boundary layer profiles: Kerho [54], unmodified Langtry-Menter transition model, computational roughness model. NACA 0012 airfoil, $Re_c = 1.25 \times 10^6$, $\alpha = 0^o$, $Tu = 0.1\%$, distributed roughness applied $x/c = 0.0314 - 0.0539$

A slight discrepancy is the shift in the profile seen in the more aft chord locations ($x/c = 0.40$ in Figure 7.14 and $x/c = 0.50$ in Figure 7.15). This is the result of a turbulent boundary layer developing too rapidly in the simulation, caused by a large production of k from the turbulence model. The trend was consistently observed across all roughness configurations even those which demonstrated a lag in onset prediction. The likely cause of this discrepancy is in the intermittency function in the transition model. The length of the transition region is determined within the intermittency equation, and effectively controls how rapidly the production of turbulent kinetic energy is switched on. As the model was calibrated using test cases that transition without the influence of roughness, the inability to accurately simulate the development of a roughness induced transition is not surprising. This issue and initially proposed solution is discussed in more depth following the presentation of the remaining cases.

Another observation recorded by Kerho and Bragg was the "state" of the boundary layer at varying chord locations for all the test configurations. The categories used to describe the boundary layers were laminar, transitional, and fully turbulent. The criterion used to determine the onset of transition in the experiment was where the integrated intermittency ($\hat{\gamma} = \frac{1}{T}\int_0^T \gamma(t)\,dt$,$t \in [0,T]$) measurement began to rise.

Due to the nature of RANS simulations, it is not possible to determine the integrated intermittency parameter as defined in the experiments, therefore a different approach must be taken to determine the location of transition onset. As suggested by Thompson [109] a good indicator determining the onset of transition is the boundary layer shape factor ($H = \delta^*/\theta$). Under ideal conditions, a Blasius profile will retain a constant shape factor until the onset of transition where it will drop substantially. Realistically it takes some time for the boundary layer to develop into a characteristic laminar shape, therefore the shape factor rises initially, then plateaus, and finally begins to drop after the onset of transition. The criterion for onset used in the present study is the point after the inflection in the shape factor plot as demonstrated in Figure 7.17. Also shown is the theoretical Blasius shape factor for a laminar and turbulent boundary layer, the profile shown does not ever obtain a value comparable to a Blasius ($H = 2.59$) as the roughness promotes transition before the boundary layer fully develops to a theoretical Blasius laminar profile.

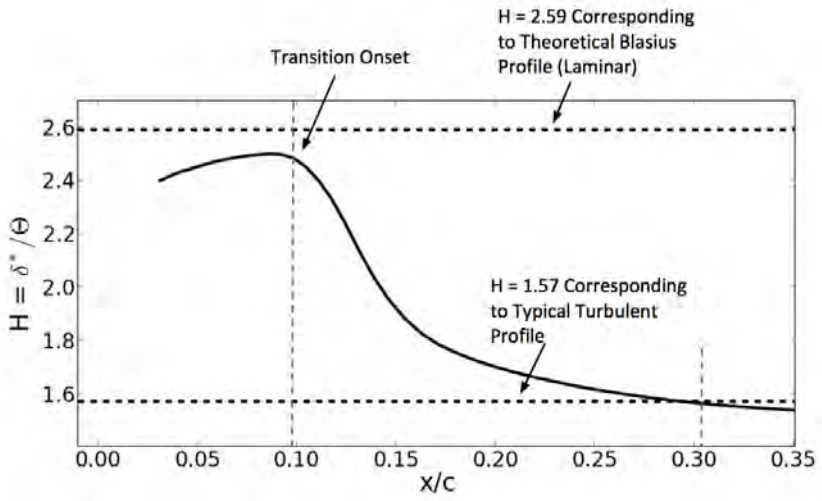

Figure 7.17. Plot of boundary layer shape factor along chord, NACA 0012 airfoil, $Re_c = 1.25 \times 10^6$, $\alpha = 0^o$, $Tu = 0.1\%$, distributed roughness applied $x/c = 0.0314 - 0.0539$

Additionally, a criterion for where the boundary layer obtains a fully turbulent state must be established. As the boundary layer is constantly growing, there is no single profile that can be used to determine the final shape that an ideal "fully" turbulent boundary layer will obtain. The experimental study defines the location where the boundary layer obtains self-similarity when normalized by momentum thickness (θ) as a "fully" turbulent state. For consistency, the current study uses the same criteria. Figure 7.18 demonstrates how the evolving boundary layer will obtain self-similarity when normalized by momentum thickness. Additionally, one can use the point of intersection between the shape factor plot and ideal turbulent profile as a criterion for a "fully" turbulent state.

Comparison of Figures 7.17 and 7.18 shows that both methods for determining where the boundary layer achieves a fully turbulent state are in close agreement. After defining the criteria for transition onset, and obtaining a fully turbulent profile, the status of the boundary layer for various test configurations was examined. Figure 7.19 compares the results from the roughness amplification model to the experimental results of Kerho and Bragg [3].

As seen in Figure 7.19, the model does a good job tracking the change of transition onset location as the location of the roughness is moved along the chord. That is, the experimental test that transitions earliest is mirrored in the simulation and the relative locations of onset across the configurations match up. There is a slight delay in onset prediction in some of the cases. However, on the whole, the model does a good job predicting the change in onset characteristics as the location of the roughness is moved. This has very desirable implications as despite the fact the changes in the placement of roughness are relatively small, the model is able to represent the movement of transition location consistently.

There is another very clear trend in Figure 7.19 and that is the length of the "transitional" region is repeatedly under predicted. This can be rephrased as the model forces the turbulent boundary layer to develop too rapidly and the effects of this are visible in Figure 7.14 and 7.15 where at the more aft chord locations, the computed boundary layer profile is shifted to the left of the experimental. As discussed, the root of

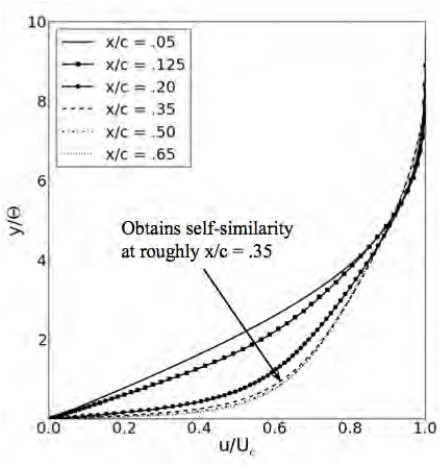

Figure 7.18. Plot of boundary layer normalized by momentum thickness at several chord locations, NACA 0012 airfoil, $Re_c = 1.25 \times 10^6$, $\alpha = 0^o$, $Tu = 0.1\%$, distributed roughness applied $x/c = 0.0314 - 0.0539$

this discrepancy can be traced back to the production term of the intermittency transport equation. The calibration of the F_{length} function that determines the length of the transitional region was performed using the results from the ERCOFTAC cases where transition occurred "naturally", and appears to inadequately represent roughness induced transition.

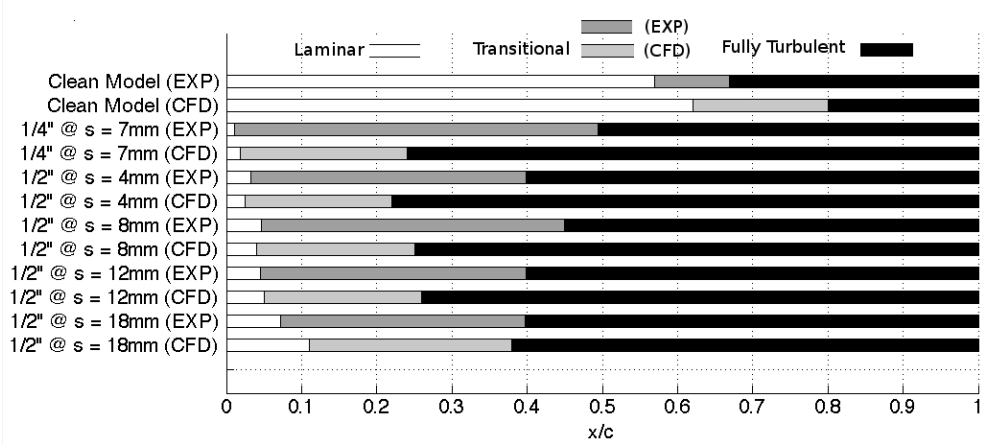

Figure 7.19. Comparison of boundary layer states for simulations run at $Re_c = 1.25 \times 10^6$, details of test configurations can be found in Table 7.1

Comparison to Texas A&M Results

NACA 63_3-418

Results from the roughness model are compared to the experimentally recorded values. The error bars shown for the NACA 63_3-418 experimental results correspond to the 25% and 75% spanwise turbulent locations which were described in Chapter 3. The onset of transition in the computational simulations once more based on the boundary layer shape factor. The first configuration examined was the roughness pattern with a height of $140\mu m$ ($k/c = 172 \times 10^{-6}$) at 15% distribution density. Some judgment must be used to determine how to convert the given parameters into an equivalent sand grain roughness height k_s. Once more, the input in simulations is actually the non-dimensional sand grain roughness height. As mentioned, it was initially assumed for the highest density cases, the k_s/c value input would simply be the non-dimensional roughness height (k/c). Cases run with this assumption were actually used to help calibrate the source term function that modifies the transition criteria.

When the decision was made to use the boundary condition function calibrated to the flat plate test cases, adjustments needed to be made to the parameter input for the airfoil cases. The input parameter was reduced until the transition results matched best with the experimental data. This was done by establishing a metric based on the error between the predicted and experimentally recorded transition location. For notation purposes, let $x_{t25},\ x_{t50},\ x_{t75}$ be the chordwise locations where 25%, 50% and 75% of the span is turbulent respectively, and x_{tc} be the location the roughness model predicts transition. For each case that both computational and experimental data is available for, the error function is defined:

$$E(k_s/c) = \begin{cases} 0, & x_{t25} \leq x_{tc} \leq x_{t75} \\ (x_{tc} - x_{t50})^2, & x_{tc} < x_{t25} \ \text{ or } \ x_{tc} > x_{t75} \end{cases} \tag{7.2}$$

The function is designed to equal zero if the predicted transition location falls in the region bounded by the 25% and 75% locations. If the predicted location falls outside this region, the distance to the 50% experimentally recorded location is squared. Squaring the distance to 50% location helps penalize the instances where the projections from the model are far off from the experimental results. The error for a given k_s/c input is then the sum of this function applied to each case, E_i:

$$J(k_s/c) = \sum E_i(k_s/c) \tag{7.3}$$

The k_s/c value that matched the $140\mu m$ ($k/c = 172 \times 10^{-6}$) at 15% density the best was 80×10^{-6}. Figures 7.20 through 7.22 demonstrate the models performance for these cases.

After settling on an input parameter that best matched one of the roughness configurations, the procedure was to use the assumed relation:

$$\frac{k_s}{k} = f(\Lambda_k) \tag{7.4}$$

to determine the density parameter $f(\Lambda_k)$. This could then be used to calculate the k_s inputs for the other roughness heights with the same distribution densities. Inserting $k_s/c = 80 \times 10^{-6}$ into Equation 7.4:

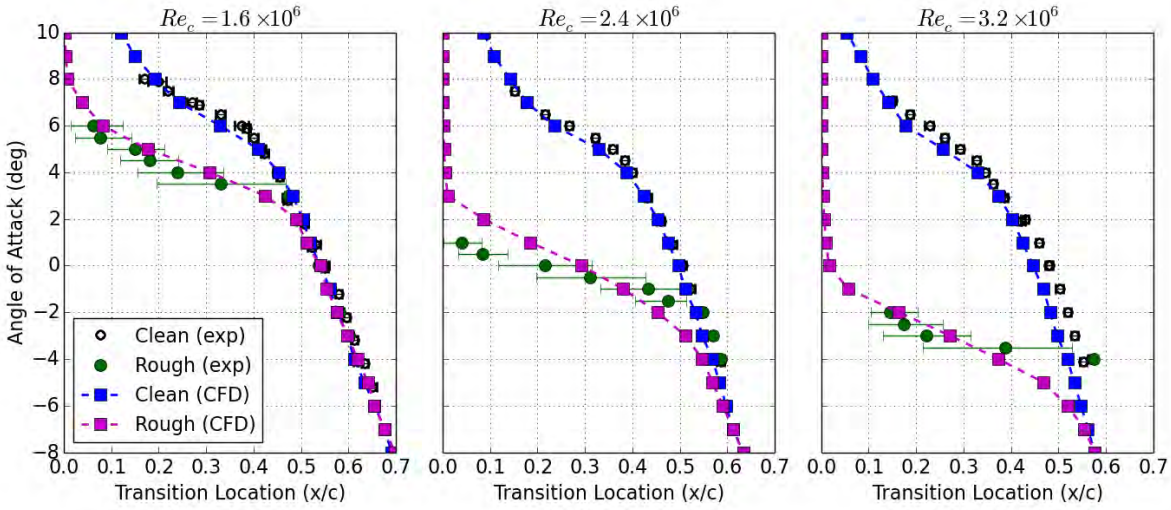

Figure 7.20. Comparison of upper surface transition location prediction with experimental results, NACA 63_3-418 airfoil, $k/c = 172 \times 10^{-6}$ roughness applied from $x/c = -0.13 : 0.02$, distribution density 15%, $k_s/c = 80 \times 10^{-6}$ input into roughness model.

$$\frac{k_s}{k} = \frac{k_s/c}{k/c} = \frac{80 \times 10^{-6}}{172 \times 10^{-6}} = 0.47 \approx f(\Lambda_k) \tag{7.5}$$

results in a density parameter of 0.47. This will be used to compute the input parameter for other roughness heights that use the same density configuration.

Table 7.2. Summary of input parameter k_s compared to physical parameters of roughness configurations for NACA 63_3-418 airfoil

$k(\mu\text{m})$	k/c $(\times 10^{-6})$	Density	$f(\Lambda_k)$	k_s/c $(\times 10^{-6})$
140	172	15%	0.47	80
100	123	15%	0.47	57
140	172	9%	0.44	75
140	172	3%	0.41	70
200	246	3%	0.41	101

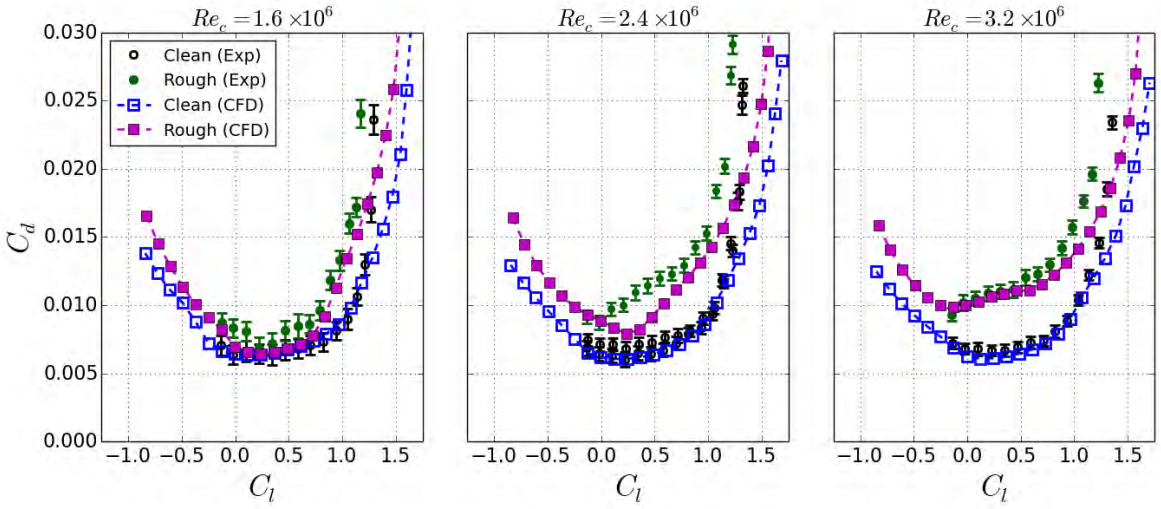

Figure 7.21. Predicted drag polars compared to experimental results, NACA 63_3-418 airfoil, $k/c = 172 \times 10^{-6}$ roughness applied from $x/c = -0.13 : 0.02$, distribution density 15%, $k_s/c = 80 \times 10^{-6}$ input into roughness model.

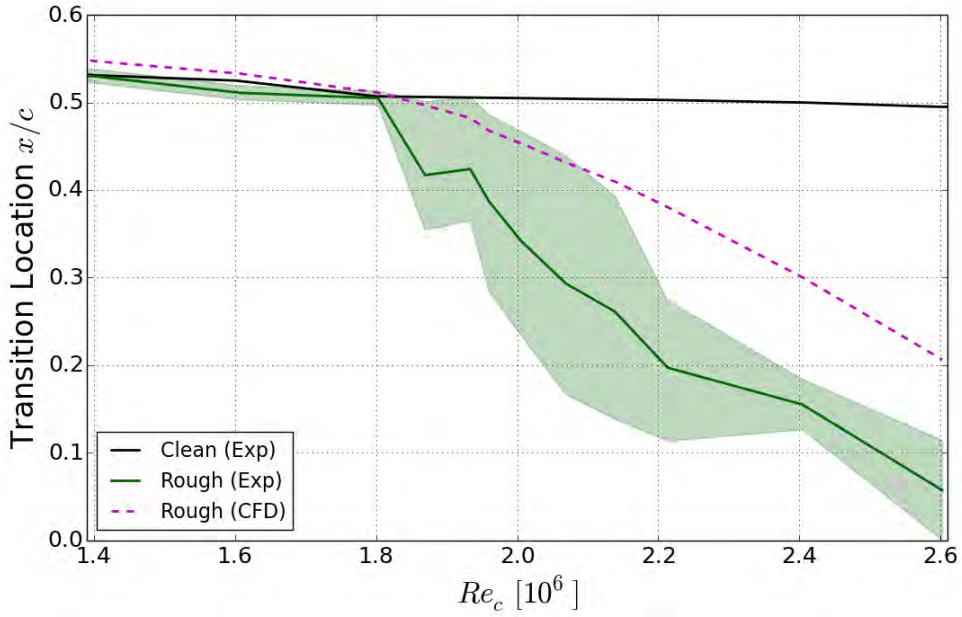

Figure 7.22. Comparison of upper surface transition location prediction, angle of attack fixed at 0 degrees, Re_c varied by increasing freestream velocity. NACA 63_3-418 airfoil, $k/c = 172 \times 10^{-6}$ roughness applied from $x/c = -0.13 : 0.02$, distribution density 15%, shaded region corresponds to 25% and 75% spanwise turbulent locations, $k_s/c = 80 \times 10^{-6}$ input into roughness model.

The results of the roughness model applied to the NACA 63_3-418 cases demonstrates good agreement with the experimental results at the $k/c = 172 \times 10^{-6}$ roughness height. There does appear to be an under prediction of drag at a Reynolds number of 2.4×10^6, but the shift in transition location tracks well with the experimental data. Figure 7.22 demonstrates how the shift in transition location changes with Reynolds number. For this particular roughness configuration, the model tends to under-predict the change in transition location at higher Reynolds numbers.

Moving onto the cases with the roughness height of $k/c = 123 \times 10^{-6}$ at 15% distribution density, the density parameter, $f(\Lambda_k) \approx 0.47$, determined previously was used to generate the k_s/c input parameter used for the roughness model. Keeping everything in non-dimensional terms, the relationship between the input parameter and the physical height becomes $k_s/c = f(\Lambda_k) \cdot (k/c)$. Inserting the values into this expression leads to an input parameter of 57×10^{-6}. Figures 7.23 - 7.25 show the results of the model with this input parameter compared to the associated experimental results.

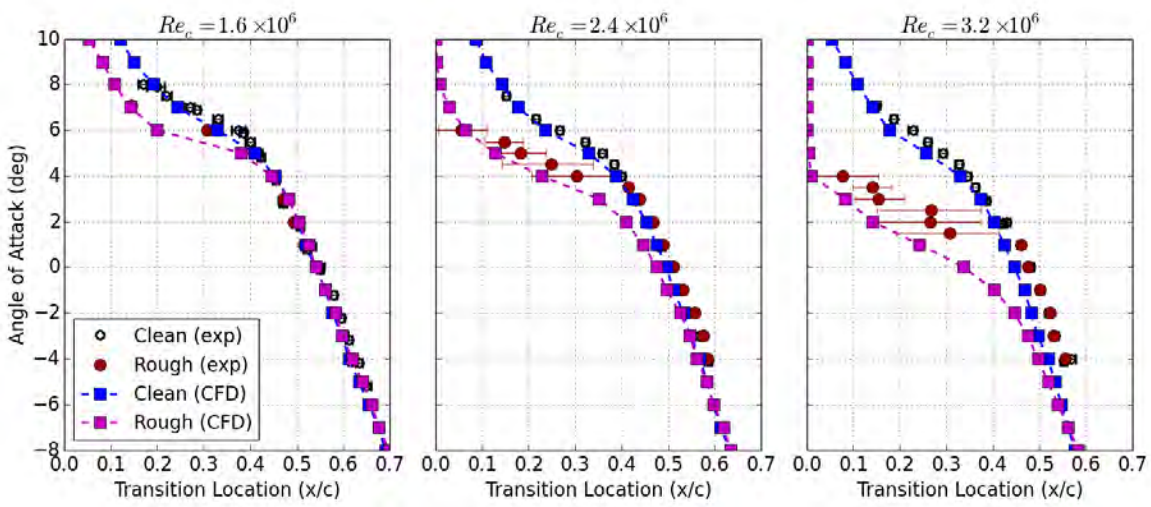

Figure 7.23. Comparison of upper surface transition location prediction with experimental results, angle of attack fixed at 0 degrees, Re_c varied by increasing freestream velocity. NACA 63_3-418 airfoil, $k/c = 123 \times 10^{-6}$ roughness applied from $x/c = -0.13 : 0.02$, distribution density 15%, $k_s/c = 57 \times 10^{-6}$ input into roughness model.

The results demonstrate favorable agreement with the predicted transition location for the cases at a Reynolds number of 1.6 and 2.4 million. There is some discrepancy at the highest Reynolds number shown where the model tends to predict transition too early. This can also be seen in Figure 7.25, where there is a slight but consistent premature prediction of transition on the chord. This trend is the opposite of what is seen as the Reynolds number is increased for the cases with higher roughness heights at the same distribution density (Figure 7.22). This demonstrates some of the complications involved in trying to create a universally valid roughness model, where applying corrections to fix disagreement in one case can cause further discrepancies in others.

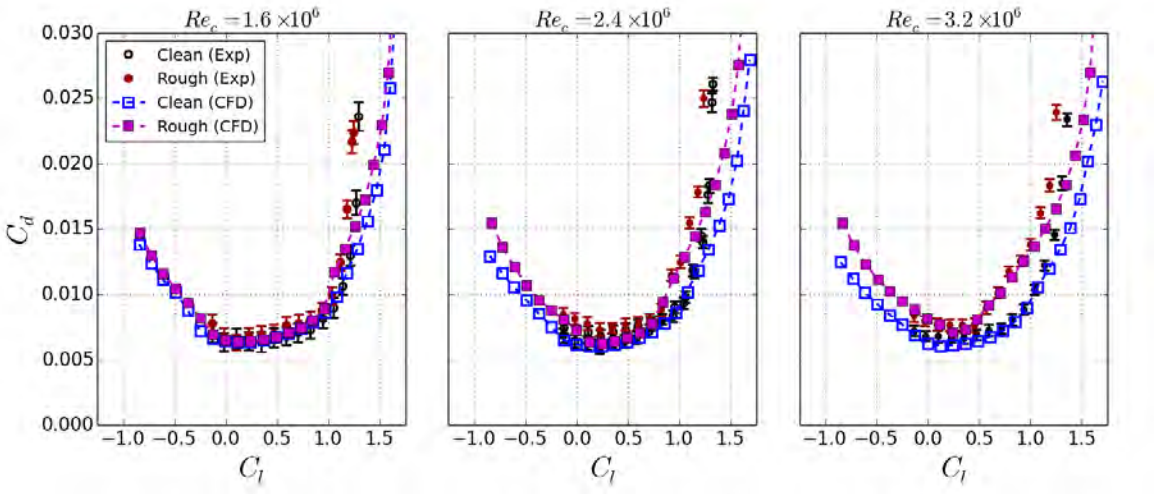

Figure 7.24. Predicted drag polars compared to experimental results, NACA 63_3-418 airfoil, $k/c = 123 \times 10^{-6}$ roughness applied from $x/c = -0.13 : 0.02$, distribution density 15%, $k_s/c = 57 \times 10^{-6}$ input into roughness model.

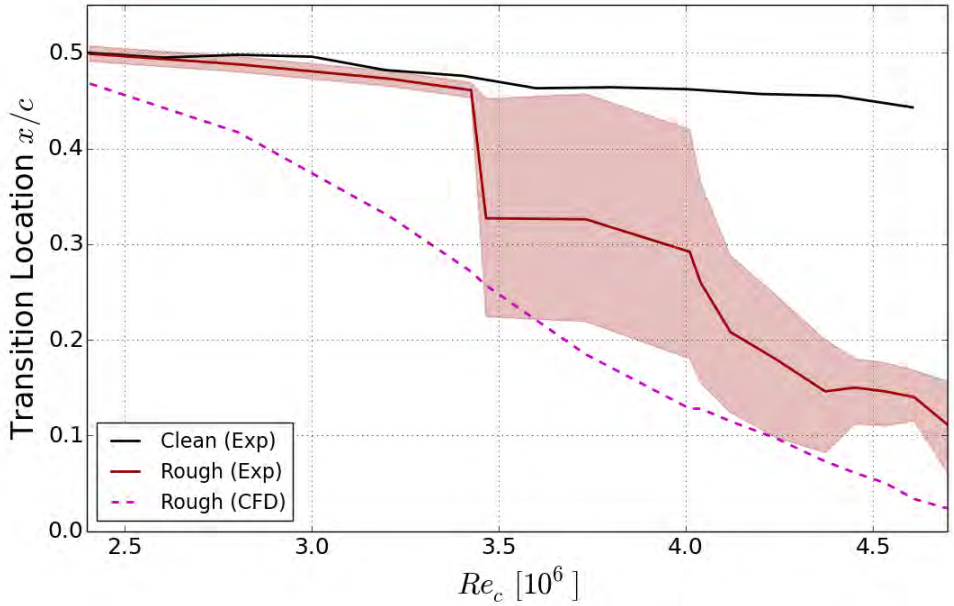

Figure 7.25. Comparison of upper surface transition location prediction with experimental results, NACA 63_3-418 airfoil, $k/c = 123 \times 10^{-6}$ roughness applied from $x/c = -0.13 : 0.02$, distribution density 15%, $k_s/c = 57 \times 10^{-6}$ input into roughness model.

To account for changes in distribution density, the input parameter was once more reduced until the predicted results matched best with the experimental data. Although this is not exactly ideal, a key point to recognize is that the same k_s/c value is input into the model across all Reynolds numbers and angles of attack. The importance lies not in the exact value of this parameter, but that a single scalar can represent the effects of the roughness pattern on the airfoils performance under the the entire range of flow conditions. Figures 7.26 and 7.27 show the behavior of the model compared against the experimental results for the $k/c = 172 \times 10^{-6}$ height at 9% distribution density cases with $k_s/c = 75 \times 10^{-6}$ as the input parameter.

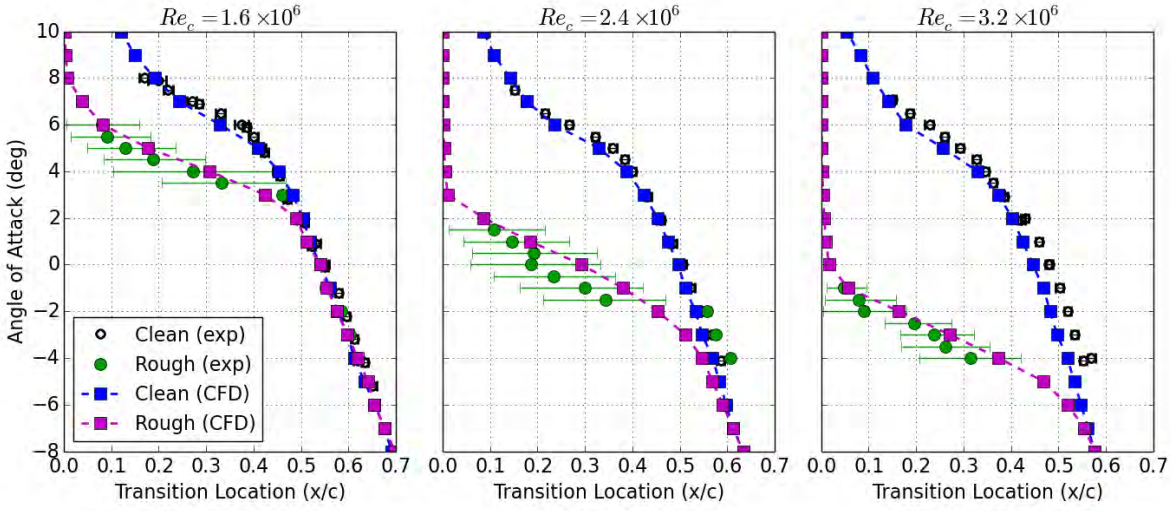

Figure 7.26. Comparison of upper surface transition location prediction with experimental results, NACA 63_3-418 airfoil, $k/c = 172 \times 10^{-6}$ roughness applied from $x/c = -0.13 : 0.02$, distribution density 9%, $k_s/c = 75 \times 10^{-6}$ input into roughness model.

The predicted transition locations match very well with the experimental data across all Reynolds numbers for this roughness configuration. A similar under prediction of drag to the 15% density pattern at this height occurs at $Re_c = 2.4 \times 10^6$, but for the most part, the drag predictions align well with the experimental results. Figures 7.28 and 7.29 show the results of the model compared against the experimental results for the $k/c = 172 \times 10^{-6}$ height at 3% distribution density cases with $k_s/c = 70 \times 10^{-6}$ as the input parameter.

Once more, both the predicted transition locations and the drag polars for these cases show good agreement with the experimental results. Despite the fact this parameter is selected by determining what input produces the best output, the results still have significance. Work does need to be done to provide a more clear way to convert a particular roughness distribution to an equivalent sand grain roughness height. This unfortunately is beyond the scope of the current work, and although it has received a fair amount of attention in the literature, little consensus has been reached on the process. From the present perspective, it is the self consistency of the results for each particular distribution that should be considered. The input is only changed when the roughness configuration is changed, and for a given input the results match well with what was experimentally recorded.

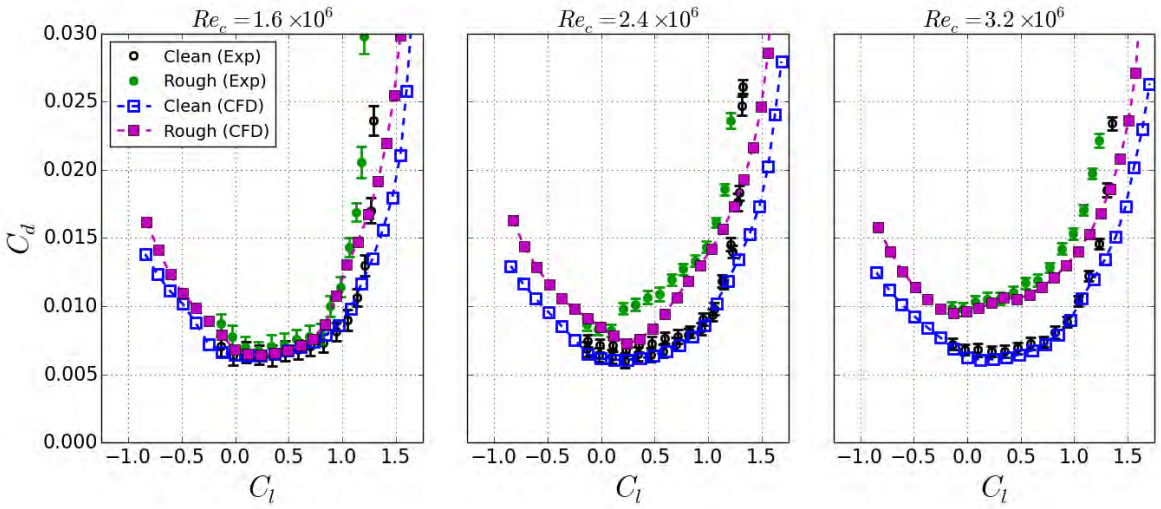

Figure 7.27. Predicted drag polars compared to experimental results, NACA 63_3-418 airfoil, $k/c = 172 \times 10^{-6}$ roughness applied from $x/c = -0.13 : 0.02$, distribution density 9%, $k_s/c = 75 \times 10^{-6}$ input into roughness model.

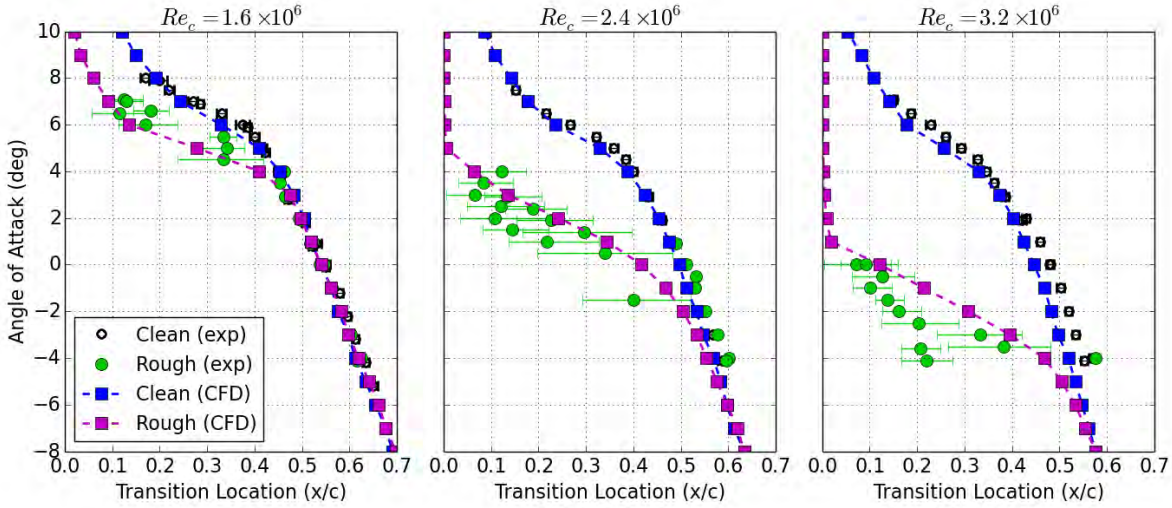

Figure 7.28. Comparison of upper surface transition location prediction with experimental results, NACA 63_3-418 airfoil, $k/c = 172 \times 10^{-6}$ roughness applied from $x/c = -0.13 : 0.02$, distribution density 3%, $k_s/c = 70 \times 10^{-6}$ input into roughness model.

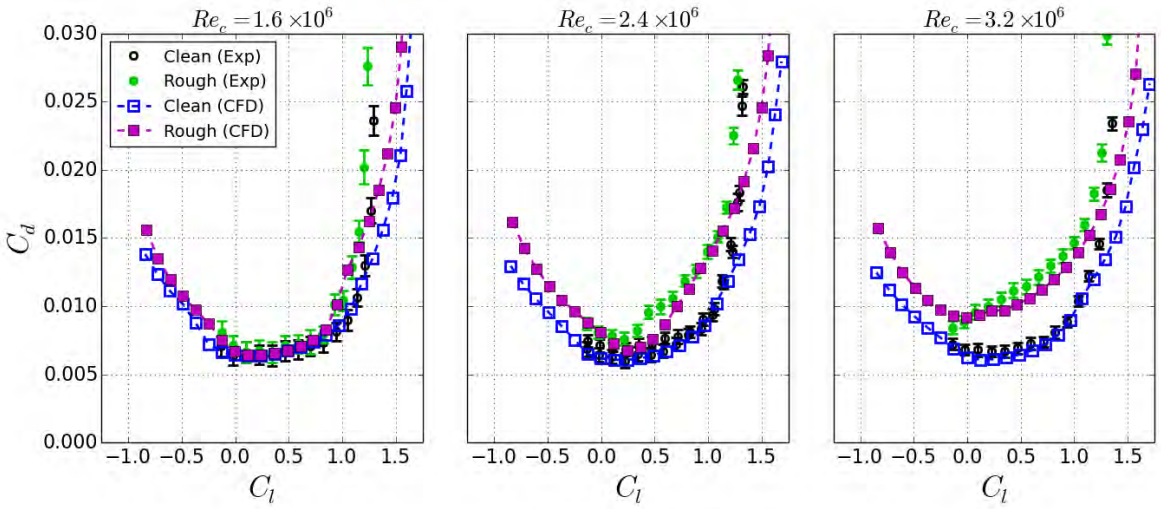

Figure 7.29. Predicted drag polars compared to experimental results, NACA 63_3-418 airfoil, $k/c = 172 \times 10^{-6}$ roughness applied from $x/c = -0.13 : 0.02$, distribution density 3%, $k_s/c = 70 \times 10^{-6}$ input into roughness model.

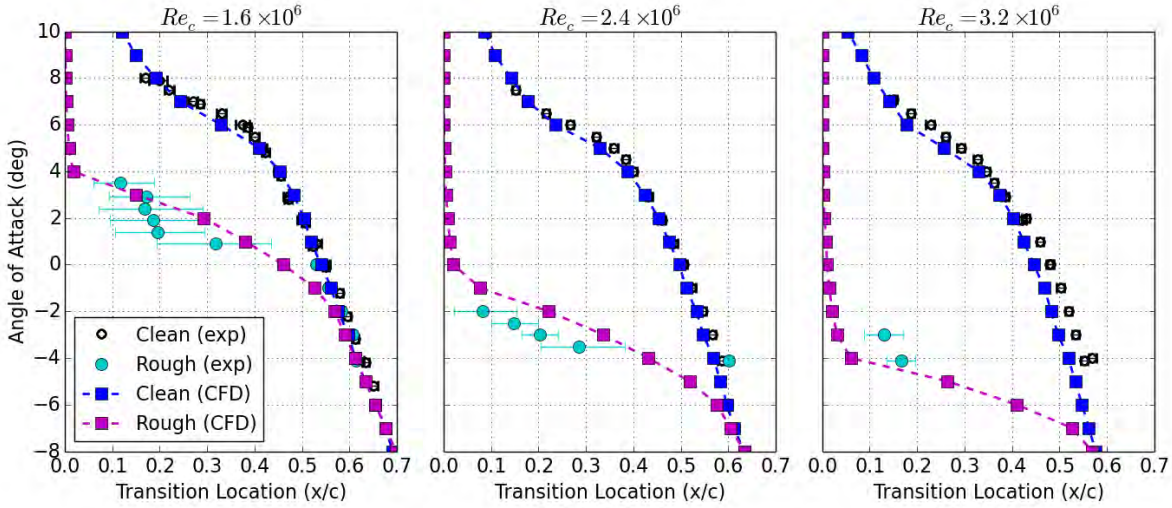

Figure 7.30. Comparison of upper surface transition location prediction with experimental results, NACA 63_3-418 airfoil, $k/c = 246 \times 10^{-6}$ roughness applied from $x/c = -0.13 : 0.02$, distribution density 3%, $k_s/c = 101 \times 10^{-6}$ input into roughness model.

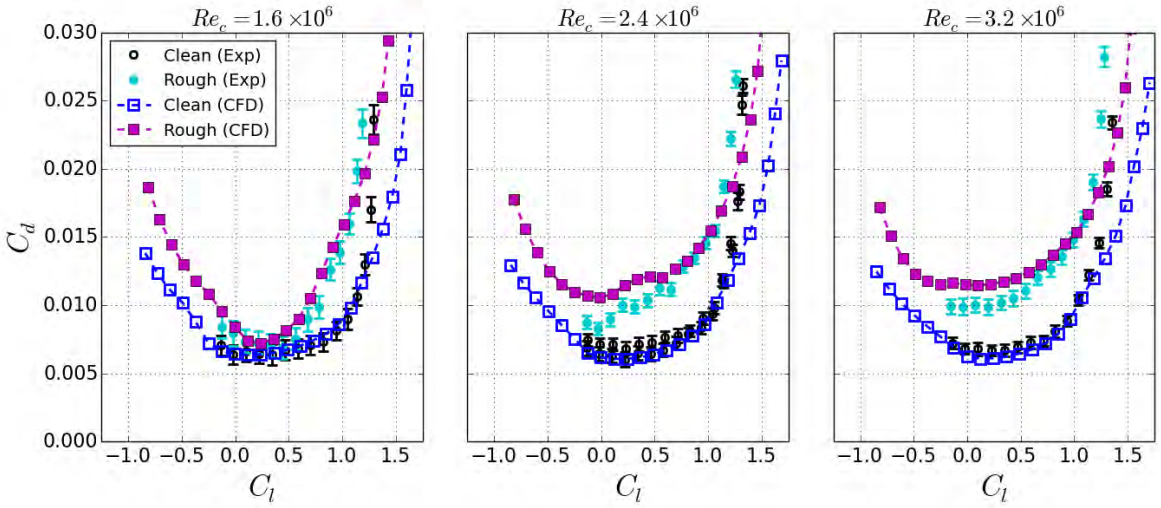

Figure 7.31. Predicted drag polars compared to experimental results, NACA 63_3-418 airfoil, $k/c = 246 \times 10^{-6}$ roughness applied from $x/c = -0.13 : 0.02$, distribution density 3%, $k_s/c = 101 \times 10^{-6}$ input into roughness model.

S814 Airfoil

The S814 airfoil tests used a different roughness pattern than the NACA 63_3-418 so more considerations needed to be made regarding the input parameter. In addition to subtle changes in the height of the material used to generate the roughness, the patterns themselves were different. For the S814, the shape of all the elements was held constant so only circles were used. This effectively increases the average height to diameter ratio of the roughness pattern by removing the wider elliptical shapes. Beginning once again with the intermediate roughness height, the input parameter that matched the $k/c = 154 \times 10^{-6}$ at 3% distribution density best was $k_s/c = 80 \times 10^{-6}$. The results of the roughness model applied to the S814 with this roughness pattern are shown in Figures 7.32 and 7.33.

The transition locations were recorded slightly differently and are therefore presented accordingly. The S814 airfoil behaved more "critically" under the influence of roughness, meaning the movement of transition location towards the leading edge occurred rapidly after a certain angle of attack. This is indicated in the figures with a data point at $x/c = 0$ representing the angle where the transition location was at the edge of the roughness itself. The model has trouble predicting this abrupt shift, but does correctly identify the angle where transition would occur immediately. The drag polars match up very well with the experimental results despite the upper (suction) surface transition location being predicted too far forward for some of the cases. The reason the drag prediction remains accurate despite some discrepancies in the transition location, is that the model predicts the lower (pressure) surface transition location too far aft. The errors in transition location prediction effectively cancel each other out in the drag measurement, with more turbulent kinetic energy than is physically present being produced on the upper surface and less on the lower. As more of the airfoil surface is covered with a turbulent boundary layer, both viscous and pressure drag rise. A correction for this deficiency is under active investigation.

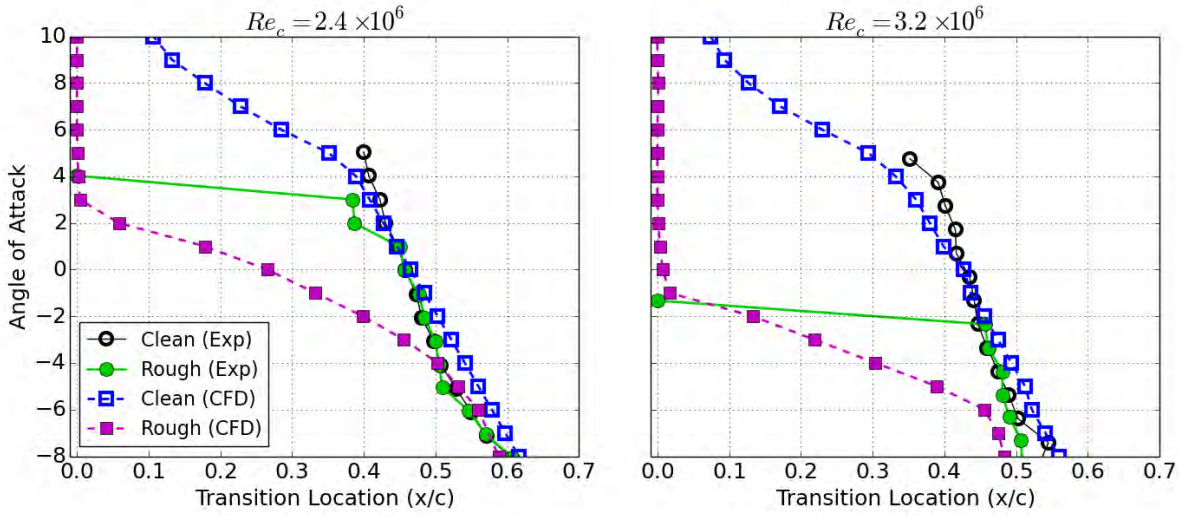

Figure 7.32. Comparison of upper surface transition location prediction with experimental results, S814 airfoil, $k/c = 154 \times 10^{-6}$ roughness applied from $x/c = -0.14 : 0.025$, distribution density 3%, $k_s/c = 80 \times 10^{-6}$ input into roughness model.

The next roughness height tested was $k/c = 117 \times 10^{-6}$ also at 3% distribution density. Inserting the k_s/c input and roughness height k/c from the $k/c = 154 \times 10^{-6}$ experimental cases into Equation 7.4 yields approximately 0.52 as the density function $f(\Lambda_k)$. Using this parameter to compute the input for the lower roughness height gives a k_s/c value of 60×10^{-6}. The results of the simulations with this input compared to the experimental results are shown in Figures 7.23 and 7.24. The change in the transition location again exhibits a more gradual movement than what is observed experimentally. However, it captures the angle of attack where transition occurs at the location of the roughness.

Table 7.3. Summary of input parameter k_s compared to physical parameters of roughness configurations for NACA *S*814 airfoil

$k(\mu$ m)	k/c ($\times 10^{-6}$)	Density	$f(\Lambda_k)$	k_s/c ($\times 10^{-6}$)
125	154	3%	0.52	80
95	117	3%	0.52	60
225	276	3%	0.52	141

The drag polars also show good agreement with the experimental results, and the model is even able to pick up the stalling at very low angles of attack. There are still some discrepancies at high C_l values, but these are caused by the turbulence models inability to predict separation on the suction surface. The fact the drag polars match so well with the input determined by multiplying the physical height parameter with the derived density function $f(\Lambda_k)$ further upholds the assumption $k_s/k = f(\Lambda_k)$. This trend also holds true with the results of the highest roughness height tested ($k_s/c = 101 \times 10^{-6}$) applied to the roughness model. On the whole, the results for both the NACA 63_3-418 and the S814 are in good agreement with the experimental data from Texas A&M.

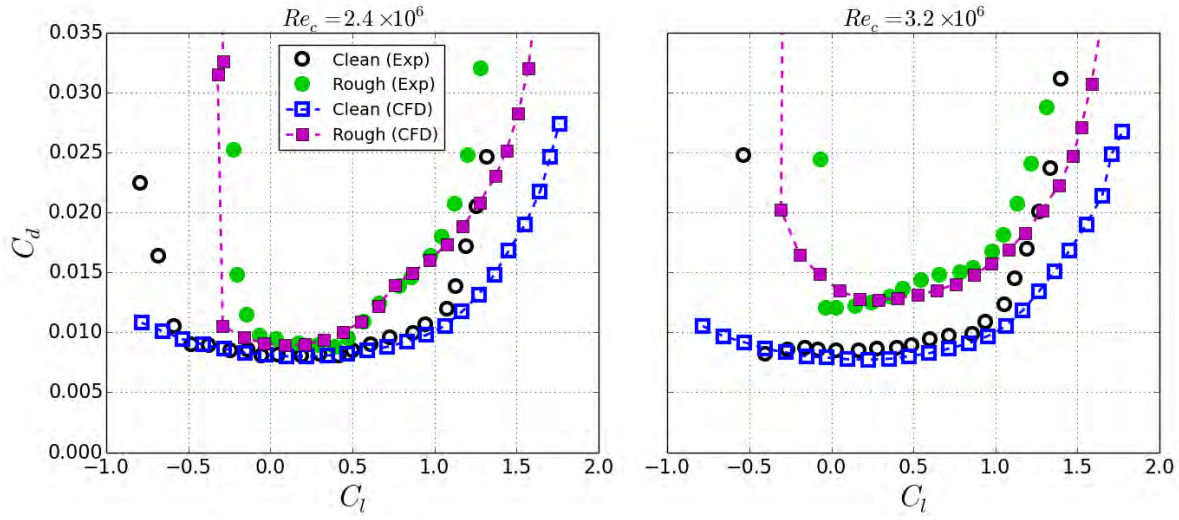

Figure 7.33. Predicted drag polars compared to experimental results, S814 airfoil, $k/c = 154 \times 10^{-6}$ roughness applied from $x/c = -0.14 : 0.025$, distribution density 3%, $k_s/c = 80 \times 10^{-6}$ input into roughness model.

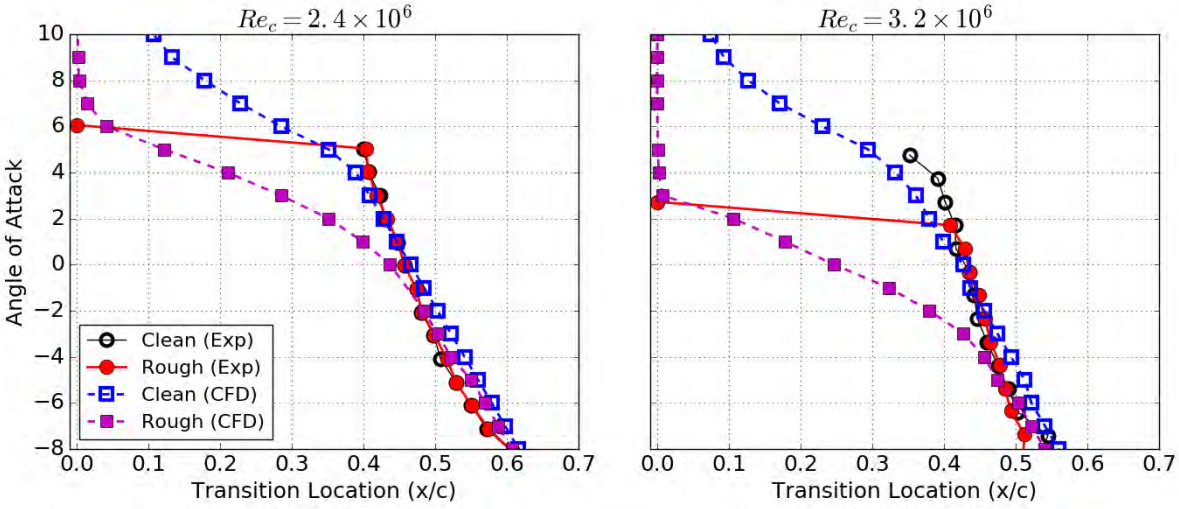

Figure 7.34. Comparison of upper surface transition location prediction with experimental results, S814 airfoil, $k/c = 117 \times 10^{-6}$ roughness applied from $x/c = -0.14 : 0.025$, distribution density 3%, $k_s/c = 60 \times 10^{-6}$ input into roughness model.

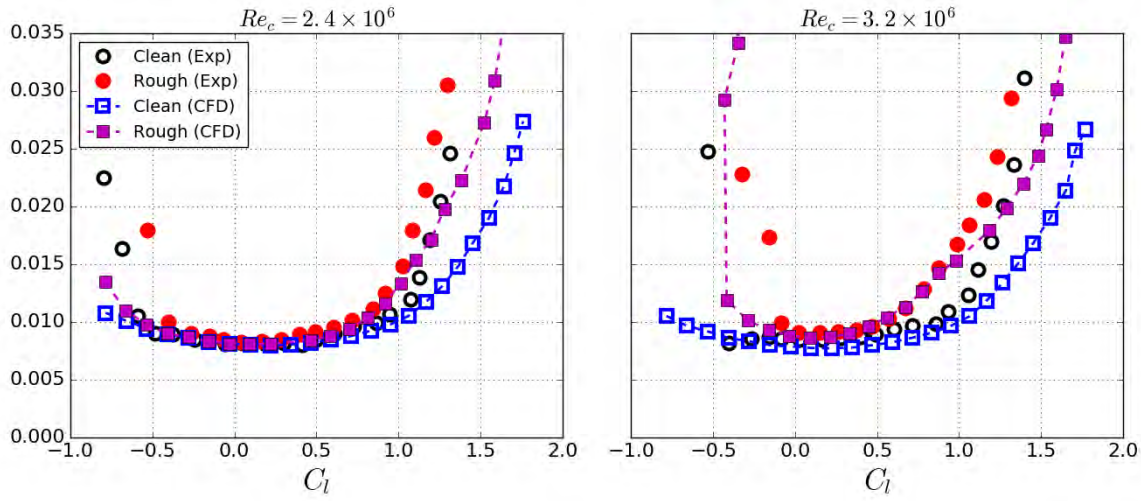

Figure 7.35. Predicted drag polars compared to experimental results, S814 airfoil, $k/c = 117 \times 10^{-6}$ roughness applied from $x/c = -0.14$: 0.025, distribution density 3%, $k_s/c = 60 \times 10^{-6}$ input into roughness model.

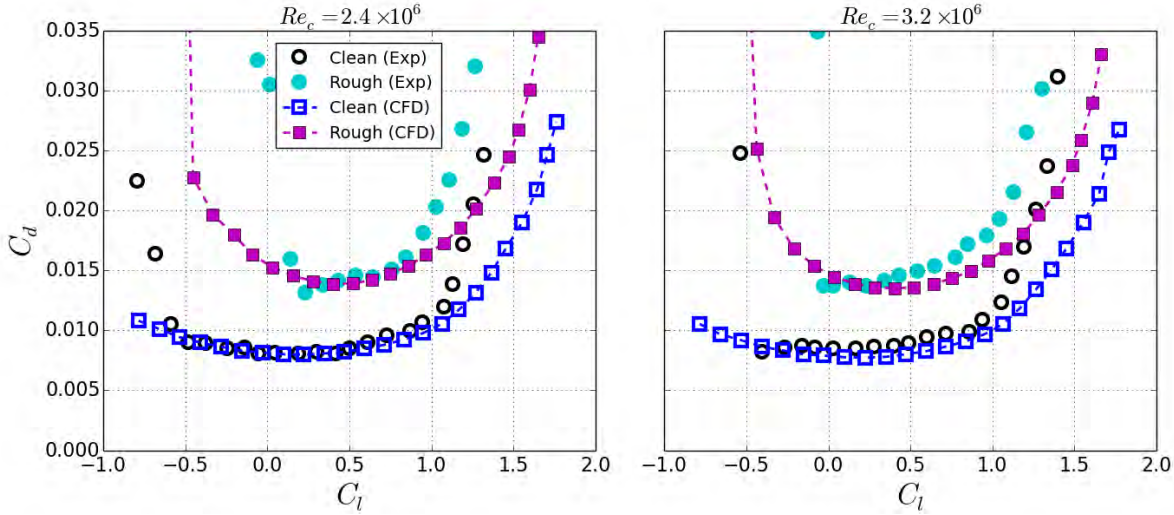

Figure 7.36. Predicted drag polars compared to experimental results, S814 airfoil, $k/c = 276 \times 10^{-6}$ roughness applied from $x/c = -0.14$: 0.025, distribution density 3%, $k_s/c = 141 \times 10^{-6}$ input into roughness model.

Chapter 8

Conclusions

An extensive study has been conducted to better understand the impact of surface roughness on boundary layer transition and other airfoil aerodynamic characteristics. The motivation behind the effort was to help quantify the effect of leading edge erosion on wind turbine performance, and develop tools to predict these effects. Close collaboration between the experimental and computational teams helped optimize the configurations tested for calibrating the roughness model with the data generated. Additionally, the collaboration helped identify cases that would be of interest to investigate more thoroughly. Through this effort, a vast amount of experimental data has been generated and a high fidelity roughness model developed to predict surface roughness effects on boundary layer transition. This work has focused on the development of the surface roughness model which has been implemented in a RANS solver.

The experimental work focused on observing the impact of leading edge roughness on boundary layer transition and aerodynamic properties of two different airfoils. The airfoils tested were an 18% thick NACA 63_3-418 and a 24% thick S814 representative of an outboard and midspan section of a wind turbine blade respectively. Distributed roughness was simulated by cutting patterns out of vinyl decals and applying to the leading edge of the airfoils. The extent of the roughness along the chord was determined by looking at the region with the highest probability for accumulation using the ice accretion code LEWICE. The distribution density tested was determined by examining in-field measurements of blades with some level of leading edge contamination. The height of the roughness elements was controlled by using vinyl of various thicknesses. Boundary layer profiles along the leading edge of the airfoils were analyzed to determine the heights of roughness that would produce Re_k values roughly in the sub-critical range previous experiments have noted.

Experimental results from both airfoils tested produced intuitive results with regard to the impact of roughness height. With an increase in roughness height, the transition location moved forward along the chord and drag subsequently increased for all Reynolds numbers. The effect of distribution density was harder to quantify exactly, but there was a general trend with increasing density moving the transition location forward and increasing drag. The author cautions against extrapolating this behavior as it has been noted that increasing density beyond a certain level will actually decrease the impact a roughness distribution has on the flow. The range of distribution densities tested in this study was not wide enough to experience this phenomenon. Regardless, the number of different roughness configurations tested was sufficiently high to generate useful roughness correlations.

From a practical perspective, the aerodynamic coefficients are of greater interest than transition location. However, to accurately capture these values outside of the configurations tested, the fundamental cause of the increase in drag needed to be modeled. The challenges associated with modeling transition are numerous due to the physical complexity of the problem and high sensitivity of the process to external conditions. A number of methods for transition prediction have been outlined and comparisons between them have been made. The class of transition prediction methods that are 3-D and parallel compatible have been selected

as the best candidates for implementing a generalized model that predicts the influence of roughness on boundary layer transition.

The methodology introduced to account for the effects of roughness on transition extends a recently developed correlation based transition model by adding an additional scalar field quantity to account for roughness. The quantity is used to modify the transition onset criteria in the transition model and empirically calibrated using the data from the experiments presented. A large portion of the current work was dedicated to exploring the use of correlation based transition models, as this is the platform on which the roughness model is built. Many of these models have not been tested at high Reynolds numbers so attention was directed at examining cases in this flow regime. A number of sensitivities of local correlation transition models were demonstrated and resolutions discussed to help further the proper use of these models. These include the strong dependence on user determined parameters such as freestream turbulence intensity, computational grid quality, and turbulence model settings.

The basic concept of adding an additional transport equation to account for surface roughness was initially proposed by Dassler, Kozulovic, and Fiala in 2010. The fundamental idea remains the same, but the functions that interact with the transition model have been reformulated. Many of the calibration steps have been explicitly outlined, both in an attempt to be transparent about the process and so to help motivate similar efforts on problems related to complex empirically driven correlations. Results from the initial experimental study on the NACA 63_3-418 were used to calibrate the reformulated roughness model. The was applied to a number of different roughness distribution, that varied in both roughness element hight and distribution density. For all the roughness distributions tested, the model was able to simulate the change in transition location at a variety of Reynolds numbers and angles of attack. A particularly noteworthy result is the ability to both identify a critical angle of attack or Reynolds number where transition will occur at the roughness itself, and the model can also accurately represent the shift in transition location forward for sub-critical heights.

A validation study of the roughness model was performed on the data generated from the tests with the S814 airfoil. The airfoil provided a number of challenges as the experimentally recorded transition behavior is difficult to model accurately. The transition location was observed to move rapidly forward at a particular angle of attack. The model had some difficulty representing the abrupt shift in transition location, and in essence, smoothed out the movement of forward. Nonetheless, the drag polars still matched very well with the the experimental results in the intermediate angle of attack range. At high positive angles of attack the predictions began to deviate, however, this problem can be traced back the underlying turbulence model and not the roughness model itself. Additionally, the roughness model was able to capture the premature stall seen at negative angles of attack.

A portion of the work discussed roughness characterization and the associated challenges. Unfortunately, a universal resolution does not appear possible at the present, so a set of assumptions were made. From the perspective of the current model, the question of interest is whether or not it is possible to map a roughness pattern to some scalar value. The value itself must be determined in an ad hoc manner, but the significance lies in the models ability to represent the effects of that particular distribution across a wide range of flow conditions using only a scalar input. Also, even if the exact input value of a roughness distribution is unknown, the model can still provided insight on an airfoils relative sensitivities to roughness. This could mean applying the same input to multiple airfoils and identifying the ones that are impacted most/least. Even though the input would represent an unknown roughness distribution, varying this value will represent varying the severity of roughness.

Despite all of the work conducted, a number of questions remain, and like many scientific studies more

questions have been generated. From the authors perspective, specific areas that could use additional investigation are as follows.

- The formal characterization of roughness patterns into an equivalent sand grain roughness.
- The absolute value of the boundary condition function in the roughness model. The decision to use the flat plate calibrated function was done based on the assumption these results represented a "true" equivalent sand grain roughness height. In some ways this is more about picking a set of results and using that as the definition, but it would be desirable to have a set of results calibrated to a carefully described roughness parameter.
- A more statistical approach to defining the transition location. The model itself provides a singular transition location, but in reality there is temporal and spanwise variation in this value.
- More validation of the model with experimental results. This will likely always hold true as by definition this model relies on experimental data for accuracy.

Appendix A

Low Order Method

The roughness model proposed throughout the current work has been shown to accurately predict transition behavior for a variety of roughness configurations. Despite this, there are several noteworthy drawbacks to the methodology. What stands out in particular, is the fact a full RANS simulation with five turbulence equations is needed for the model. It is easy to see that in some practical applications, this would make the model prohibitively expensive computationally to use. Therefore, a similar methodology was sought out for use with a lower order panel method. The code used to explore a low order method was XFOIL due to its popularity in the aerospace community. Within XFOIL a number of boundary layer parameters can be computed, including the momentum thickness Reynolds number (Re_θ) and the skin friction coefficient (C_f) that can be used to computed a k_s^+ value.

The fundamental idea behind the roughness amplification is that the integrated effects of surface roughness can be correlated to a change in transition onset momentum thickness Reynolds number, $Re_{\theta t}$. To construct a relationship between the effects of a particular roughness distribution and the transition behavior associated with that configuration, the following parameters were used. The metric for change in transition location was chosen as the ratio of the "clean" $Re_{\theta t}$ value with the roughness impacted value, $Re_{\theta t,rough}$. The $Re_{\theta t,rough}$ parameter is determined by looking at value of Re_θ at the location transition occurred under the influence of a particular roughness configuration. The other value used in the correlation was the summation of a function of flow and roughness parameters available at the surface, F_k. The function was integrated over the region between the stagnation point and the end of the roughness distribution. Different functions F_k were considered while fixing transition location parameter $Re_{\theta t,rough}/Re_{\theta t}$.

The initial correlation function used was only dependent on the dimensionless roughness height k_s^+. This parameter is defined:

$$k_s^+ = \sqrt{\frac{\tau_w}{\rho}}\frac{k_s}{\nu} \tag{A.1}$$

To compute this quantity using values extracted from XFOIL, τ_w was determined using the skin friction coefficient C_f, defined:

$$C_f = \frac{\tau_w}{\frac{1}{2}\rho U_\infty^2} \tag{A.2}$$

with some algebra, and the assumption of a unit chord length:

$$k_s^+ = \sqrt{\frac{\tau_w}{\rho}}\frac{k_s}{\nu} = \sqrt{\frac{2\tau_w}{\rho U_\infty^2}}\frac{U_\infty k_s}{\nu\sqrt{2}} = \sqrt{\frac{C_f}{2}}Re_c k_s \tag{A.3}$$

The user does have to input a representative k_s value, but the remaining quantities are directly available from XFOIL.

The approximation $Re_k \approx (k_s^+)^2$ was used loosely in conjunction with the findings of White et al. that the roughness induced disturbance energy scaled with Re_k^2. The function used was:

$$F_k = (k_s^+)^4 \tag{A.4}$$

The correlated quantity was then the summation of this function over the region of the surface impacted by roughness. There was an additional multiplier by the chord Reynolds number, as well as a fractional power applied to the integrated sum. These modifications were shown to produce a better data collapse. The correlated quantity I_k is then computed:

$$I_k = \left(\frac{Re_c^{0.5}}{c} \int_{sp}^{re} F_k \, ds \right)^{\frac{1}{4}} = \left(\frac{Re_c^{0.5}}{c} \int_{sp}^{re} (k_s^+)^4 \, ds \right)^{\frac{1}{4}} \tag{A.5}$$

The bounds of this integral are from the stagnation point (sp) to the edge of the roughness (re). The integral is normalized by chord length so that it remains non-dimensional.

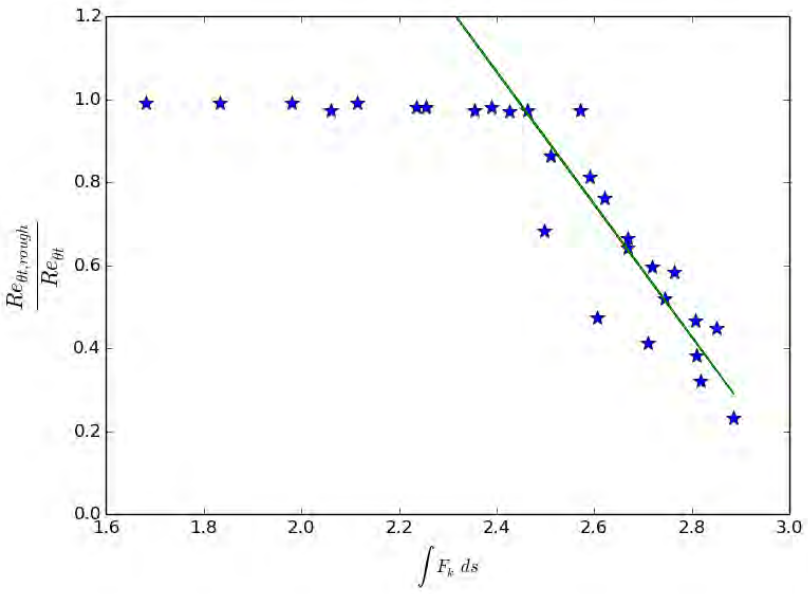

Figure A.1. Integrated roughness parameter, I_k, compared to the ratio $Re_{\theta t,rough}/Re_{\theta t}$, NACA 63_3-418 airfoil, $k/c = 172 \times 10^{-6}$ roughness applied from $x/c = -0.13 : 0.02$, distribution density 15%, $k_s/c = 80 \times 10^{-6}$ used in correlation calculations for consistency with roughness amplification model.

Figure A.1 shows a comparison of this integrated parameter to the ratio $Re_{\theta t,rough}/Re_{\theta t}$ for the NACA 63_3-418 airfoil cases with a roughness height of 140 μm at a distribution density of 15%.

What can be observed is that below some threshold value, $I_{k,crit}$, the ratio is unity (1). This simply means the transition location does not change from the clean configuration for those cases. After reaching this threshold value, a linear line can be fit through the remaining points. In general, the interaction of surface roughness and the surrounding flow field is very much non-linear, however, the idea here is to capture the non-linearities in the F_k function.

To determine where the "threshold" value, $I_{k,crit}$, the points were binned, and then the average value in the bins was computed. Once this average dropped below 0.9, it was assumed this was the value the linear best fit line should start. If a bin did not contain any points, it was not considered. After constructing a best fit line beyond the threshold value, there is a relationship between the ratio $Re_{\theta t,rough}/Re_{\theta t}$ and the integrated roughness parameter I_k.

$$\frac{Re_{\theta t,rough}}{Re_{\theta t}} = f(I_k) \tag{A.6}$$

$$f(I_k) = \begin{cases} 1.0 & I_k < I_{k,crit} \\ C_{I1} I_k + C_{I2} & I_k \geq I_{k,crit} \end{cases} \tag{A.7}$$

Eq. A.6 and A.7 can be used to predict the transition location on an airfoil under the influence of surface roughness using only quantities available in XFOIL. The procedure for determining the roughness impacted transition location as well as the lift and drag is outlined in the following.

1.) Run XFOIL with viscous terms at the angle of attack, Reynolds number, Mach number, etc. desired.

2.) Pull boundary layer quantities from solution, and store such that at each chordwise location, there are associated values of the boundary layer parameters.

3.) Compute k^+ using C_f, Re_c, and some k value for that case.

4.) Construct F_k function and integrate from the stagnation point to the leading edge of the roughness on what-ever surface is being analysed. Finalize computation of I_k for that particular case.

5.) Insert value I_k into Eq. A.7, to determine $Re_{\theta t}$ ratio.

6.) Look at stored boundary layer quantities to determine clean $Re_{\theta t}$, then compute $Re_{\theta t,rough}$.

7.) Search in stored boundary layer quantities for $Re_{\theta t,rough}$ value and pull the associated x/c value. This is the roughness induced transition location.

8.) Repeat steps 4-7 for opposite surface if necessary.

9.) Run XFOIL again, with transition fixed on each surface at location computed. This provides an estimate of the lift and drag under the influence of roughness for this case.

A code framework was constructed in python to facilitate the steps outlined above. The entirety of which is available in an open source repository such that the reader can verify and explore the procedure themselves. One of the key ideas is to define a class instance for each XFOIL run, and store the boundary

layer properties as attributes of that class. This also allows derived quantities to be computed upon initialization of the instance to reduce computational costs if some sort of iterative method is used to try and find some optimal F_k. Finally a method is included in the class to compute the integral over a rough region. This helps simplify code to compute a sequence of these integrals, as each method can pre-compute the bounds of the integral for the instance it is operating on. That is, as the stagnation point will move for each angle of attack, quite a bit of logic would have to be introduced to a script if only the raw arrays were considered.

A.1 Results - NACA 63_3-418

Using the correlation function and procedure described in the previous section, the following results were obtained. The same k_s value that was input to the roughness amplification model for each roughness distribution was used to compute k_s^+ in the results shown.

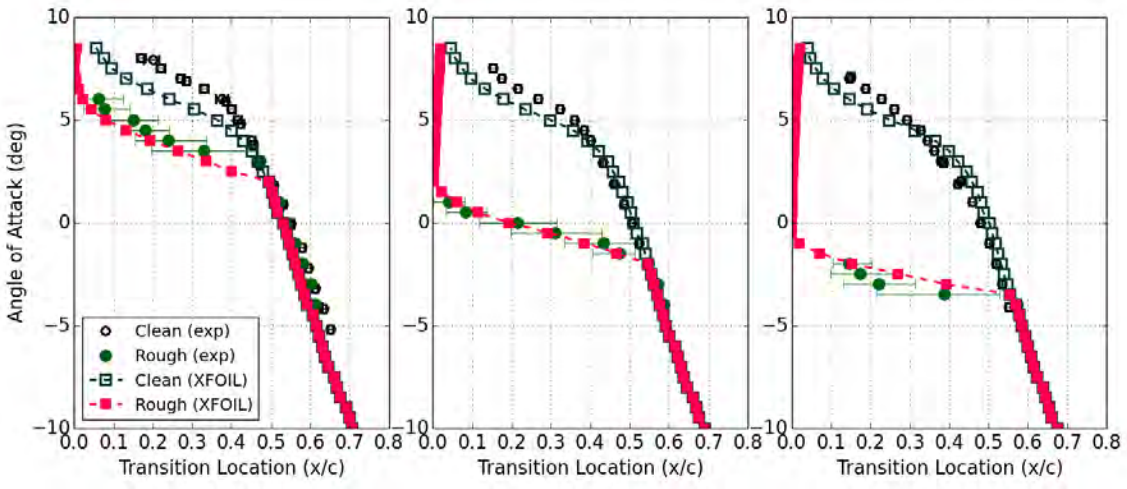

Figure A.2. Comparison of upper surface transition location prediction with experimental results, NACA 63_3-418 airfoil, $172 \times 10^{-6}\ k/c$ roughness applied from $x/c = -0.13 : 0.02$, distribution density 15%. $N_{crit} = 6$ used for free transition prediction in XFOIL, $k_s/c = 80 \times 10^{-6}$ used in correlation calculations.

As shown in Figure A.2, the predicted values of the upper surface location for the NACA 63_3-418 airfoil with $172 \times 10^{-6}\ k/c$ roughness are in excellent agreement with the experimental results. This is not terribly surprising as the correlation function was generated with these results. Figure A.3 demonstrates the results of applying the same function to the NACA 63_3-418 airfoil with $123 \times 10^{-6}\ k/c$ roughness.

For the $123 \times 10^{-6}\ k/c$ roughness cases, the method tends to predict the transition location too early on the chord at higher Reynolds numbers. The reason for this is not definitively clear, but there may be differences in the scaling of k_s^+ with roughness height, as opposed to with Reynolds number. The results support a hypothesis that an increase to the k_s^+ parameter due to an increase in chord Reynolds number will have less of an impact on transition behavior than an increase in the physical roughness height.

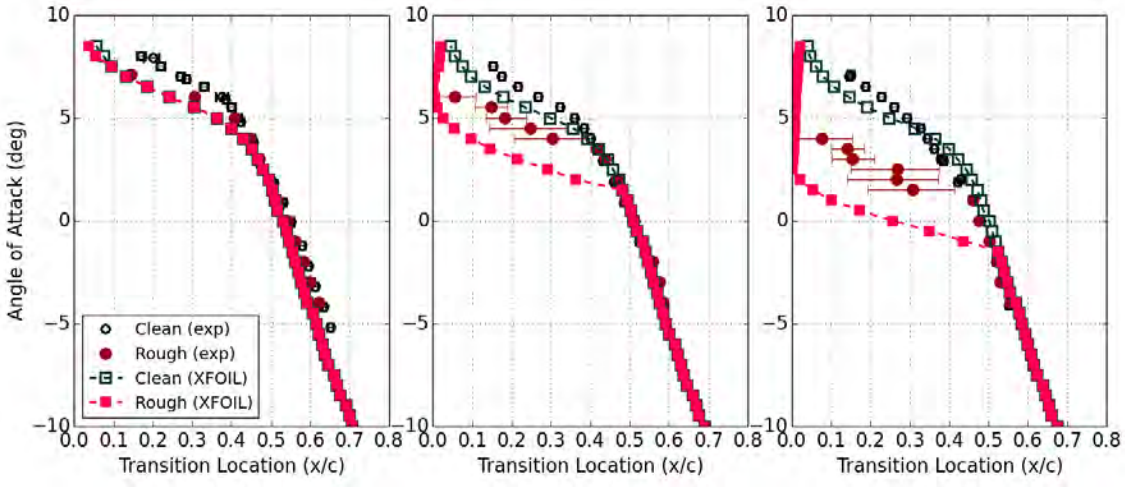

Figure A.3. Comparison of upper surface transition location prediction with experimental results, NACA 63_3-418 airfoil, $123 \times 10^{-6}\ k/c$ roughness applied from $x/c = -0.13 : 0.02$, distribution density 15%. $N_{crit} = 6$ used for free transition prediction in XFOIL, $k_s/c = 57 \times 10^{-6}$ used in correlation calculations.

Unfortunately, only the upper (suction) surface transition location was recorded in the experiment so there is no way to verify the predictions for the transition location on the lower (pressure) surface. Nonetheless, the method was used on the lower surface so a prediction of lift and drag could be made by fixing the transition locations. Figure A.4 shows the predicted drag polars for the NACA 63_3-418 airfoil with $172 \times 10^{-6}\ k/c$ roughness.

The lift and drag results are not as consistent as the transition prediction. At moderate lift coefficients, roughly between -0.5 and 0.5, the drag predictions are reasonably close to the experimental for all Reynolds numbers. However, for the two larger Reynolds numbers, the predictions at higher C_l values tend to underestimate drag. Some of the discrepancy can be traced back to the panel method itself, and the insufficiency to correctly predict drag at higher angles of attack.

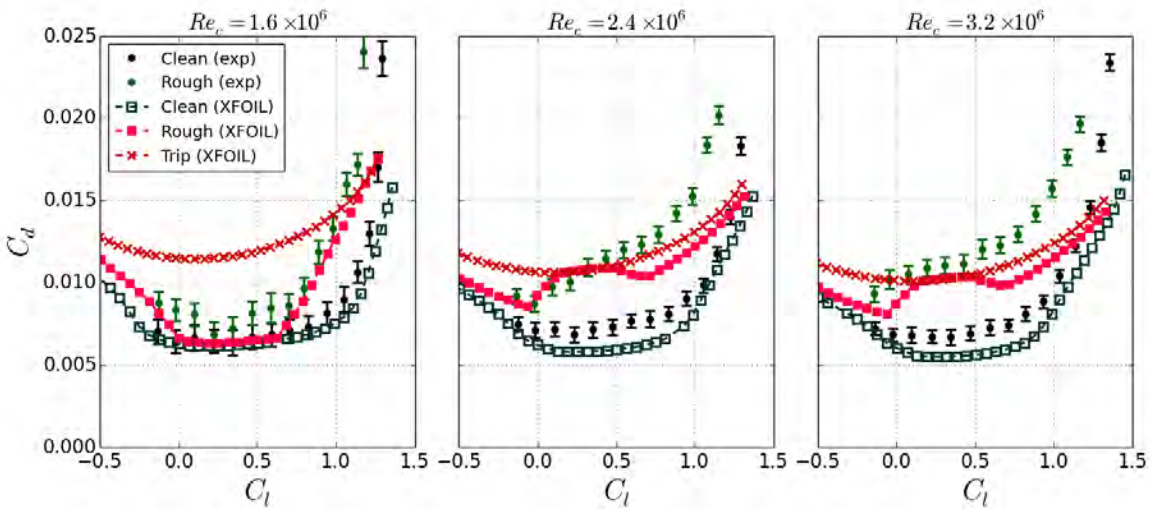

Figure A.4. Predicted drag polars compared to experimental results, NACA 63_3-418 airfoil, $k/c = 172 \times 10^{-6}$ roughness applied from $x/c = -0.13 : 0.02$, distribution density 15%. $N_{crit} = 6$ used for free transition prediction in XFOIL, $k_s/c = 80 \times 10^{-6}$ used in correlation calculations.

A.2 Results - S814

The predictions based on the procedure described generate favorable for the NACA 63_3-418 airfoil cases. A much more difficult test, however, would be to apply the same methodology to the S814 airfoil with the various roughness configurations. Figure A.5 shows the predicted transition locations for the S814 using the same correlation function as the NACA 63_3-418. Drag polars for the cases with the transition locational manually set are shown in Figure A.6.

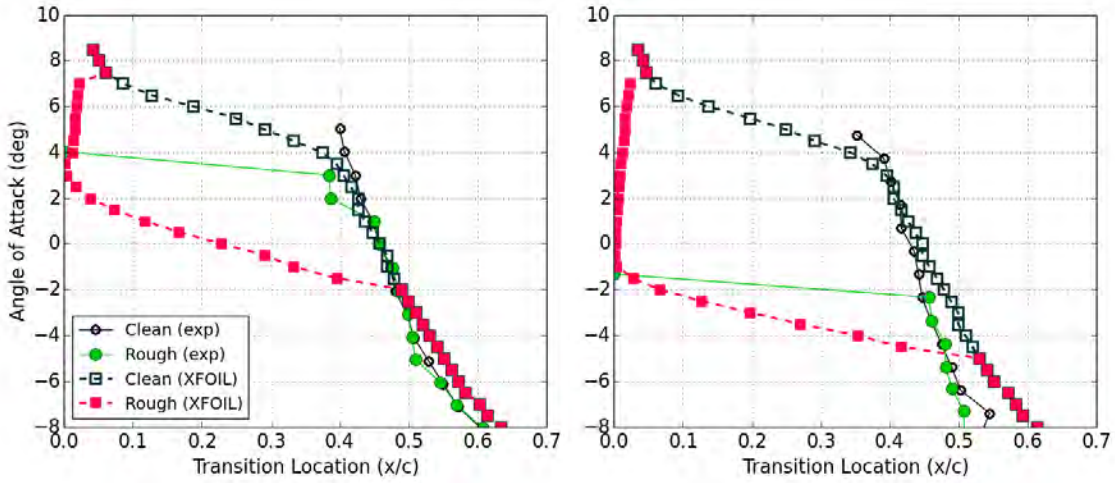

Figure A.5. Comparison of upper surface transition location prediction with experimental results, S814 airfoil, 172×10^{-6} k/c roughness applied from $x/c = -0.13 : 0.02$, distribution density 15%. $N_{crit} = 6$ used for free transition prediction in XFOIL, $k_s/c = 80 \times 10^{-6}$ used in correlation calculations.

The transition predictions for the S814 airfoil are not quite as accurate as the NACA 63_3-418, but considering the simplicity of the method, are certainly reasonable. The drag predictions follow a similar trend to the NACA 63_3-418 cases where the lift and drag is accurately captured at low to moderate angles of attack, but then begin to deviate substantially at higher C_l values. Some of this can again be attributed to XFOIL not fully capturing the flow behavior at higher angles of attack.

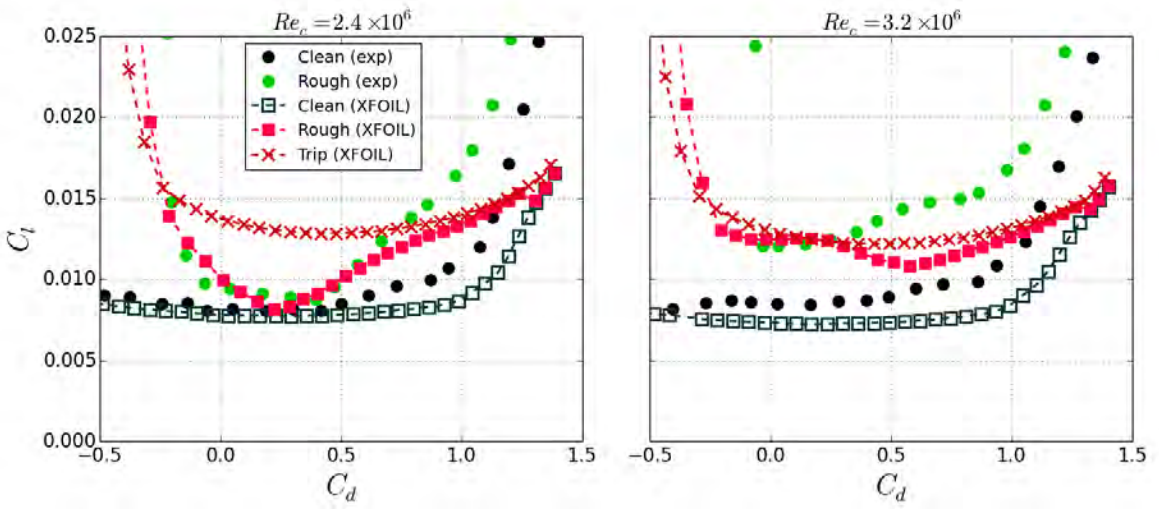

Figure A.6. Predicted drag polars compared to experimental results, S814 airfoil, 172×10^{-6} k/c roughness applied from $x/c = -0.13 : 0.02$, distribution density 15%. $N_{crit} = 6$ used for free transition prediction in XFOIL, $k_s/c = 80 \times 10^{-6}$ used in correlation calculations.

Appendix B

Bezier Points for Airfoils

This Appendix lists the control points for each of the airfoils used throughout the report. A graphical representation of the curves and representative airfoils is also provided. The points used to generate the Bezier curves were taken directly from the experimental model, so the number of points on the airfoils differ from one to another. Also, features such as a finite length trailing edge appear in the control points and may differ slightly from the formal definition.

To recover the curves used as the airfoil surface definitions the following equations can be used:

$$[x(t) \;\; y(t)] = \sum_{i=0}^{n} B_i^n(t)\mathbf{b}_i^T, \;\; t \in [0,1] \tag{B.1}$$

where $\mathbf{b}_0, \mathbf{b}_1, ..., \mathbf{b}_n$ are given by $\mathbf{b}_i = [x_i, y_i]$, which simply correspond to rows in the tables provided. The $B_i^n(t)$ corresponds to i^{th} degree Bernstein polynomial evaluated at some point t:

$$B_i^n(t) = \binom{n}{i}(t)^i(1-t)^{n-i}, \; i = 0,1,...,n \tag{B.2}$$

The number of points and spacing along the surface can be determined by constructing a vector of the parametric variable t.

Table B.1. Control points for upper surface of NACA 63_3-418 airfoil

x/c	y/c
-0.00032	0.00325
-0.00032	0.03245
0.04109	0.04083
0.03574	0.04963
0.07501	0.08231
0.17028	0.10042
0.27523	0.11680
0.38410	0.15081
0.54283	0.11610
0.82137	0.02759
1.0	0.00117

Table B.2. Control points for lower surface of NACA 63_3-418 airfoil

x/c	y/c
-0.00032	0.00325
-0.00032	-0.01868
0.02946	-0.03028
0.07461	-0.07293
0.13396	-0.02670
0.21411	-0.07614
0.34263	-0.15613
0.54276	-0.01986
0.81762	-0.01680
0.87635	0.01554
1.0	-0.00117

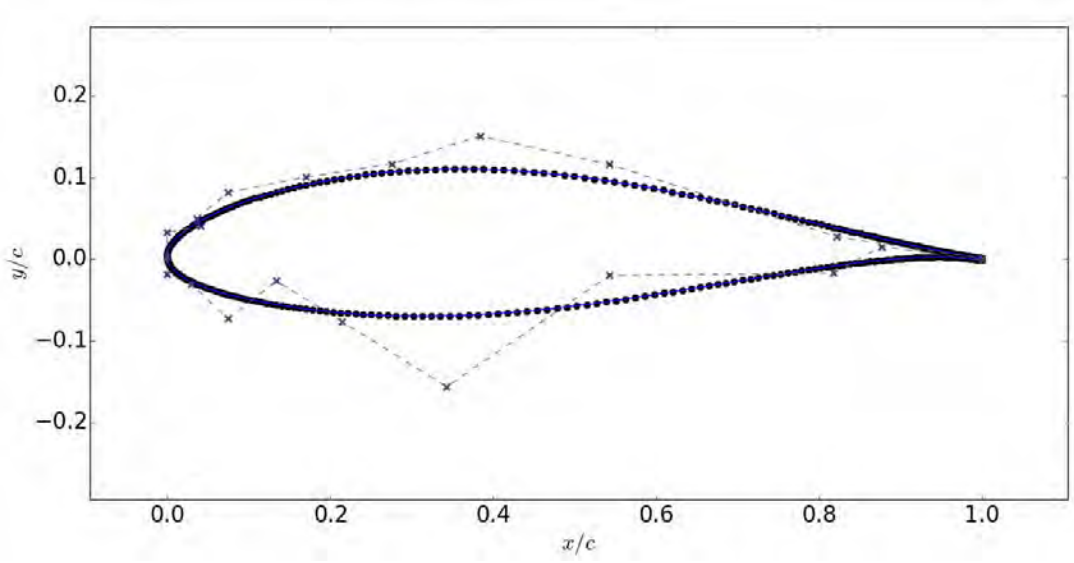

Figure B.1. Graphical representation of Bezier curves used for NACA 63_3-418 airfoil, control points indicated by x's with the dashed line connecting them.

Table B.3. Control points for upper surface of S814 airfoil

x/c	y/c
0.0	0.0
0.0	0.02233
0.02993	0.04320
0.06068	0.08949
0.27258	0.16451
0.40656	0.15298
0.54220	0.09946
0.67278	0.06281
0.79170	0.08273
0.88871	0.03871
1.0	0.00156

Table B.4. Control points for lower surface of S814 airfoil

x/c	y/c
0.0	0.0
0.0	-0.04789
0.13376	-0.12979
0.26191	-0.21731
0.32311	-0.13783
0.40945	-0.06446
0.53294	-0.05003
0.67731	-0.02273
0.80207	0.01612
0.89630	0.02363
1.0	-0.00156

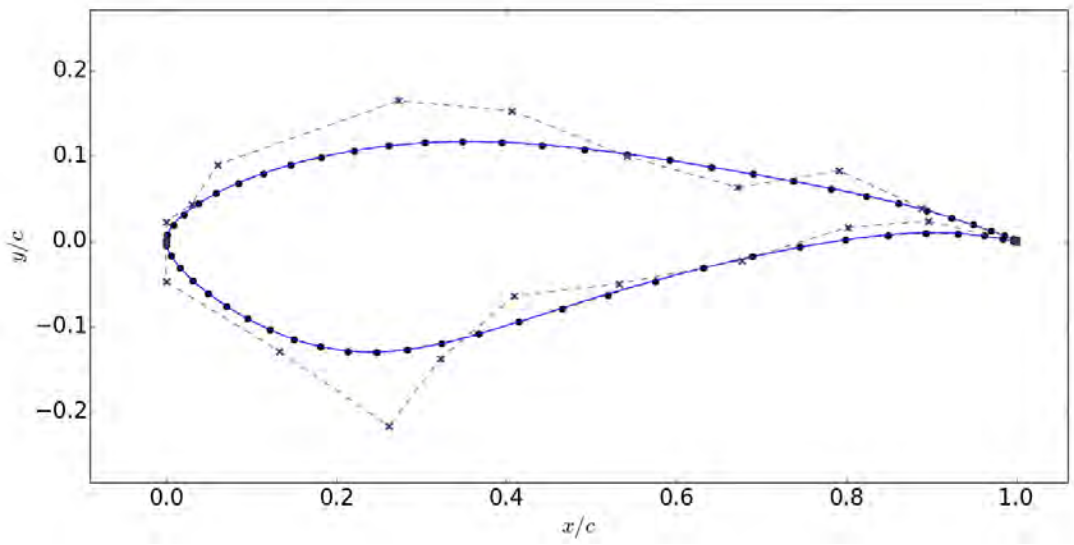

Figure B.2. Graphical representation of Bezier curves used for S814 airfoil, control points indicated by x's with the dashed line connecting them.

Table B.5. Control points for upper surface of NLF(1)-0414F airfoil

x/c	y/c
0.0	0.0
0.0	0.0373
0.0506	0.0183
0.0359	0.0589
0.1043	0.0594
0.1784	0.0575
0.2764	0.0988
0.4058	0.1203
0.5698	0.0847
0.6637	0.0514
0.6889	0.0700
0.7111	0.0944
0.7440	0.0285
0.8333	0.0002
0.8609	0.0070
0.9325	-0.0194
1.0	-0.0271

Table B.6. Control points for lower surface of NLF(1)-0414F airfoil

x/c	y/c
0.0	0.0
0.0	-0.0087
-0.0057	-0.0144
0.0439	-0.0379
0.1225	-0.0403
0.3130	-0.0684
0.4576	-0.0750
0.5528	-0.0536
0.6149	-0.0577
0.6725	-0.0756
0.7501	-0.0556
0.7522	-0.0323
0.7780	-0.0286
0.8016	-0.0287
0.8678	-0.0282
0.9080	-0.0219
1.0	-0.0275

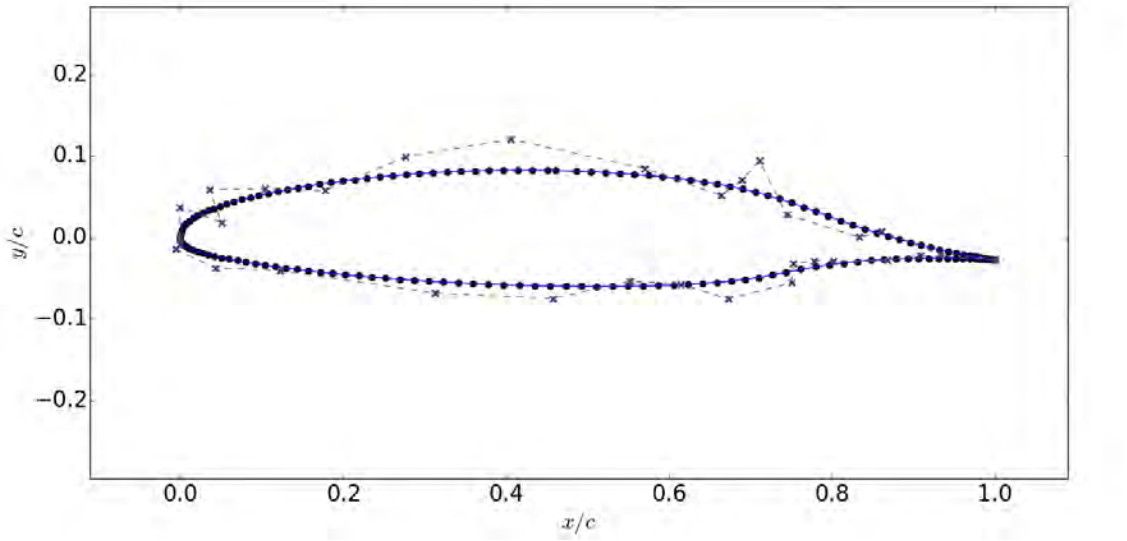

Figure B.3. Graphical representation of Bezier curves used for NLF(1)-0414F airfoil, control points indicated by x's with the dashed line connecting them.

Appendix C

Optimization Algorithms

Throughout this dissertation a number of objective functions are formulated and said to have been optimized by some iterative method. This appendix provides the mathematical details of both a gradient descent and a BFGS Quasi-Newton algorithm that are used to minimize all the functions described. A Quasi-Newton algorithm

General Problem

Given some function $f : \mathbb{R}^n \to \mathbb{R}$, determine some value $\mathbf{x}^*$ that minimizes $f(\mathbf{x})$.

$$\min_x f(\mathbf{x}) \tag{C.1}$$

In gradient based optimization, the idea is to find a step direction, $\mathbf{p}$, that will result in a reduction in magnitude of the function. Ideally $f : \mathbb{R}^n \to \mathbb{R}^+$, such that all values $\mathbf{x}$ will generate a positive $f(\mathbf{x})$, so this simplifies to a simple decrease in the function value. The step direction can be computed though a variety of methods, but the present work focuses on a gradient descent and BFGS Quasi-Newton algorithm.

Let $\mathbf{x}_k$ represent the value of the function variable $\mathbf{x}$ at the current iteration k. Given a known step direction at that iteration, $\mathbf{p}_k$, a sub-problem is set up. This is because while the algorithms that generate the direction can guarantee a function decrease, there is no indication of how "far" to perturb the current vector $\mathbf{x}_k$ in that direction. The sub-problem is often referred to as a backtracking line search, where a scalar value $\alpha \in \mathbb{R}$ is used to scale the step direction $\mathbf{p}_k$. The value of $\mathbf{x}$ at the next iteration then becomes $\mathbf{x}_{k+1} = \mathbf{x}_k + \alpha\mathbf{p}_k$. The initial choice, α_0, of this value is 1 (one) and it is decreased until certain conditions are met. The criteria for determining a value of α in the backtracking line search are known as the Wolfe Conditions. Formally, one must choose as α_i such that the following hold true:

$$\begin{aligned} f(\mathbf{x}_k + \alpha_i\mathbf{p}_k) &\leq f(\mathbf{x}_k) + c_1\alpha_i\nabla\mathbf{p}_k^T f(\mathbf{x}_k) \\ \mathbf{p}_k^T\nabla f(\mathbf{x}_k + \alpha_i\mathbf{p}_k) &\geq c_2\nabla\mathbf{p}_k^T f(\mathbf{x}_k) \end{aligned} \tag{C.2}$$

with $0 < c_1 < c_2 < 1$.

After the backtracking line search $f(\mathbf{x}_{k+1}) < f(\mathbf{x}_k)$, and the sub-iteration is repeated until a stopping condition, such as a sufficiently low function value, is met. Regardless of how the search direction is

determined, this same sub-iteration is applied. The following values are used as constants in the line search algorithm: $c_1 = 10^{-4},\ c_2 = 0.9,\ c_3 = 0.99$.

Backtracking Line Search (C.3)

Start :

$\alpha_i \leftarrow 1$

check :

$f(\mathbf{x}_k + \alpha_i \mathbf{p}_k) \leq f(\mathbf{x}_k) + c_1 \alpha_i \nabla \mathbf{p}_k^T f(\mathbf{x}_k)$

$\mathbf{p}_k^T \nabla f(\mathbf{x}_k + \alpha_i \mathbf{p}_k) \geq c_2 \nabla \mathbf{p}_k^T f(\mathbf{x}_k), \qquad 0 < c_1 < c_2 < 1$

if (true) :

$\mathbf{x}_{k+1} \leftarrow \mathbf{x}_k + \alpha_i \mathbf{p}_k$ (break)

else:

$\alpha_{i+1} \leftarrow c_3 \alpha_i, \quad c_3 < 1$

Steepest Descent and Finite Difference Approximations

The simplest method to compute the step direction is to use the gradient directly and at each iteration define:

$$\mathbf{p}_k = -\nabla f(\mathbf{x}_k) \tag{C.4}$$

with ∇ the gradient operator:

$$\nabla f(\mathbf{x}_k) = \left[\frac{\partial f}{\partial x_1},\ \frac{\partial f}{\partial x_2},\ ...,\ \frac{\partial f}{\partial x_n} \right] \tag{C.5}$$

The partial derivatives are computed using a finite difference approximation with consideration of floating point arithmetic. To help avoid loss of significant digits, the step size is chosen as $\delta = \sqrt{\varepsilon} x_i$ with ε machine zero set at 2×10^{-16}. The algorithm for computing the partial derivatives is a central difference approximation:

$$\delta = \sqrt{\varepsilon} x_i \tag{C.6}$$

$$x_{i+} = x_i + \delta, \quad x_{i-} = x_i - \delta$$
$$h = x_{i+} - x_{i-}$$
$$\frac{\partial f}{\partial x_i} = \frac{f(x_{i+}) - f(x_{i-})}{h}$$

Although algebraically identical, h and 2δ will potentially differ slightly due to finite precision floating point operations. This technique is used in any instance throughout the report a partial derivative is computed, primarily in the context of a function optimization.

Quasi-Newton Algorithm

More sophisticated techniques for computing the search direction will utilize some information about the second derivative of the function (or approximate second derivative). A "full" Newton algorithm will use the exact Hessian matrix $\nabla^2 f(\mathbf{x})$ in the computation of the step direction. The Hessian matrix is defined:

$$\nabla^2 f(\mathbf{x}) = \begin{bmatrix} \frac{\partial f}{\partial x_1^2} & \frac{\partial f}{\partial x_1 x_2} & \cdots & \frac{\partial f}{\partial x_1 x_n} \\ \vdots & \vdots & \ddots & \vdots \\ \frac{\partial f}{\partial x_1 x_n} & \frac{\partial f}{\partial x_2 x_n} & \cdots & \frac{\partial f}{\partial x_n^2} \end{bmatrix} \tag{C.7}$$

The step direction is then:

$$\mathbf{p}^{(k)} = -\nabla^2 f(\mathbf{x}_k)^{-1} \nabla f(\mathbf{x}_k) \tag{C.8}$$

In this expression $\nabla^2 F(\mathbf{x}_k)^{-1}$ represents the inverse of the Hessian matrix. This term can be troublesome as matrix inversions are computationally expensive and matrix itself must remain non-singular.

The strict requirements of a full Newton algorithm have motivated a class of methods designed to approximate the inverse Hessian matrix. These are known as Quasi-Newton methods. They are based on a generalized secant method where successive gradient vectors are used to approximate an update to the Hessian matrix. The initial guess, H_0, is typically the identity matrix and as the method iterates the approximation becomes more accurate. There are numerous references that detail the background and proofs related to the algorithms discussed, the reader is directed to Nocedal and Wright [110] for more information. Presented here is the BFGS algorithm implemented throughout this work:

BFGS Algorithm (C.9)

Start : $\mathbf{p}_0 \leftarrow -H_0 \nabla f(\mathbf{x}_0)$

Perform backtraking line search to find α s.t. Wolfe conditions are met

$\mathbf{x}_{k+1} \leftarrow \mathbf{x}_k + \alpha \mathbf{p}_k$

$\mathbf{s}_k \leftarrow \mathbf{x}_{k+1} - \mathbf{x}_k$

$\mathbf{y}_k \leftarrow \nabla f(\mathbf{x}_{k+1}) - \nabla f(\mathbf{x}_k)$

$H_{k+1} \leftarrow \left(\mathbf{I} - \rho_k \mathbf{s}_k \mathbf{y}_k^T\right) H_k \left(\mathbf{I} - \rho_k \mathbf{y}_k \mathbf{s}_k^T\right) + \rho_k \mathbf{s}_k \mathbf{s}_k^T \quad \text{with:} \quad \rho_k = \frac{1}{\mathbf{y}_k^T \mathbf{s}_k}$

$\mathbf{p}_{k+1} \leftarrow -H_{k+1} \nabla f(\mathbf{x}_{k+1})$

Appendix D

Sample OVERFLOW Input Files

This chapter contains a sample input file used for an o-type grid with roughness model.

```
$GLOBAL
   RESTRT = .F., GRDWTS = .T., CHIMRA = .F., NQT = 505,
   NSTEPS = 10000, NSAVE = 5000, NFOMO = 1,
   SAVE_HIORDER = 2, ISTART_QAVG = 9990000,
   MULTIG = .F., FMG = .F., NGLVL = 0,
   $END
$OMIGLB
   IRUN = 0, I6DOF = 0,
   DYNMCS = .F., NADAPT = 0,
   $END
$DCFGLB
   DQUAL = 1.0, MORFAN = 1, NORFAN = 5,
   $END
$GBRICK
   OBGRIDS = .F.,
   $END
$BRKINP
   $END
$GROUPS
   $END
$FLOINP
   ALPHA = 0.0,  FSMACH = 0.2,  REY = 2.4e6,
   RETINF = 1e1, XKINF = 9.0e-5,
   $END
$VARGAM $END
$GRDNAM
   NAME = 'naca63-418',
  $END
$NITERS
   $END
$METPRM
   IRHS = 0, ILHS = 2, IDISS = 4,  BIMIN = 1.0,
  $END
$TIMACU
   ITIME = 1, DT = 0.8, CFLMIN = 0.8, CFLMAX = 0.0,
  $END
$SMOACU
   ISPEC = 2,  SMOO = 0.0,  DIS2 = 0.0,  DIS4 = 0.02,  FSO = 6,
   $END
$VISINP
   VISC = .T., ISTRAIN = 2,
   $END
$BCINP
   IBTYP =    5,  606,  10,  21,  47,
   IBDIR =    2,    2,   1,   3,  -2,
   JBCS  =    1,  211,   1,   1,   1,
   JBCE  =   -1,  306,   1,  -1,  -1,
   KBCS  =    1,    1,   1,   1,  -1,
   KBCE  =    1,    1,  -1,  -1,  -1,
   LBCS  =    1,    1,   1,   1,   1,
```

```
   LBCE  =   -1,   -1,  -1,   1,  -1,
   BCPAR1(2) = 80.0e-6,
   $END
$SCEINP $END
$SIXINP $END
```

References

[1] R. Ehrmann, E. White, D. Maniaci, R. Chow, C. Langel, and C. van Dam, "Realistic leading-edge roughness effects on airfoil performance," in *31st Applied Aerodynamics Conference*, 2013.

[2] J. Bons, "A review of surface roughness effects in gas turbines," *Journal of Turbomachinery*, vol. 132, no. 021004, pp. 1–16, 2010.

[3] M. Kerho and M. Bragg, "Airfoil boundary-layer development and transition with large leading-edge roughness," *AIAA Journal*, vol. 35, no. 1, pp. 75–84, 1997.

[4] R. Mayle, "The role of laminar-turbulent transition in gas turbo engines," *Journal of Turbomachinery*, vol. 113, no. 4, pp. 509–537, 1991.

[5] M. Keegan, D. Nash, and M. Stack, "On erosion issues associated with the leading edge of wind turbine blades," *Journal of Applied Physics*, vol. 46, pp. 1–20, 2013.

[6] A. Sareen, C. Sapre, and M. Selig, "Effects of leading edge erosion on wind turbine blade performance," *Wind Energy*, vol. DOI: 10.1002/we.1649, 2013.

[7] R. van Rooij and W. Timmer, "Roughness sensitivity considerations for thick rotor blade airfoils," *Journal of Solar Energy Engineering*, vol. 125, pp. 468–478, 2003.

[8] R. Ramsay, M. Hoffmann, and G. Gregorek, "Effects of grit roughness and pitch oscillations on the s815 airfoil," Tech. Rep. 442-7820, National Renewable Energy Lab, 1996.

[9] D. Berg, "A review of the workshop on wecs blade-surface roughness," in *ASME Wind Energy Symposium*, 1994.

[10] L. Rayleigh, "On the stability of instability of certain fluid motions," *Proc. London Math. Soc*, vol. s1-11, no. 1, pp. 57–72, 1879.

[11] G. Schubauer and H. Skramtad, "Laminar-boundary-layer oscillations and transition," Tech. Rep. 909, National Advisory Committee for Aeronautics, 1943.

[12] H. Schlicting, *Boundary-Layer Theory*. McGraw-Hill, 1968.

[13] P. Klebanoff, K. Tidstrom, and L. Sargent, "The three-dimensional nature of boundary-layer instability," tech. rep., National Bureau of Standards, 1961.

[14] T. Herbert, "Secondary instabilities of boundary layers," *Annual Review of Fluid Mechanics*, vol. 20, pp. 487–526, 1988.

[15] A. Craik, "Wave-induced longitudinal-vortex instability in shear flows," *Journal of Fluid Mechanics*, vol. 125, pp. 37–52, 1982.

[16] M. V. Morkovin, "On the many faces of transition," in *Symposium on Viscous Drag Reduction*, 1969.

[17] M. Morkovin, E. Reshotko, and T. Herbert, "Transition in open flow systems - a reassessment," *Bulletin of the American Physical Society*, vol. 39, no. 9, p. 1882, 1994.

[18] T. Cebeci, *Stability and Transition: Theory and Application*. Horizons Publishing, 2004.

[19] J. van Ingen, "A suggested semi-empirical method for the calculation of the boundary layer transition region," Tech. Rep. VTH-74, Technische Hogeschool Vliegtuigbouwkunde, 1956.

[20] A. Smith and Gamberoni, "Transition, pressure gradient and stability theory," Tech. Rep. ES 26388, Douglas Aircraft Company, 1956.

[21] M. Drela and M. Giles, "Viscous-inviscid analysis of transonic and low reynolds number airfoils," *AIAA Journal*, vol. 25, no. 10, pp. 1347–1355, 1987.

[22] R. Brodeur and C. van Dam, "Transition prediction for a two-dimensional Reynolds-averaged navier-stokes method applied to wind turbine airfoils," *Wind Energy*, vol. 4, pp. 61–75, 2001.

[23] E. Mayda, *Boundary-layer Transition Prediction for Reynolds-averaged Navier-Stokes Methods*. PhD thesis, University of California, Davis, 2007.

[24] B. Abu-Ghannam and R. Shaw, "Natural transition of boundary layers - the effects of turbulence, pressure gradient and flow history," *Journal of Mechanical Engineering Sciences*, vol. 22, no. 5, pp. 213–228, 1980.

[25] S. Dhawan and R. Narasimha, "Some properties of boundary layer flow during the transition form laminar to turbulent motion," *Journal of Fluid Mechanics*, vol. 3, no. 4, pp. 418–436, 1958.

[26] J. Steelant and E. Dick, "Modelling of bypass transition with conditioned navier-stokes equations coupled to an intermittency transport equation," *International Journal for Numerical Methods in Fluids*, vol. 23, pp. 193–220, 1996.

[27] E. Warren and H. Hassan, "Transition closure model for predicting transition onset," *Journal of Aircraft*, vol. 35, no. 5, pp. 769–775, 1998.

[28] Y. Suzen and P. Huang, "Modeling of flow transition using and intermittency transport equation," *Journal of Fluids Engineering*, vol. 112, pp. 273–284, 2000.

[29] K. Walters and J. Leylek, "A new model for boundary-layer transition using a single-point RANS approach," *Heat Transfer*, vol. 6, no. IMECE2002-32740, pp. 67–79, 2002.

[30] R. Mayle and A. Schulz, "The path to predicting bypass transition," in *International Gas Turbine and Aeroengine Congress and Exhibition*, 1996.

[31] J. Coder and M. Maughmer, "Computational fluid dynamics compatible transition modeling using an amplification factor transport equation," *AIAA Journal*, vol. 52, no. 11, pp. 2506–2512, 2014.

[32] L. Mack, "Transition and laminar instability," Tech. Rep. CR-153203, NASA, 1977.

[33] R. Langtry and F. Menter, "Correlation-based transition modeling for unstructured parallelized computation fluid dynamics codes," *AIAA Journal*, vol. 47, no. 12, pp. 2894–2906, 2009.

[34] S. Medida, *Correlation-based Transition Modeling for External Aerodynamic Flows*. PhD thesis, University of Maryland, College Park, 2014.

[35] J. Coder and M. Maughmer, "One-equation transition closure for eddy-viscosity turbulence models in cfd," in *50th AIAA Aerospace Sciences Meeting including the New Horizons Forum and Aerospace Exposition*, 2012.

[36] F. Menter, P. Smirnov, T. Liu, and R. Avancha, "A one-equation local correlation-based transition model," *Flow, Turbulence and Comb*, vol. DOI: 10.1007/s10494-015-9622-4, 2015.

[37] T. Corke, A. Bar-Sever, and M. Morkovin, "Experiments on transition enhancement by distributed roughness," *Physics of Fluids*, vol. 29, no. 10, pp. 3199–3213, 1986.

[38] H. Dryden, "Combined effects of turbulence and roughness on transition," *ZAMP Zeitschrift fr Angewandte Mathematik und Physik*, vol. 9, no. 5-6, pp. 249–258, 1958.

[39] C. Merkle and T. Kubota, "An analytical study of the effects of surface roughness on boundary-layer transition," Tech. Rep. AD/A-004 786, Flow Research Inc., 1973.

[40] J. Kendall, "The effect of small-scale roughness on the mean flow profile of a laminar boundary layer," *Instability and Transition*, vol. 1, pp. 296–302, 1990.

[41] P. Klebanoff and K. Tidstrom, "Mechanism by which a two-dimensional roughness element induces boundary-layer transition," *Physics of Fluids*, vol. 15, no. 7, pp. 1173–1186, 1972.

[42] F. Ergin and E. White, "Unsteady and transitional flows behind roughness elements," *AIAA Journal*, vol. 44, no. 11, pp. 2504–2514, 2006.

[43] M. Acalar and C. Smith, "A study of hairpin vortices in a laminar boundary layer. part 1. hairpin vortices generated by a hemisphere protuberance," *Journal of Fluid Mechanics*, vol. 175, pp. 1–41, 1987.

[44] I. Tani, H. Komoda, and Y. Komatsu, "Boundary-layer transition by isolated roughness," Tech. Rep. 375, Aeronautical Research Institute, University of Tokyo, 1962.

[45] N. Gregory and W. Walker, "The effect of transition of isolated surface excrescences in the boundary layer," Tech. Rep. 2779, Aeronautical Research Council, 1951.

[46] M. Mochizuki, "Smoke observations on boundary layer transition caused by a spherical roughness element," *Journal of Physical Society of Japan*, vol. 16, no. 5, pp. 995–1007, 1961.

[47] P. Klebanoff, W. Cleveland, and K. Tidstrom, "On the evolution of a turbulent boundary layer induced by a three-dimensional roughness element," *Journal of Fluid Mechanics*, vol. 237, pp. 101–187, 1992.

[48] R. Norman, *On Obstacle-generated Secondary Flows in Laminar Boundary Layers and Transition to Turbulence*. PhD thesis, Illinois Institute of Technology, 1972.

[49] M. Bernardini, S. Pirozzoli, P. Orlandi, and S. Lele, "Compressible boundary layer transition induced by isolated roughness elements," in *Center for Turbulence Research, Proceedings of the Summer Program*, 2012.

[50] J. Nikuradse, "Laws of flow in rough pipes," Tech. Rep. 1292, NACA, 1933.

[51] A. Braslow and E. Knox, "Simplified method for determination of critical height of distributed roughness particles for the boundary-layer transition at mach numbers from 0 to 5," Tech. Rep. 4363, National Advisory Committee for Aeronautics, 1958.

[52] E. Feindt, "Untersuchungen u ber die abha ngigkeit des umschlages laminar turbulent von der oberfla chenrauhigkeit und der druckverteilung," *DFL Bericht*, vol. 43, 1956.

[53] L. Levanthal and E. Reshotko, "Preliminary experimental study of disturbances in a laminar boundary-layer due to distributed surface roughness," Tech. Rep. 81-0588, Case Western Reserve University, 1981.

[54] M. Kerho, *Effect of Large Distributed Roughness Near an Airfoil Leading Edge on Boundary-Layer Development and Transition*. PhD thesis, University of Illinois at Urbana-Champaign, 1995.

[55] K. Singh and J. Lumley, "Effect of roughness on the velocity profile of a laminar boundary layer," *Applied Science Res.*, vol. 24, pp. 168–186, 1971.

[56] M. Lessen and S. Gangwani, "Effect of small amplitude waviness upon the stability of laminar boundary layers," *Physics of Fluids*, vol. 19, no. 4, pp. 510–514, 1976.

[57] J. Robertson, *Surface Resistance as a Function of the Concentration and Size of Roughness Elements*. PhD thesis, Iowa State University, 1961.

[58] N. Denissen and E. White, "Continuous spectrum analysis of roughness-induced transient growth," *Physics of Fluids*, vol. 21, no. 11, pp. 1–13, 2009.

[59] A. Tumin, "Multimode decomposition of spatially growing pertubations in a two-dimensional boundary layer," *Physics of Fluids*, vol. 15, no. 9, pp. 2525–2540, 2003.

[60] N. Denissen, *Roughness-Induced Transient Growth: Continuous Spectrum Receptivity and Secondary Instability Analysis*. PhD thesis, Texas A&M University, 2011.

[61] B. Aupoix and P. Spalart, "Extensions of the Spalart-Allmaras turbulence model to account for wall roughness," *International Journal of Heat and Fluid Flow*, vol. 24, no. 4, pp. 454–462, 2003.

[62] A. Hellsten and S. Laine, "Extension of the $k-\omega$ - sst turbulence model for flows over rough surfaces," in *AIAA Atmospheric Flight Mechanics Conference*, 1997.

[63] S. Medida, J. Baeder, N. Nigam, and P. Chen, "Variable surface roughness modeling for skin friction estimation," in *52nd Aerospace Sciences Meeting*, 2014.

[64] D. Wilcox, *Turbulence Modeling for CFD*. DCW Industries, 2006.

[65] T. Knopp, B. Eisfeld, and J. Bartolome Calvo, "A new extension for $k-\omega$ turbulence models to account for wall roughness," *International Journal of Heat and Fluid Flow*, vol. 30, no. 1, pp. 54–65, 2009.

[66] B. Aupoix, "A general strategy to extend turbulence models to rough surfaces: Application to smiths k-l model," *J. Fluids Eng*, vol. 129, no. 10, pp. 1245–1254, 2007.

[67] B. Aupoix, "Roughness corrections for the k shear stress transport model: Status and proposals," *J. Fluids Eng*, vol. 137, no. 2, pp. 021202–021202–10, 2014.

[68] J. van Ingen, "The e^n method for transition prediction. historical review of work at TU Delft," in *38th Fluid Dynamics Conference and Exhibit*, 2008.

[69] M. Stripf, A. Schulz, H.-J. Bauer, and S. Wittig, "Extended models for transitional rough wall boundary layers with heat transfer - part i: Model formulations," *Journal of Turbomachinery*, vol. 131, no. 031016, pp. 1–10, 2009.

[70] W. Elsner and P. Warzecha, "Numerical study of transitional rough wall boundary layers," *Journal of Turbomachinery*, vol. 136, no. 011010, pp. 1–11, 2014.

[71] P. Dassler, D. Kozulovic, and A. Fiala, "Modelling of roughness-induced transition using local variables," in *V European Conference on Computational Fluid Dynamics*, 2010.

[72] P. Dassler, D. Kozulovic, and A. Fiala, "An approach to modelling the roughness-induced boundary layer transition using transport equations," in *European Congress on Computational Methods in Applied Sciences and Engineering*, 2012.

[73] R. Ehrmann, *Effect of Surface Roughness on Wind Turbine Performance*. PhD thesis, Texas A&M University, 2014.

[74] J. Hidore, "Investigation of data quality for wind tunnel internal balance testing," Master's thesis, Texas A&M University, 2013.

[75] W. Wright, "User manual for the NASA Glenn ice accretion code Lewice: Version 2.0," Tech. Rep. CR-1999-209409, NASA, 1999.

[76] B. Wilcox, *Roughness Sensitivity Comparisons of Wind Turbine Blade Sections*. PhD thesis, Texas A&M University, 2016.

[77] C. Navier, "Mémoire sur les lois du mouvement des fluides," *Mem. Acad. R. Sci. Paris*, vol. 6, pp. 389–416, 1823.

[78] A. Cauchy, *Exercices de mathmatiques*. Bure Bure frres, 1828.

[79] G. Stokes, "On the theories of internal friction of fluids in motion," *Trans. Camb. Phil. Soc.*, vol. 8, pp. 287–305, 1845.

[80] C. Wang, "Exact solutions of the steady-state Navier Stokes equations," *Annual Review of Fluid Me-chanics*, vol. 23, pp. 159–177, 1991.

[81] A. Chorin, "Numerical solution of the Navier-Stokes equations," *Mathematics of Computation*, vol. 22, pp. 745–762, 1968.

[82] L. Berselli, T. Iliescu, and W. Layton, *Mathematics of Large Eddy Simulation of Turbulent Flows*. Springer, 2006.

[83] E. van Driest, "On turbulent flow near a wall," *Journal of the Aeronautical Sciences*, vol. 23, no. 11, pp. 1007–1011, 1956.

[84] T. Cebeci, G. Mosinskis, and A. Smith, "Calculation of compressible adiabatic turbulent boundary layers," *AIAA Journal*, vol. 8, no. 11, pp. 1974–1982, 1970.

[85] B. Baldwin and T. Barth, "A one-equation turbulence transport model for high Reynolds number wall-bounded flows," Tech. Rep. 102847, NASA, 1990.

[86] P. Spalart and S. Allmaras, "A one-equation turbulence model for aerodynamic flows," in *30th Aerospace Sciences Meeting and Exhibit*, 1992.

[87] J. Bardina, P. Huang, and T. Coakley, "Turbulence modeling, validation, testing and development," Tech. Rep. 110446, NASA, 1997.

[88] L. Kral, "Recent experience with different turbulence models applied to the calculation of flow over aircraft," *Progress in Aerospace Sciences*, vol. 34, pp. 481–541, 1998.

[89] W. Jones and B. Launder, "The prediction of laminarization with a two-equation model of turbulence," *International Journal of Heat and Mass Transfer*, vol. 15, pp. 301–314, 1972.

[90] D. Wilcox, "Multiscale model for turbulent flows," *AIAA Journal*, vol. 26, pp. 1311–1320, 1988.

[91] D. Wilcox, "A half century historical review of the $k-\omega$ model," in *29th Aerospace Sciences Meeting*, 1991.

[92] F. Menter, "Improved two-equation $k-\omega$ turbulence models for aerodynamic flows," Tech. Rep. 103975, NASA, 1992.

[93] B. Launder, G. Reece, and W. Rodi, "Progress in the development of a Reynolds-stress turbulent closure," *Journal of Fluid Mechanics*, vol. 68, no. 3, pp. 537–566, 1975.

[94] C. Spezial, S. Sarkar, and T. Gatski, "Modeling the pressure-strain correlation of turbulence: an invariant dynamical systems approach," *Journal of Fluid Mechanics*, vol. 227, pp. 245–272, 1991.

[95] S. Nasizima and A. Yoshizawa, "Turbulent channel and couette flows using an anisotropic $k-\varepsilon$ model," *AIAA Journal*, vol. 25, no. 3, pp. 414–420, 1987.

[96] P. Spalart, W. Jou, M. Strelets, and S. Allmaras, "Comments on the feasibility of les for wings, and on a hybrid RANS/LES approach," in *Advances in DNS/LES, 1st AFOSR International Conerence on DNS/LES*, 1997.

[97] R. Chow and C. van Dam, "Verification of computational simulations of the NREL 5 MW rotor with a focus on inboard flow separation," *Wind Energy*, vol. 15, no. 8, pp. 967-981, 2012.

[98] P. Spalart, "Detached-eddy simulation," *Annual Review of Fluid Mechanics*, vol. 41, pp. 181–202, 2009.

[99] T. Pulliam and D. Chaussee, "A diagonal form of an implicit approximate-factorization algorithm," *Journal of Computational Physics*, vol. 39, pp. 347–363, 1981.

[100] T. Pulliam, "Development of implicit methods in CFD NASA Ames Research Center 1970's - 1980's," *Computers and Fluids*, vol. 41, pp. 65–71, 2011.

[101] T. Pulliam, "High order accurate finite-difference methods: as seen in overflow," in *AIAA Computational Fluid Dynamics Conference*, 2011.

[102] E. V. Driest and C. Blumer, "Boundary layer transition: Freestream turbulence and pressure gradient effects," *AIAA Journal*, vol. 1, no. 6, pp. 1303–1306, 1963.

[103] P. Spalart and C. Rumsey, "Effective inflow conditions for turbulence models in aerodynamic calculations," *AIAA Journal*, vol. 45, no. 10, pp. 2544–2558, 2007.

[104] M. Kato and B. Launder, "The modeling of turbulent flow around stationary and vibrating square cylinders," in *9th Symposium on Turbulent Shear Flows*, 1993.

[105] R. McGhee, J. Viken, and W. Pfenninger, "Experimental results for a flapped natural-laminar flow airfoil with high lift/drag ratio," Tech. Rep. TM-85788, NASA, 1984.

[106] C. Langel, "A transport equation approach to modeling the influence of surface roughness on boundary layer transition," Master's thesis, University of California, Davis, 2014.

[107] R. Langtry, *A Correlation-Based Transition Model using Local Variables for Unstructured Parallelized CFD codes*. PhD thesis, University of Stuttgart, Germany, 2006.

[108] D. Wilcox, "Simulation of transition with a two-equation turbulence model," *AIAA Journal*, vol. 32, no. 2, pp. 247–255, 1994.

[109] B. Thompson, "A critical review of existing methods of calculating the turbulent boundary layer," Tech. Rep. 3447, Aeronautical Research Council Reports and Memoranda, 1967.

[110] J. Nocedal and S. Wright, *Numerical Optimization*. Springer-Verlag, 2006.

DISTRIBUTION:

External (electronic)

M. Derby	Department of Energy	

SNL Internal (electronic)

MS0825	M. F. Barone	1515
MS1124	D. C. Mania	8821
MS1124	D. G. Minst	8821
MS1124	J. A. Paquette	8821
MS0899	Technical Library	9536


Sandia National Laboratories